Insights into the distribution and mobility of base metals in the sheeted dike complex formed at fast-spreading ridges (Pito Deep, EPR)

by

Khalhela Zoeller

BSc, Dalhousie University, 2011

A Thesis Submitted in Partial Fulfillment

of the Requirements for the Degree of

MASTER OF SCIENCE

in the School of Earth and Ocean Sciences

© Khalhela Zoeller, 2014
University of Victoria

All rights reserved. This thesis may not be reproduced in whole or in part, by photocopy
or other means, without the permission of the author.

Supervisory Committee

Insights into the distribution and mobility of metals in the sheeted dike complex formed at fast-spreading ridges (Pito Deep, EPR)

By

Khalhela Zoeller

BSc, Dalhousie University, 2011

Dr. Kathryn Gillis, Supervisor
(School of Earth and Ocean Sciences)

Dr. Laurence Coogan, Departmental Member
(School of Earth and Ocean Sciences)

Dr. Dante Canil, Department Member
(School of Earth and Ocean Sciences)

Committee Members

Dr. Kathryn Gillis (School of Earth and Ocean Sciences)
Supervisor

Dr. Laurence Coogan (School of Earth and Ocean Sciences)
Departmental Member

Dr. Dante Canil (School of Earth and Ocean Sciences)
Department Member

Abstract

Hydrothermal fluid circulation is an important process in the formation and evolution of ocean crust. A tectonic window located at Pit Deep (NE corner Easter Microplate) provides an ideal location to examine a 3-dimensional view of ocean crust formed at the fast-spreading East Pacific Rise. Fluid conditions at depth suggest that mobilization and leaching of the metals in the crust should occur; yet previous work has shown that not all of the metals have been removed from the crust. This study focuses on the base metal (Cu, Ni, Mn, Co, Zn, and Pb) content of the bulk rock and mineral components in the sheeted dike complex. There is no observable trend of metal mobility with depth, geographic location, or dominant alteration phase. Secondary mineral analyses (using LA-ICP-MS) show that metals are redistributed throughout the sheeted dikes, entering into secondary sulphides, chlorite, and amphibole. Temperature and mineral stability is a primary control of metal mobility in these rocks. Due to highly variable metal concentrations and observed temperatures of alterations, the hydrothermal cell is suggested to be a continuously evolving system, and can cause the large variability observed in the metal distribution in the sheeted dikes.

Table of Contents

Supervisory Committee **ii**

Abstract **iii**

Table of Contents **iv**

List of Figures **vii**

List of Tables **ix**

Chapter 1: Introduction **1**

1.1 Mid-Ocean Ridges and Axial Hydrothermal Systems **1**

1.2 Metal Mobility and Development of Fe-Cu deposits **7**

1.3 Thesis Objective **8**

1.4 Geological Setting and Sample Suite **9**

1.5 Summary of previous petrological studies at Pito Deep **13**

1.5.1 Igneous Petrology 13

1.5.2 Metamorphic Petrology and Geochemistry 14

Chapter 2: Base Metal Mobility Constrained from Bulk Rock Compositions **19**

2.1 Introduction **19**

2.2 Assessment of Fresh Rock Compositions **20**

2.3 Calculation of Protolith Metal Concentrations **20**

2.3.1 Changes in metal mobility with depth and region 29

2.3.2 Role of secondary mineral assemblage in metal mobility 32

2.4 Discussion **33**

2.4.1 Comparison of Pito Deep to Hess Deep and Hole 1256D 35

2.4.2 Quantifying the Source Region for Fe-Cu Ore Formation 37

2.4.3 Summary 43

Chapter 3: Mineralogical Controls on Metal Mobility **45**

3.1 Introduction **45**

3.2 Sample Suite **45**

3.3 Analytical Techniques **46**

3.4 Petrologic Characteristics and Major Element Compositions of Igneous and Metamorphic Minerals **49**

3.4.1 Plagioclase 49
3.4.2 Clinopyroxene 49
3.4.3 Fe-Ti Oxides 50
3.4.4 Phyllosilicates 52
3.4.5 Amphibole 54
3.4.6 Fe-Cu Sulphides 54
3.5 Mineral Base Metal Compositions **57**
3.5.1 Plagioclase 57
3.5.2 Clinopyroxene 59
3.5.3 Fe-Ti Oxides 64
3.5.4 Chlorite and Mixed-layer Clays 68
3.5.5 Amphibole 76
3.5.6 Fe-Cu Sulphide 82
3.6 Metal content of secondary phases hosted in Hydrothermal Breccias **86**
3.7 Modal Abundance and Mass Balance **91**
3.7.1 Modal Abundance 91
3.7.2 Mass Balance Calculation 94
3.8 Summary of the effect of mineralogy on base metal mobility **100**
3.8.1 Primary mineral base metal sources 100
3.8.2 Secondary mineral metal sinks 101
3.8.3 Primary phase versus replacement mineral 104
3.8.4 Direct precipitate versus secondary chlorite 106

Chapter 4: Discussion **107**
4.1 Introduction **107**
4.2 Environmental controls on base metal mobility **107**
4.2.1 Temperature 108
4.2.2 Fluid Chemistry 111
4.2.2.1 Redox State 112

4.2.2.2 pH 113
4.2.2.3 Salinity 114
4.2.3 Mineral Stability and Fluid Saturation 115
4.3 Timing of metal mobilization 118
4.4 Summary 124

Chapter 5: Conclusions and Future Work 127
5.1 Conclusions 127
5.2 Future Work 129

References 131

Appendices 142
Appendix A: Analytical Parameters, Precision and Accuracy of Mineral Analyses 142
Appendix A.1 Electron Microprobe Analyses 142
Appendix A.2: Laser Ablation Inductively Coupled Plasma Mass Spectrometry (LA-ICP-MS) Analyses 143
Appendix A.2.1: Accuracy and Precision of LA-ICP-MS Data 143
Appendix A.2.2 Comparison of Data from EMP and LA-ICP-MS 146
Appendix B: Thin Sections 147
Appendix B.1: Thin Section Descriptions 147
Appendix B.2: Glossary of Textures (Pictures) 169
Appendix C: Maps of Metal Distribution 173

List of Figures

Figure 1.1: Conceptual model of fluid flow 3

Figure 1.2: Variation of fluid temperature in ocean crust 3

Figure 1.3: 2D model of thermal instabilities in the root zone of the hydrothermal system 5

Figure 1.4: Location of Pito Deep 10

Figure 1.5: Outcrop photos of lithological units 11

Figure 1.6: Geological maps of Pito Deep with dive tracks 12

Figure 2.1: Plots of bulk rock base metal concentrations versus Y for EPR glass 22

Figure 2.2: Plots of bulk rock Δ metal versus MgO (wt%) 25

Figure 2.3: Plots of bulk rock metal concentration versus bulk rock S for Pito Deep samples 26

Figure 2.4: Plots of bulk rock Δ metal values versus depth at Pito Deep 30

Figure 2.5: Maps of Δ metal distribution at Pito Deep 31

Figure 2.6: Plots of secondary mineral modal abundance versus Δ metal Values 34

Figure 2.7: Plots of Δ metal versus depth at Pito Deep, Hess Deep, and Hole 1256D 36

Figure 2.8: Sources and sinks of base metals at the seafloor 38

Figure 3.1: Regional maps of Pito Deep showing sample locations 47

Figure 3.2: Plot of Fe-Ti oxide major element mineral composition 51

Figure 3.3: Classification scheme for phyllosilicates based on Si 53

Figure 3.4: Classification scheme for phyllosilicates based on Al 53

Figure 3.5: Classification of amphiboles 55

Figure 3.6: Major element composition of Fe-Cu sulphides 56

Figure 3.7: Plots of base metal concentrations in primary clinopyroxene 60

Figure 3.8: Plots of base metal concentration versus major elements in Fe-Ti oxides 66

Figure 3.9: Plots base metal content in chlorite and mixed-layer clay 69

Figure 3.10: Si cation versus base metal content in phyllosilicates 70

Figure 3.11: Plots base metal content in phyllosilicates based on mode of occurrence 71

Figure 3.12: Ni and Mn versus major elements in phyllosilicates 73

Figure 3.13: Plots of base metal concentration in amphibole 77

Figure 3.14: Plots of base metal content versus tetrahedral Al in amphiboles 79

Figure 3.15: Tetrahedral Al from amphiboles versus depth 80

Figure 3.16: Plots of Ni, Co, Cu, and Zn versus Fe in pyrite 83

Figure 3.17: Plots of base metals in chlorite from hydrothermal breccias and groundmass 88

Figure 3.18: Plots of Cu mobility in secondary silicates from Pito Deep 102

Figure 3.19: Plots comparing base metal content in primary versus secondary phases 105

Figure 4.1: Illustration summarizing the mobilization and redistribution of metals at Pito Deep 120

List of Tables

Table 2.1: Base metal concentrations, Δ values, and % depletion/enrichment in the sheeted dikes 28

Table 2.2: Parameters used to constrain the region of alteration needed to form a VMS deposit 41

Table 3.1: Plagioclase base metal concentrations 58

Table 3.2: Base metal concentration in clinopyroxene and comparison to calculated magmatic values 63

Table 3.3: Base metal concentrations in Fe-Ti oxides 67

Table 3.4: Concentration of base metals in chlorite and mixed-layer clays. 75

Table 3.5: Base metal concentrations in amphibole 81

Table 3.6: Base metal concentration in Fe-Cu sulphides. 85

Table 3.7: Base metal concentration in silicate and sulphide minerals found in the hydrothermal breccias. 90

Table 3.9: Modal abundance of primary and secondary minerals. 93

Table 3.10a: Comparison of bulk rock calculated and measured Zn values 96

Table 3.10b: Comparison of bulk rock calculated and measured Co values 97

Table 3.10c: Comparison of bulk rock calculated and measured Ni values 98

Table 3.10d: Comparison of bulk rock calculated and measured Mn values 99

Chapter 1

Introduction

1.1 Mid-Ocean Ridges and Axial Hydrothermal Systems

Hydrothermal circulation at mid-ocean ridges is an important process that influences crustal accretion and alteration processes, and the extraction of a significant proportion of global heat budget. Studies of ancient and modern ocean crust provide insight into the processes occurring at mid-ocean ridges. These studies have been conducted by means of ocean crust drill holes (e.g. IODP Hole 1256D; Dziony, et al., 2008; Alt et al., 2010), tectonic windows (e.g. Pito Deep; Barker, et al., 2008; Pollock, et al., 2009), and ophiolites (e.g. Troodos; Cann & Gillis, 2004; Jowitt et al., 2012).

Global heat flux studies show that high temperature hydrothermal fluids exiting the seafloor transport large quantities of heat from the ocean crust (Morton and Sleep, 1985; Coogan, 2008; Coogan and Dosso, 2012; Hutnak and Fisher, 2007; Stein and Stein, 1994). Quantifying the heat flux along a specific section of mid-ocean ridge can be difficult because the total power output of a hydrothermal system, along with the horizontal dimensions of a cell, are needed (Fontaine and Wilcock, 2007). However generalized numerical models of fluid and heat flux give insight into the possible range of values. The heat released from the lower ocean crust, that cools to ~1000°C, can range from ~0.33-1 MJ of heat released per kg of lower ocean crust created (4-12 TJ m^{-2}; Coogan, 2008).

Hydrothermal convection is driven by the substantial heat loss from the lower ocean crust (both the latent heat of crystallization and cooling of the magma; Mottl, 1983). Along fast-spreading mid-ocean ridges, thin (10's m), narrow (<2 km) axial

magma chambers (AMC) generally lie less than 1 km below the seafloor (Detrick, 1991; Sinton and Detrick, 1992; Hooft et al., 1997; Detrick et al., 1987). Seismic studies identify a crustal low velocity zone beneath the narrow AMC, that is interpreted as a partially solidified crystal mush zone (Detrick et al., 1987; Sinton and Detrick, 1992).

A conceptual model of axial hydrothermal circulation involves seawater entering and permeating down into the crust through fracture networks and faults in a recharge zone, heating up as it travels through the hydrothermal root zone closer to the AMC, and rising up through the crust in a discharge zone due to changes in the buoyancy of the fluid (Figure 1.1). Hydrothermal fluid flow in ocean crust occurs as pervasive fluid flow along small fractures and grain boundaries and focused flow through faults and fractures (e.g. Alt, 1995; Barker et al., 2010).

Three-dimensional numerical models for active MOR hydrothermal systems suggest that circulation cells may organize themselves into narrow pipe-like, high temperature, up-flow (discharge) zones that are surrounded by cool to warm down-flow (recharge) zones (e.g., Coumou et al., 2008). These models predict that circulation cells are not continuous and stationary features, but rather, they can stop and start at a given location, and migrate along the axis (e.g. Coumou et al., 2006, 2008; Fontaine and Wilcock, 2007). Due to this unstable cell structure, temperature variation within the crust will not be consistent. Studies of temperature distribution from the geologic record, within the zones of recharge and discharge, confirm that temperature is not a smooth gradient with depth, but that temperature increases only occur close to the AMC, and within close proximity to the narrow discharge zone (Figure 1.2; Coogan, 2008). Causes

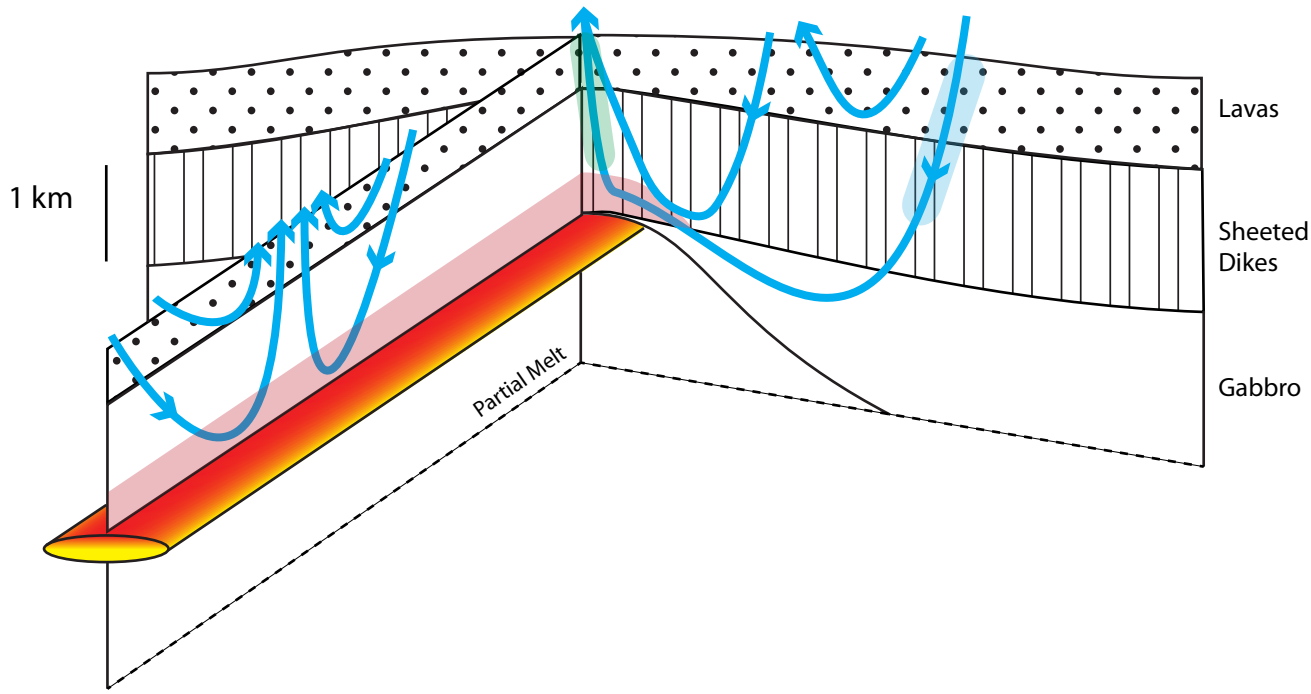

Figure 1.1: Conceptual model of hydrothermal circulation parallel and perpendicular to the ridge axis. Down-welling fluid in a recharge zone (highlighted blue region) travels into the crust where it can reach a high-temperature root zone adjacent to the AMC (highlighted red). The buoyancy changes, the fluids rise in a discharge zone (highlighted green), and can exit along the ridge axis as high-temperature vent fluids. (modified from Alt, 1995).

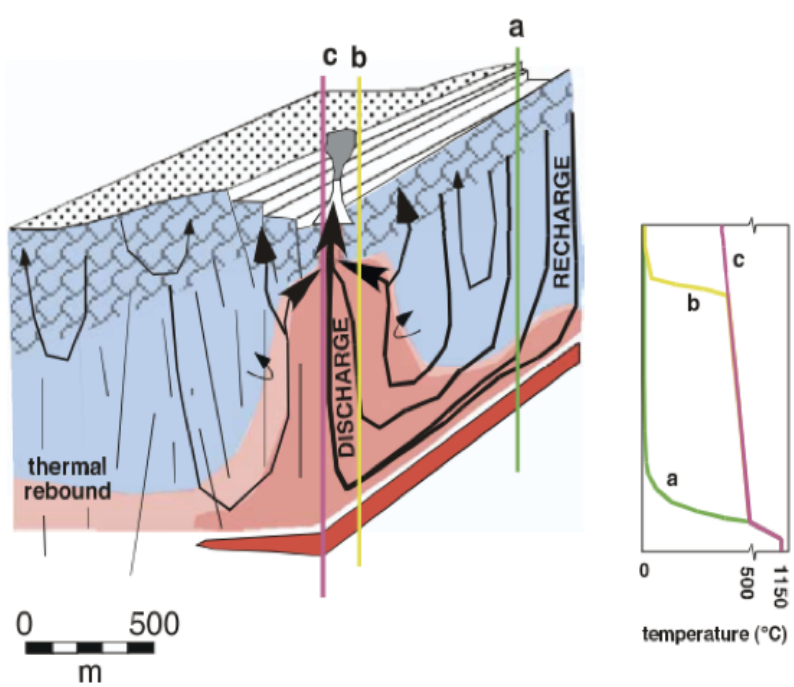

Figure 1.2: Illustration of the temperature gradients and variations within on-axis ocean crust at points a, b, and c. a) as cool fluid enters the crust at a recharge zone, there is no increase in temperature until the hot root zone. b) High temperature upwelling fluid adjacent to the pipe-like discharge zone will remain hot until the lava-dike transition where it will either become highly focused flow or mix with down-welling cool fluids. c) localized high-temperature fluid within the pipe-like discharge zone will retain its high temperatures until it exits onto the seafloor (modified from Coogan, 2008).

of hydrothermal cell shut down or migration include changes in crustal permeability or splitting of plumes caused by thermal instabilities in the root zone.

Changes in the permeability can trigger the migration or shutdown of a hydrothermal cell. One cause of decreased permeability is clogging of the fluid flow path by mineral precipitation. For example, when high temperature, Si-saturated fluids cool, they precipitate quartz (cooling can occur within the fault zone due to mixing with recharging seawater). This may shutdown or change the path of fluid flow within the hydrothermal cell (Fisher, 1998; Wells and Ghiorso, 1991; Cann and Strens, 1989; Lowell and Germanovich, 1995; Lowell et al., 1993). Dike emplacement can also cause significant permeability changes. Along fast-spreading ridges, dike emplacement is a common process, occurring on decadal time periods (Curewitz and Karson, 1998; Delaney et al., 1998: Umino et al., 2008). Intrusion of a dike into previously cooled crust creates a zone of tension at the head or leading edge of the dike. This zone of tension builds compressive forces in the surrounding rock that ultimately leads to fracturing. As multiple diking events occur a network of fractures form, consequently changing the permeability of the crust with each intrusion. Thus, dike emplacement may affect the flow path of fluid by altering the direction and/or location of the convective cell.

The migration or cessation of hydrothermal cells may also be triggered by the splitting of the hydrothermal cell within the root zone. Models of hydrothermal circulation suggest that thermal instabilities within the root zone (or thermal boundary layer above the AMC) cause an effect called “splitting”, where additional plumes of up-flowing fluid form between dominant zones of discharge and recharge (Figure 1.3; Coumou et al., 2008). These instabilities can act to strengthen the outflow velocities of an

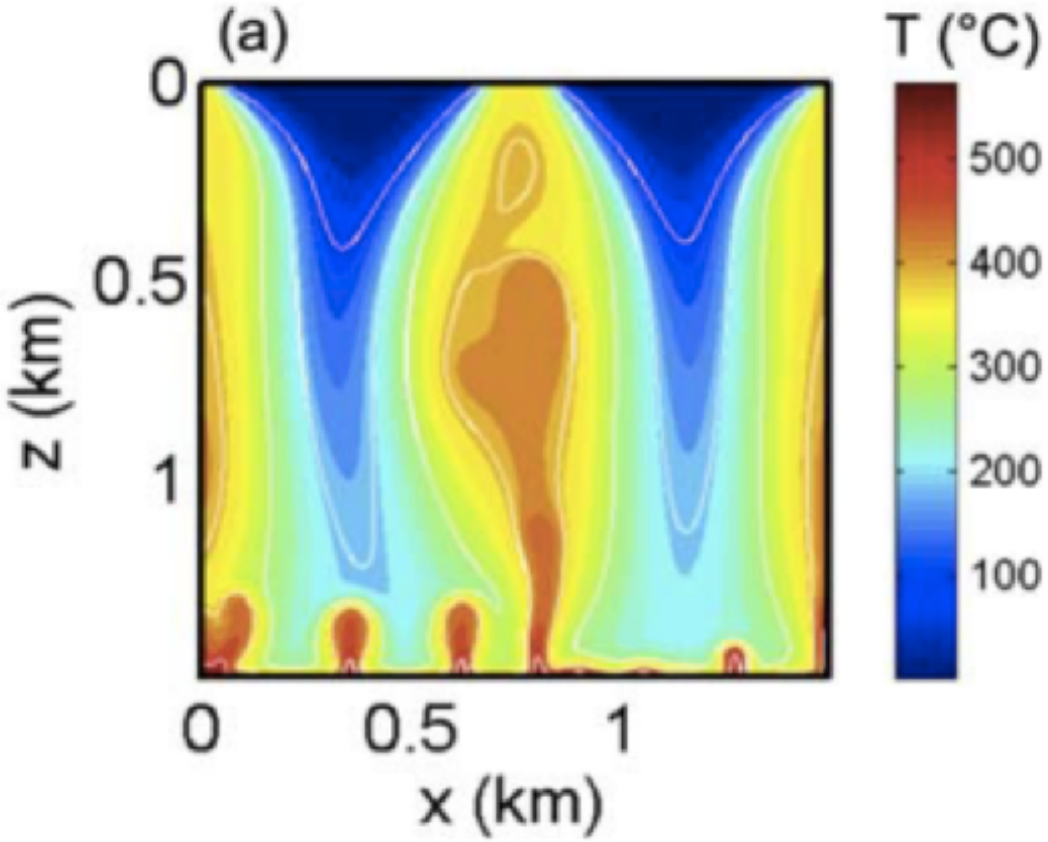

Figure 1.3: A 2D numerical model of thermal instabilities within the hydrothermal cell is constrained by three major zones of upwelling. Within the root zone between the major zones of upwelling fluids, thermal instabilities can occur, which can disturb and alter the momentum of the major up-flow zones. (Fontaine and Wilcock, 2007). The y-axis, z (km), is the distance down into the ocean crust.

individual discharge zone, and subsequently weaken an alternate discharge zone to the point where it can no longer reach the seafloor, essentially shutting down the vent (Coumou et al., 2006, 2008). In many instances, when the outflow in a discharge zone has shut down it is replaced by an inflow of seawater, creating a recharge zone for several hundred years (Coumou et al., 2008).

Insights into the chemistry of hydrothermal fluids have come from samples of vent fluids and experimental studies that simulate fluid-rock interactions in the crust (e.g., Bischoff and Seyfried, 1979; Seward, 1979; Backer et al., 1985; Seewald and Seyfried, 1990; Von Damm, 1990; Saccocia and Gillis, 1995; Marchig et al., 1997; Edmond, 2011). In comparison to seawater, hydrothermal fluids are enriched in base metals (e.g. Pb, Zn, Cu), have variable Cl^- concentrations, low pH of 3.2-5, high temperatures (100-400°C), and can be enriched in S complexes.

Temporal and spatial changes in hydrothermal circulation limit our ability to predict the exact history of fluid-rock interaction at a single point in the ocean crust. However, studies of the patterns of alteration and metal mobility recorded in altered sheeted dike complexes help constrain the evolution of the hydrothermal system. Ophiolites, tectonic windows, and drill holes give insight into the effects of the hydrothermal system on the alteration of the crust (Saccocia & Gillis, 1995; Cann & Gillis, 2004; Alt et al., 2010). With further research of the alteration of ocean crust our understanding of how hydrothermal fluids vary with time and location will continue to advance.

1.2 Metal Mobility and Development of Fe-Cu deposits

Studies of modern and ancient ocean crust have demonstrated that hydrothermal interactions in sheeted dike complexes liberate metals into hydrothermal fluids and carry them to the seafloor to form a black smoker or volcanogenic massive sulphide (VMS) deposit (Richardson et al., 1987; Alt et al., 1987; Gillis et al., 2001; Gillis, 2002; Alt and Bach, 2003; Teagle, et al., 2004). A VMS deposit is an accumulation of multiple black smokers or hydrothermal vents, and may be of economic significance. In this study, the term deposit is meant to simply an accumulation of sulphides, but that not that there is economic value.

Fe-Cu hydrothermal ore deposits are distributed globally along the network of mid-ocean ridges (Hekinian et al., 1980; Humphris and Cann, 2000; Galley et al., 2007; Edmond, 2011). The size and distribution of these deposits are primarily controlled by the rate of crustal spreading. Along fast- spreading ridges ore deposits are small (<3000 tonnes compared to >300,000 tonnes on slow-spreading ridges), and occur at relatively regular spatial intervals (25-54 km) along MOR segments based on the distribution of hydrothermal plumes detected in the water column (Baker et al., 2004; Galley et al., 2007; Hannington et al., 2010, 2011a).

The dominant source of metals for black smokers and VMS deposits is the sheeted dike complex, where metals are leached by interactions with high temperature fluids. The volume of sheeted dike required to build a seafloor deposit is not well constrained. Mass balance calculations comparing fresh and altered rocks have been conducted on ophiolites (Troodos) and the TAG hydrothermal deposit found along the slow-spreading Mid-Atlantic Ridge (Humphris and Cann, 2000; Jowitt et al., 2012).

Results demonstrate that to form a VMS deposit of 300,000 tonnes, or greater, there needs to be a source region of at least 1-2 km^3. These results are consistent with the observed increase in the spatial distribution of massive deposits along slow-spreading ridges (200 km or greater; Hannington et al., 2011). The volume of rock required to produce a typical deposit at fast-spreading ridges has not yet been calculated.

1.3 Thesis Objective

The primary objective of this thesis is to gain a better understanding of how some base metals (Cu, Zn, Ni, Mn, Co, Pb) are distributed throughout the sheeted dike complex exposed at Pito Deep and what processes contribute to this distribution. To accomplish this goal, new petrographic and mineral major and trace element data were collected, and published bulk rock data was analyzed. Specific questions addressed in this thesis include:

1) Are base metals regionally enriched or depleted in the sheeted dike complex?
    a. Does the dominant secondary mineralogy, geographic location, or depth influence the mobility of metals?
    b. How much altered ocean crust is needed to form a ore deposit at a fast-spreading mid-ocean ridge?
2) What are the mineralogical sources and sinks of the base metals in the sheeted dikes?
    a. Are primary silicate minerals sources of base metals?
    b. Are secondary silicate minerals an important sink of base metals?
    c. What is the role of Fe-Cu Sulphides?

3) What conditions and processes influence the metal concentrations of hydrothermally altered dikes?

1.4 Geological Setting and Sample Suite

Pito Deep, located on the NE corner of the Easter Microplate, is a tectonic rift that exposes ~4km of vertical relief of the mid- to upper-ocean crust (Figure 1.4; Naar and Hey, 1991; Hekinian et al., 1996; Hey et al., 2004). This crustal section formed ~3 My ago along the East Pacific Rise (EPR) at a super-fast spreading rate of >140 mm/yr (Hey et al., 2004). Tectonic rifting is caused by slow extension that started ~1 My ago at a rate of ~10 mm/yr (Karson et al., 2005).

Ocean crust formed at fast-spreading mid-ocean ridges is divided into three major lithologic zones, which are all observed at Pito Deep: the lavas or volcanic sequence, the sheeted dike complex, and the gabbro sequence (Figure 1.5).

In-depth studies of two areas (Area A and Area B) were conducted during the R/V Atlantis AT11-23 cruise (Karson, *Pito Deep Cruise Report*, 2005). Area A and Area B include two NE facing submarine scarps that expose the volcanic section composed of flows and pillows (~500 m thick), the sheeted dike complex (700-1000 m thick), and often thin exposures (<400 m) of the uppermost gabbros (Figure 1.6; Hekinian et al., 1996; Karson, *Pito Deep Cruise Report*, 2005; Perk et al., 2007). The transition from the sheeted dike complex to the lava sequence is gradual, over a vertical distance of 80-200 m. The sheeted dikes are steeply dipping (65°-80° away from the EPR) and strike to the NE. Area A is ~5 km wide and represents almost 70 kyrs of spreading history. Area B is 15 km east of Area A, ~7 km wide, and shows almost 97 kyrs of spreading history.

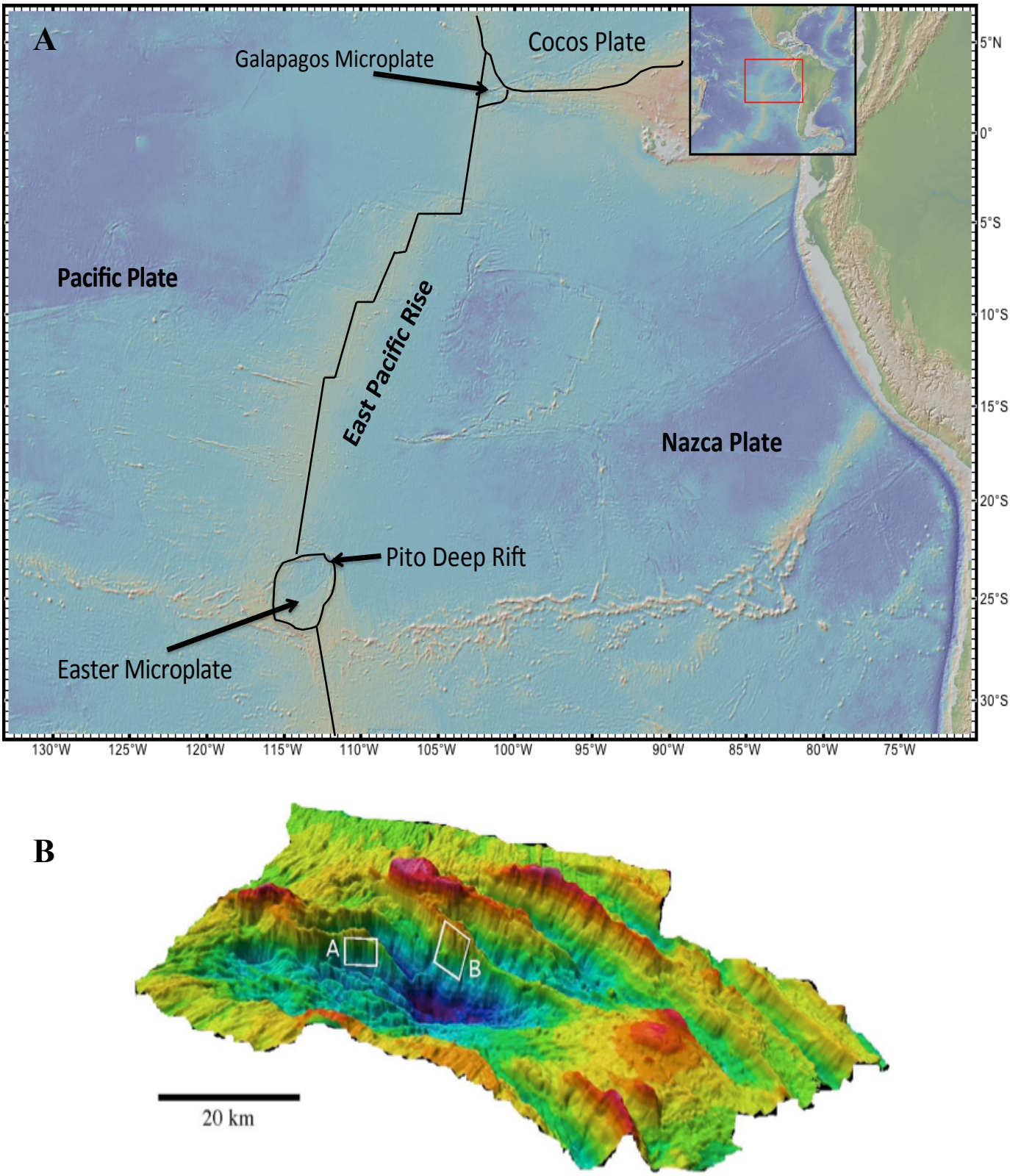

Figure 1.4: A) Location of Pito Deep with respect to the East Pacific Rise (GeoMapApp, 2013).
B) Three-dimensional bathymetric map of Pito Deep showing the locations of Area A and B. (Pito Deep Cruise Report, 2005)

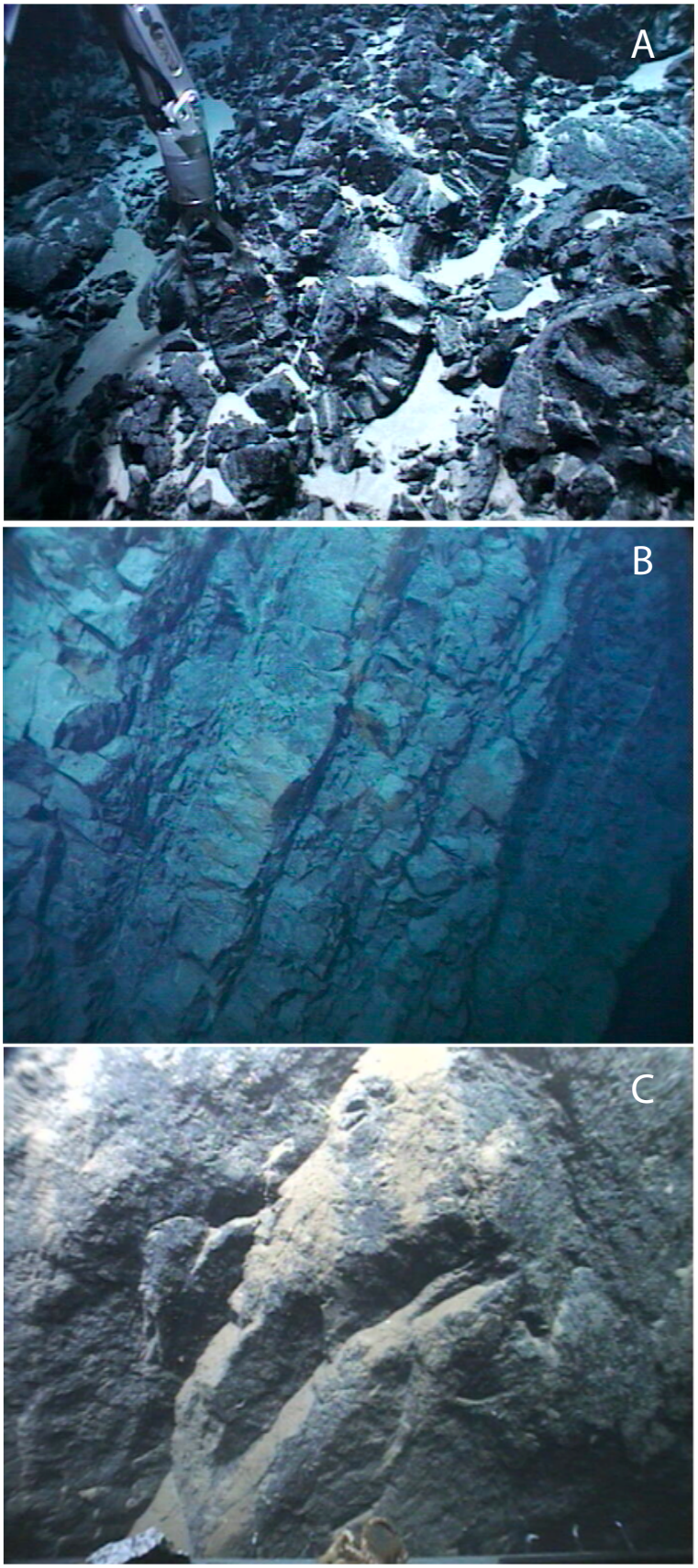

Figure 1.5: outcrop photos of the lithological zones at Pito Deep. Photos taken from ROV Jason.
(A) a sample being taken of a pillow (2634 meters below sea-level (mbsl), J2-122-3, sample 022105-0836).
(B) a typical exposure of sheeted dikes, moderatly dipping NW, (3505 mbsl, J2-119-1).
(C) massive gabbro exposure (4168 mbsl, J2-122-3).

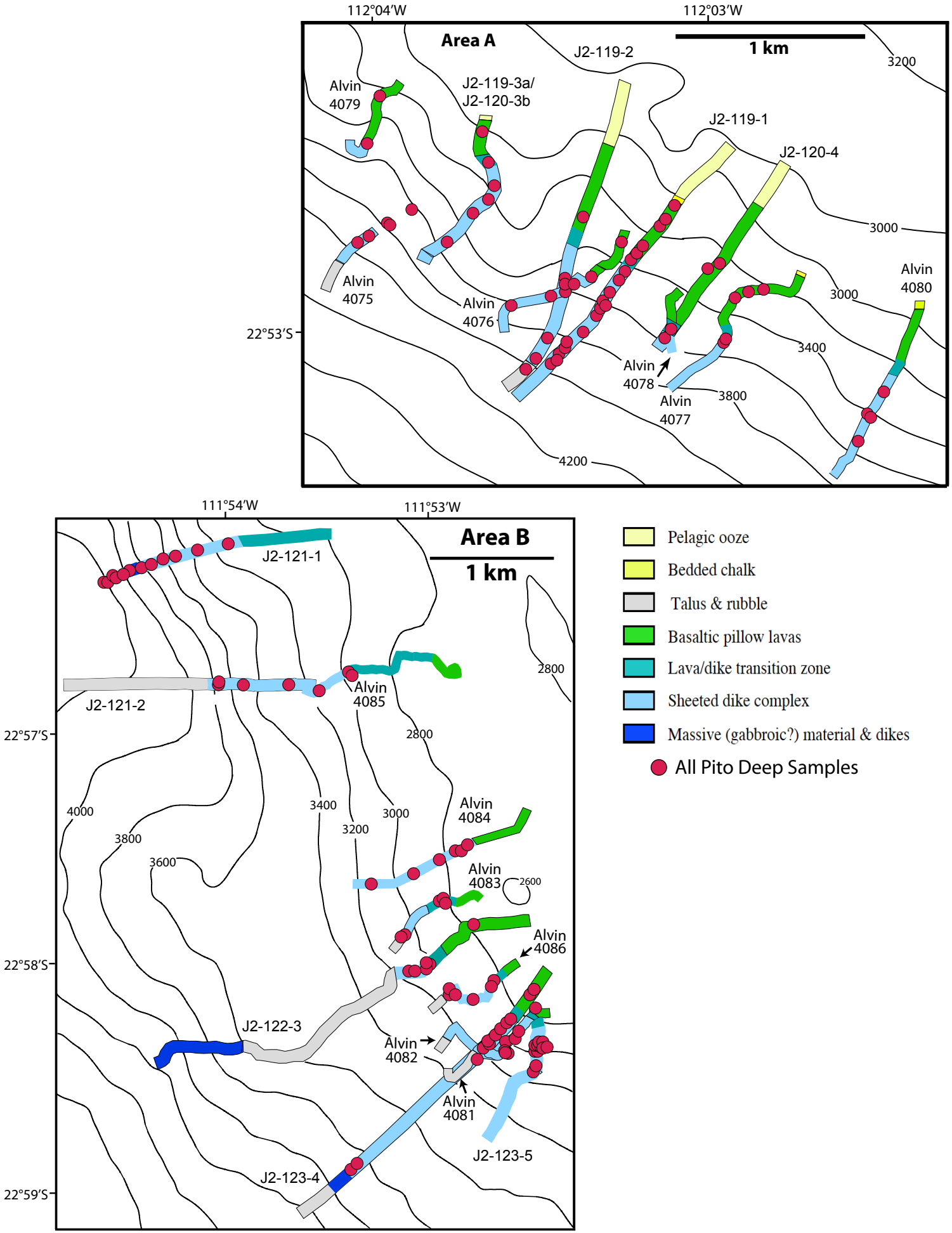
112°04'W
112°03'W
Area A
1 km
J2-119-2
J2-119-3a/
J2-120-3b
J2-119-1
J2-120-4
Alvin
4079
Alvin
4075
Alvin
4076
Alvin
4078
Alvin
4077
Alvin
4080
3200
3000
3000
3400
3800
4200
22°53'S
111°54'W
111°53'W
Area B
1 km
J2-121-1
J2-121-2
Alvin
4085
2800
2800
22°57'S
4000
3800
3600
3400
3200
3000
Alvin
4084
Alvin
4083
2600
Alvin
4086
22°58'S
J2-122-3
Alvin
4082
Alvin
4081
J2-123-5
J2-123-4
22°59'S
Pelagic ooze
Bedded chalk
Talus & rubble
Basaltic pillow lavas
Lava/dike transition zone
Sheeted dike complex
Massive (gabbroic?) material & dikes
All Pito Deep Samples

Towed DSL-120 side-scan and high resolution bathymetric surveys were used to locate possible outcrops and plan the submersible transects. During evenings, Seabeam and magnetometer mapping of the general Pito Deep area were completed. Submersibles Alvin and Jason II accomplished several dives, with a total of 20 dive tracts (Figure 1.6, Appendix B.1). High-resolution photos of outcrops were collected during the Alvin and Jason II dives and are archived at http://4dgeo.whoi.edu/alvin/, http://4dgeo.whoi.edu/jason/. ROV Jason II completed long transects (several km's) along the escarpments, collecting samples every <1 m to >10 m, and locally measuring the orientation of geological structures. The manned submersible, Alvin, was used in smaller areas of interest or where an increased degree of manoeuvrability was needed. A suite of 435 samples was collected from Area A and Area B from each lithological unit (excluding sedimentary) (Figure 1.6). From the suite of 435 samples, 193 are from the sheeted dike complex; these samples are the focus of this thesis.

1.5 Summary of previous petrological studies at Pito Deep

The following sections summarize previous work conducted on the igneous and metamorphic petrology, and geochemistry of the sheeted dike complex exposed at Pito Deep.

1.5.1 Igneous Petrology

The sheeted dikes are predominantly aphyric with rare plagioclase or olivine phenocrysts. Grain size ranges from <0.05 mm up to a maximum of 4 mm, with zones of interstitial groundmass dependent on grain size (Heft et al., 2008). The primary mineral assemblage is: plagioclase, clinopyroxene, magnetite/ilmenite, and Fe-Cu sulphides.

The lavas and sheeted dikes at Pito Deep are normal mid-ocean ridge basalts (n-MORB) that range from moderately unfractionated to more evolved (Mg# 66-42, Mg#=Mg/Mg+Fe), with no major difference between Area A or Area B (Heft et al., 2008; Pollock et al., 2009). The majority of Pito Deep samples are depleted in highly incompatible elements with ratios of moderately incompatible elements near unity (Heft et al., 2008; Pollock et al., 2009). The compositions of Pito Deep samples overlap those of other southern East Pacific Rise basalts and Hess Deep samples.

1.5.2 Metamorphic Petrology and Geochemistry

Alteration of the sheeted dike complex is a result of high-temperature hydrothermal fluid interactions with the rocks. Understanding the alteration assemblages and patterns is key to understanding the temporal and spatial, chemical and physical evolution of ocean crust.

The sheeted dike complex at Pito Deep has an average degree of alteration of 27%, ranging from <10% up to 85% (Heft et al., 2008). Therefore, all samples from the sheeted dike complex have had some degree of fluid-rock interaction. Chlorite and amphibole are the dominant alteration phases present. Plagioclase is the freshest igneous mineral and is variably altered (0-70%) to secondary plagioclase ± chlorite ± amphibole ± trace epidote ± chlorite-smectite. Secondary plagioclase was identified by low An (An_{0-40}), low MgO (<0.10wt%), and low FeO (<0.6wt%) contents (Heft et al., 2008). Clinopyroxene is variably altered (0-100%) to chlorite, amphibole, mixtures of chlorite and amphibole, or clay minerals. Replacement of clinopyroxene by amphibole is more common than chlorite (72% of samples versus 16% of samples) (Heft et al., 2008). In some samples titanomagnetite is observed to be rimmed by titanite and Fe-Cu sulphides

are rimmed with Fe-oxyhydroxides (not necessarily in the same sample) (Heft et al., 2008). Veins varying from <0.1mm up to a few cm's wide are found throughout the sheeted dike complex. Most commonly they contain assemblages of quartz, chlorite, epidote, amphibole and clay minerals.

In the sheeted dikes chlorite is predominantly chlinochlore with Mg# ranging from 0.29 to 0.71. Chlorite replaces plagioclase, clinopyroxene, and interstitial areas. There is no direct correlation with chlorite chemistry and the primary phase being replaced, degree of replacement, or geographic location (Heft et al., 2008). The proportion of chlorite in mixed-layer chlorite/smectite is between 4% to 66% (Heft et al., 2008; classification after Bettison and Schiffman, 1988).

Amphibole in the sheeted dikes is dominantly calcic and ranges from actinolite to magnesiohornblende, with a Mg# from 0.33 to 0.82 (classificaion after Leake et al., 1997; Heft et al., 2008). Similar to chlorite, there is no relationship between amphibole composition, mode of occurrence or geographic location. Amphibole replacing a primary phase is chemically the same as an amphibole infilling a vein (both within the same sample and between different samples) (Heft et al., 2008).

Studies of hydrothermal fluid flow have suggested that fault zones along mid-ocean ridges help focus and funnel hydrothermal fluids in and out of the ocean crust. At Pito Deep, an ~40m wide fault zone with 6 ~1m wide highly deformed faults within essentially undeformed upper sheeted dikes was studied in detail (Barker, et al., 2010). Although the fluid flow is highly focused within the fault zone, there is little to no difference in the degree of alteration in adjacent wall-rock dikes compared to dikes found further away from the fault zone. Elevated $^{87}Sr/^{86}Sr$ values and Mg concentrations in the

fault breccias suggest that the fault was a focused zone of discharge and that these high temperature fluids mixed with cool down-welling fluids.

To maintain the high temperatures observed in the exiting fluids and the large influx of cool fluid indicated by the enrichment of Mg and radiogenic Sr, the ratio of hot to cool fluid within the fault zone is between 3:1 and 7:1 and the total fluid/rock ratio within the fault zone could range from 50-100 (Barker, et al., 2010). If the fault zone found at Pito Deep is representative of upflow zones beneath hydrothermal vents elsewhere along the EPR, then it suggests that hydrothermal fluids evolve both chemically and thermally during ascent and that black smoker fluids exiting the seafloor do not necessarily represent the fluids within hydrothermal root zones.

Documented alteration assemblages and patterns, in the sheeted dike complex, led to the development of a conceptual model for the evolution of crustal hydrothermal metamorphism at Pito Deep (Heft et al., 2008). Hot upwelling fluids alter the crust to a chlorite- or amphibole-dominant assemblage, while locally mobilizing the metals and alkali elements. When the discharging plume reduces output or shuts down, the upwelling high temperature fluids may mix with down-welling seawater or warm, evolved recirculating fluids. This can cause metal precipitation in secondary minerals with the sheeted dikes or in fault zones. The convective hydrothermal cell can migrate along a mid-ocean ridge segment. Therefore a single piece of ocean crust may be subject to more than one hydrothermal cell, causing the variability observed in alteration patterns at Pito Deep.

Variations in the $^{87}Sr/^{86}Sr$ of altered bulk rocks help constrain the extent of pervasive hydrothermal fluid flow at spreading centers. Strontium isotopic ratios are used

because the mobility of Sr in the presence of fluid at greenschist facies conditions promotes exchange of Sr isotopes between fluid and rock, and therefore can be used to quantitatively assess the amount of fluid that has interacted with ocean crust (Alt and Bach, 2003; Gillis et al., 2005).

Barker et al. (2008) used $^{87}Sr/^{86}Sr$ of altered dikes to determine the extent of pervasive fluid flow in the sheeted dike complex at Pito Deep. A minimum fluid flux through the sheeted dike complex is constrained to be between 1.5 and 2.6×10^6 kg m^{-2} at Pito Deep, with an average fluid/rock ratio of 0.86. In general, Sr-isotope profiles throughout the sheeted dike complex show no depth variation, suggesting that fluid flow was essentially uniform. The preferred interpretation of these profiles is that there is no observable affect on the reactivity of the crust caused by variations in spreading rate, crustal thickness, protolith composition, and dominant alteration phase, and therefore Pito Deep can be a comparable model for other MOR locations (Barker et al, 2008).

To further understand fluid-rock interactions at fast-spreading ridges, a study of the sulphur concentrations, $\delta^{34}S$, and $Fe_2O_3/Fe_2O_3^{Total}$, was conducted on a sub-suite of Pito Deep samples with Sr-isotope data, to investigate the behaviour of seawater sulphate in the sheeted dikes (Barker et al., 2010). Bulk rock analyses show a loss of 400-550ppm of S from the sheeted dikes, and a minimal increase (1.5‰) of $\delta^{34}S$. This indicates that most seawater SO_4^{2-} precipitates as anhydrite before the fluid reacts with the sheeted dike complex, and hydrothermal fluids must be enriched in H_2S after reaction with the sheeted dikes. Since Sr would also partition into anhydrite, a minimum fluid flux of approximately 3×10^6 kg m^{-2} of fluid would have to pass through the sheeted dikes to compensate for the observed $^{87}Sr/^{86}Sr$ values. That quantity of fluid is sufficient to

transport 60% of the latent heat of crystallization from the ocean crust (Barker, et al., 2010).

Chapter 2

Base Metal Mobility Constrained from Bulk Rock Compositions

2.1 Introduction

Sheeted dike complexes formed at fast-spreading ridges and in ophiolites have shown that high-temperature hydrothermal alteration acts to mobilize base metals (e.g. Gillis, 2002; Cann and Gillis, 2004; Jowitt et al., 2012). On a regional and local scale base metals may be enriched or depleted in the dikes (e.g., Heft et al., 2008), however, a significant proportion of sheeted dike complexes formed at fast-spreading ridges show little to no change in the base metal content (Gillis et al., 2001; Stewart et al., 2002; Heft et al., 2008; Neo et al., 2009). Understanding the extent of and controls on base metal mobility within the crust is important, as it is the source for white and black-smokers, and VMS deposits.

Studies on the controls of base metal mobilization have provided insights into the effect specific chemical and physical properties of hydrothermal fluids have on base metal content. Temperature, salinity, redox state, and pH can all effect how a metal partitions into the fluid (e.g. Seward, 1979; Bischoff and Seyfried, 1979; Seyfried, 1982; Seewald and Seyfried, 1990; Seyfried and Ding, 1993). The controlling parameters of base metal mobility will be discussed in more detail later in this chapter.

The goals of this chapter are to quantify the gains and losses of base metals in the sheeted dike complex at Pito Deep, and to compare the results with other sections of fast-spreading ridge segments and ophiolites. In addition, a mass balance calculation is used

to assess if the observed extent of base metal loss in the sheeted dikes is sufficient to form Fe-Cu ore deposits formed at fast-spreading ridges.

2.2 Assessment of Fresh Rock Compositions

Knowledge of the base metal concentrations of unaltered sheeted dikes is necessary to calculate the gains or losses of base metals due to hydrothermal alteration. The Pito Deep sample suite does not include fresh rock or glass samples. Therefore, fresh glass data from the global compilation of Jenner & O'Neill (2012) was used to define the range of fresh rock compositions to compare with the altered Pito Deep samples. To identify data suitable for comparison with Pito Deep basalts, the following criteria were used to filter the Jenner & O'Neil database: 1) geologic setting, only data from mid-ocean ridge spreading centers; and 2) similar geochemical characteristics, only samples with ratios of immobile trace elements (La/Sm, Nb/Zr, La/Y) that fall within the range of the freshest Pito Deep basalts. The final database consisted of 251 glass samples.

2.3 Calculation of Protolith Metal Concentrations

Calculation of how base metal concentrations vary with differentiation of the parental magma help constrain the concentrations of base metals in the unaltered sheeted dikes. Following the approach of Jowitt et al. (2012), the revised glass database from Jenner & O'Neill (2012) was used to define magmatic differentiation trends by plotting Y against Mn, Zn, Co, Ni, Cu, and Pb. These trends were fit to a least squares regression in the form of a power law curve c (equation 1):

$$M_e=AY^B \quad (1)$$

Where M_e is the calculated base metal concentration (ppm) at a given concentration of Yttriun (Y), and A and B are regression coefficients defined by the individual base metal. The fit of the data to a differentiation trend was assessed by determining root mean square of deviations (RMSD) between the model and data:

$$RMSD= \sqrt{[\Sigma(M_e-M_g)^2/n]} \quad (2)$$

Where M_e is the calculated base metal concentration from equation 1, M_g is the measured base metal concentration in the glass sample, and n is the number of samples used to define the model. Yttrium concentration was used as a proxy for differentiation as it is an immobile element and therefore has not changed from the fresh rock value. Plots of magmatic differentiation trends show Cu, Ni, and Co against Y having negative correlation, and Zn, Pb, Mn, and S display a positive correlation (Figure 2.1). These trends are reflective of the compatibility of these base metals during differentiation, because Y will increase with increasing differentiation. Copper, Ni, and Zn are compatible elements that leave the melt as differentiation occurs. Zinc, Pb, Mn, and S are incompatible elements that are concentrated in the melt as differentiation occurs.

The mobility of base metals in the Pito Deep sheeted dikes is assessed by comparing the differentiation trends defined by the glass data to the altered rock data (Figure 2.1). The altered rock database (188 samples) includes samples from the sheeted dike complex reported in Barker et al. (2008); Heft et al. (2008); Pollock et al. (2009).

The change in base metal content (ΔM) is the difference between the calculated protolith base metal concentration (M_e, equation 1) and the altered bulk rock base metal concentration (M_a):

$$\Delta M= M_a - M_e \quad (3)$$

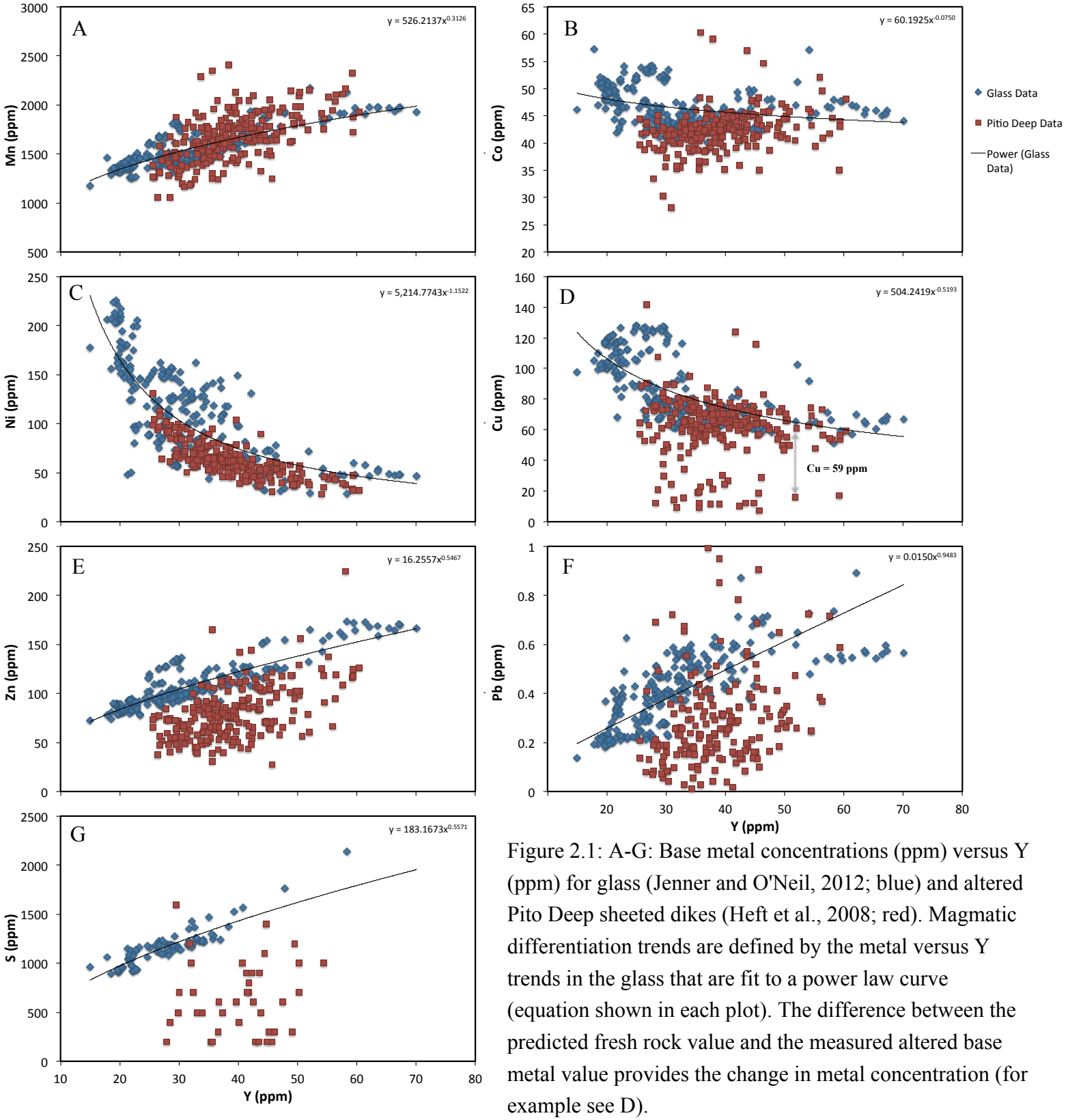

Figure 2.1: A-G: Base metal concentrations (ppm) versus Y (ppm) for glass (Jenner and O'Neil, 2012; blue) and altered Pito Deep sheeted dikes (Heft et al., 2008; red). Magmatic differentiation trends are defined by the metal versus Y trends in the glass that are fit to a power law curve (equation shown in each plot). The difference between the predicted fresh rock value and the measured altered base metal value provides the change in metal concentration (for example see D).

An example of this calculation is shown in Figure 2.1d. An altered rock with a bulk Y concentration of 52 ppm and Cu concentration of 16 ppm, has a calculated fresh bulk rock Cu concentration of 75ppm; therefore, the altered sample has lost 59 ppm of Cu.

The root mean square of deviations (equation 2) of the calculated fresh glass value is used to determine uncertainty in the ΔM values (equation 3). Values that fall within the range of uncertainty show no base metal mobility; outside of this range + ΔM values identify enrichment and - ΔM values depletion.

Each base metal studied at Pito Deep shows varying degrees of enrichment and depletion. Cobalt, Cu, Mn, Zn and Pb all show depletion in samples from the sheeted dikes. On average Co, Cu, Mn, Zn, and Pb have been depleted by 21.3%, 50.3%, 15.7%, 36.3%, and 59.2%, respectively, of the protolith fresh rock concentrations (Table 2.1, Figure 2.1). The average percentage of the sheeted dike samples that show this depletion of Co, Cu, Mn, Zn, and Pb are 1.5%, 25%, 18.9%, 94.9% and 70.6%, respectively. Therefore, with the exception of Zn and Pb, substantial leaching of the base metals has not occurred within the sheeted dikes. Nickel was also examined, and was observed to have no change in the bulk rock base metal content, it was neither enriched nor depleted in any sheeted dike samples. Manganese is enriched by 17% of the protolith concentrations in 29.6% of the sheeted dikes, and Pb shows enrichment of over 300% of the original Pb concentration in 10% of the samples (suggesting Pb has been actually been added to the system). Bulk rock S data was available for 46 sheeted dike samples (Barker et al., 2008). Ninety-seven percent of these samples show significant S depletion, with an average removal of ~57% of the total S (Table 2.1).

To investigate the effect of protolith composition on ΔM values, plots of each Δ base metal values were plotted against MgO (Figure 2.2). Delta Cu, Zn, Ni, Pb, and S show no relationship with MgO. Delta Mn, and to a lesser extent ΔCo, display a weak negative correlation with MgO, suggesting that Mn, and Co are slightly more mobilized from less evolved magmas (high MgO).

The effect of bulk rock S on base metal mobility in the sheeted dikes is important to consider because Fe-Cu sulphides, the sole S source, are thought to be the major source of base metals. Plots of fresh glass S against base metal concentrations (Figure 2.3) show a strong positive relationship between Pb and Zn. This suggests that as S leaves the system Pb and Zn do as well, and that Pb and Zn may be primarily hosted in Fe-Cu sulphides. Cu, Ni, and Co show no strong correlation with S, and therefore S does not have a controlling effect on the mobility of these base metals.

To test if the loss of S is related to base metal leaching, plots of Δ base metal in the sheeted dike samples against ΔS were created. Figure 2.3g illustrates an example trend between ΔCu and ΔS. The overall lack of correlation between ΔCu and ΔS shows that Cu does not always leave the system if S does; this suggests that Cu was redistributed or an additional source of Cu is present in the sheeted dike complex. However, some samples that have substantial depletion of both Cu and S have a positive correlation suggesting that when S leaves the system so does Cu. In other words, the breakdown of chalcopyrite has occurred, removing both Cu and S from the system, but Cu has not been precipitated back into the secondary phases. The samples that show both S and Cu loss are fresh samples (<10% alteration); therefore there are no significant secondary mineral hosts of Cu in these samples. Plots of ΔMn, ΔZn, ΔNi, ΔCo, and ΔPb

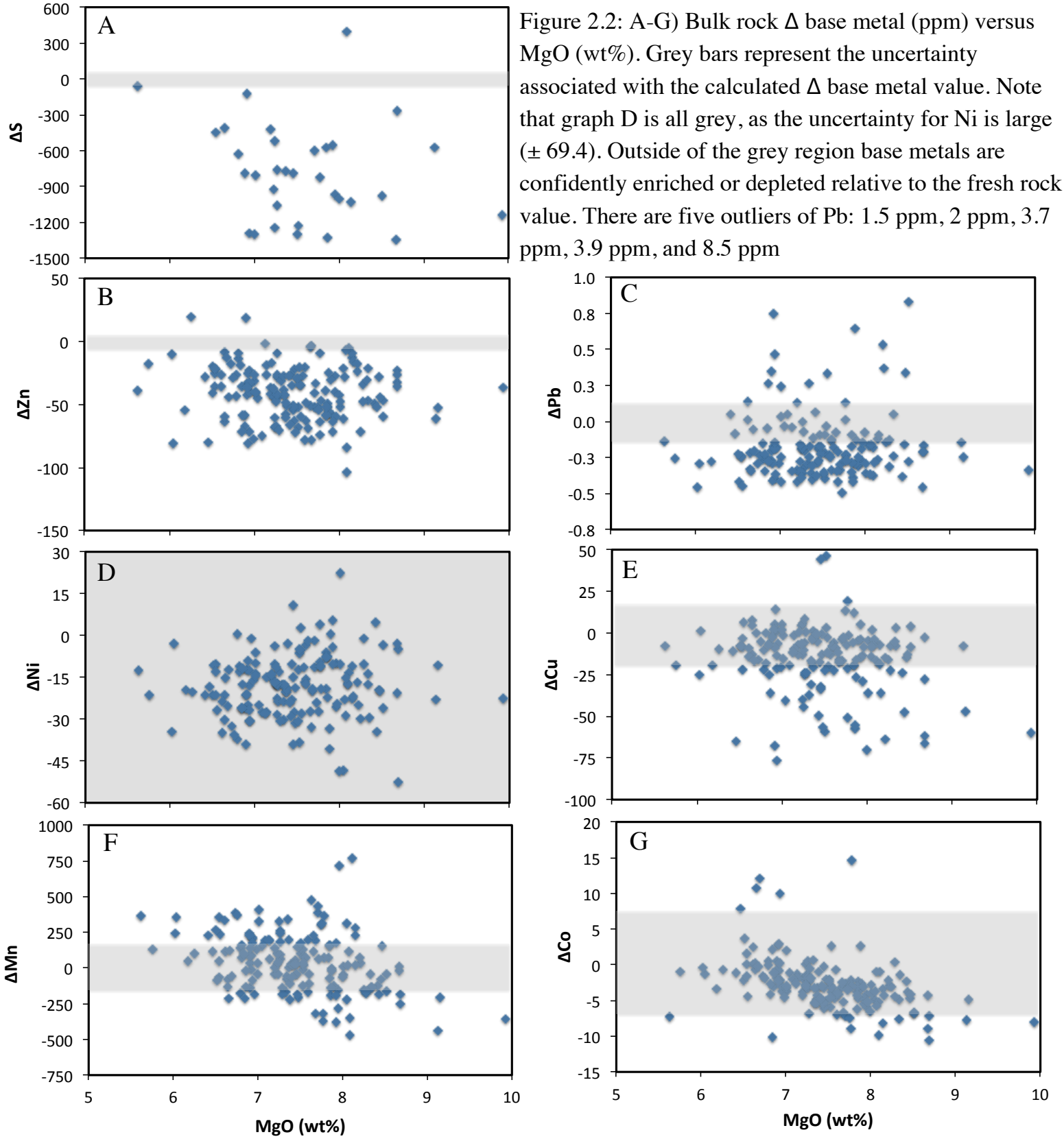

Figure 2.2: A-G) Bulk rock Δ base metal (ppm) versus MgO (wt%). Grey bars represent the uncertainty associated with the calculated Δ base metal value. Note that graph D is all grey, as the uncertainty for Ni is large (± 69.4). Outside of the grey region base metals are confidently enriched or depleted relative to the fresh rock value. There are five outliers of Pb: 1.5 ppm, 2 ppm, 3.7 ppm, 3.9 ppm, and 8.5 ppm

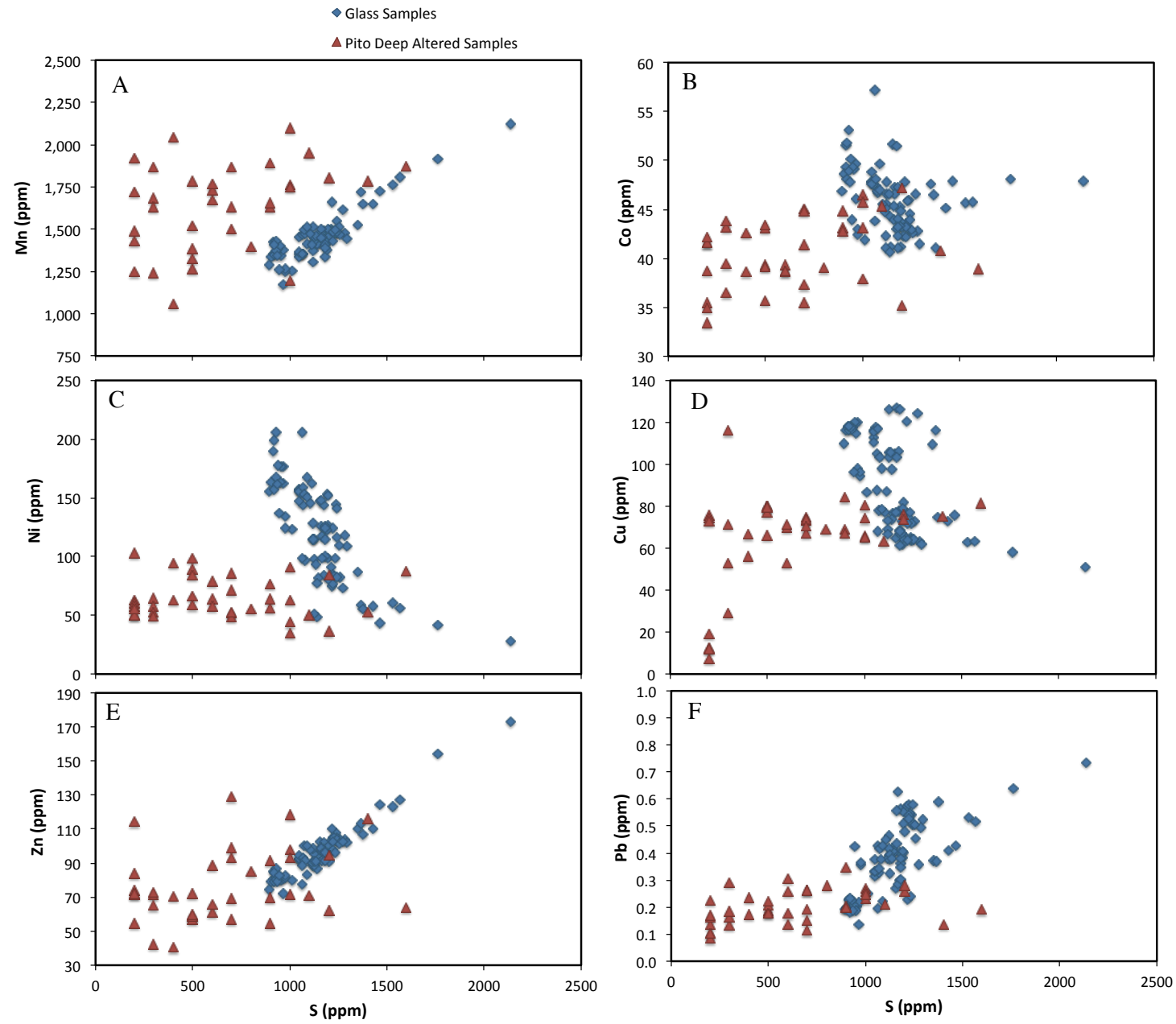

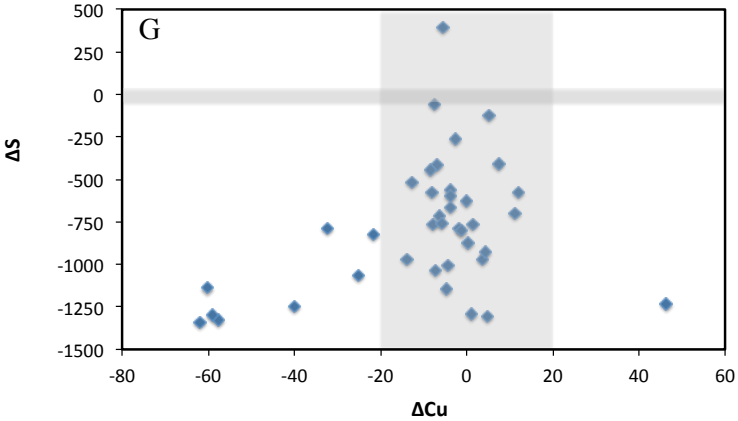

Figure 2.3: A-F) Bulk rock base metal values (ppm) versus S (ppm) in glass samples (blue) and the altered sheeted dikes samples (red). G) ΔS versus ΔCu plot showing the relationship of Cu depletion (in some samples) with S depletion. Grey bars represent the uncertainty assoicated with the ΔS and ΔCu values, and values that lie outside of the grey zone are confidently depleted.

against ΔS show no correlation; therefore the processes controlling S mobility are not the controlling parameters of the mobility of any of these base metals in the sheeted dikes. Mineralogical controls of base metal mobility are examined in Chapter 3.

The approach used here to calculate Δ values does not account for changes in mass of the rock (e.g. Jowitt et al., 2012). Changes in mass were not considered in this study because: 1) the sheeted dikes are not highly altered (on average 27%) and igneous textures are still preserved in the samples which is indicative of limited or no change in mass or volume, and 2) maximum mass fluxes through the sheeted dikes is constrained by best-estimate water/rock ratios of ~1, possibly suggesting that only small increases in mass could occur in the form of anhydrite (which has not been observed in the sheeted dikes at Pito Deep) or water (<1.2wt%; Coogan and Dosso, 2012).

Table 2.1: Base metal concentrations, Δ values, and % depletion/enrichment in the sheeted dikes

Metal	Altered Bulk Rock concentration (ppm)	Range in Δ metal values (ppm)	Uncertainty based on fresh rock values (ppm, 1σ)	% samples that show depletion	Average % (ppm) depletion from the protolith	% samples that show enrichment	Number of samples
Mn	1060-2410	-662 to 770	±148	18.9	15.7 (-250)	29.6	169
Co	30-60	-13.1 to 14.7	±7.73	1.5	21.3 (-9.8)	2.9	175
Ni	28-113	-52.4 to 22.5	±69.4	0	N/A	0	175
Cu	7-140	-76.2 to 51.2	±19.9	25	50.3 (-40.5)	2.3	175
Zn[1]	30-220	-104. to 74.4	±8.46	94.9	36.3 (-42.7)	1.7	175
Pb[2]	0.09-1.6	-0.49 to 8.54	±0.141	70.6	59.2 (-0.3)	10	170
S	200-1600	-1341 to 392	±17.9	97.4	56.7 (-806)	2.6	39

[1] excludes Zn outliers at 9ppm and 1242ppm
[2] excludes 5 outliers with Pb ranging from 2-10ppm.

A previous study of alteration patterns in the sheeted dikes at Pito Deep examined bulk rock metal mobility (Heft et al., 2008). Overall reported ΔCu, ΔZn, and ΔMnO values are very similar to those calculated here, however Cu, and Zn have a maximum depletion of -75 ppm and -70 ppm, respectively, which is lower than what is calculated here. Furthermore, ΔMnO shows more enrichment and depletion than what is observed in this study. ΔNi and ΔCo were not calculated by Heft et al. (2008). Differences observed between the studies likely reflect a more rigorous approach taken here, in that the database of glass samples used for the calculation of protolith base metal compositions was more thoroughly refined and a larger database was used. In addition, the uncertainty in the study was quantitatively determined by the RMSD and the standard deviation of the fresh rock samples.

2.3.1 Changes in base metal mobility with depth and region

A tectonic window, such as Pito Deep, provides valuable insight into the possible effects of depth and location on the depletion or enrichment of base metals in the sheeted dikes. Plots of ΔM versus depth below the lava-sheeted dike transition show no systematic change in ΔM values (Figure 2.4), which is consistent with Heft et al. (2008).

The benefit of a tectonic window, such as Pito Deep, is that it provides a 3D view of the distribution of base metals in the ocean crust, unlike a drill core, which only provides insight into variations with depth. The regional trends of Δ base metal values were assessed using geographic information system (GIS) software ArcGIS.

Contour maps of ΔM for each base metal in Area A and Area B show localized zones (tens of meters) of enrichment and depletion. For example, Figure 2.5 shows the regional distribution of ΔCu and ΔZn in Area A of Pito Deep; contour maps of ΔM for all

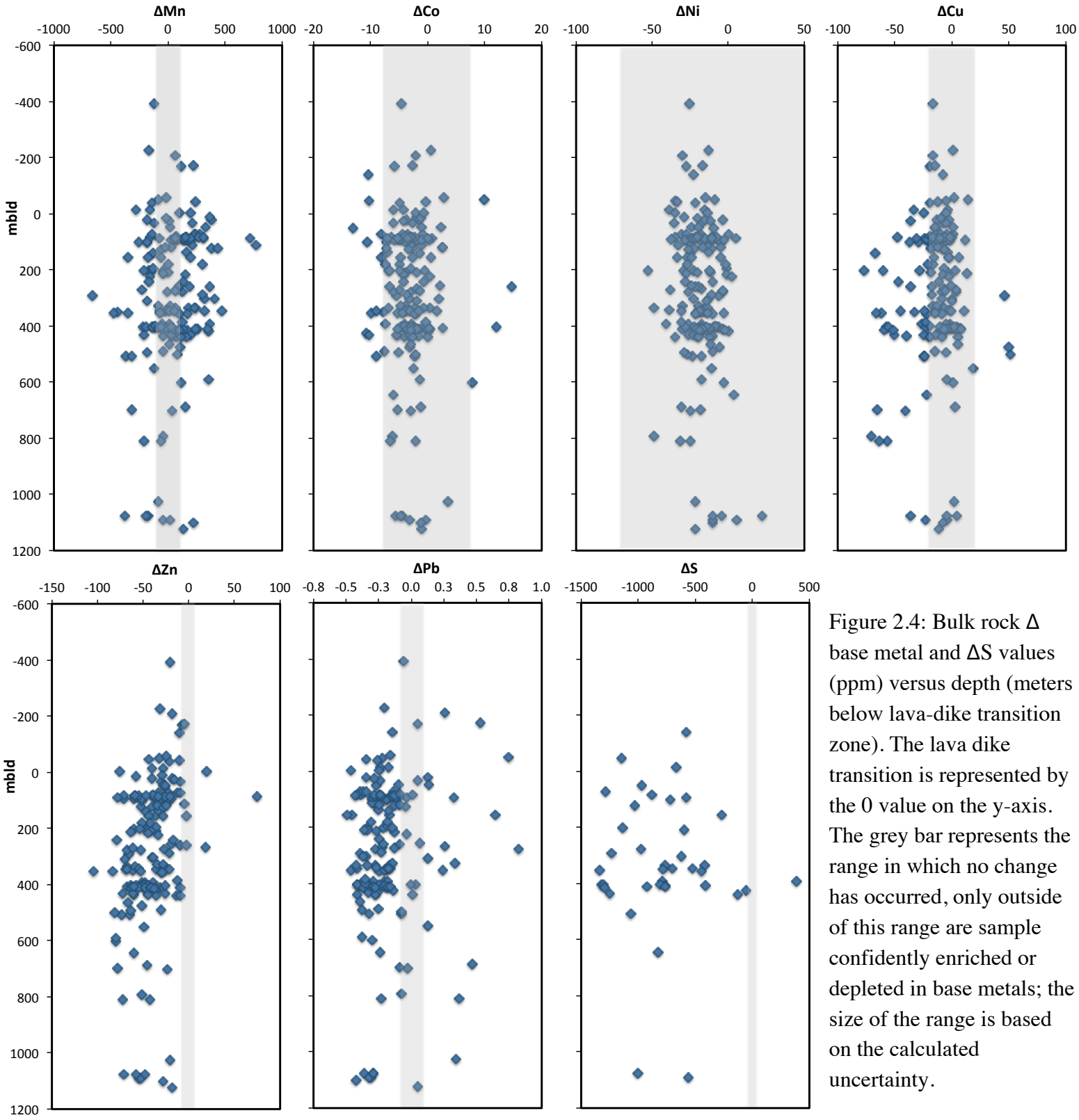

Figure 2.4: Bulk rock Δ base metal and ΔS values (ppm) versus depth (meters below lava-dike transition zone). The lava dike transition is represented by the 0 value on the y-axis. The grey bar represents the range in which no change has occurred, only outside of this range are sample confidently enriched or depleted in base metals; the size of the range is based on the calculated uncertainty.

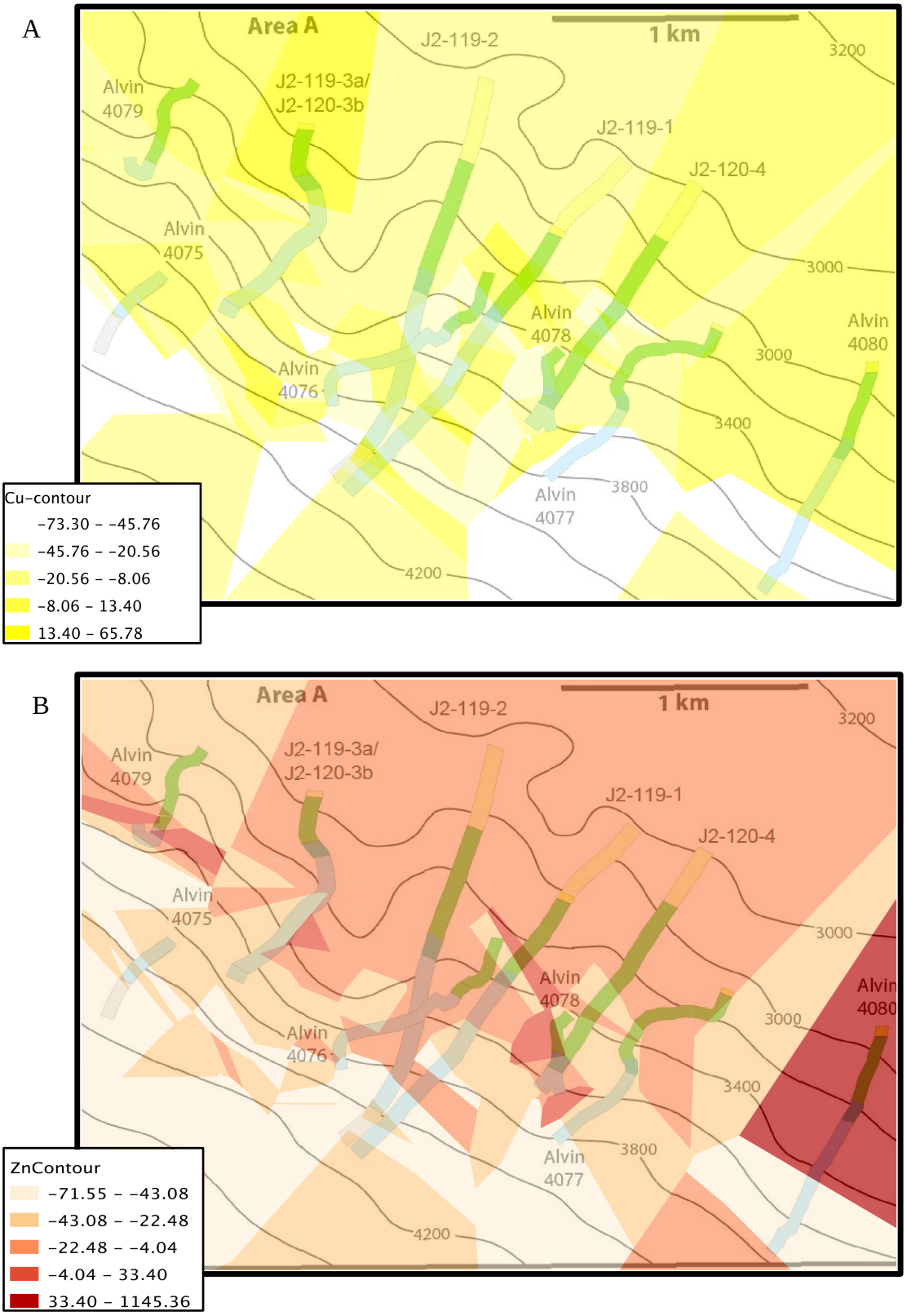

Figure 2.5: Example maps of the regional distribution of Δ metal values in Area A, Pito Deep. A) ΔCu, B) ΔZn. the remaining maps can be found in Appendix C.

studied base metals are given in Appendix C. Maps for the Δ values of each base metal did not reveal any pattern or systematic variation in the distribution of zones of enrichment or depletion. This may reflect the sampling density and the large distances between transects (0.3 to >1km).

Studies of base metal distribution at Hess Deep and the Troodos ophiolite show a similar lack of regional trends in base metal concentrations (excluding relationships to zones of epidosite which do show almost complete leaching of metals in the ophiolite; Gillis et al., 2001; Cann and Gillis, 2004; Jowitt et al., 2012). Hess Deep is a comparative tectonic rift exposing ~1My old sheeted dikes, formed along a fast-spreading EPR (Stewart et al., 2002). A regional map of Cu content at Hess Deep shows the same lack of systematic trend of Cu depletion and enrichment throughout the region (Gillis et al., 2001).

2.3.2 Role of secondary mineral assemblage in base metal mobility

Secondary mineral assemblages have been shown to influence the extent of base metal mobility in altered dikes (Barker et al., 2008; Jowitt et al., 2012). It is important, therefore, to assess the effect that secondary mineral assemblages have on the base metal concentration. Overall, the sheeted dikes are relatively fresh, with an average of 27% altered (ranging from 0-80%; Heft et al., 2008). Previous work showed that the dominant alteration phase in the sheeted dikes is amphibole replacing groundmass and clinopyroxene (Heft et al., 2008). In contrast, samples included in this study (discussed later) are largely dominated by chlorite or assemblages of chlorite with amphibole.

To assess if there is a relationship between the degree of alteration and the mobility of base metals in the sheeted dikes, plots of total modal abundance of secondary

minerals versus ΔM values were created (Figure 2.6). No relationship between the degree of alteration to the total depletion or enrichment of the base metals was observed. Additionally, plots of the modal abundance of the dominant secondary phase were considered (e.g. whether the modal abundance of chlorite relates to changes in base metal content). There are no observed trends of bulk rock base metal mobility with respect to chlorite or amphibole-dominated assemblages. Modal abundance values from Pito Deep were from Heft et al., (2008). The overall role of secondary mineral assemblages on base metal concentrations will be discussed in detail in Chapter 3.

2.4 Discussion

This detailed study of base metal mobility in the sheeted dikes at Pito Deep provides insight into the degree and variability of metal mobilization from the ocean crust. The distribution of base metals at Pito Deep shows no regional or depth trends and therefore suggests there is no systematic pattern of base metal mobility in the sheeted dike complex. Samples from the sheeted dikes range from fresh (<5%) to >65% altered, and are observed to have a wide range in the degree of base metal depletion or enrichment. This suggests that metal redistribution may be a significant process occurring in fast-spreading ocean crust.

2.4.1 Comparison of Pito Deep to Hess Deep and Hole 1256D

To assess if the range of base metal mobility observed at Pito Deep is typical of fast-spreading crust, the approach used here to calculate the ΔM values was applied to Hess Deep and IODP Hole 1256D for Mn, Zn, Ni, Co, Cu, and Pb (S data not available)

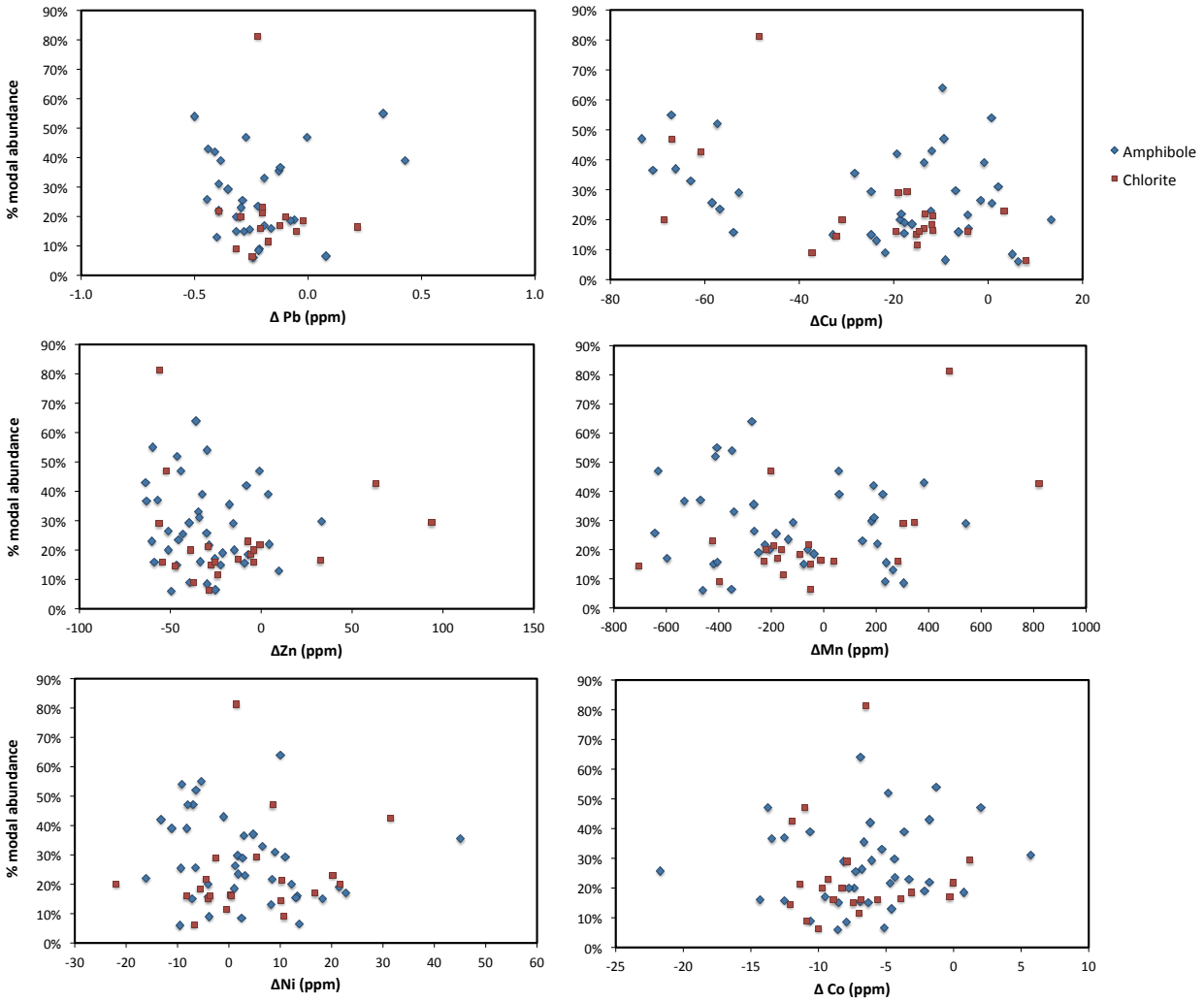

Figure 2.6: Dominant secondary mineral modal abundance (%) versus Δ metal values. Mineral modal abundance are from this study and Heft et al. (2008). Samples with chlorite dominated assemblages shown in red and samples with amphibole dominated assemblages shown in blue.

(Stewart et al., 2002; Neo et al., 2009). Hess Deep and Hole 1256D were selected because they are the best-studied sections of ocean crust formed at fast-spreading ridges. Plots of each Δ base metal versus depth show that, similar to Pito Deep, Hess Deep and Hole 1256D have no systematic trends in base metal mobility with depth and that the extent of mobility is equivalent (Figure 2.7). In samples from Hess Deep and IODP Hole 1256D the average depletion of Co, Ni, Cu, and Zn is 12%, 40%, 40%, and 60%, respectively, of their original bulk rock base metal concentration. Hole 1256D and Hess Deep have some samples that show Mn and Pb enrichment, respectively, by more than 20% of their protolith bulk rock metal concentration.

Pito Deep, Hess Deep, and Hole 1256D show similar degrees of alteration and secondary mineral assemblages in the sheeted dikes (Heft et al., 2008; this study), and have similar Sr isotopic compositions (~0.7024-0.7029; Barker et al., 2008); and now it has been observed that the mobility of base metals is the also similar. The relative depletion of base metals from the sheeted dikes at all locations is Zn > Pb >> Cu > Mn > Co; while bulk rock Ni content has remained unchanged. Therefore, Pito Deep alteration patterns caused by hydrothermal circulation can be considered analogous to other locations of fast-spreading ocean crust.

2.4.2 Quantifying the Source Region for Fe-Cu Ore Formation

Fe-Cu ore deposits (black-smokers and VMS deposits) occur at intervals of 25-54 km along the EPR (Chapter 1; Hannington, et al., 2011). Although fast-spreading ridge deposits are rarely of economic significance, it is interesting to assess the amount of crust needed to be altered in order to form a deposit. Studies of ocean crust have found that

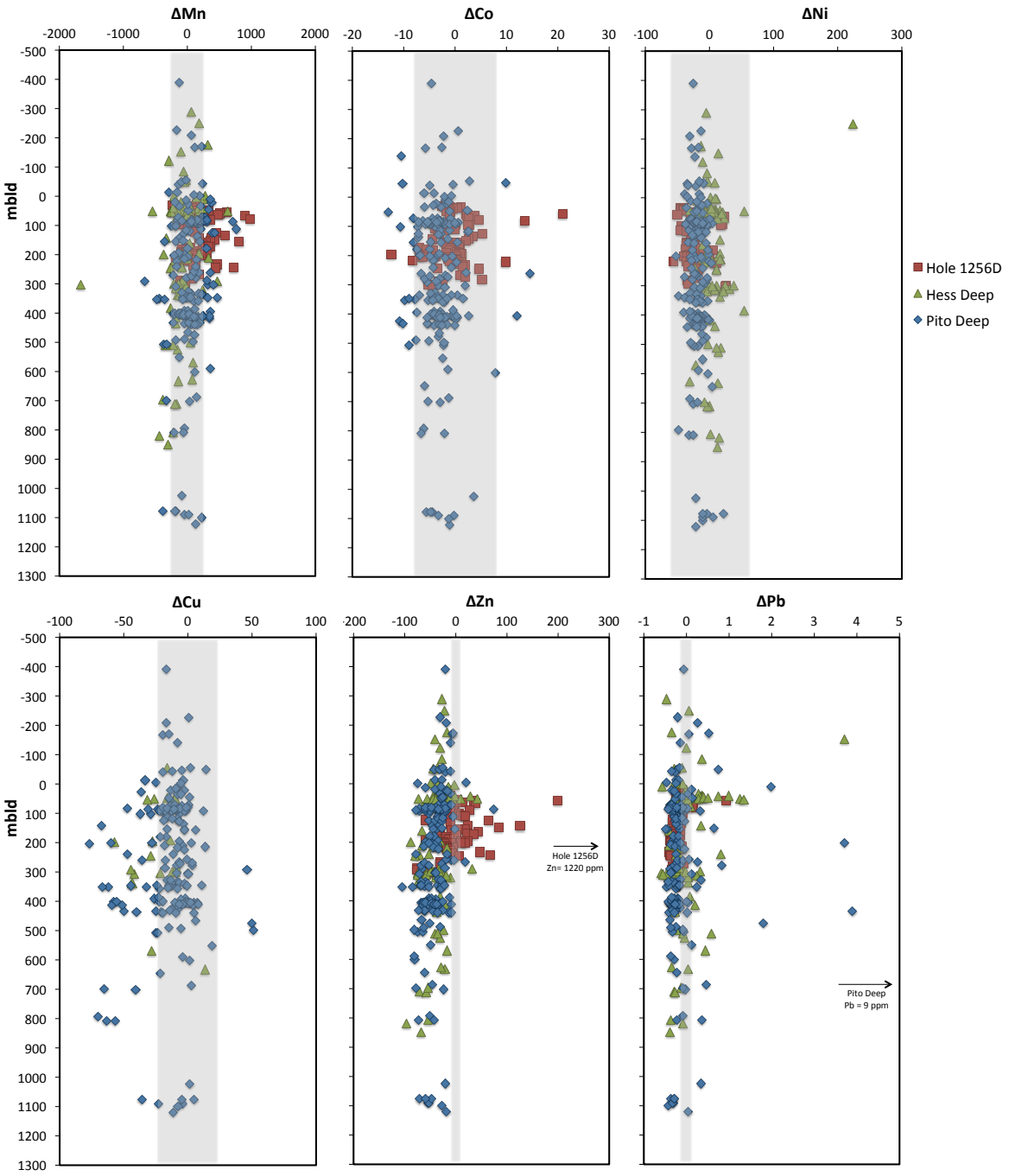

Figure 2.7: Bulk rock Δ base metal values (ppm) versus depth (meters below lava-dike transition zone) at Pito Deep (blue), Hess Deep (green), and IODP Hole 1256D (red) (missing symbols means no data was available). Grey bar represents the uncertainty associated with the Δ base metal calculation; only samples that lie outside this range are considered enriched or depleted in base metals.

base metal mobilization dominantly occurs within the sheeted dike complex (Herzig & Hannington, 1995; Humphris, et al., 1998; Galley, et al., 2007).

To determine whether the degree of leaching observed in the sheeted dikes at Pito Deep is sufficient to form a typical fast-spreading ridge ore deposit, a mass-balance model (based on Humphris and Cann, 2000) is used to calculate the size of a source region needed to account for the base metal content of these sulphide deposits. This calculation requires knowledge of the sources and possible sinks of base metals at the seafloor, as fluids exit the ocean crust (Figure 2.~~8~~). The source of base metals is from the alteration of the sheeted dikes as high-temperature fluids interact with the rock and liberate the base metals. High temperature fluids that exit the crust as focused fluid flow will deposit the studied base metals in three possible locations: 1) a massive sulphide deposit, 2) near-field sediments formed from the fallout from the vent plume, and 3) the water column as particulate matter (Figure 2.8). Assuming that the concentration of base metals leached from the source region is equivalent to the mass of base metal in the deposit, the mass in the near-field sediments, and the base metals that are released into the water column, a simple mass balance can be calculated (Humphris and Cann 2000):

$$M_{sr} = [(M_d\,[Cu_d]) + (R_f\,t\,[Cu_f]) + (R_s\,t\,[Cu_s])] * [Cu_{sr}]^{-1} \qquad (4)$$

Where M_{sr} is the unknown mass of the source region needed to create a sulphide deposit, $[Cu_{rz}]$ is the concentration of Cu available from base metal loss from the sheeted dike complex, M_d and $[Cu_d]$ are the mass of the sulphide deposit and concentration of Cu in the sulphide deposit, respectively, t is the total time the deposit was forming, R_f is the rate of fluid discharge from a single hydrothermal chimney, $[Cu_f]$ is the concentration of Cu in the discharging fluid, R_s is the rate of near-field sediment accumulation, $[Cu_s]$ is the

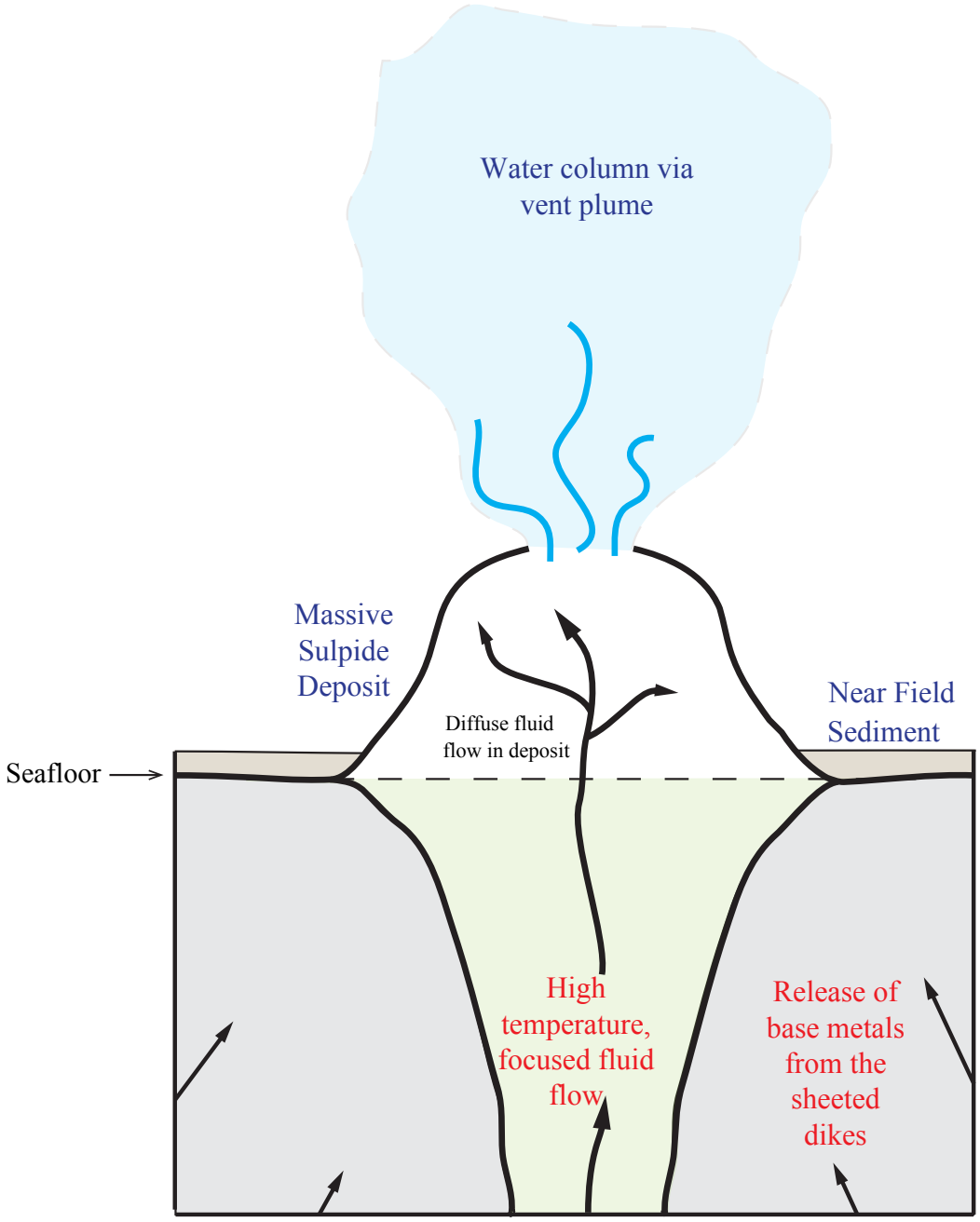

Figure 2.8: Cartoon of the sources and deposition of base metals at the seafloor, consequently forming a massive sulphide deposit. The source of metals are in red, and the sinks of metals are in blue. Note that this is not to scale and that the near field sediments is only a thin layer on the ridge axis.

concentration of Cu in the near-field sediment, and [Cu_{sr}] is the concentration of Cu lost from the source region.

Copper is used to constrain the size of the source region because it is found either in the fluid or in sulphide phases, and Cu has the largest and most robust database in published literature for the values required in the calculation.

The only source of Cu for this calculation is the hydrothermally altered sheeted dikes. This study shows that only 25% of the sheeted dikes display Cu loss and the average ΔCu value is -40.5 ppm. Therefore, total volume of ocean crust needed to form a deposit M_{sr} was multiplied by 4 to compensate and accurately represent the amount of source rock needed at Pito Deep.

Although the source can be constrained as single entity (the sheeted dikes), the possible sinks are more diverse. As fluids exit the crust there are three major sinks for the base metals to enter: 1) an ore deposit (e.g. black smoker or VMS deposit), 2) the water column via expelling fluids, and 3) near-field sediments adjacent to a deposit. The magnitude of the sinks concentration of Cu was calculated using published data for hydrothermal vent fields along the East Pacific Rise (Table 2.2). Along fast-spreading ridges the life span of a vent is estimated to be between 10-100 years (Hannington et al., 2010). This range is used to constrain the possible source region needed to form 3000 tonne deposit.

The deposit size used in this calculation is the maximum size (3000 tonnes) observed along the EPR because smaller deposits are not easily studied and their sizes are poorly constrained (Humphris et al., 1998; Hannington et al., 2011a). EPR deposits are small relative to those found on slower spreading ridges due to more frequent volcanic

activity and variability in hydrothermal output. When volcanic eruptions occur, pre-existing deposits may be destroyed and covered, therefore limiting the size that an individual deposit can grow. The Cu concentration in EPR ore deposits range from <1wt% up to ~30wt%, due to the variability of hydrothermal fluid compositions at the time of formation. The Cu concentration used for this model is the average concentration from 17 EPR sites studied (average 4.9±3 wt% Cu; Hannington, 2013).

The concentration of Cu in the vent fluid (2.59±0.24 ppm) is the average of 284 vent sites along fast-spreading mid-ocean ridges that have exiting fluid temperatures >200°C (Coogan & Dosso, 2012). The uncertainty of the average Cu concentration is considered an underestimate of the error associated with these values due to multiple samples collected from the same source (discussed further in Coogan &Dosso, 2012). The rate of fluid discharge is not well constrained; a fluid discharge rate of 4.73E+07 ±1.56E+07 kg/year is used (Hannington et al., 2010). The large uncertainty is due to the limited published values and the large range observed in the discharge rate (Table 2.2).

The Cu concentration of near-field sediment used is the average values of only 3 vent sites with published data along the EPR, 0.22 ± 0.11 wt% Cu (Hannington, 2013). The rate of sedimentation is estimated as 1.13 x 10^6 kg/yr; no uncertainty was available (Hannington, 2013).

Table 2.2: Parameters used to constrain the region of alteration needed to form a VMS deposit

Range of Parameters	Value used in model (±1 st dev)	Min	Max	Reference
Total Cu loss from sheeted dikes ppm, [Cu_{sr}]	40.5 (17)	19.9	76.2	This study
Mass of Deposit (tonnes), M_d	3000		<3000	(Hannington, et al., 2010; Herzig & Hannington, 1995)
Deposit Cu (wt%), [Cu_d]	4.9 (3)	1.3	11.1	(Hannington, 2013)
Lifetime (yrs), t	10-100	10	100	(Hannington et al., 2010)
Fluid discharge (kg/yr), R_f	4.73E+07 (1.56E+07)	3.16E+07	6.32E+07	(Hannington et al., 2010, Von Damm, 1990)
Fluid Cu (ppm), [Cu_f]	2.59 (0.24)	2.35	2.83	(Coogan and Dosso, 2012)
Near-field Cu deposition (kg/yr), R_s	1.13E+06	1.13E+06		(Hannington, 2013)
Near-field sediment Cu (wt%), [Cu_s]	0.22 (0.11)	0.1	0.33	(Hannington, 2013)

* Density of basalt and the deposit are 2800 and 2500 kg/m^3, respectively, used to calculate the volume of the source region and deposit.

The formation of a sulphide deposit along a fast-spreading mid-ocean ridge, that has Cu depletion of 39 ppm and is formed on the timescale of 10-100 years, would require a source region of 4.42 $x10^9$ kg to 1.03 x 10^{10} kg (0.002-0.004 km^3), respectively, to form a 3000 tonne deposit. The propagated uncertainty from the values used to calculate the source region is ±48% of the calculated total. Since ~ 25% of the sheeted dike samples are observed to be depleted in Cu, then the source region would be 4 times the size, $1.77x10^{10}$ kg to $4.12x10^{10}$ kg (0.006 km^3 to 0.015 km^3), respectively, to form a 3000 tonnes deposit (see Appendix D.2 for more model details).

To test if the calculated source region is reasonable for a fast-spreading ridge, previous work on hydrothermal vent sites and cell size are used to assess the area that hydrothermal fluids pass through. Since the source region is not a cubic feature, the size of the source region will be constrained by the axial valley and the thickness of the sheeted dike complex, as this is the area of high-temperature alteration. Along a fast-spreading ridge an axial valley width of >500 m (Backer et al., 1985; Karson, 2002) is possible, however seismic studies show in one location a more constrained zone of high-temperature fluid flow of 200 m across the ridge axis (Tolstoy et al., 2008). The height of the sheeted dikes is variable at Pito Deep, however a minimum thickness of 500 m is used to calculate the maximum length of the source region needed (Perk et al., 2007; Heft et al., 2008). The calculated length is from 63 to 147 m, depending on the lifetime of the hydrothermal system (10-100 years). Therefore the volume of a source region needed to form a deposit of $11m^3$ (3000 tonnes) over 100 years would be:

200 m (wide) * 500 m (deep) * 147 m (long) = 14 700 000 m^3 = 0.015 km^3

Active hydrothermal sites are observed to occur at intervals of 25-54 km along fast-spreading ridges (Baker and Urabe, 1996; Hannington et al., 2011a), and hydrothermal cell and seismicity studies have suggested that the distance between major recharge and discharge zones is <500 m (Coumou et al., 2008; Tolstoy et al., 2008). Therefore the modelled source region can easily produce deposits anywhere from 0.5-25 km along fast-spreading ridges. This suggests that no external introduction of base metals into the hydrothermal system (e.g. magmatic fluids) is needed to be able to produce sulphide deposits along fast-spreading ridges, and that deposits may occur more frequently than currently estimated.

In comparison, the study completed by Humphris and Cann (2000) calculated that to form a 300,000 tonne deposit along a slow-spreading ridge (where the crust is estimated to have lost 45 ppm of Cu) a 1-2 x 10^{12} kg (0.36-0.71 km^3) source region of altered rock would be needed. As a result, a deposit that is 100 times bigger needs a source region that is ~50 times larger (keeping in mind that more Cu has been removed from the sheeted dikes). Although the total volume of crust needed for a source region is large, with respect to the hydrothermal and mid-ocean ridge system, the amount of crust needed to form any one deposit is surprisingly small.

2.4.3 Summary

The results presented in this chapter have shown that neither the degree of alteration or the dominant mineral assemblage affects the release of base metals from the sheeted dikes. There is no systematic trend of base metal mobility with depth or region, and not all base metals are removed from the system equally. The depletion of the studied base metals in samples from the sheeted dike complex is highly variable, the absolute

values range as follows: Zn and Pb show over 70% of the samples have lost over 35% of their original Zn and Pb content; 25% of samples show Cu depletion of 50% their original concentration; 1.5% of samples show Co depleted by 21.3% of their original concentration, Mn shows enrichment in 29.6% of the samples and depletion in 18.9% of the samples, and finally that bulk rock Ni has not changed in concentration from the original fresh rock concentration. The relative depletion of metals is: Zn >Pb>> Cu > Mn > Co and Ni shows no change. In other words, Zn and Pb have preferentially left the system; some of Cu, Mn, and Co may have been mobilized and redistributed back into the altered rocks, never became mobilized, or left the system (will be discussed in detail in Chapter 4); and all Ni either remained in the system and did not become mobilized or was mobilized and all of it was redistributed back into the rock.

Comparisons of Pito Deep to Hess Deep and Hole 1256D show numerous similarities in Sr-isotopes, alteration patterns, and in base metal mobility at each location. Therefore Pito Deep is analogous to other fast-spreading ridges, and can be used to help interpret processes occurring at depth along fast-spreading ridges.

Finally, the observed leaching of the studied base metals from the sheeted dike complex only requires a small section of the crust to form a typical EPR seafloor Fe-Cu ore deposit. The calculated size of the source region is comparable (the relative size) to a previously calculated source region at the TAG hydrothermal site and is a reasonable volume for a typical hydrothermal cell along fast-spreading ridges. The small size of the source region suggests that there is no additional source of metals in the hydrothermal fluids, and that more deposits are most likely to be present than currently estimated along fast-spreading ridges.

Chapter 3

Mineralogical Controls on Metal Mobility

3.1 Introduction

To understand the mobility of metals in the sheeted dike complex exposed at Pito Deep documented in Chapter 2, the metal content of key igneous and metamorphic minerals (plagioclase, clinopyroxene, Fe-Ti oxides, Fe-Cu sulphides, chlorite, mixed-layer clays, and amphibole) were measured. Standard major element and base metal (Cu, Ni, Mn, Zn, Co, Pb) compositions of these minerals were analysed in 20 samples distributed throughout Pito Deep and whose alteration characteristics are representative of the broader sample suite.

This study determines what base metals reside in each mineral and attempts to show how base metals partition and redistribute (precipitate back into a secondary phase) when interacting with hydrothermal fluids. This work further expands the petrographic and geochemical database of Pito Deep samples (and subsequently the global oceanic basalt database) and contributes to our understanding of the evolution of oceanic crust.

3.2 Sample Suite

A petrographic and geochemical database of 291 samples collected from Pito Deep was compiled from previous studies (Barker et al., 2008; Heft et al., 2008; Pollock et al., 2009). This database includes bulk rock geochemical data, mineral compositions (amphibole, chlorite, plagioclase, epidote), % alteration, dominant alteration phase, grain size, and modal abundance.

Based on these data, 20 samples were selected for detailed study that are representative of the degree of alteration (<5% up to 90%), the modal abundance of secondary minerals, bulk rock geochemical trends (changes in metal concentrations determined in Chapter 2, $^{87}Sr/^{86}Sr$), and the geographical distribution between the two study areas (Figure 3.1). It was also necessary to select samples based on grain size (in particular for amphibole and Fe-Ti oxide analysis) in order to analyze individual mineral grains using the LA-ICP-MS (typical spot size of 30-40μm). See Appendix B.1 for thin section descriptions.

3.3 Analytical Techniques

Major element compositions of igneous and hydrothermal silicate and oxide minerals were determined using the University of British Columbia's CAMECA SX-50 Electron Microprobe (EMP); operating in wavelength-dispersion mode with a beam size of 1-5 μm, accelerating voltage of 15 kV, peak count time of 20s, a background count time of 10 s, and a beam current of 20 nA. Sulphide minerals were analyzed on the same EMP under the same conditions as the silicates and oxides, except the accelerating voltage was 20 kV.

Trace element compositions of igneous and hydrothermal silicate and Fe-Ti oxide minerals were determined using the Laser Ablation and Inductively Coupled Plasma Mass Spectrometer (LA-ICP-MS) at the University of Victoria. The instrument used was a New Wave 213 nm Nd-YAG UV laser and a Thermo X-Series ICP-MS.

Mineral data were calibrated against the international standards NIST 615, 613 and 611. The NIST standards were analyzed at the beginning of each analytical session,

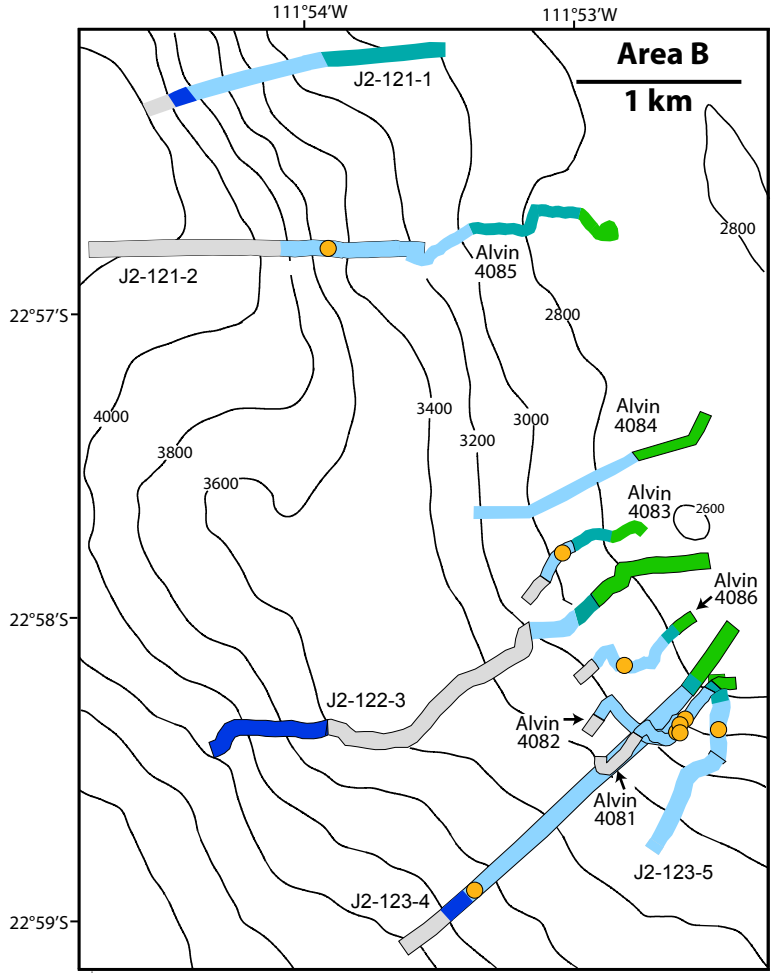

Figure 3.1: Regional maps of Area A and Area B at Pito Deep, EPR, showing the locations (yellow dots) of the 20 representative samples studied for mineral compositions. Transect information can be found in Appendix B.

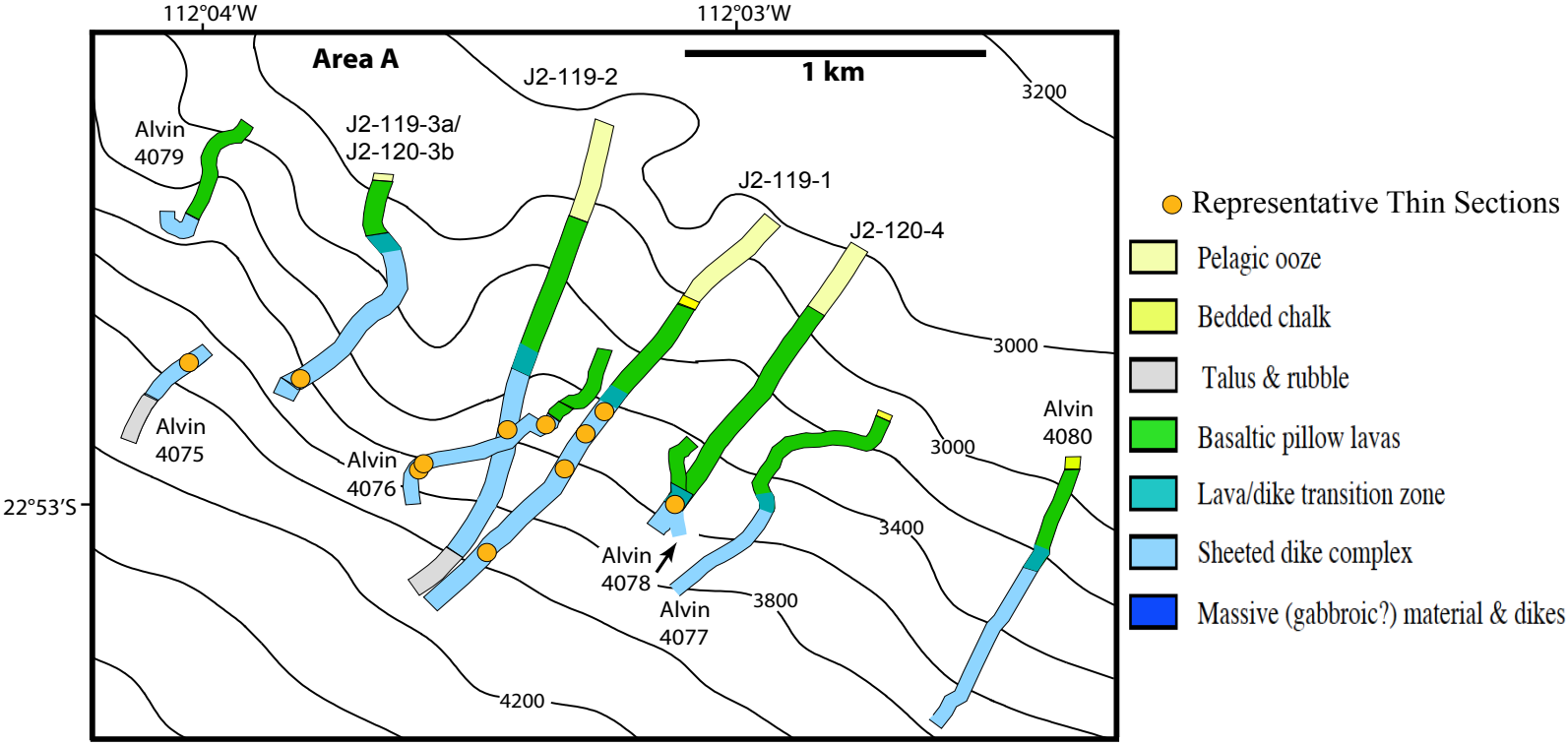

before and after each sample change, and after every 10 analyses. The trace elements analyzed include: ^{65}Cu, ^{60}Ni, ^{66}Zn, ^{208}Pb, ^{55}Mn, ^{59}Co, ^{29}Si, ^{42}Ca, ^{27}Al, ^{138}Ba. Data collected after November 1, 2012 also included ^{23}Na, ^{25}Mg, ^{39}K, ^{47}Ti, ^{57}Fe, ^{63}Cu, ^{67}Zn, and ^{68}Zn and glass standard BCR2g to monitor reproducibility. Silicon was used as an internal standard for the silicate minerals, and Al was used for the Fe-Ti oxides. For each spot analyzed by LA-ICP-MS the corresponding Si or Al concentration collected from EMP analysis was used as an internal standard for each mineral. The parameters (beam size, voltage, energy) of the instrument were adjusted for each mineral depending on grain size and whether the mineral was homogenous or not.

Lead data was collected for all minerals studied, using LA-ICP-MS for silicates and Fe-Ti oxides and EMP for the sulphides. Due to the very low concentration of Pb in all minerals (<1 ppm and a detection limit of ~0.1 ppm), the data collected is not of a high quality. In many analyses from LA-ICP-MS the counts per second (cps) of Pb were highly irregular (e.g. noisy with large peaks and very low cps) making it difficult to differentiate from the background noise. Lead data in Fe-Cu sulphides from the EMP all showed concentrations below the detection limit of 0.1 wt%. The Pb concentrations provided in this study were the best data available and considered to be reasonable approximations.

Appendix A provides the EMP and LA-ICP-MS parameters (energy, beam size, quality, etc.) used for each analytical session. Fe-Cu sulphides were not analyzed using LA-ICP-MS because high concentrations of S and Cu can contaminate the system, effecting future analytical work.

3.4 Petrologic Characteristics and Major Element Compositions of Igneous and Metamorphic Minerals

Petrographic observations and major element data are used to determine the igneous and metamorphic mineral assemblages in the samples suite.

3.4.1 Plagioclase

Primary plagioclase is unaltered in approximately 80% of the samples from Pito Deep, with the remaining 20% being altered to assemblages of amphibole, chlorite or mixed-layer clays, with a modal abundance of at least 10-15% fresh plagioclase in each sample. Plagioclase is subhedral to euhedral, with grain sizes of <0.5 mm up to 1.5 mm. The anorthite content of plagioclase ranges from An_{78} to An_{25}, with 98% of the grains falling between An_{45} to An_{60}. Secondary plagioclase is distinguished from primary plagioclase based on chemical criteria, with anorthite contents $<An_{40}$ and $>An_{60}$ (Heft et al., 2008). Secondary plagioclase is not included in this study due to its small grain size and was not possible to identify using the LA-ICP-MS.

3.4.2 Clinopyroxene

Primary clinopyroxene is preserved in all samples and the grain size of the unaltered clinopyroxene ranges from <0.1mm up to 1mm. Clinopyroxene has a large compositional range of Mg# (0.54 and 0.86) between samples, but are relatively homogeneous within individual samples (±0.1, 1std). The wollastonite, enstatite, and ferrosilite contents (assuming all Fe is FeO) range from Wo_{25-45}, En_{35-62}, and Fe_{9-31}.

The degree of alteration of clinopyroxene varies from 5% to up to 95%, with an average of 25%. It is altered to assemblages of amphibole, chlorite, and mixed-layer

clays. Previous work identified rare secondary clinopyroxene (Heft et al., 2008), however due to its very fine grain size it was not investigated in this study.

3.4.3 Fe-Ti Oxides

The Fe-Ti oxides, ilmenite or titanomagnetite, comprise 2% to 10% of the studied samples, with titanomagnetite occurring in all samples and ilmenite in only three samples. Ilmenite is fine grained (<0.05mm) and cubic. Titanomagnetite ranges from 0.05-0.5mm in size. Unaltered grains of titanomagnetite have sharp boundaries, can be cubic or skeletal, and may have oxidization rims. Ilmenite has FeO^T (total Fe) from 38-52wt% and TiO_2 from 45-52wt%, towards the ilmenite end-member along the ilmenite-hematite solid solution series, whereas titanomagnetite has FeO^T from 60-80wt% and TiO_2 from 10-30wt%, towards the ulvospinel end of the ulvospinel-magnetite solid solution series (Figure 3.2). Exsolution lamellae in titanomagnetite are observed optically (reflective light) in some samples. Grains that do not lie along the ilmenite-titanomagnetite trend (Figure 3.2) show an increase in SiO_2 and CaO and an overall decrease in FeO and TiO_2, due to the alteration of titanomagnetite to titanite (confirmed by EMP analysis).

To assess if the Fe-Ti oxide assemblages are typical for fast-spreading crust, the results of this study are compared to Hole 1256D. A study on the Fe-Ti oxides dispersed throughout the lava sequence and sheeted dikes showed typical ilmenite compositions of FeO^T 48wt% and TiO_2 50wt%, and titanomagneitie has, on average, FeO^T and TiO_2 compositions of 68wt% and 20wt%, respectively (Dziony et al., 2008). The similarity between the two locations confirms that Pito Deep Fe-Ti oxides are typical of oceanic basalts formed at fast-spreading ridges.

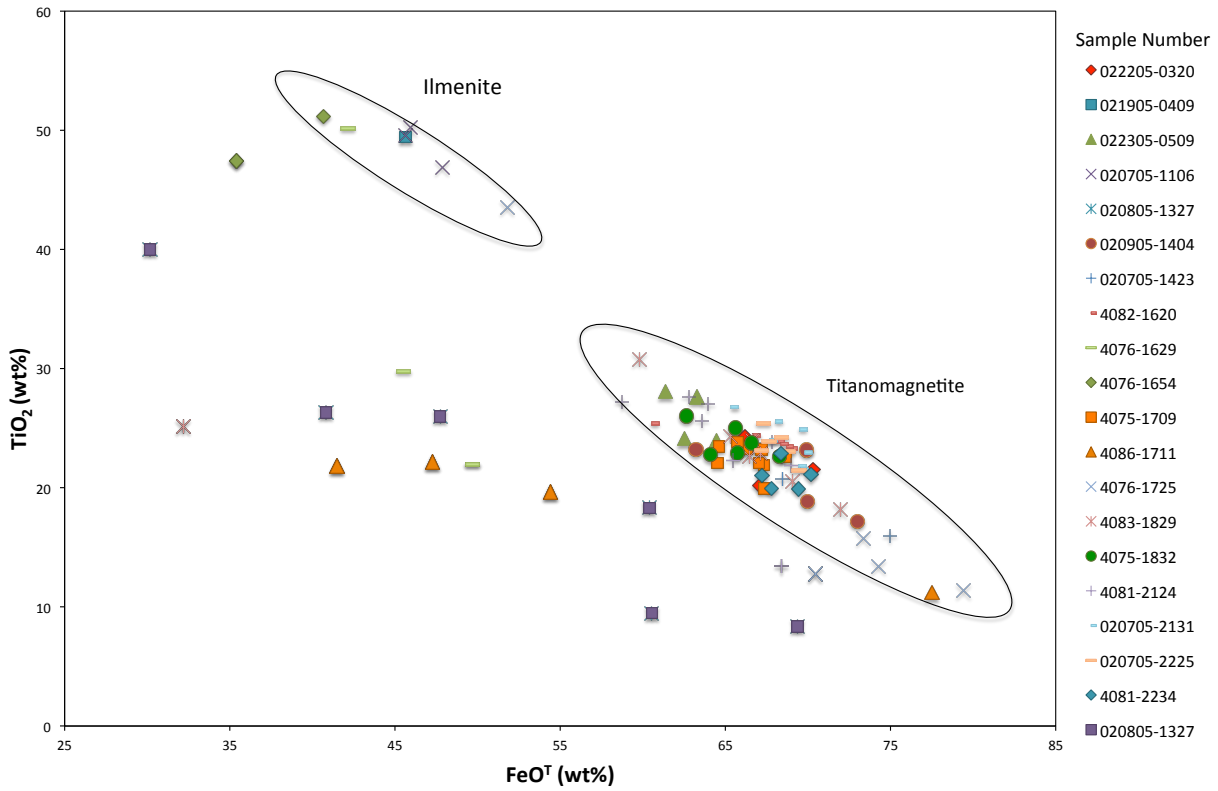

Figure 3.2: FeO (total) versus TiO_2 (wt%) for Fe-Ti oxides. Circled trends indicate expected range in values for titanomagnetite and ilmenite solid solutions. Data that lie to the left of these trends are considered partially altered to titanite (based on major element data)

3.4.4 Phyllosilicates

Following the approaches of Bettison and Schiffman (1988) and Schiffman and Fridleifsson (1991), chlorite and mixed-layer clays were differentiated using stoichiometric criteria. All minerals were recalculated on the basis of 28 anhydrous oxygens. Plots of Si versus Fe# (Fe/(Fe+Mg) (Figure 3.3) and Si+Al+Fe+Mg versus total Al confirm the presence of chlorite and mixed-layer clays (Figure 3.4). Chlorite and mixed-layer clays can be found co-existing in ~25% of the samples containing phyllosilicates, however most samples do show a dominance of either chlorite or mixed-layer clays (Figure 3.3). Mixed-layer clays contain 1-26% interlayered smectite (average 14%) (interlayer abundance calculated following Bettison and Schiffman, 1988). Chlorite analysis from previous work shows the same range in Si composition (5-9.5) and Fe# (0.2-0.8) (Heft et al., 2008). Observations from this study show that chlorite is the dominant alteration phase (84% of the 20 representative samples).

Phyllosilicates replace clinopyroxene, interstitial areas, and plagioclase, in decreasing order of abundance respectively. Chlorite replacing clinopyroxene is well defined (a pure grain of chlorite, not intermixed with other minerals) and distinctively green, but where it replaces interstitial groundmass it occurs as a mass of fine grained chlorite and can be mixed with another mineral. Mixed-layer clays are dominantly brown and present as masses of fine and irregularly oriented grains.

Talc is present as distinct, very fine (<0.1mm) grains in 5% of the samples. Within these samples, talc comprises less than 1%. Due to the trace amount of talc it is not considered further in this study.

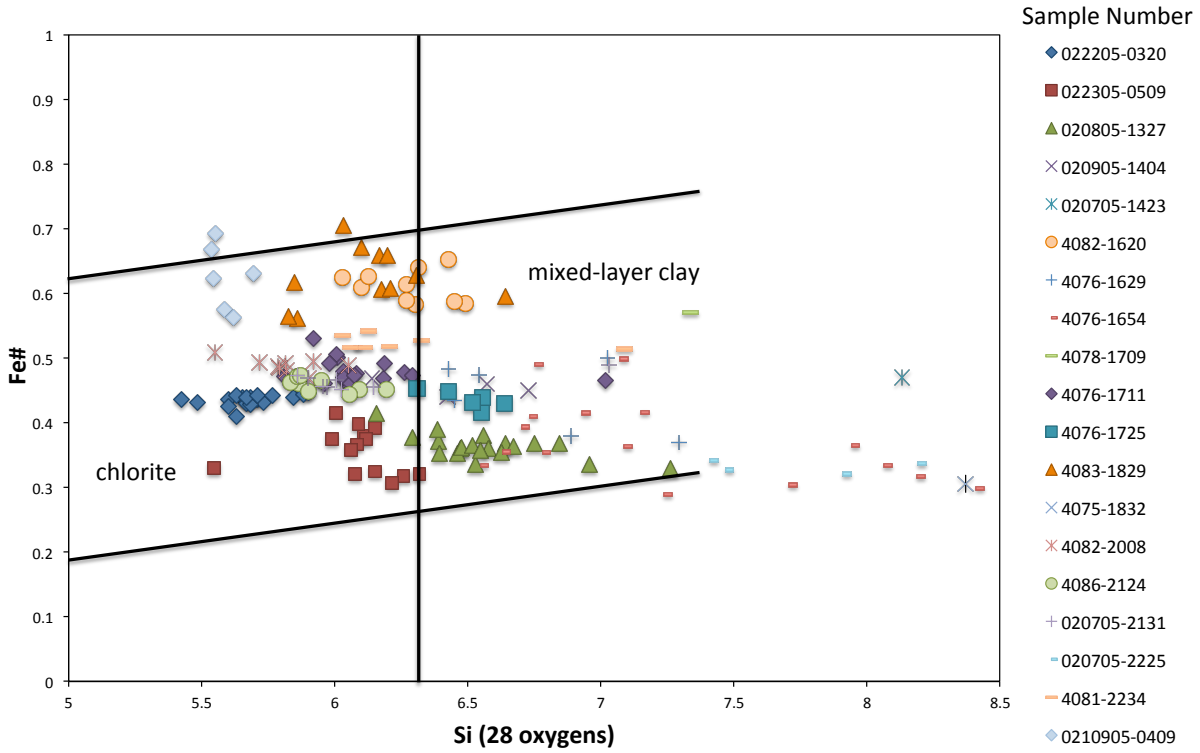

Figure 3.3: Fe# (Fe/Fe+Mg) versus Si (based on 28 oxygens) for phyllosilicates. All data recalculated based on 28 oxygens. Si values above ~6.3 are considered mixed-layer clays and <6.3 is chlorite (Bettison and Schiffman, 1988).

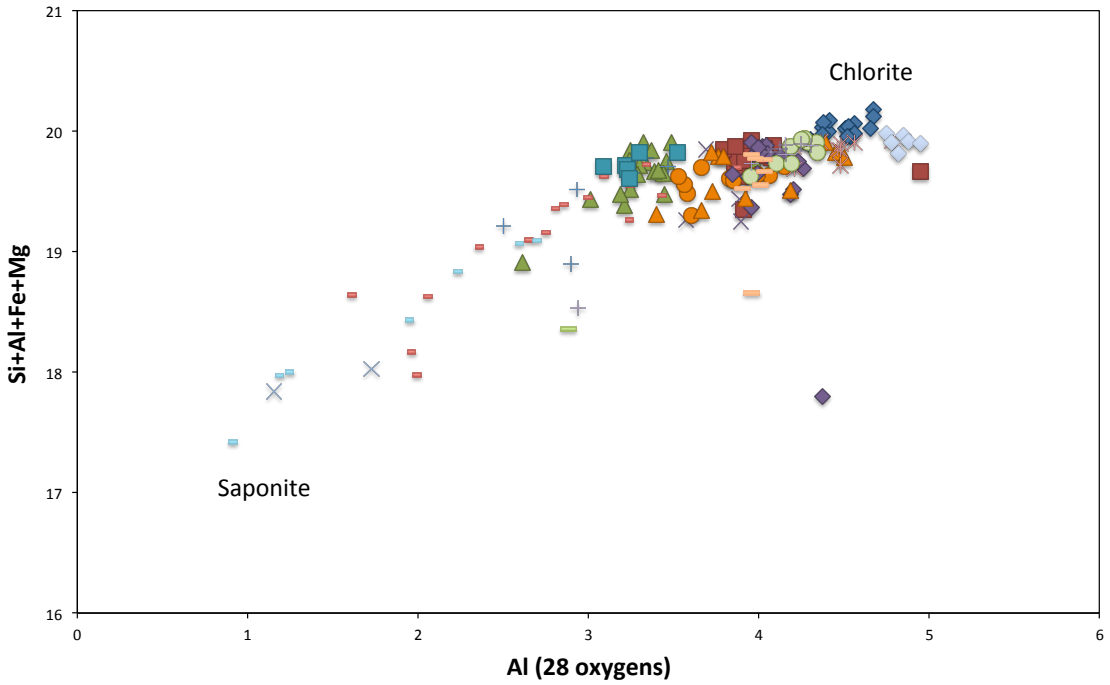

Figure 3.4: Sum of major non-interlayer cations (Si+Al+Fe+Mg) versus total Al for the Pito Deep phyllosilicates (all analyses recalculated based on 28 oxygens). Phyllosilicates fall along the trend between pure chlorite and pure saponite; total Al > 4 is considered chlorite (based on Figure 9 from Schiffman and Fridleifsson, 1991). Symbol legend found on Figure 3.3.

3.4.5 Amphibole

Secondary amphibole is fine-grained and acicular, and can partially to completely replace clinopyroxene (<5% up to 98%) or can occur as aggregates of fine grained crystals replacing the groundmass (where it is commonly associated with chlorite). Chlorite and amphibole can be hard to distinguish due to their grain size and usually occur intermixed.

A plot of Si versus Mg# (Mg/Mg+Fe) illustrates the compositional variation of amphibole, from magnesiohornblende to actinolite (Figure 3.5). Magnesiohornblende is the dominant amphibole present. Previous amphibole analyses fall within range of the analyses conducted here, and magnesiohornblende is shown to be more abundant than actinolite (Heft et al., 2008).

Due to the grain size of amphibole, only 6 samples have grains suitable for trace element analysis, and only 2 of those 6 samples have amphibole as a dominant alteration phase.

3.4.6 Fe-Cu Sulphides

All samples contain trace amounts of Fe-Cu sulphides, with a modal abundance of less than 1%. Pyrite (FeS_2) and, to a lesser extent, chalcopyrite ($CuFeS_2$) are the two dominant sulphides, with only rare pyrrhotite (FeS) (Figure 3.6). Sulphide inclusions in chlorite, mixed-layer clays, and amphibole are not observed optically, but are identified on the basis of substantial Cu counts during LA-ICP-MS analysis and were subsequently removed from the timeslice. Chalcopyrite and pyrite identification was based on the varying intensity of the Cu peaks from LA-ICP-MS time slices.

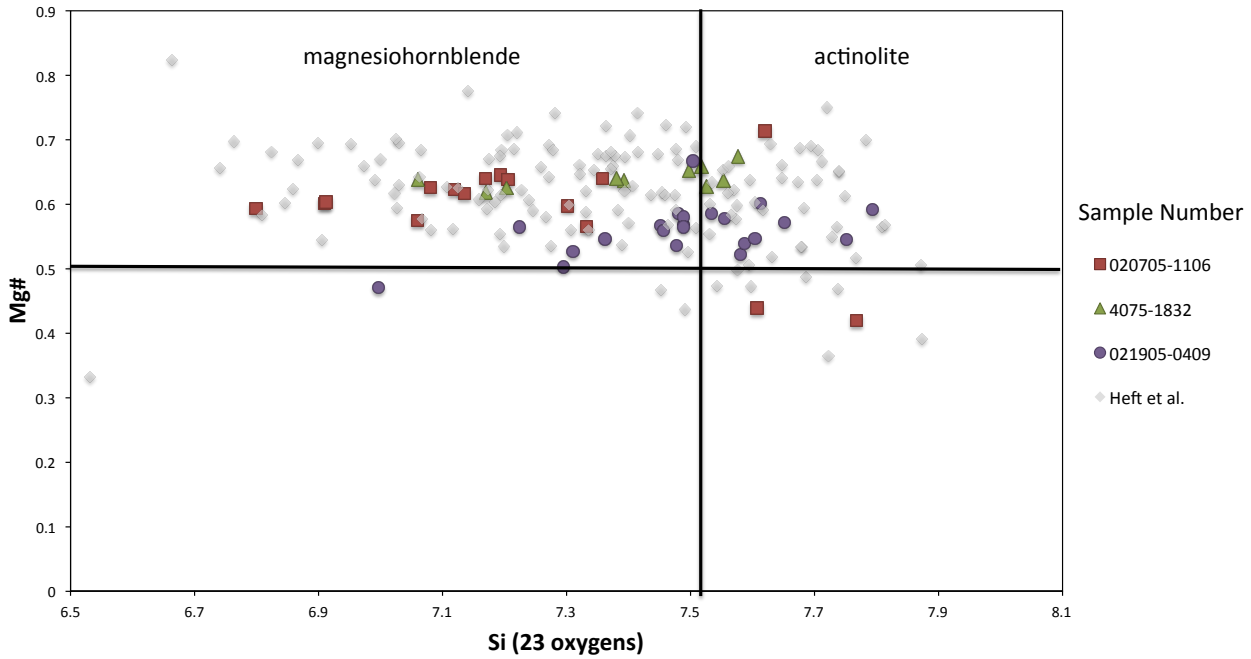

Figure 3.5: Mg# (Mg/Fe^{2+}+Mg) versus Si. Amphibole analyses were recalculated based on 23 oxygens using the 15eNK method, which minimizes the Fe^{3+}content (Leake et al., 1997). Mg# > 0.5 and Si < 7.5 is considered to be magnesiohornblende and Si > 7.5 is considered to be actinolite (nomenclature based on Leake et al., 1997). Previously published amphibole data from Pito Deep are shown for comparison (grey symbols; Heft et al., 2008).

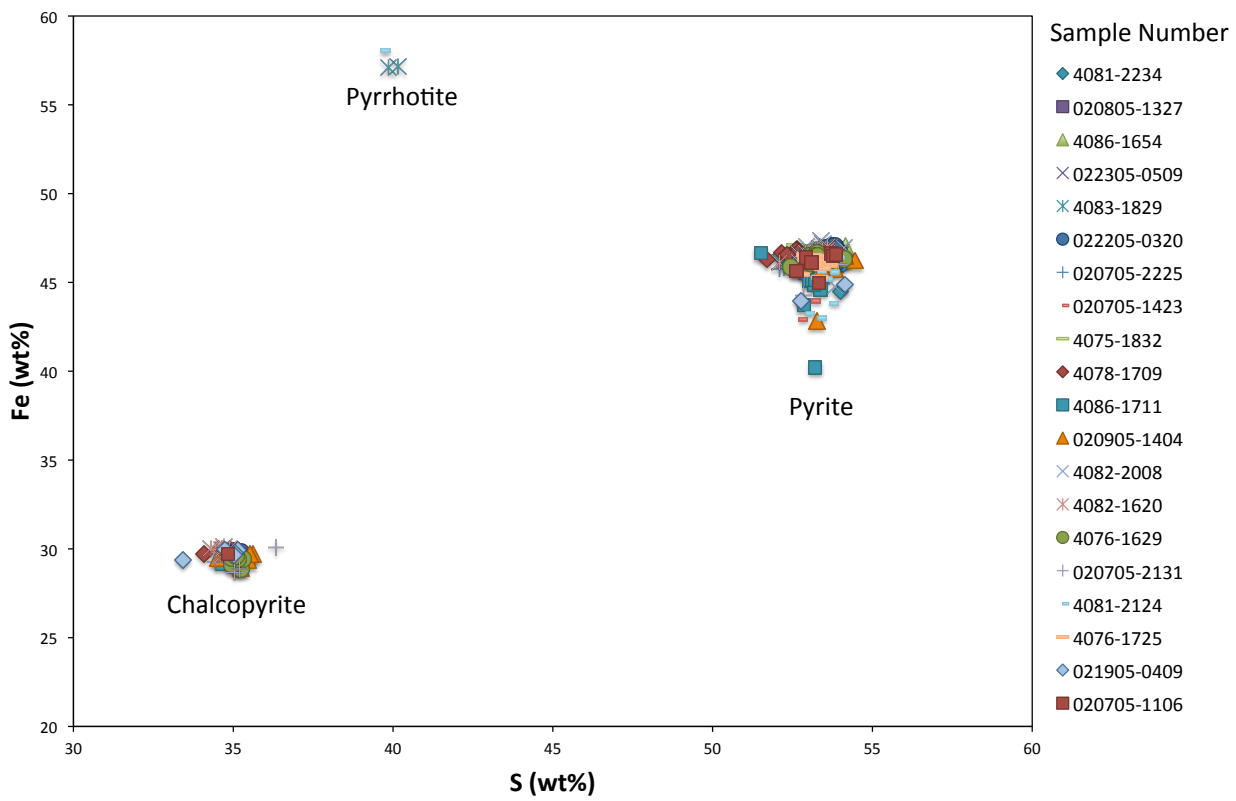

Figure 3.6: Fe (wt%) versus S (wt%) for Pito Deep Fe-Cu sulphides.

Pyrrhotite is found, in two samples only, as very fine isolated globules (<0.01mm). Pyrite and chalcopyrite range from <0.05mm up to 2mm, however chalcopyrite is commonly finer grained than pyrite (<0.1mm). The sulphides are grouped as groundmass sulphides (which can occur as isolated grains/inclusions in secondary minerals/void-filling) or vein-filling sulphides.

3.5 Mineral Base Metal Compositions

Base metal data was collected for all silicate minerals, Fe-Ti oxides, and Fe-Cu sulphides to evaluate the mineralogical sources or sinks for the base metals. Data can be found in Appendix D.3.

3.5.1 Plagioclase

The base metal content of primary plagioclase was determined in a subset of samples (Table 3.1). Typical ranges of Mn, Co, Ni, Cu, Zn, and Pb contents are: 10-30 ppm, 1-3 ppm, 1-10 ppm, 1-5 ppm, 3-10 ppm, and 0.1-0.3 ppm, respectively. These low concentrations do not significantly contribute to the bulk rock values, even though plagioclase is modally significant. Therefore, no additional plagioclase data was collected.

Table 3.1: Plagioclase base metal concentrations

Mineral	Concentrations (ppm)	Mn	Co	Ni	Cu	Zn	Pb
Plagioclase	Max	130.5	13.9	74.0	23.6	16.9	0.7
	Min	10.0	0.2	0.2	0.1	0.9	0.1
	Average	39.2	2.7	9.0	4.1	6.7	0.3
	Median	35.0	1.4	2.6	1.9	5.6	0.3
	Stdev	24.5	3.1	17.2	6.4	3.9	0.2
	n	31	28	21	23	29	13

Detection Limit for Mn=10 ppm, Co=0.15 ppm, Ni=0.2 ppm, Cu=1 ppm, Zn=0.75 ppm, Pb=0.1 ppm

3.5.2 Clinopyroxene

The base metal concentration of clinopyroxene was determined for all of the studied samples. Overall, Mn, Ni, Zn, and Co have the highest concentrations in clinopyroxene, whereas Cu and Pb have significantly lower concentrations. Typical ranges in concentration of Mn, Ni, Zn, Co, Cu, and Pb are: 1300-2300 ppm, 100-200 ppm, 20-100 ppm, 40-60 ppm, 1-8 ppm, and 0-1 ppm, respectively (Table 3.2, Appendix D.3).

In general, clinopyroxene contains trace amounts of all the base metals studied and concentrations are representative of the magmatic phase (discussed below). Overall, individual samples have either consistently high or low base metal contents. However, concentrations of Mn, Ni, Zn, and Co in clinopyroxene can vary from grain to grain (within the same sample) up to 45% of the average concentration, while Cu and Pb can vary up to 86% and 95%, respectively (Figure 3.7).

To assess if the clinopyroxene base metal compositions are magmatic, expected magmatic values (Cpx_{Metal}) were calculated using published partition coefficients (K_d) and the calculated fresh bulk rock metal concentrations ($Melt_{Metal}$) determined in Section 2.3:

$$[Cpx_{Metal}] = K_d * [Melt_{Metal}] \qquad (5)$$

Published K_d values were limited to only a few available studies on metal partitioning between clinopyroxene and basaltic melt. K_d values of Cu between clinopyroxene and melt range from 0.04 to 0.19 (Lee et al., 2012; Fellows and Canil, 2012, respectively). Both values were used to calculate the range of possible magmatic Cu concentrations in clinopyroxene. K_d values for Mn, Zn, Co, Ni from Le Roux et al.

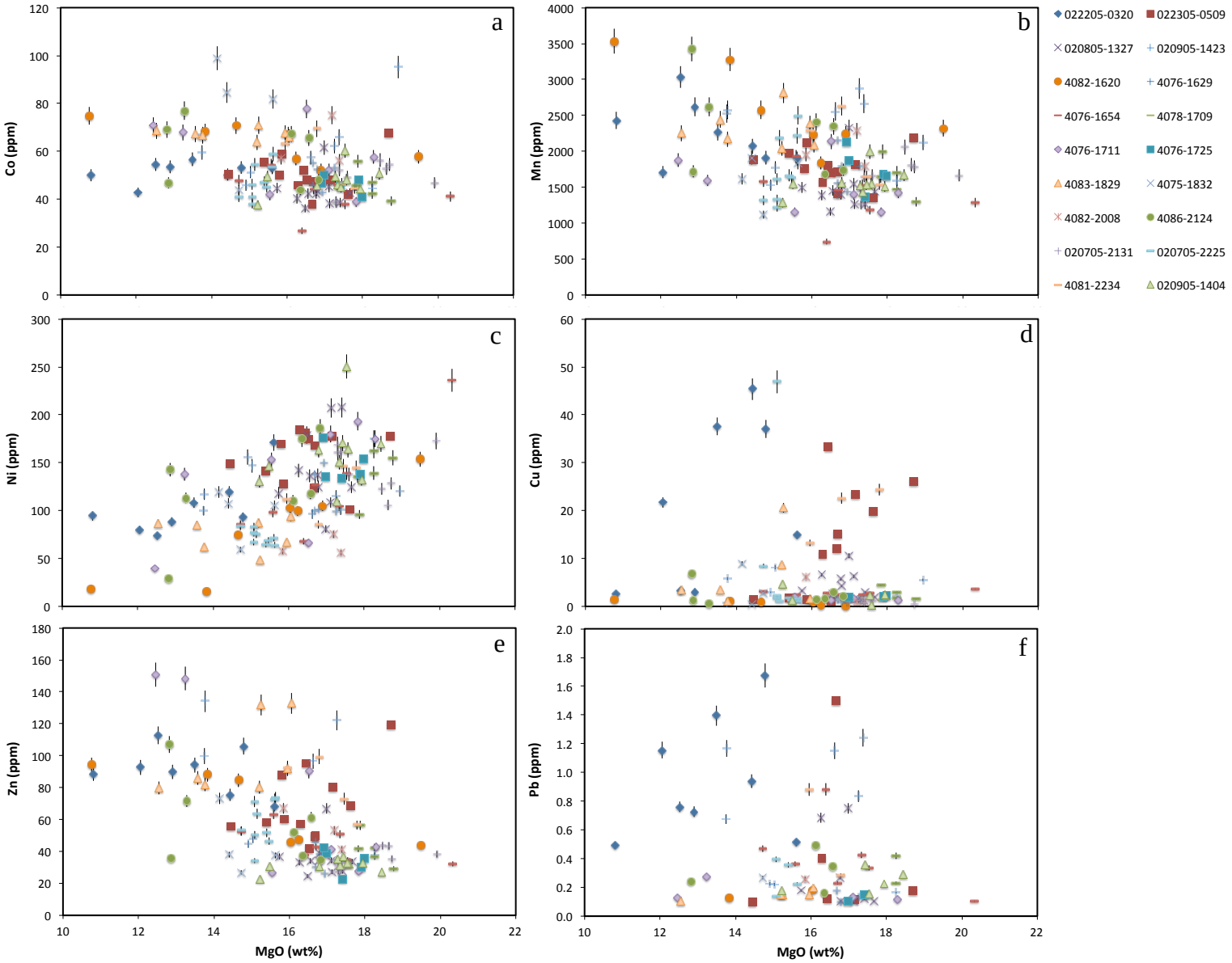

Figure 3.7: a-f) Base metal concentrations (ppm) versus MgO (wt%) for primary clinopyroxene. Error bars determined by the NIST values that are closest to the base metal concentration and are the percent error associated with each metal (therefore the error bars appear smaller as concentration decreases; for details see Appendix A.2).

(2011) are used as they represent an internally consistent data set that is suitable for MORB. The K_d value for Pb from Hart and Dunn (1993) was used as it is the only published value for Pb partitioning into clinopyroxene.

Table 3.2 summarizes the calculated base metal concentrations and the analyzed concentrations in clinopyroxene. The similarity between calculated and analyzed base metal concentrations in the studied samples indicates that clinopyroxene base metal contents are magmatic.

The base metal content of magmatic clinopyroxene is influenced by magmatic differentiation and crystallographic controls. To evaluate the influence of magmatic differentiation, metal contents were plotted against MgO as a proxy for differentiation. Concentrations of Co, Zn, and Mn increase, while Ni decreases with decreasing MgO, suggesting that magmatic differentiation is a controlling parameter of base metal concentrations (Figure 3.7). Copper in clinopyroxene does not correlate with MgO and therefore is not controlled by magmatic differentiation as is observed by the other base metals or by the bulk rock plots (note the quality of Pb data limits the interpretation of the magmatic effect of Pb). Although Fe-Cu sulphide inclusions in clinopyroxene may be a possible reason for the lack of correlation, there were no large peaks of counts per second of Cu in LA-ICP-MS analysis and therefore does not suggest a Fe-Cu sulphide inclusion.

Crystallographic controls in clinopyroxene are determined by the availability of Fe and Mg in the M1 site, and Ca in the M2 site (Morimoto, 1989). Both Cu and Pb can fit into the M1 and M2 sites, however the ionic radius of each element limits their ability to substitute into these sites (Blundy and Wood, 1994). The ideal ionic radius for an element to enter into the M1 site is ~0.7Å and the M2 site is ~1Å. Based on the ionic

radii of each base metal Mn (0.95Å) and Zn (0.9Å) will preferentially partition into the M2 site and Ni (0.7Å) and Co (0.75Å) will enter into the M1 site. Since Cu (~0.6Å) and Pb (>1.2Å) have lower and higher ionic radii, respectively, they will not easily enter into either site (Adam and Green, 2006). In addition, experimental work by Adam & Green (2006) showed that partition coefficients for Cu and Pb into clinopyroxene do not fit the ideal parabolic trend of K_d versus cation radius (in fact Cu shows a converse relationship), and therefore they did not publish K_d values for Pb or Cu. Adam & Green (2006) concluded that unknown factors at the time of crystallization must occur that cannot be accounted for by a generalized model.

In summary, the clinopyroxene analyzed in this study is magmatic. Magmatic differentiation is the main control of the concentration of Mn, Ni, Zn, and Co in the mineral. It cannot be concluded that Cu and Pb are directly controlled by differentiation because there is no trend of MgO with Cu or Pb in the clinopyroxene. Additionally, the quality of the Pb data limits what can be interpreted. Future experimental work will need to be done to conclude, with confidence, the dominant control of Cu and Pb in the clinopyroxene.

Table 3.2: Measured base metal concentrations in clinopyroxene compared to calculated magmatic base metal concentrations in clinopyroxene.

Metal	Partition Coefficient	Resource		Calculated Fresh Bulk Rock Concentration (ppm)*	Calculated Clinopyroxene Concentration (ppm)	Measured Clinopyroxene Concentration (ppm)
Cu	0.04	Lee et al., 2012	Max	94.1	3.76	46.8
			Min	64.2	2.57	1.02
			Average	81.1	3.24	6.62
			Median	80.7	3.22	2.45
			Stdev	7.61	0.304	9.35
			n	37	37	96
Cu	0.19	Fellows and Canil, 2012	Max	94.1	17.9	46.8
			Min	64.2	12.2	1.02
			Average	81.1	15.4	6.62
			Median	80.7	15.3	2.45
			Stdev	7.61	1.45	9.35
			n	37	37	96
Mn	1.11	Le Roux et al., 2011	Max	1880	2090	3532
			Min	1450	1610	738
			Average	1610	1790	1864
			Median	1610	1790	1717
			Stdev	104	115	531
			n	37	37	129
Zn	0.48	Le Roux et al., 2011	Max	149	71.3	151
			Min	95.2	45.7	22.4
			Average	115	55.1	57.4
			Median	114	54.7	43.9
			Stdev	12.7	6.11	30.4
			n	37	37	127
Co	1.06	Le Roux et al., 2011	Max	47.1	50.0	98.8
			Min	44.3	46.9	26.6
			Average	46.0	48.7	53.7
			Median	45.9	48.7	50.1
			Stdev	0.71	0.76	13.5
			n	37	37	129
Ni	3.24	Le Roux et al., 2011	Max	78.7	255	250
			Min	22.7	73.4	15.5
			Average	43.6	141	126
			Median	42.5	137	125
			Stdev	13.6	43.9	45.5
			n	36	36	129
Pb	0.072	Hart and Dnnn, 1993	Max	0.71	0.05	2.04
			Min	0.33	0.02	0.10
			Average	0.46	0.03	0.43
			Median	0.45	0.03	0.23
			Stdev	0.08	0.01	0.44
			n	37	37	73

* Fresh rock values calculated following the procedures outlined in Section 2.3

Limit of detection: Mn=300 ppm, Co=24 ppm, Ni=30 ppm, Cu=1 ppm, Zn=20 ppm, Pb=0.1 ppm

3.5.3 Fe-Ti Oxides

The base metal concentration of ilmenite and titanomagnetite was determined in 15 samples of the 20 samples studied. The Fe-Ti oxides in the remaining 5 samples were too fine grained to be analyzed. In total only 3 grains of ilmenite were successfully analyzed for base metals.

Manganese and Zn are the most abundant base metals present in both Fe-Ti oxides, with Co, Ni, Cu, and Pb having much lower concentrations (Table 3.3). The typical range of Mn, Co, Ni, Zn, Cu, and Pb contents in titanomagnetite are: 1000-5000 ppm, 5-20 ppm, 20-40 ppm, 150-300 ppm, 5-15 ppm, and 0.2-0.7 ppm, respectively (note that most Pb concentrations are below detection limit). Base metal concentrations in ilmenite were difficult to constrain due to limited number of analyses and quality of those analyses (small grain size and low concentrations, Table 3.3), however Mn is generally higher in ilmenite, reaching concentrations up to 9000 ppm.

In samples with co-existing ilmenite and titanomagnetite, Mn will preferentially partition into the ilmenite phase over titanomagnetite (Rumble, 1976). Titanomagnetite is partially to fully exsolved in many samples, with discrete ilmenite lamellae. Therefore the distribution of Mn within a grain will vary substantially depending on the distribution of lamellae. Due to the size of the lamellae it was not possible to analyze a lamellae separate from the host grain.

The control of the crystal structure on trace element concentrations has not been studied for MORB-hosted Fe-Ti oxides. With no available K_d values for metal partitioning between melt and oxide it is not possible to assess the effect of magmatic differentiation on the base metal content in Fe-Ti oxides. Experimental studies on Fe-Ti

oxide grains show the variability of base metal concentrations within the crystal structure of titanomagnetite (Sidhu et al., 1978; Sidhu, 1988). The ionic radii, electronegativities, and solubility products of Co^{2+}, Ni^{2+}, and Zn^{2+} are very close to those of Fe^{2+} and can generally occupy the octahedral site. Cu^{2+} has a very similar ionic radius but the electronegativity differs by more than 0.1 from Fe^{2+} and subsequently is less likely to enter into the site (Rumble, 1976; Sidhu et al., 1978, 1980; Deer et al., 1992). Furthermore, studies on the solubility of magnetite in aqueous solutions have shown that the breakdown of Fe-Ti oxides can release iron into the fluid as Fe^{2+}, $FeOH^{+}$, $Fe(OH)_2$, or $Fe(OH)^{-}_3$, subsequently freeing available sites for elements such as Ni and Co (Elsdon, 1972). Therefore Ni, Co, and Zn will enter into the crystal structure of Fe-Ti oxides instead of Cu.

To determine if metals enter into the crystal structure of altered or fresh titanomagnetite at Pito Deep, plots of base metals against FeO, Fe_2O_3, and TiO_2 for altered and unaltered oxides were created (Figure 3.8 shows FeO and TiO_2 plots; plots of Fe_2O_3 can be found in Appendix D.3). Neither fresh nor altered titanomagnetite display any distinct correlation between Co, Ni, Mn, Cu, Zn, or Pb and FeO, Fe_2O_3, or TiO_2. This suggests that these metals do not consistently replace either Fe^{2+}, Fe^{3+}, or Ti in fresh or altered titanomagnetite, but can substitute all of the major components.

In altered titanomagnetite (oxides that do not lie on the FeO-TiO_2 trend, Figure 3.2) no distinct trends are present with respect to major element substitution, however for the base metals analyzed, the concentration of some grains increases and becomes much more variable in Fe-Ti oxides that are considered altered (Figure 3.8). Therefore the

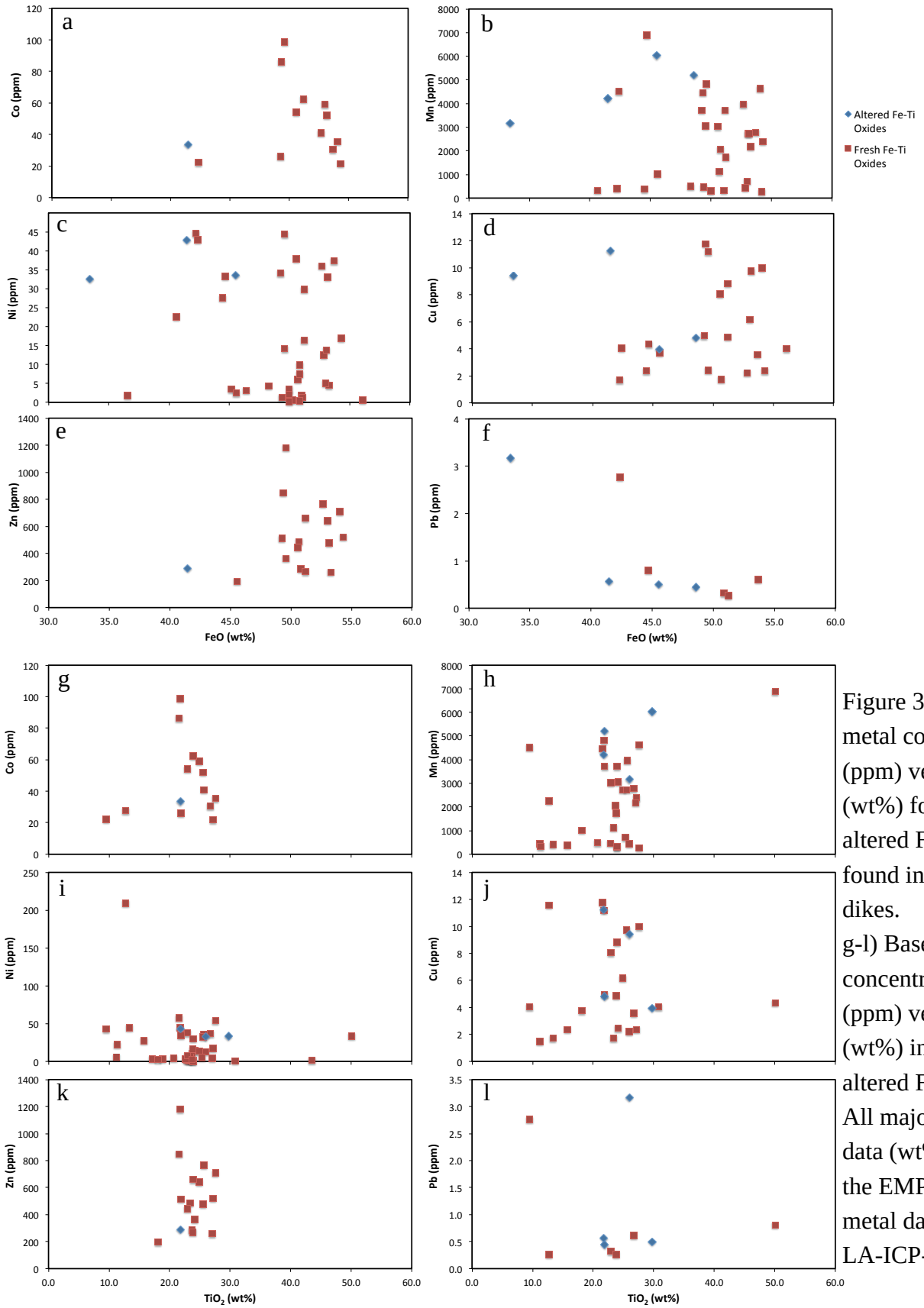

Figure 3.8: a-f) Base metal concentrations (ppm) versus FeO (wt%) for fresh and altered Fe-Ti oxides found in the sheeted dikes.
g-l) Base metal concentrations (ppm) versus TiO_2 (wt%) in fresh and altered Fe-Ti oxides. All major element data (wt%) is from the EMP and base metal data are from LA-ICP-MS.

break down of titanomagnetite and ilmenite may increase the ability of the base metals to partition into the crystal structure.

Studies on the breakdown of magnetite in soils have shown that in unaltered magnetite Co, Ni, and Zn are uniformly distributed throughout the crystal, with Cu and Mn being concentrated near the surface of the crystal (Sidhu et al., 1980). As the crystal breaks down to hematite the Co, Ni, Zn, and Cu will form a surface layer rich in the elements, and Mn will remain within the crystal structure. Due to grain size, core to rim analyses could not be conducted and this idea could not be tested. Although the lithology is different, there is potential for metal concentrations to vary from core to rim, therefore, variation in analysis location on the grain could be a contributing factor to the variation in base metals concentrations observed.

Table 3.3: Base metal concentrations in Fe-Ti oxides

Mineral	Concentrations (ppm)	Mn	Co	Ni	Cu	Zn	Pb
Titanomagnetite	Max	4814	98.8	209.2	11.8	1180	2.77
	Min	258	21.8	0.2	1.51	195	0.27
	Average	2044	47.5	22.3	5.57	539	0.85
	Median	2117	40.8	11.2	4.06	501	0.33
	Stdev	1560	24.4	35.6	3.61	257	1.08
	n	30	13	38	21	16	5
Ilmenite	Max	6887	33.6	42.9	11.2	288.6	3.18
	Min	3154	33.6	1.7	4.0	288.6	0.45
	Average	5100	33.6	28.8	6.8	288.6	1.11
	Median	5216	33.6	33.3	4.8	288.6	0.58
	Stdev	1471	N/A	15.7	3.3	N/A	1.17
	n	5	1	5	5	1	5

Limit of detection: Mn = 200ppm, Co = 20 ppm, Ni = 5 ppm, Cu = 1 ppm, Zn = 150 ppm, Pb = 0.2 ppm

3.5.4 Chlorite and Mixed-layer Clays

The phyllosilicates in the sheeted dike samples are divided into two groups based on their composition: chlorite and mixed-layer clays (Section 3.4). All the phyllosilicates contain substantial amounts of Mn, Co, Zn, Ni, and Cu, with little to no Pb (Table 3.4). Chlorite has typical ranges of Mn 1000-3500 ppm, Co 30-150 ppm, Zn 50-300 ppm, Ni 25-400 ppm, Cu 3-100 ppm, and Pb 0.3-0.9 ppm. In comparison, mixed-layer clays show typical ranges of: Mn 700-2000 ppm, Co 25-250 ppm, Zn 50-300 ppm, Ni 100-600 ppm, Cu 5-100 ppm, and Pb 0.5-1.5 ppm. Although the range of concentrations is large for the entire sample suite, variation within a single sample is much smaller (Figure 3.9). For an individual sample the range in the concentration of each metal is 10-25% in chlorite, and 10-45% in mixed layer clays. Overall, the base metal contents in chlorite and mixed-layer clays are within the same range of each other, except for Ni and Pb. Nickel and Pb can be present at almost double the concentration in the mixed-layer clays compared to chlorite (Figure 3.10), this will be discussed below. Note that Pb concentrations are very low, and the data should only be used for limited interpretation.

It is also important to consider if the mode of occurrence influences the base metal concentrations in phyllosilicates (Figure 3.11). The mode of occurrence is divided into: clinopyroxene replacement, groundmass replacement, and void-filling. The phyllosilicate replacing either clinopyroxene or groundmass show the same range of concentrations (± 35% within an individual sample) and compositionally overlap one another. The void-filling phyillosilicates fall within the same compositional range, however, they all plot at the high or low end (depending on the metal), and show a significantly smaller range (±15% within the same sample).

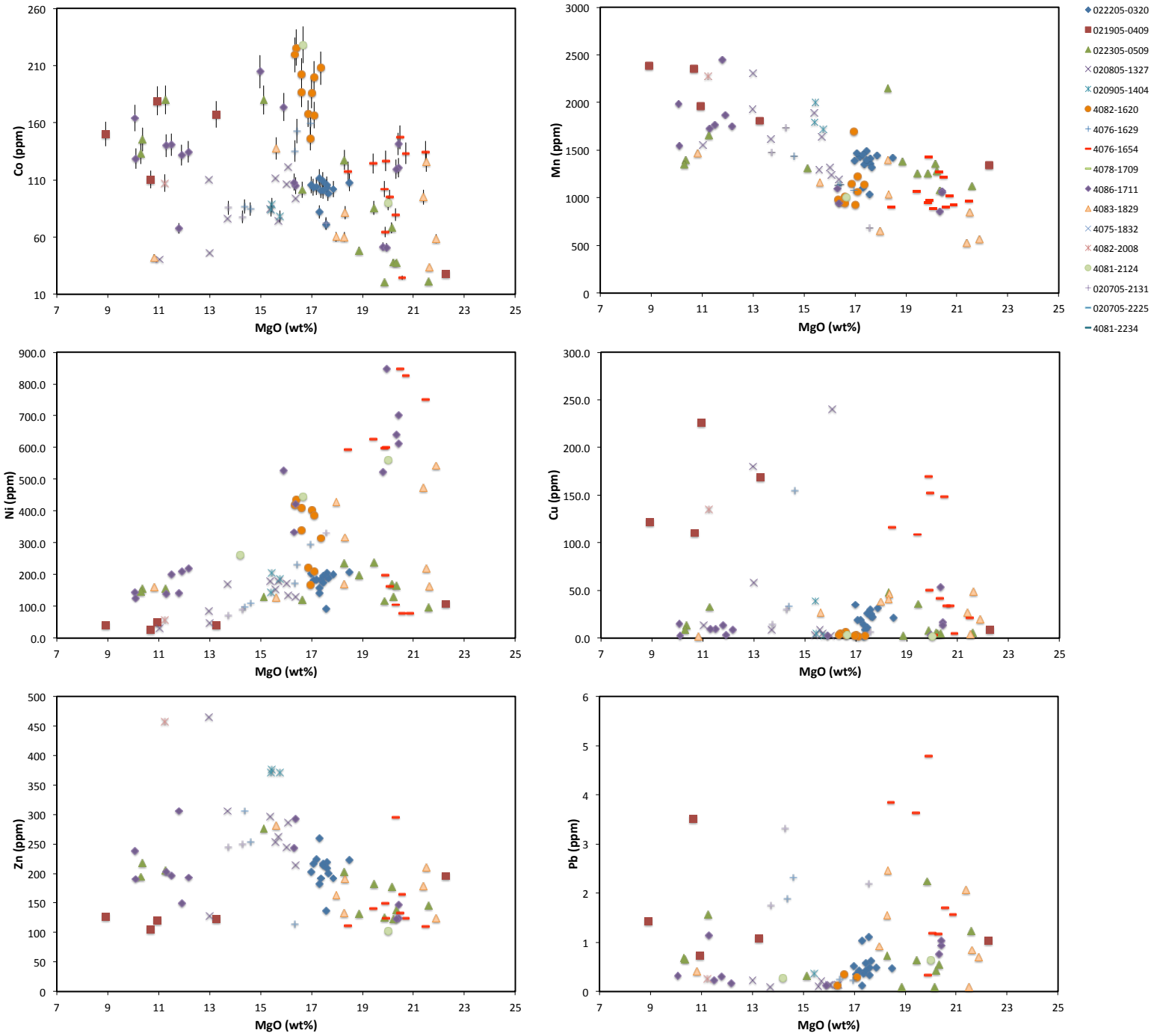

Figure 3.9: a-f) Base metal concentrations (ppm) versus MgO (wt%) for secondary chlorite and mixed-layer clays. Error bars determined by the NIST values that are closest to the base metal concentration and are the percent error associated with each metal (therefore the error bars appear smaller as concentration decreases; for details see Appendix A.2).

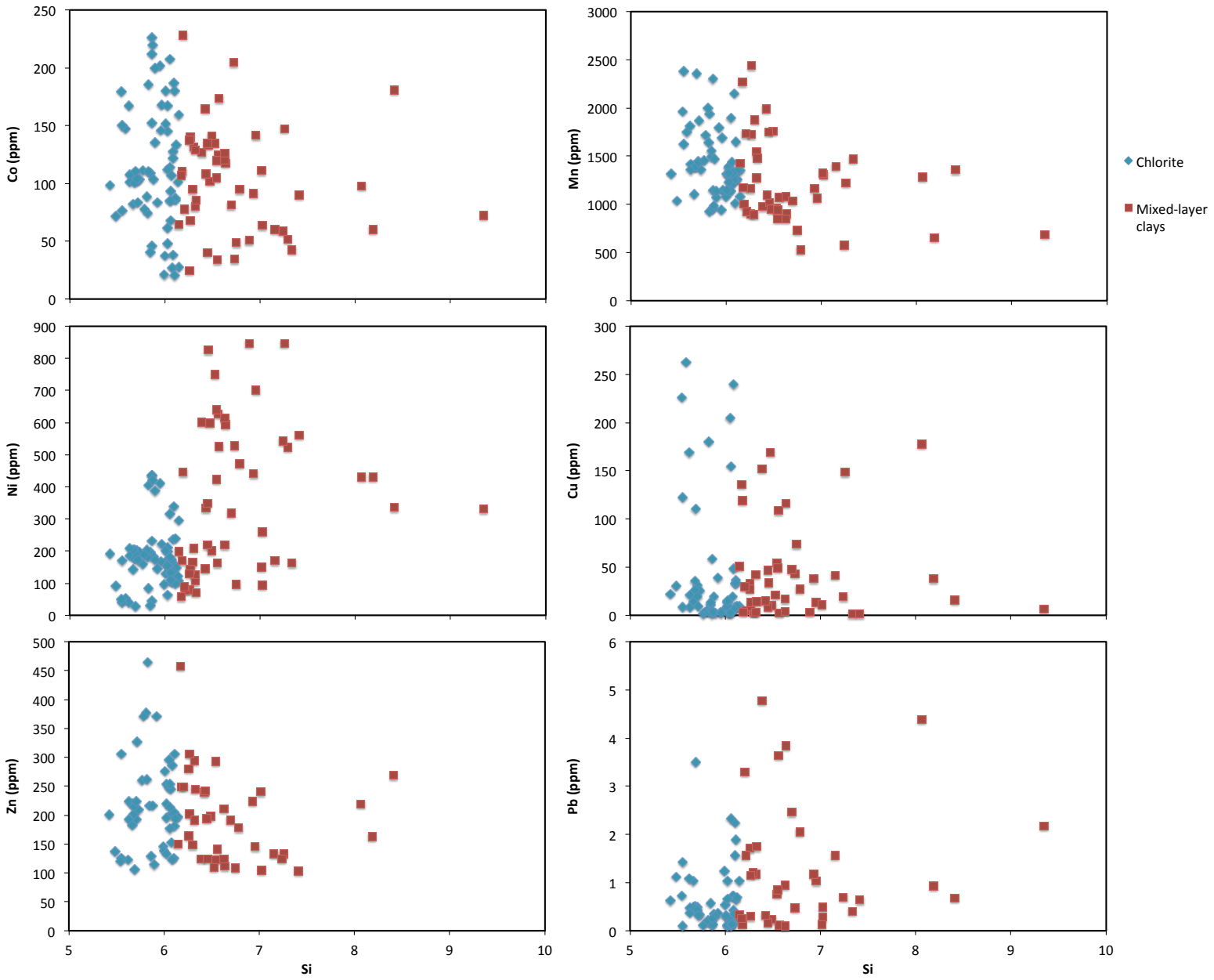

Figure 3.10: Si cation versus base metal concentrations (ppm) for chlorite and mixed-layer clays to determine the effect of temperature based on the mineralogy.

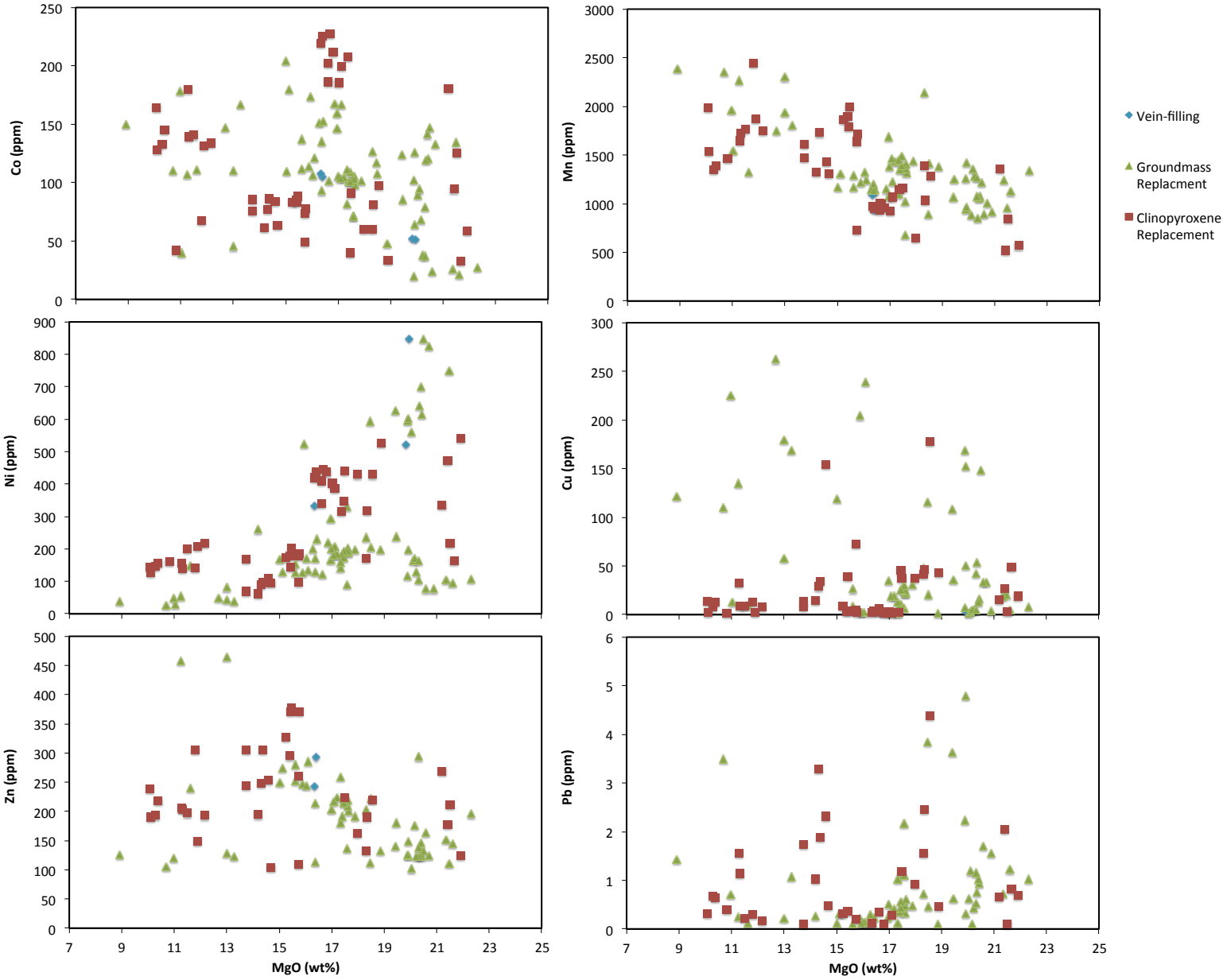

Figure 3.11: Base metal concentrations (ppm)versus MgO (wt%) in phyllosilicates that replace groundmass (green), clinopyroxene (red), or fill-in veins (blue)

Crystallographic controls on base metal partitioning are not well known for the phyllosilicates. Nickel and Mn can enter into an octahedral site (Bailey, 1988). Iron and Mg freely exchange with one another in the octahedral sites, therefore Ni and Mn have the potential to replace Fe or Mg (Bailey, 1988; Deer et al., 1992). To test this prediction, base metal concentrations were plotted against FeO and MgO. Additionally, plots against Al_2O_3 were created to see if metals could replace Al. No correlations between Co, Zn, Cu, or Pb and the major elements were observed, whereas Ni and Mn show negative correlations with FeO and MgO, respectively (Figure 3.9, 3.11, and 3.12). These trends imply that Ni replaced Fe, and Mn replaced Mg in the octahedral sites.

The trends of Ni and Mn against MgO content mimic those of clinopyroxene. In clinopyroxene Ni shows a positive relationship with respect to MgO, and Mn shows a negative relationship with respect to MgO. Absolute Mn concentrations in chlorite and mixed-layer clays are similar to those of the clinopyroxene (can be ~1.5 times higher, but normally have similar concentrations). Nickel, however, can be ~2 times higher in chlorite and almost 8 times higher in mixed-layer clays (within the same sample). These trends suggest that Ni and Mn content in chlorite and mixed-layer clays are dependent on the primary phase it replaces. For Mn, the absolute concentration is controlled by primary clinopyroxene, but for Ni there is an additional control of the absolute concentration as concentrations can be significantly higher than clinopyroxene. Previous work on Ni in phyllosilicates has shown that Ni-enriched clay minerals (garnierites) are common due to Ni entering into the octahedral site (Manceau et al., 1985). This will be discussed further later in this chapter.

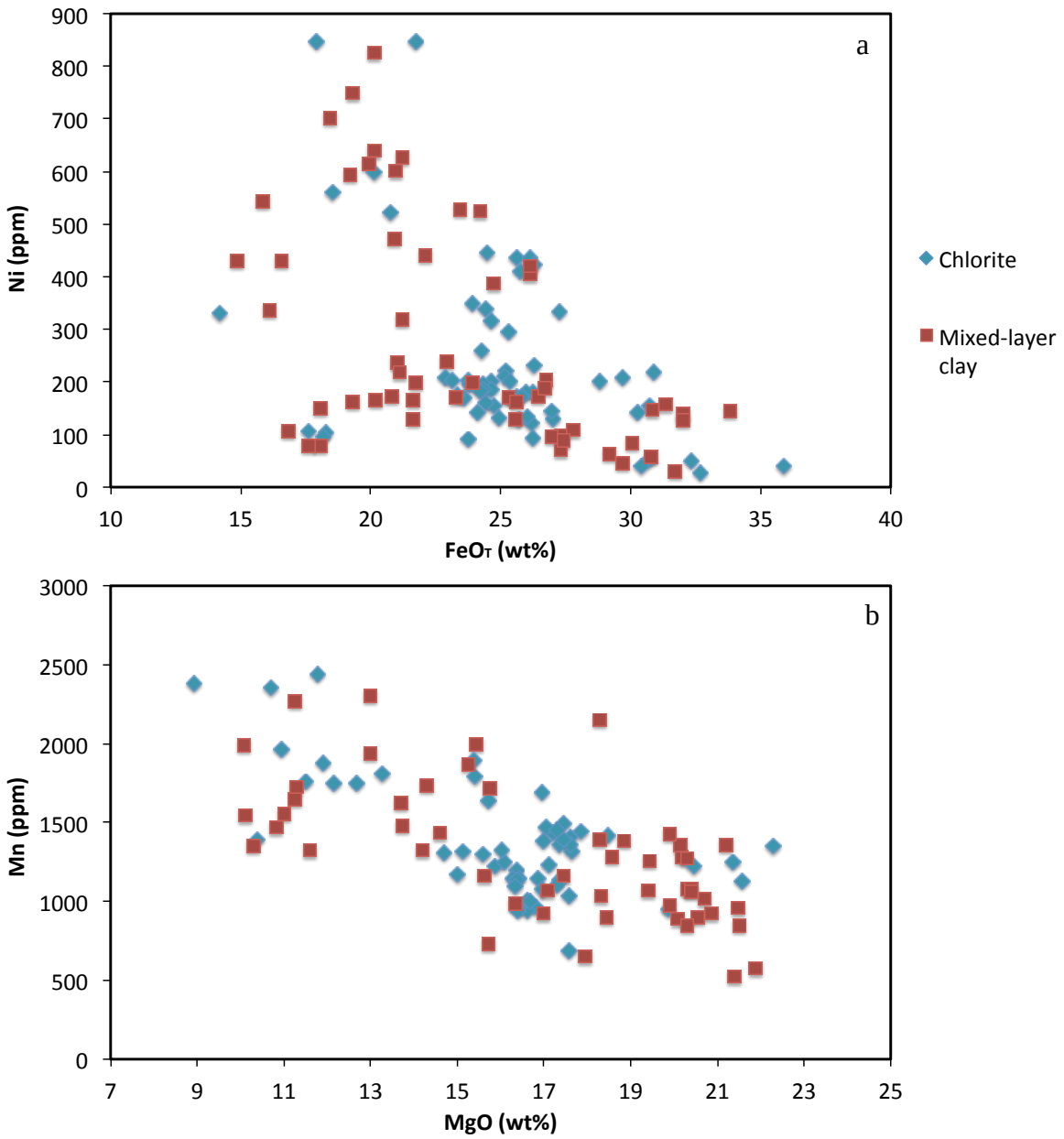

Figure 3.12: a) Ni (ppm) versus FeO (wt%) and b) Mn (ppm) versus MgO (wt%) for phyllosilicates. The negative correlation suggests these base metals are replacing Fe and Mn in the crystal structure.

There is no correlation between Co and Zn with MgO for either chlorite or mixed-layer clays. Overall, the median concentrations of each base metal are considerably higher in chlorite and mixed-layer clays relative to clinopyroxene. In chlorite and mixed-layer clays the concentration of Co is 1-2 times higher, and Zn is 2-4 times higher. Therefore the primary phase has no controlling effect on the partitioning of Co and Zn into the phyllosilicates. Copper and Pb show no trends with respect to MgO in either clinopyroxene or secondary phyllosilicates, and suggest that the primary phase is not a controlling factor.

The variety of phyllosilicates present in the sheeted dikes is indicative of temperature conditions, in addition to other environmental parameters. Base metal partitioning has been experimentally determined to be temperature sensitive, and therefore must be taken into consideration (Seewald and Seyfried, 1990). The transition from mixed-layer clays to chlorite can occur over a temperature range of 200°C up to 360°C (Schiffman and Fridleifsson, 1991; Robinson et al., 2002). Previous work on Pito Deep samples constrain mixed-layer clays to be stable between 180-210°C, and chlorite from a minimum temperature of 160-270°C up to 450°C (Robinson et al., 2002; Heft et al., 2008).

To assess if temperature affects the base metal contents in phyllosilicates, base metal concentration was plotted against Si (Figure 3.10). Silicon was used as a proxy for temperature because with increased Si, chlorite transitions to mixed-layer clay and temperature decreases. There is no correlation between the content of most base metals and Si, however Ni and Pb show overall higher concentrations with increasing Si content. Therefore, as temperature decreases Ni and Pb will partition into the mixed-layer clay

phase instead of chlorite. The other metals are not to be directly controlled by temperature with respect to metal content in secondary phyllosilicates.

In summary, the base metal content of phyllosilicates is not controlled by a single parameter. The concentration of Mn appears to be inherited by the primary phase of clinopyroxene of which the phyllosilicate is replacing. Lead does not show a strong relationship, but does have overall higher concentrations in the phyllosilicates as temperature decreases (Si content increases). Unlike the other base metals, both the primary phase and temperature affect Ni at the time of reaction. The relative concentration of Ni is inherited by clinopyroxene, however, the absolute concentration increases with decreasing temperature. Therefore if mixed-layer clays replace clinopyroxene the Ni content will be higher than chlorite. Cobalt, Zn, and Cu can all be present in the phyllosilicates, however are dominantly controlled by the crystal structure.

Table 3.4: Concentration of base metals in chlorite and mixed-layer clays.

Mineral	**Concentrations (ppm)**	**Mn**	**Co**	**Ni**	**Cu**	**Zn**	**Pb**
Chlorite	Max	2383	226	437	262	465	3.51
	Min	928	20.4	27.3	1.77	105.8	0.108
	Average	1423	114	180	41.2	217	0.662
	Median	1355	106	173	13.66	207	0.439
	Stdev	350	51.9	97.8	66.5	77.7	0.665
	n	65	67	67	58	50	52
Mixed-layer clay	Max	2443	228	847	178	458	4.79
	Min	528	24.5	56.6	1.647	103.2	0.111
	Average	1222	103	351	42.6	193	1.277
	Median	1127	105	324	26.6	191	0.893
	Stdev	431	44.7	233	49.1	74.8	1.254
	n	44	51	52	47	39	38

Limit of detection: Mn = 500 ppm, Co = 20 ppm, Ni = 15 ppm, Cu = 1.5 ppm, Zn = 100 ppm, Pb = 0.1 ppm

3.5.5 Amphibole

Actinolite and magnesiohornblende are the two dominant types of amphibole present in the sheeted dikes; unlike chlorite, the number of available samples with large enough grains for LA-ICP-MS is only 3 of the 20 samples studied (Section 3.4). Mangenese, Co, Ni, and Zn are the most abundant base metals present in amphibole, Cu has highly variable concentrations, and Pb only has measurable concentrations in 17 amphibole grains (55% of total amphibole analyzed) due to a high detection limit of 0.5 ppm (Table 3.5). A typical range of Mn, Co, Ni, Zn, Cu and Pb is between 1500-3000 ppm, 60-100 ppm, 50-150 ppm, and 40-140 ppm, 3-25 ppm, and 0.3-0.9 ppm, respectively. Outliers of high and low concentrations occur for each of the metals; the order of magnitude of these outliers is the same as the general range. In samples where amphibole replaces clinopyroxene, the base metal contents have similar ranges as previously stated (Figure 3.13). In one sample that has predominantly vein-filling amphibole, the typical range of Mn, Co, Ni, Zn, Cu, and Pb is 2000-2500 ppm, 60-80pm, 50-100 ppm, 100-150 ppm, 5-30 ppm, and 0.3-0.7 ppm, respectively (sample 021905-0409; Figure 3.13).

Experimental studies have shown that amphibole can accommodate a wide range of minor and trace elements in its crystal structure due to the multiple sites of substitution, most commonly in the M1, M2, and M3 sites. Cobalt, Mn, and Zn can replace Mg in any of these sites, and Ni may replace Fe (e.g. Adam and Green, 2006). Major element versus base metal plots help assess the possible crystallographic controls on the base metal concentrations. There is a weak negative correlation between Mn with respect to MgO, and conversely there is a positive correlation between Ni and MgO

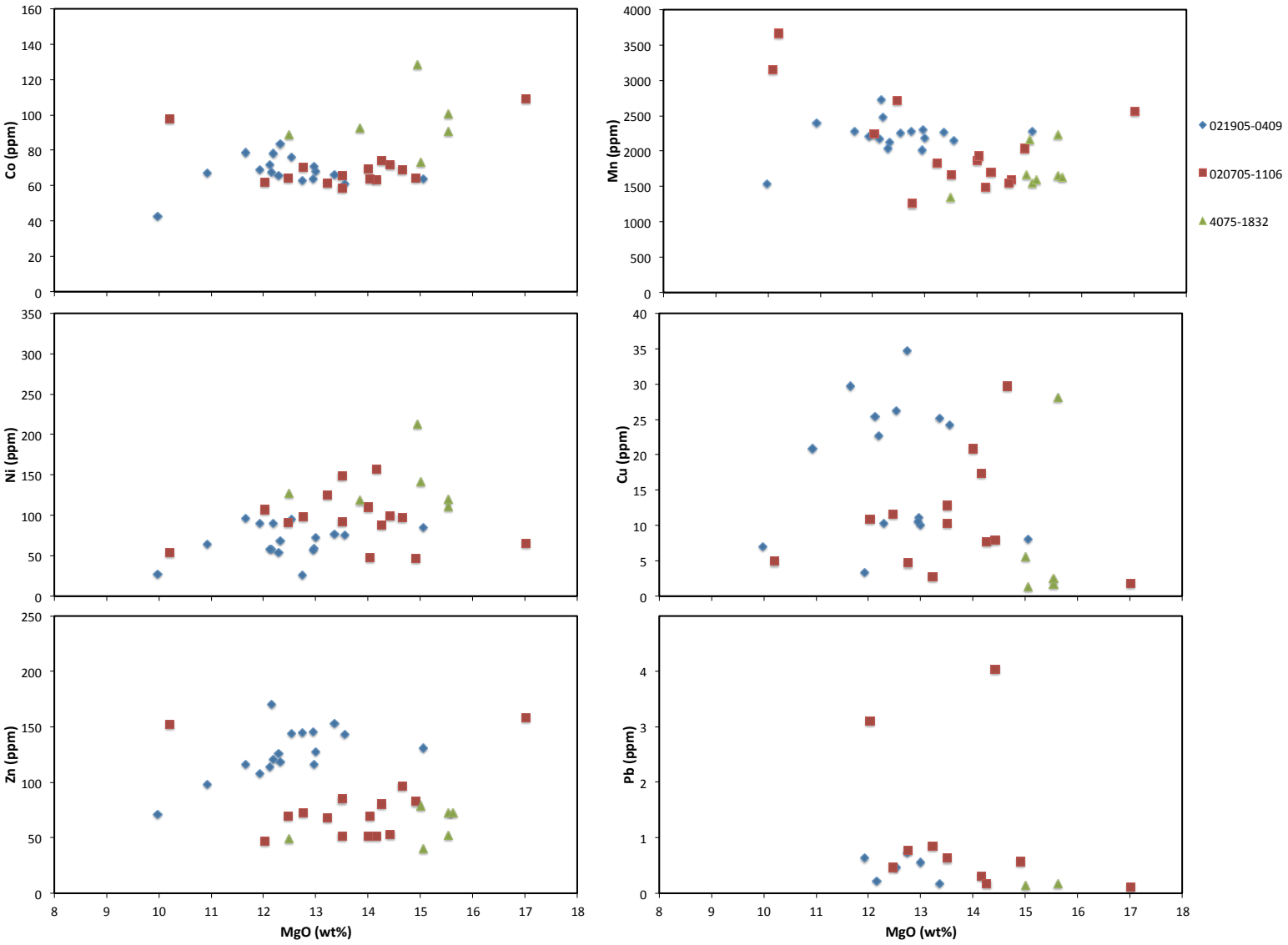

Figure 3.13: Base metal concentrations (ppm) versus MgO (wt%) in Pito Deep amphibole. Data plotted by sample number, refer to legend for specific sample number.

(Figure 3.13). In addition the absolute concentrations of Ni and Mn in the amphiboles are within the same range observed in clinopyroxene from the same sample. These relationships and similar concentrations suggest that the primary control of Ni and Mn content in amphibole is clinopyroxene.

Similar to clinopyroxene, Cu and Pb concentrations in amphiboles show no correlation with major element or other base metal contents. Amphibole dominantly replaces clinopyroxene, but some samples have amphibole in-filling veins, which are interpreted to have directly precipitated from the fluid. There is no chemical distinction between the two modes of occurrence. For Cu and Pb there does not seem to be any mineralogical factor that controls how the metals partition into amphibole.

Base metal mobility is known to be temperature sensitive (Seewald and Seyfried, 1990). Experimental studies show that Al_2O_3, TiO_2, and Na_2O contents increase with increasing temperature in amphiboles (Liou et al., 1974). Tetrahedral Al is used to qualitatively assess if temperature impacts the uptake of base metals into the amphibole (Figure 3.14; e.g., Kirchner and Gillis, 2012). Zinc and, to a lesser extent, Co and Mn show decreasing concentrations with Al^{IV} for the whole data population, suggesting less uptake of these elements with increasing temperature. In contrast, Ni, Cu, and Pb show no trends with Al^{IV}. To ascertain if there is an increase in temperature with depth, Al^{IV} plotted against depth shows that there is no systematic trend in the sheeted dikes (Figure 3.15)

In summary, some base metal contents in amphibole are impacted by the primary phase it is replacing (Ni and Mn in clinopyroxene), and others are impacted by the

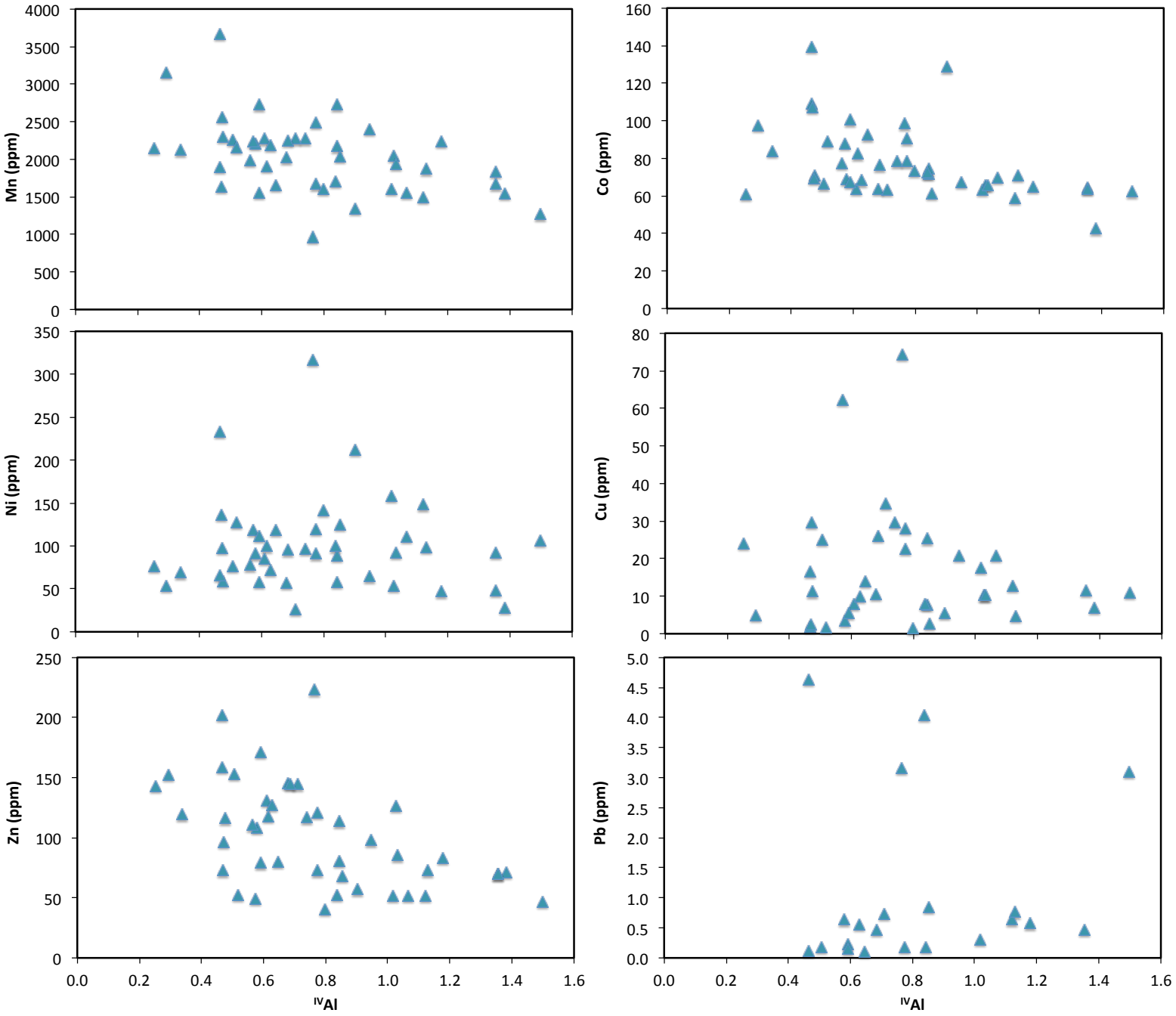

Figure 3.14: Base metal concentrations (ppm) versus tetrahedral Al in amphibole. All analyses recalculated on basis of 23 oxygens.

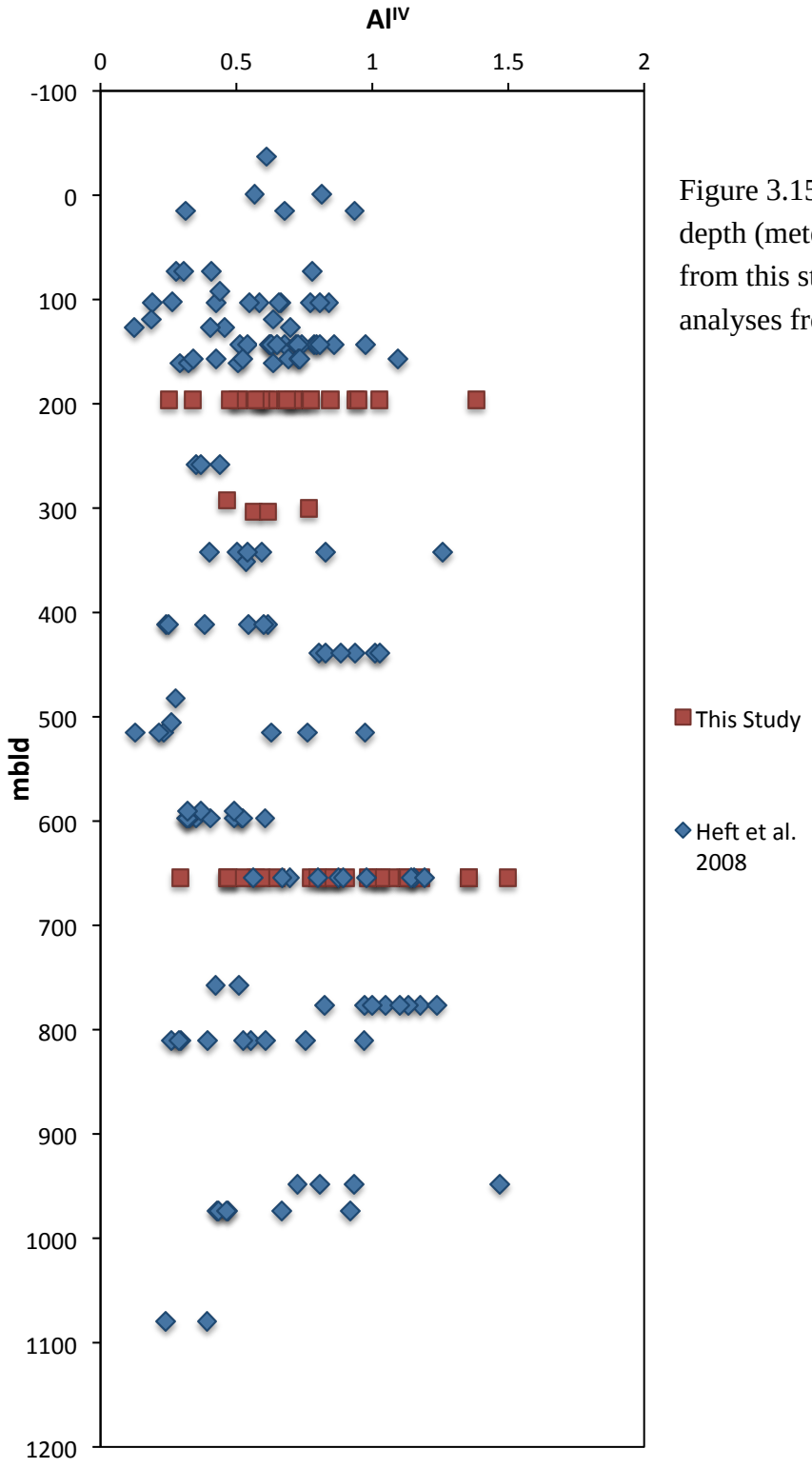

Figure 3.15: Tetrahedral Al in amphibole versus depth (meters below lava-dike transition). Analyses from this study in red, and previously published analyses from Heft et al. (2008) in blue.

temperature of fluid-rock interaction (Zn, and possibly Co, and Mn). Copper and Pb are present in trace concentrations and have no observable control.

Table 3.5: Base metal concentrations in amphibole.

Mineral	Concentrations (ppm)	Mn	Co	Ni	Cu	Zn	Pb
Actinolite	Max	3667	109	136	62.5	171	0.65
	Min	1556	60.8	53.7	1.8	49	0.5
	Average	2305	81.5	88.7	14.7	113	0.30
	Median	2222	77.3	81.2	9.1	118	0.19
	Stdev	539	16.4	26.6	16.6	38.2	0.22
	n	16	16	16	14	16	7
Magnesiohornblende	Max	2722	139	317	83.5	224	4.64
	Min	969	42.7	26.8	1.416	40.4	0.5
	Average	1886	74.6	106.8	20.2	96.1	1.45
	Median	1905	70.3	96.3	12.9	81.7	0.693
	Stdev	396	19.8	63.4	19.9	45.7	1.56
	n	28	28	28	25	28	14

Detection limits: Mn = 400 ppm, Co = 20 ppm, Ni = 25 ppm, Cu = 1 ppm, Zn = 40 ppm, Pb = 0.5 ppm

3.5.6 Fe-Cu Sulphides

Pyrite and chalcopyrite are the dominant Fe-Cu sulphides present in the sheeted dikes, with trace pyrrhotite. Due to the fine grain size and trace amounts, pyrrhotite is interpreted to be a primary phase in these samples. No general compositional trends for pyrrhotite can be assessed due to the limited data (Table 3. 6); however, negative correlations between Co, Ni, and Cu versus Fe suggest these metals replace Fe in the crystal structure.

Pyrite occurs as a primary and secondary phase in the groundmass, or as a void-filling phase in the studied samples. It is difficult to differentiate primary from secondary pyrite, however pyrite surrounded by a rim of secondary silicate minerals such as chlorite or amphibole is interpreted to be secondary. This is because the pyrite has no blocky habit and appears to be replacing an area of groundmass, along with the chlorite or amphibole. A typical range of Fe and S in the pyrite is 46-47 wt%, and 53-54 wt%, respectively, but Fe can be as low as 40 wt%, and S can reach 51.5 wt% (Fig. 3.6). Base metal concentrations are variable, though the typical range of Mn, Co, Zn, Ni, Cu, and Pb is: 50-150 ppm, 300-500 ppm, 50-500 ppm, 10-100 ppm, and100-500 ppm, respectively (Table 3.6). Lead is below the limit of detection in all samples (detection limit is 0.1 wt%). The compositional variability of each base metal within a sample is approximately ± 25-30%.

Variation in the Fe concentration in pyrite is caused by the introduction of a different element, in this case Ni or Co, into the crystal structure (Figure 3.16). Nickel and Co reach concentrations up to ~4 wt% (7 wt% at the maximum). Zinc and Cu are also observed in trace amounts in pyrite, however their concentrations are less than Ni

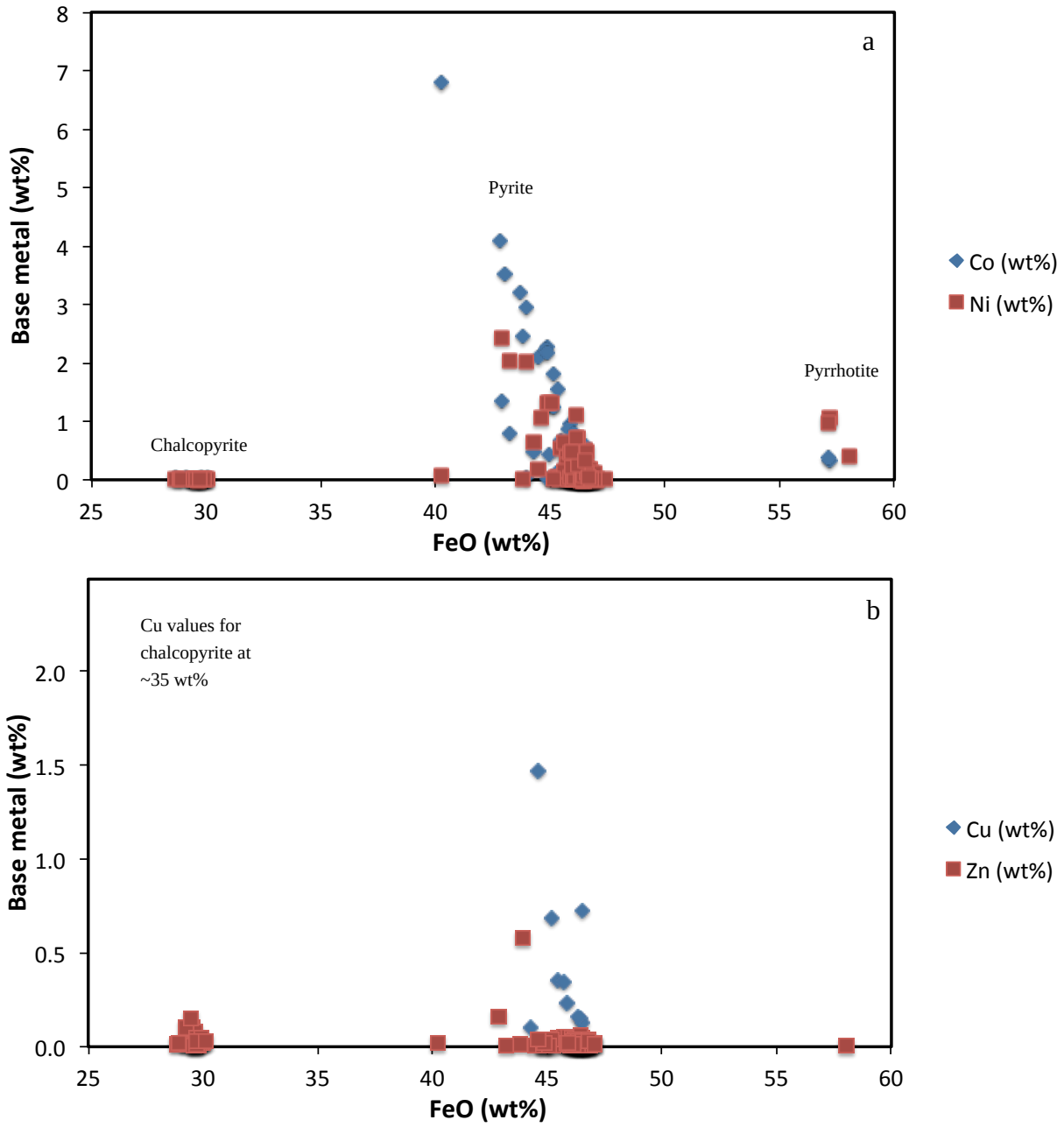

Figure 3.16: a) Ni and Co (wt%) versus Fe (wt%) in Fe-Cu sulphides. b) Cu and Zn (wt%) versus Fe (wt%) in Fe-Cu sulphides. Decreases in Fe concentrations in pyrite, pyrrhotite, and chalcopyrite (onlyZn) relate to the introduction of a new base metal in the crystal structure.

and Co. Nickel, Co, Zn, an Cu have been previously observed in small amounts in solid solution pyrite, all of which can substitute for Fe (Craig and Scott, 1974). Most pyrite minerals with high Ni or Co contents are not associated with a rim of secondary minerals, suggesting they may be magmatic. Copper and Zn are also observed at elevated concentrations at maximum 1.5 wt% (14800 ppm) and 0.5 wt% (5870 ppm), respectively. Nonetheless, previous work has suggested that increased concentrations of Zn and Cu may be more likely due to inclusions of sphalerite or chalcopyrite within the pyrite grain instead of a substitution into the crystal structure (Craig and Scott, 1974).

Chalcopyrite is present only as a secondary or void filling phase. All secondary chalcopyrite is surrounded by a secondary phase (chlorite or amphibole), showing that chalcopyrite has replaced some groundmass. Copper is the major base metal present in chalcopyrite, ranging from 32.8-34.9 wt%, and is the most important sink of Cu in the sheeted dikes. The typical range of Mn, Ni, Zn, and Co is 50-200 ppm, 0-150 ppm, 0-400 ppm, and 50-150 ppm, respectively. All Pb is present below the limit of detection (0.1 wt%). The typical range in base metal content within a sample is ± 25%. Unlike pyrite, Ni, Co, and Zn do not show substantial increases in concentration, however Zn reaches a maximum concentration of 1600 ppm. A possible explanation for the higher Zn contents is the similarity of the structure of sphalerite and chalcopyrite. It has been suggested that a solid solution of ZnS in $CuFeS_2$ could occur, which may explain the variation of Zn seen in the chalcopyrite (Craig and Scott, 1974).

In summary, the base metals Ni, Co, Mn, and Zn can all be present in Fe-Cu sulphides. Ni and Co and, to a lesser extent Zn and Cu, can easily substitute for Fe in pyrite. Zinc and Cu may be present in pyrite as inclusions of sphalerite and chalcopyrite,

respectively, however due to the limited grains with Zn and Cu enrichment and the minor concentrations (<2 wt%) this is difficult to confirm. Manganese can be present in trace amounts, however Fe-Cu sulphides are not a significant host of Mn. Due to the lack of Pb data, it can not be determined what the absolute concentration of Pb is or where the Pb resides within the crystal structure.

Table 3.6: Base metal concentration in Fe-Cu sulphides.

Mineral	Concentrations (ppm)	Mn	Co	Ni	Cu	Zn	Pb
Pyrrhotite	Max	107	3780	10700	-	138	bdl
	Min	107	3267	4076	-	138	bdl
	Average	107	3523	8173	-	138	bdl
	Median	107	3523	9743	-	138	bdl
	Stdev	107	363	3580	-	138	bdl
	n	1	2	3	0	1	3
Pyrite	Max	403	68162	24500	14791	5896	bdl
	Min	55.2	65.1	96.2	1151	13.4	bdl
	Average	147	3726	1835	4444	262	bdl
	Median	134	540	448	2981	171	bdl
	Stdev	80.9	8867	3763	4256	533	bdl
	n	91	148	154	10	131	247
Chalcopyrite	Max	264	625	353	34.9	1608	bdl
	Min	56.2	69.7	107	32.9	13.4	bdl
	Average	132	299	218	34.2	343	bdl
	Median	123	291	211	34.3	254	bdl
	Stdev	52.7	137	82.4	0.372	367	bdl
	n	31	14	22	54	32	54

Detection limits: Mn = 0.006 wt%, Co = 0.1 wt%, Ni = 0.01 wt%, Cu = 0.1 wt% (for chalcopyrite Cu = 0.3 wt%), Zn = 0.01 wt%, Pb = 0.001 wt%

3.6 Metal content of secondary phases hosted in Hydrothermal Breccias

Hydrothermal breccias were analyzed to examine if base metal concentrations vary in secondary minerals found in the groundmass of sheeted dikes versus minerals that were considered a direct precipitate from the fluid (focusing on chlorite, epidote, and Fe-Cu sulphides). The sample breccias were collected from faults at Pito Deep and were selected based on the presence of minerals that are confidently direct precipitates. Due to the limited samples available for Pito Deep, samples from Hess Deep were incorporated to enhance the database. Six breccias were analyzed using LA-ICP-MS, and two samples were analyzed with EMP (due to time constraints).

The benefit of examining hydrothermal breccias is that chlorite, epidote, and sulphides are direct precipitates from a hydrothermal fluid and can be texturally identified in the breccia matrix. By comparing the base metal content of chlorite and sulphides from the altered sheeted dikes to a direct precipitate, it is possible to gain a better understanding of how the fluids affect the concentration of base metals in these minerals. Furthermore, the benefit of epidote is that in some samples it is a co-precipitate with chlorite, and therefore a comparison of base metals in each mineral can help us understand if certain metals prefer one mineral to the other.

Chlorite that precipitates directly from a fluid forms a distinctive “wormy” texture, and has the typical vibrant green characteristic of chlorite (photomicrograph of texture found in Appendix B.2). Chlorite major element concentrations in the breccias fall within the range observed in the groundmass of the sheeted dikes. Typical ranges of Mn, Co, Zn, Ni, Cu, and Pb concentrations are: 2000-3200 ppm, 100-200 ppm, 200-300 ppm, 50-150 ppm, 10-110 ppm, and 0.2-0.9 ppm, respectively (Table 3.7). The variability

within an individual sample is ±20-30%, such that a sample has consistently low or high concentrations. Base metal concentrations show the same general trends observed in groundmass chlorite, however the Mn and, to a lesser extent, Co concentrations in the breccia extend to higher values than those of the groundmass chlorite. Nickel, Co, Pb, and Cu contents fall within the range of values seen in the groundmass chlorites (Figure 3.17). Chlorite in hydrothermal breccias is a direct precipitate and consequently does not inherit primary phase trends, but simply records the hydrothermal fluid chemistry at the time of precipitation. In summary, chlorite in the breccias is compositionally the same as the groundmass chlorite. This suggests that a dominant control of base metal content in chlorite (in both the breccias and dikes) is the hydrothermal fluid composition, however it is not the only control for Ni and Mn. Although most breccia chlorite values lie within the same range as the groundmass chlorite, the trends observed (decreasing Mn and increasing Ni) with increasing MgO suggests that relative concentration of Ni and Mn is regulated by the primary clinopyroxene

In the breccias, epidote forms euhedral large grains (0.5-1mm) commonly surrounded by quartz and associated coeval chlorite. Typical ranges of Mn, Co, Zn, Ni, Cu, and Pb in epidote are: 600-1200 ppm, 0.2-0.5 ppm, 2-5 ppm, 5-12 ppm, 0.15-0.5 ppm, and 0.3-2 ppm, respectively (Table 3.7). The variability within a sample can be ±80-100%, however with such small concentrations the large variability is only a maximum of 10 ppm. Epidote is also found in the sheeted dike complex, however it is very fine grained and often constrained to a vein, as a result no data was collected. Epidote is not a significant sink of metals in any sample.

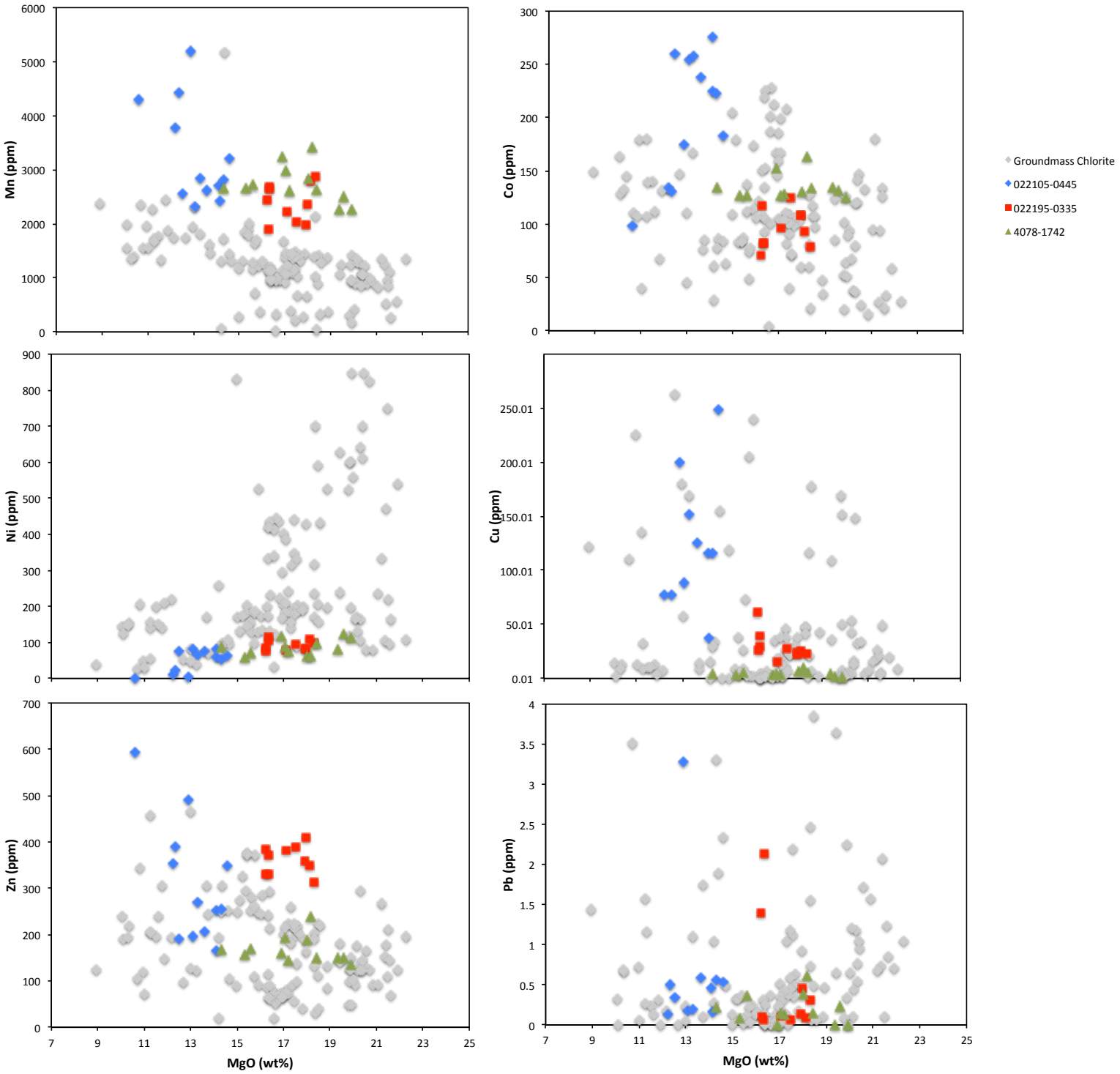

Figure 3.17: Base metal concentrations (ppm) versus MgO (wt%) in chlorites formed by direct precipitation in hydrothermal breccia samples versus groundmass chlorite (grey) from the sheeted dike complex.

Pyrite and chalcopyrite occur in the matrix of the breccias and are interpreted as direct precipitates from the fluid. Pyrite major element compositions overlap those that occur in the groundmass; with S from 52-53wt% and Fe 46-47wt%. Pyrite base metal concentrations also fall within the range observed for groundmass pyrite. Manganese, Ni, Co, Zn, and Cu are all <1 ppm (Pb is not detected in the sulphides), however enrichments do occur and can reach maximum concentrations of 8450 ppm, 450 ppm, 1450 ppm, 100-220 ppm, and 1520 ppm, respectively. Similar to groundmass pyrite Fe decreases with increasing concentration of any or all of the base metals (e.g. Ni and Co)

Chalcopyrite major element compositions in the hydrothermal breccias are similar to those in the groundmass of the sheeted dikes; Cu is 34wt% (±0.6wt%), and S is 34wt% (±0.6wt%). Manganese, Co, Zn, and Ni concentrations are on commonly negligible, and Pb is below detection limits (Table 3.7). The consistent enrichment of Zn may be a result of solid solution of ZnS with $CuFeS_2$, or the substitution of Zn into the crystal structure. Due to the minor concentration, the latter may be more likely.

Table 3.7: Base metal concentration in silicate and sulphide minerals found in the hydrothermal breccias.

Mineral	Concentrations (ppm)	Mn	Co	Ni	Cu	Zn	Pb
Chlorite	Max	5203	275.9	124.2	1369	593	11.8
	Min	1910	71.6	3.35	1.45	135	0.059
	Average	2824	148.2	78.0	101	275	0.840
	Median	2655	130.9	81.5	25.8	253	0.238
	Stdev	703	57.7	28.2	244	115	2.15
	n	34	34	33	34	34	31
Epidote	Max	3322	1.27	19.0	1.15	7.27	9.35
	Min	452	0.138	1.15	0.217	0.210	0.017
	Average	1125	0.466	9.65	0.55	3.45	1.47
	Median	690	0.233	11.6	0.288	3.53	0.444
	Stdev	936	0.383	7.13	0.52	2.33	2.98
	n	10	9	6	3	10	9
Pyrite	Max	8420	1450	425	1520	219	bdl
	Min	44.3	26.1	1.5	8.21	22.4	bdl
	Average	419	350	94.8	132	38.9	bdl
	Median	37	253	47	226	40	bdl
	Stdev	1620	386	120	301	67.6	bdl
	n	27	27	27	27	27	27
Chalco-pyrite	Max	198	288	639	353000	275	bdl
	Min	44.3	26.4	37.8	33800	4.7	bdl
	Average	121	146	268	347000	67.5	bdl
	Median	122	153	275	348000	51	bdl
	Stdev	66.2	97.7	192	3810	80.6	bdl
	n	16	16	16	16	16	16

3.7 Modal Abundance and Mass Balance

To ensure that all metal-bearing minerals have been accounted for, a mass balance for each of the base metals was calculated using the modal abundance of the key mineral phases and their compositions. The following section describes procedures and results for modal abundances and mass balance calculation.

3.7.1 Modal Abundance

Two approaches were used to determine the modal abundance of the primary and secondary minerals in the sheeted dikes. First, a least-squares calculation was used to calculate the percentage of each mineral depending on its compositions. The second approach was point counting a subset of samples used for the least-squares calculation to confirm the validity of this approach.

The least-squares matrix calculation (Draper and Green, 1997) was used to calculate the modal abundance of the primary and secondary minerals. The first input parameter for the calculation is the average major element compositions (SiO_2, TiO_2, Al_2O_3, FeO, MnO, MgO, CaO, Na_2O) of the four dominant phases for each sample. Only four phases were used as this gave the best sum of the modes (closest to 100%); if more than four phases were considered the least-squares calculation was no longer useful as the total modes were significantly over or under 100% (±50%). The four phases included in the calculation are clinopyroxene, plagioclase, a dominant secondary phase (chlorite or amphibole), and Fe-Ti oxides (Table 3.9). This limits the secondary phases present in the rock to just one, which is often not the case. However, due to the small modal abundance of a second secondary phase, and the similarities observed in the secondary silicate base metal content, ignoring a possible fifth phase will not effect the mass balance

calculations. The second input parameter is the bulk rock compositions for each sample. It's important to note the bulk rock compositional data were collected for a powder prepared from a rock chip cut adjacent to the thin section billet, and that the volume of this rock chip was larger than the thin section billet. Thus, the bulk rock will not represent the thin section with 100% accuracy. This is particularly important for calculating the modes of the sulphide (see below). To test the calculated modal abundances, 25% of the samples were point counted and compared with calculated values. The two methods provide mineral modes within 5-15% of each other (Table 3.9), therefore the matrix calculation was deemed appropriate. The results of the least-squares calculation are reported in Table 3.9.

To calculate the sulphide modal abundance, Cu and S bulk rock data were used (since chalcopyrite and pyrite make up the dominant sulphide phases). The sum of Cu concentrations in the four phases used in the least squares calculation is subtracted from the bulk rock Cu concentration, giving the concentration of the remaining Cu in the system. The remaining Cu is assumed to be hosted in chalcopyrite, allowing for the calculation of the modal abundance of chalcopyrite. Equation 6 shows the calculation used, where % Chalco, %Plag, %Cpx, %Sec, and %Ox are the modal abundance of chalcopyrite, plagioclase, clinopyroxene, dominant secondary phase, and Fe-Ti Oxides, respectively, and [Cu]plag, [Cu]cpx, [Cu]sec, [Cu]ox, and [Cu]chalco are the median Cu concentrations found in plagioclase, clinopyroxene, the dominant secondary phase, Fe-Ti oxides, and chalcopyrite, respectively:

$$\%Chalco = 100* \frac{([Cu]_{BR} - (\%Plag*[Cu]_{plag} + \%Cpx*[Cu]_{cpx} + \%Sec*[Cu]_{sec} + \%Ox*[Cu]_{ox}))}{[Cu]_{chalco}} \quad (6)$$

Assuming that all S resides in the sulphide phases, the S associated with chalcopyrite was subtracted from the bulk rock sulphur, and any remaining S was assigned to pyrite. Pyrrhotite was not considered because of its very low modal abundance.

Table 3.9: Modal abundance of primary and secondary minerals.

Sample ID	Method*	CPX (%)	PLAG (%)	CHL (%)	AMPH (%)	Fe-Ti OXIDE (%)	PYR (%)	CHALCO (%)	Total** (%)
020705-1106	Calc	-	39	-	60	0.02	0.14	0.02	100
020705-1423	Calc	42	45	8	-	7	0.03	0.03	100
	PC	44.3	41	8.8	-	5.1	0.13	0.53	100
020705-2131	Calc	45	44	5	-	8	0.08	-	100
020705-2225	Calc	47	29	19	-	5	0.02	0.08	100
020805-1327	Calc	47	38	12	-	4	0.09	-	100
020905-1404	Calc	42	47	6	-	8	0.08	0.01	100
021905-0409	Calc	-	36	6	54	4	0.14	0.02	100
022205-0320	Calc	48	45	5	-	5	0.16	0.01	100
022305-0509-b	Calc	43	47	10	-	3	0.09	-	100
4075-1832	Calc	5	47	-	43	4	0.10	-	100
4076-1629	Calc	40	45	15	-	2	0.09	-	100
4076-1654	Calc	37	43	19	-	2	0.29	0.02	100
	PC	32	45	13.5	7	2.5	-	-	100
4076-1725	Calc	43	46	7	-	6	0.08	0.01	100
4078-1709	Calc	44	45	6	-	5	0.08	0.01	100
4081-2124	Calc	45	45	6	-	7	0.08	-	100
	PC	43.7	40.3	7.9	1.9	5.6	-	0.6	100
4081-2234	Calc	49	42	2	-	10	0.18	0.01	100
	PC	42.9	41.6	10.3	-	4.8	0.4	-	100
4082-1620	Calc	49	45	5	-	5	0.09	0.01	100
	PC	36.9	42.3	15	-	4.8	1	-	100
4082-2008	Calc	38	37	23	-	4	0.09	-	100
4083-1829	Calc	46	44	7	-	3	0.09	-	100
4086-1711	Calc	45	47	3	-	7	0.09	0.01	100

*Calc=calculated using least-squares matrix, PC= point counted.
**Totals have been normalized to sum to 100%, before normalization totals ranged from 98% to 103%

3.7.2 Mass Balance Calculation

The metal content of all samples was calculated by mass balance and compared to the measured whole rock composition to ensure that all the key sources and sinks of base metals have been accounted for. Calculated bulk base metal content was determined using median metal concentrations for each mineral and the calculated modal abundances. Table 3.10 a, b, c, and d show the results of the mass balance calculation for Zn, Co, Mn, and Ni. Lead was not calculated due to the poor quality of data collected, and Cu is not included as it was used to calculate the modal abundance of sulphides and subsequently it was already determined that all sources and sinks of Cu have been accounted for. The calculated whole rock concentrations are considered representative if they fall within 15-20% of the measured bulk rock concentrations. A mass balance of Pb was not conducted as the poor quality of the data would not produce an accurate mass balance and subsequently would not represent the distribution of the Pb between the minerals.

The calculated total metal concentration of each base metal in each sample was often very close to the measured bulk rock values. However, in some samples the calculated and measured values are significantly different from one another (±25%; Table 3.10). Total calculated whole rock metal concentrations differ from the measured values because of the large range of base metal concentrations within individual minerals from a single sample. For instance, if one or two grains of chlorite are enriched in Cu there will be an effect on the average base metal concentration; this was avoided by using the median value. In addition, the heterogeneity of the sample will affect the calculated versus measured bulk rock values (e.g. the distribution of Fe-Cu sulphides). Enrichment

or depletion variability of a base metal within an individual sample cannot be avoided, as the measured bulk rock was a destructive method. To substantiate the heterogeneity of samples, 4083-1829 and 4078-1709 are two samples that have observed patchiness of alteration; therefore uneven distribution of base metal content is likely.

Calculated total metal concentrations for Zn, Co, Mn, and Ni have been reported in this thesis (Table 3.10 a, b, c, and d respectively). Observed variations between the calculated metal content and measured bulk rock metal content are due to the high variability in the metal concentration from grain to grain for one mineral. The applicable calculation and the median base metal concentrations used can be found in Appendix D.4.

The mass balance calculations indicate the dominant hosts of each base metal within the sheeted dikes. Igneous clinopyroxene and Fe-Ti oxides are the primary sources for Mn and Zn. When alteration occurs, Mn is taken up in secondary amphibole and chlorite. When amphibole is the dominant alteration phase, and when amphibole and chlorite are co-existing, Mn will preferentially enter into amphibole. This is not the case for Zn. When alteration occurs minor amounts of Zn enters into the secondary phases, but the majority of Zn leaves the system, consistent with the bulk rock ΔZn values. Clinopyroxene is the dominant source for Co, but as alteration occurs it becomes equally redistributed into secondary chlorite and amphibole. Clinopyroxene is also the dominant source of Ni, however as alteration occurs it will preferentially enter into a phyllosilictae phase over amphibole.

In summary, all of the sources and sinks of base metals within the sheeted dikes have been accounted for in this study.

Table 3.10a: Comparison of calculated bulk rock and measured bulk rock Zn values. Data provided is the total amount of Zn from each mineral phase and sums to the bulk rock Zn concentration.

Zn concentration (ppm)	Cpx*	Plag*	Chl*	Amph*	Fe-Ti Oxides	Pyrite	Chalco *	Total Calculated Zn	Measured BR Zn*	% Difference
020705-1106	-	2.4	-	49.9	-	0.191	0.034	52.6	65	18.6%
020705-1423	42.9	2.4	4.9	-	21.1	0.049	0.066	71.4	65	-9.4%
020705-2131	15.8	3.3	4.3	-	23.6	0.048	0.010	47.0	54	13.5%
020705-2225	17.0	2.4	31.6	-	6.1	0.112	0.044	57.2	72	20.7%
020805-1327	15.2	2.0	19.1	-	0.8	0.093	0.023	37.3	41	7.9%
020905-1404	12.8	6.3	17.2	-	7.6	0.224	0.084	44.2	47	6.4%
021905-0409	-	5.8	-	66.8	1.6	0.190	0.040	74.5	84	11.1%
022205-0320	37.7	2.4	10.9	-	13.9	0.222	0.034	65.2	70	6.4%
022305-0509	28.5	2.5	15.6	-	3.9	0.196	0.030	50.7	66	23.5%
4075-1832	3.3	2.5	-	23.1	-	0.254	0.001	29.2	39	25.6%
4076-1629	20.8	3.0	48.2	-	-	0.359	0.043	72.3	62	-16.4%
4076-1654	16.2	2.3	32.8	-	4.6	0.404	0.042	56.2	64	12.2%
4076-1725	12.2	3.3	5.2	-	1.8	0.054	0.002	22.5	27	17.4%
4078-1709	19.4	2.4	10.7	-	35.0	0.121	0.025	67.7	83	18.0%
4081-2124	25.2	2.0	4.1	-	43.7	0.037	0.005	74.9	72	-3.8%
4081-2234	33.5	2.5	4.9	-	27.3	0.252	0.027	68.6	98	29.8%
4082-1620	30.5	2.3	7.1	-	78.7	0.347	0.042	119.1	116	-2.6%
4082-2008	21.9	3.0	60.7	-	-	0.141	0.032	86.3		
4083-1829	42.0	2.4	19.9	-	118.1	4.796	0.022	187.1	224	16.6%
4086-1711	31.4	2.2	6.6	-	74.4	0.255	0.016	114.8	93	-22.9%

*Abbreviations: Cpx=clinopyroxene, Plag=plagioclase; Chl=chlorite; Amph= amphibole; Chalco=chalcopyrite;
BR Zn is the measured bulk rock concentrations from previous work.
Sample 4082-2008 does not have measured bulk rock Zn concentrations.
Values calculated by multiplying the median Zn concentration by the modal abundance of each specific mineral.

Table 3.10b: Comparison of calculated bulk rock and measured bulk rock Co values. Data provided is the total amount of Co from each mineral phase and sums to the bulk rock Co concentration.

Co concentration (ppm)	Cpx*	Plag*	Chl*	Amph*	Fe-Ti Oxides	Pyrite	Chalco*	Total Calculated Co	Measured BR Co*	% Difference
020705-1106	-	0.0	-	43.6	-	0.99	-	44.7	42	-6.4%
020705-1423	26.5	1.2	3.2	-	0.74	1.31	0.034	33.5	39	15.0%
020705-2131	21.6	0.8	7.9	-	1.35	0.85	0.012	36.4	39	6.1%
020705-2225	12.8	1.2	29.9	-	0.34	0.28	0.024	44.6	36	-24.9%
020805-1327	18.5	1.0	20.0	-	0.72	0.97	-	40.8	39	-5.6%
020905-1404	19.6	2.0	7.7	-	2.45	5.27	0.043	36.5	43.4	16.0%
021905-0409	-	1.5	-	36.0	1.69	7.33	0.014	46.3	45.5	-1.8%
022205-0320	21.2	1.2	5.5	-	0.92	8.58	0.002	38.4	45	14.4%
022305-0509	20.9	1.3	4.7	-	0.16	2.08	0.005	29.0	38	24.6%
4075-1832	5.7	1.3	-	34.7	-	0.35	0.001	42.1	35	-19.7%
4076-1629	19.3	1.7	10.2	-	-	0.35	0.015	31.5	35	10.5%
4076-1654	15.4	1.1	16.0	-	0.30	0.38	0.023	33.0	39	15.2%
4076-1725	16.9	1.1	10.6	-	1.11	0.25	0.001	29.7	35	14.9%
4078-1709	21.7	1.2	4.0	-	0.95	4.65	0.020	33.9	44.8	24.4%
4081-2124	25.9	0.5	11.8	-	12.54	2.06	0.003	42.7	42	-2.8%
4081-2234	23.4	1.3	1.6	-	1.80	7.92	0.015	38.1	46	18.1%
4082-1620	30.7	2.1	4.6	-	0.86	0.88	0.031	39.6	41	2.8%
4082-2008	25.6	1.7	15.0	-	-	2.09	0.018	44.5		
4083-1829	28.9	1.2	5.2	-	1.35	0.88	0.012	37.8	45	15.3%
4086-1711	24.2	0.5	11.2	-	2.41	9.83	0.032	47.4	43	-9.8%

*Abbreviations: Cpx=clinopyroxene, Plag=plagioclase; Chl=chlorite; Amph= amphibole; Chalco=chalcopyrite;
BR Co is the measured bulk rock concentrations from previous work.
Sample 4082-2008 does not have measured bulk rock Co concentrations.
Values calculated by multiplying the median Co concentration by the modal abundance of each specific mineral.

Table 3.10c: Comparison of calculated bulk rock and measured bulk rock Mn values. Data provided is the total amount of Mn from each mineral phase and sums to the bulk rock Mn concentration.

Mn concentration (ppm)	Cpx*	Plag*	Chl*	Amph*	Fe-Ti Oxides	Pyrite	Chalco *	Total Calculated Mn	Measured BR Mn*	% Difference
020705-1106	-	10.8	-	1322	88.0	0.082	0.013	1420.5	1217	-16.7%
020705-1423	978	23.3	51.6	-	151.8	0.021	0.026	1205.1	1056	-14.1%
020705-2131	739	13.2	61.6	-	287.4	0.020	0.004	1101.5	1168	5.7%
020705-2225	527	23.2	142	-	165.7	0.048	0.017	859.2	1034	16.9%
020805-1327	633	19.8	163	-	69.4	0.040	0.009	886.2	862	-2.8%
020905-1404	692	48.1	51.8	-	267.8	0.096	0.033	1060.3	1290	17.8%
021905-0409	-	57.4	-	1171	341.7	0.081	0.016	1570.6	1238	-26.9%
022205-0320	930	22.8	72.2	-	253.7	0.095	0.013	1279.2	1332	3.9%
022305-0509	737	23.9	123	-	146.9	0.084	0.012	1031.3	1352	23.7%
4075-1832	131	24.5	-	627.0	-	0.090	0.001	782.6	1063	26.4%
4076-1629	674	24.3	183	-	-	0.127	0.019	882.1	1207	26.9%
4076-1654	814	21.8	253	-	82.8	0.173	0.016	1171.7	1531	23.4%
4076-1725	621	18.6	106	-	305.4	0.023	0.001	1050.7	1021	-2.9%
4078-1709	766	22.9	55.1	-	277.6	0.052	0.010	1121.9	1295	13.3%
4081-2124	743	16.2	57.0	-	264.7	0.022	0.002	1081.0	1217	11.2%
4081-2234	845	24.2	31.3	-	528.0	0.108	0.011	1429.2	1711	16.5%
4082-1620	1236	22.2	59.5	-	288.9	0.149	0.017	1607.1	1454	-10.5%
4082-2008	819	28.3	329	-	-	0.060	0.013	1197.7	1440	16.8%
4083-1829	993	23.1	121	-	396.0	0.052	0.008	1533.5	1766	13.2%
4086-1711	638	14.8	116	-	577.6	0.109	0.006	1347.5	1763	23.6%

*Abbreviations: Cpx=clinopyroxene, Plag=plagioclase; Chl=chlorite; Amph= amphibole; Chalco=chalcopyrite;
BR Mn is the measured bulk rock concentrations from previous work.
Sample 4082-2008 does not have measured bulk rock Mn concentrations.
Values calculated by multiplying the median Mn concentration by the modal abundance of each specific mineral.

Table 3.10d: Comparison of calculated bulk rock and measured bulk rock Ni values. Data provided is the total amount of Ni from each mineral phase and sums to the bulk rock Ni concentration.

Ni concentration (ppm)	Cpx*	Plag*	Chl*	Amph*	Fe-Ti Oxides	Pyrite	Chalco *	Total Calculated Ni	Measured BR Ni*	% Difference
020705-1106	-	10.9	-	61.6	-	0.062	0.003	72.6	75	3.6%
020705-1423	54.5	1.1	4.9	-	0.7	3.252	0.006	64.5	58	-11.1%
020705-2131	64.1	1.1	12.6	-	1.3	0.015	0.001	79.1	63	-25.4%
020705-2225	20.2	1.1	53.6	-	0.3	0.036	0.004	75.3	99	24.0%
020805-1327	61.1	1.0	43.2	-	0.7	0.233	0.002	106.3	95	-12.3%
020905-1404	65.3	2.7	21.3	-	2.4	0.072	0.008	91.8	113	18.6%
021905-0409	-	11.9	-	36.1	1.7	0.061	0.004	49.7	41	-21.1%
022205-0320	51.5	1.1	9.5	-	0.9	0.071	0.003	63.2	77	17.8%
022305-0509	48.3	1.2	13.9	-	0.2	0.063	0.003	63.6	62	-2.9%
4075-1832	7.3	1.2	-	49.0	-	0.067	0.000	57.6	66	12.9%
4076-1629	45.3	6.8	37.8	-	-	0.095	0.004	90.0	84	-6.7%
4076-1654	44.4	1.1	52.0	-	0.3	0.130	0.004	98.0	88	-11.9%
4076-1725	52.7	1.2	19.0	-	1.1	0.017	0.000	74.0	61	-21.8%
4078-1709	65.0	1.1	7.5	-	0.9	0.039	0.002	74.6	67	-10.6%
4081-2124	50.6	0.0	4.5	-	12.5	0.017	0.001	67.7	58	-17.6%
4081-2234	42.6	0.3	1.3	-	1.8	0.916	0.003	46.9	44	-6.1%
4082-1620	39.0	0.6	8.8	-	0.9	0.112	0.004	49.4	53	6.9%
4082-2008	67.3	3.0	32.6	-	-	0.045	0.003	103.1		
4083-1829	32.5	1.1	3.7	-	1.4	0.039	0.002	38.7	38	-3.2%
4086-1711	56.2	0.2	13.5	-	2.4	0.082	0.002	72.4	63	-15.3%

*Abbreviations: Cpx=clinopyroxene, Plag=plagioclase; Chl=chlorite; Amph= amphibole; Chalco=chalcopyrite;
BR Ni is the measured bulk rock concentrations from previous work.
Sample 4082-2008 does not have measured bulk rock Ni concentrations.
Values calculated by multiplying the median Ni concentration by the modal abundance of each specific mineral.

3.8 Summary of the effect of mineralogy on base metal mobility

It is commonly thought that the source of vent fluid and ore deposit base metal contents (Co, Ni, Zn, and Cu) reside in primary sulphide minerals, while Mn is controlled by the primary silicate and oxide minerals (Metz and Trefry, 2000; Seewald and Seyfried, 1990; Seyfried and Ding, 1993; Von Damm, 1990). Since complete leaching of the metals from the sheeted dikes did not occur at Pito Deep, it was important to consider all possible mineral sources and sinks of metals to better understand why complete removal of metals has not occurred.

3.8.1 Primary mineral base metal sources

The three possible primary mineral hosts of metals within the sheeted dikes are clinopyroxene, Fe-Ti oxides, and Fe-Cu sulphides. All of these minerals contain, to some extent, each of the base metals studied (note that Pb is found in such small concentrations in all minerals and in the bulk rock that interpretation is difficult due to quality of the data and not is not considered further). The dominant host, however, differs for each base metal.

Pyrite can contain high concentrations of Ni and Co in a trace amount of individual grains within the sheeted dikes. Experimental work on basaltic melts and sulphide liquids show that Ni and Co preferentially enter the sulphide liquid rather than the basaltic melt (Rajamani and Naldrett, 1978). However, clinopyroxene is modally abundant in the sheeted dikes (30-45%) and can contain several tens of ppm of Ni and Co, thus, clinopyroxene cumulatively contains the majority of Ni and Co within a sample and is the dominant host of Ni and Co. Zinc and Mn are concentrated in primary titanomagnetite and, to a lesser extent, clinopyroxene.

3.8.2 Secondary mineral metal sinks

Base metals are found in all secondary phases present in the altered sheeted dikes. Chlorite, mixed-layer clays, and amphibole comprise 5-60% of the altered sheeted dike rocks, and host 35-70%, of the bulk rock metals. Therefore, the cumulative effect of the secondary mineral assemblage can be a substantial sink for metals.

Manganese, Zn, Co, and Ni are found in secondary silicates in the sheeted dikes. Mass balance calculations illustrate that Co and Ni are hosted predominantly in chlorite relative to amphibole, and Fe-Ti oxides; Mn is hosted in titanomagnetite and amphibole; and Zn leaves the system. Lead data was not abundant for secondary phases due to the quality of analyses, therefore a mass balance calculation was not conducted and mineral preference was therefore not determined.

Copper, unlike the other base metals, is easier to trace due to its preference to partition into chalcopyrite (Rajamani and Naldrett, 1978; Lee, 2013). New data from this study shows that Cu preferentially enters secondary chalcopyrite over secondary silicates in all samples. However, as Cu is mobilized by the breakdown of chalcopyrite, the host of Cu shifts from the sulphide phase to the silicate minerals, with Cu being more strongly partitioned into chlorite over amphibole (Figure 3.18 and Figure 2.3g).

The breakdown of chalcopyrite is dominantly controlled by the stability of the sulphide with temperature. Phase equilibria of the Cu-Fe-S system illustrates that chalcopyrite remains stable at 400°C and above. Above 557°C chalcopyrite can breakdown into pyrite or dissolve completely, allowing Cu to enter into the hydrothermal system or become redistributed (Craig and Scott, 1974; Zierenberg et al., 1984; Fleet, 2006). From amphibole analyses and previous work, temperatures of over 550°C have

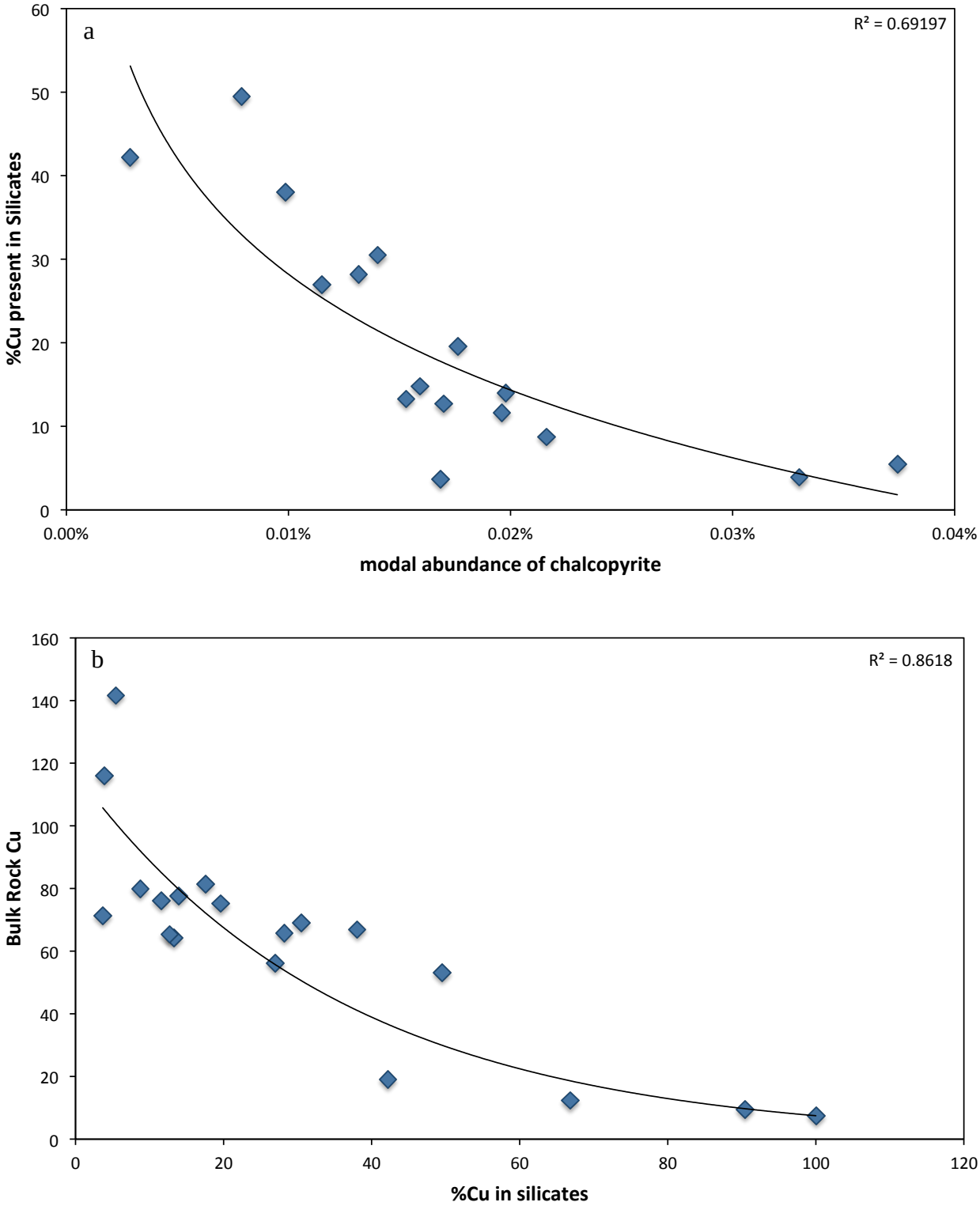

Figure 3.18: a) % of total bulk rock Cu found in the secondary silicate minerals versus the modal abundance of chalcopyrite. b) Bulk rock Cu versus the % of bulk rock Cu found in secondary silicates. The sink of Cu shifts to silicate minerals as chalcopyrite abundance decreases. The best fit power curve (in black) shows the strong correlation between bulk rock Cu and modal abundance of chalcopyrite (r^2 close to 1).

occurred at Pito Deep, and subsequently the breakdown of chalcopyrite is likely. Results from this study suggest that the Cu released into the fluid by the breakdown of chalcopyrite is not all transported away; instead some Cu remains in the system and enters into a silicate phase (generally chlorite, and to a lesser extent amphibole). This redistribution may be due to the preference of Cu to precipitate at temperatures lower than 350-400°C (Seewald and Seyfried, 1990). It is difficult to differentiate whether the Cu in secondary phases was in the crystal structure or present as a chalcopyrite inclusion, the absolute concentrations of Cu in the secondary phases (low relative to Cu found in chalcopyrite) and the time slices from LA-ICP-MS (lack of substantial peaks of Cu counts per second) suggest the Cu is present within the crystal structure. Although some secondary chalcopyrite is present, it is not the dominant host of Cu. Chapter 4 will discuss why chalcopyrite did not simply reform and become the dominant host of Cu and the other base metals.

Unlike the base metals of Zn, Pb, Co, Mn, and Cu, no change has occurred in the bulk rock Ni concentrations, suggesting that the Ni has either not been mobilized or has been precipitated back into secondary phases. Ni can easily enter into the octahedral site of a phyllosilicate mineral and previous studies of ocean crust and ophiolites have observed the presence of garnierites (hydrous Mg-Ni silicate minerals, often occurring as a mixture of serpentine, talc, sepolite, smectite, or chlorite), which sequesters Ni into the clay mineral and limits the amount of Ni that exits onto the seafloor by hydrothermal fluids (Manceau et al., 1985; Proenza et al., 2008). Chlorite and mixed-layer clays from the Pito Deep sheeted dikes are observed to have high concentrations of Ni (100’s of ppm). Due to the small bulk rock concentrations and the dominance of chlorite and

mixed-layer clays, as a secondary phase, the cumulative effect of the phyllosilicates is significant. Consequently, Ni has been mobilized and precipitated back into a local secondary phase, even though it appears Ni content has not changed.

For the sheeted dike complex at Pito Deep metals will, in general, preferentially partition into the secondary phases as follows: Cu will enter secondary chalcopyrite >>> chlorite > amphibole; Mn will enter secondary Fe-Ti oxides (if present) > amphibole > chlorite; Ni will enter mixed-layer clays and chlorite > amphibole; Co will enter chlorite > amphibole; and Zn will preferentially leave the system.

3.8.3 Primary phase versus replacement mineral

The concentration of base metals in the primary phase is a potential control on base metal concentrations in the secondary minerals. In most circumstances the absolute concentrations of Cu, Ni, and Zn have such a large range in the secondary phases, that the primary phase could not be the only control of base metal content. The absolute concentrations of Mn and Co, however, are observed to be similar in the primary and secondary phases and therefore the primary phase may be a dominant control of Mn an Co content. Figure 3.19 represents two example samples where A) chlorite has replaced clinopyroxene, and B) amphibole has replaced clinopyroxene. Both plots show that the concentrations of Mn, Co, and some Ni are very similar to the concentrations found in clinopyroxene (values close to 1 show that the secondary and primary base metal concentrations are close to each other). The similarity illustrates that Mn and to a lesser extent Co and Ni (which inherits the trend of magmatic differentiation) may be controlled by the primary clinopyroxene.

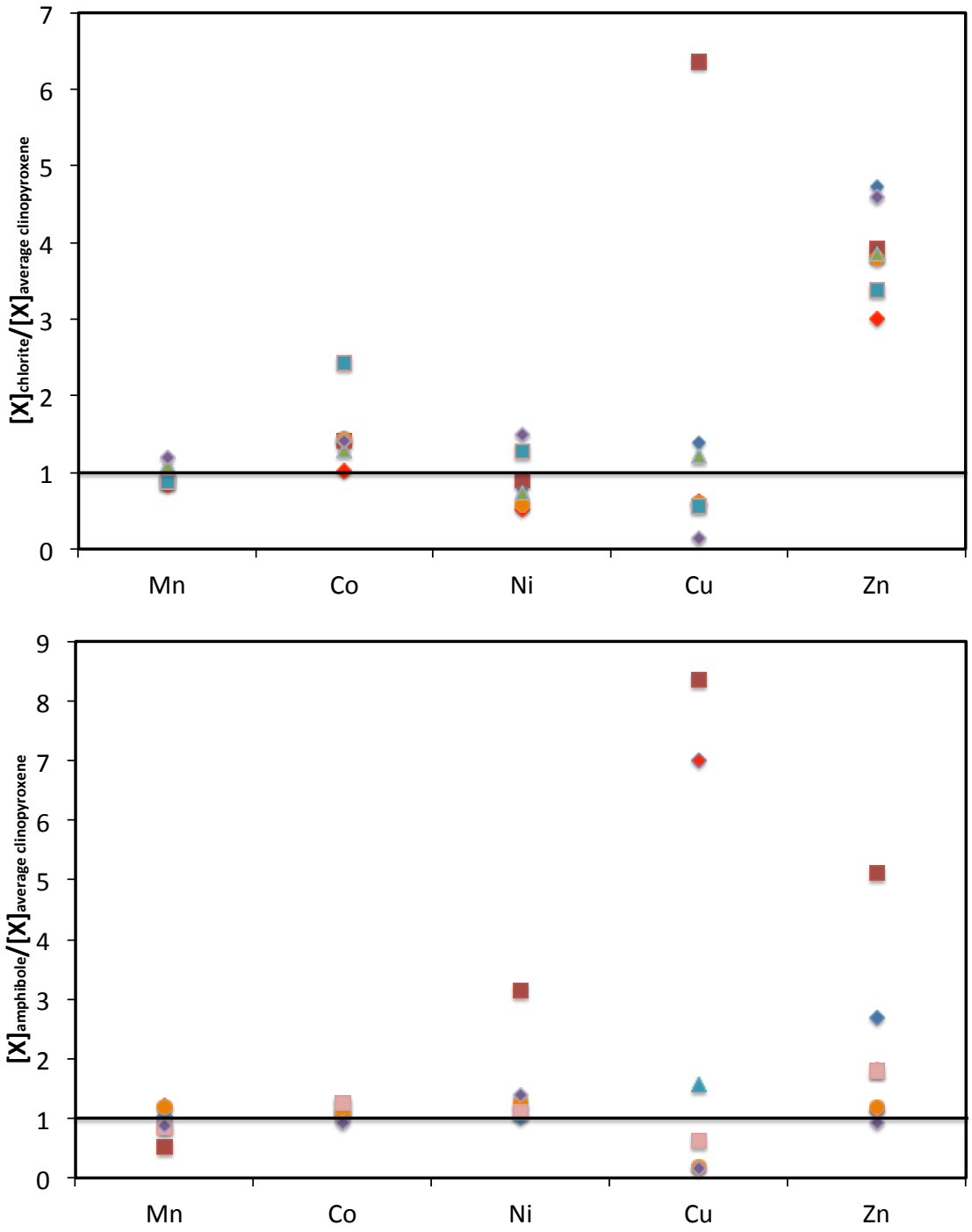

Figure 3.19: Base metal concentrations of chlorite (a) and amphibole (b) with respect to the primary phase of clinopyroxene. The closer to 1 the ratio is, the greater the influence of the primary phase of clinopyroxene on the base metal content in the secondary phase. Each symbol represent a different LA-ICP-MS analysis location within a single sample.

3.8.4 Direct precipitate versus secondary chlorite

By comparing the metal concentrations of chlorite found as a direct precipitate in the fault breccias versus the chlorite formed as replacement phase in the sheeted dikes, the relative importance of the primary phase composition versus the fluid chemistry can be further explored. Major element mineral chemistry of direct precipitate chlorite in breccias is within the range of chlorite replacing groundmass clinopyroxene in the sheeted dikes. In general, the concentrations of Mn, Co, Ni, Zn, and Cu of the direct precipitates lie within the total range observed in the groundmass secondary chlorite, but towards the higher end of these ranges (Figure 3.17). Due to the lack of difference in metal concentrations between breccia and groundmass chlorite, the fluid composition at the time of alteration will regulate element compositions in the secondary chlorite. However, Ni and Mn in groundmass chlorite do inherit the trends observed in primary clinopyroxene caused by magmatic differentiation. Subsequently, primary clinopyroxene will control the absolute concentration of Mn and the relative concentration of Ni (as Ni is observed in higher concentrations, but retains the magmatic trend).

Chapter 4

Discussion

4.1 Introduction

The regional distribution and mobility of metals was examined in Chapter 2 and gave insight into the degree of enrichment or depletion of base metals in the sheeted dike complex at Pito Deep. Chapter 3 examined the mineralogical sources and sinks of metals in the primary and secondary mineral phases. This chapter will evaluate what environmental parameters control metal mobility at Pito Deep based on constraints from experimental studies of hydrothermal fluid-rock interactions and compositions of hydrothermal fluids (e.g. Pester, et al., 2011; Seward, 1979; Seewald and Seyfried, 1990; Seyfried and Ding, 1993; Metz and Trefry, 2000; Seyfried, 1982; Mottl and Holland, 1978; Mottl et al., 1979), and the results from this study. The results of this study are then placed into the context of a hydrothermal cell to assess how the temporal and spatial evolution of the system impacts the metal budget of the ocean crust.

4.2 Environmental controls on base metal mobility

Environmental conditions that have been shown to affect the mobility of metals within the ocean crust include: temperature, fluid chemistry, and the sulphur content of the rock and fluid. The following sections will examine the role each of these parameters has in mobilizing base metals in the sheeted dike complex at Pito Deep. In addition, the location and timing of fluid-rock reactions with respect to the hydrothermal cell will be discussed.

4.2.1 Temperature

Temperature conditions within oceanic hydrothermal systems are reasonably well constrained. Metal-enriched fluids exiting the seafloor reach temperatures of over 350°C (maximum ~400°C) and these temperatures are interpreted to be the minimum values of reaction at depth (Beaulieu, 2010; Von Damm et al., 1995). Studies of hydrothermally altered sheeted dike complexes record typical temperatures of fluid-rock interaction at 250 to >450°C and variable gains and losses of base metals (Alt et al., 1996; Gillis et al., 2001, Heft et al., 2008; Alt et al., 2010).

Experimental work has predicted that temperature is a dominant controlling parameter on the mobility of base metals at mid-ocean ridges (e.g. Seward, 1981; Seewald and Seyfried, 1990). Results of a basalt alteration experiment with a Na-Ca-K-Cl fluid at seawater chlorinity, a fluid/rock mass ratio of 1, and a pressure of 400 bars, show that there is an order of magnitude increase in the concentration of Zn, Cu, Fe, and Mn in hydrothermal fluids when temperatures increase from 300°C to 350°C and finally to 400°C (Seewald & Seyfried, 1990). Increases in the temperature of the fluid resulted in a base metal- and H_2S-rich fluid that is considered representative of most high-temperature mid-ocean ridge hydrothermal fluids (Seewald and Seyfried, 1990). This experiment also predicts that as hydrothermal fluids cool, Cu and Fe will precipitate out of the fluid before Zn and Mn (Seewald and Seyfried, 1990).

Studies of base metal concentrations in vent fluids exiting the seafloor also show that the concentrations of Co, Cu, Mn, and Pb increase in the fluid with increasing temperature (Seward, 1981; Metz and Trefry, 2000; Pester et al., 2011). As temperatures rise from 320°C to 350°C, concentrations of the Co, Cu, Mn, and Pb in hydrothermal

fluids exiting the crust are observed to increase by over 50% of seawater concentrations, keeping in mind that seawater concentrations of these metals can be essentially zero, and therefore any increase is significant. This suggests that increases in temperature correlate with the mobilization and uptake of metals into the hydrothermal fluid (which is best observed by significant depletion of bilk rock Pb). There is no vent fluid data to assess the impact of temperature on Ni mobility, however because Ni is observed to have not changed from the protolith, it is predicted that Ni remains in the system independent of the temperature of the fluid. Zinc also does not show the same response to temperature as the other base metals, as Zn concentrations (~50-100 ppm) are the same in both low (<200°C) and high (up to 400°C) temperature fluids (Von Damm et al., 1985; Metz and Trefry, 2000;). Therefore, an additional parameter must promote increased Zn concentrations in the fluids at lower temperature (instead of precipitating into a secondary phase). This will be discussed in more detail below.

Although explicit temperatures cannot be determined for fluid-rock reactions in the sheeted dike complex at Pito Deep, temperature ranges may be estimated based on the secondary mineral assemblages and their compositions. Magnesiohornblende formation occurs at >450°C up to ~700°C (Liou, Kuniyoshi, & Ito, 1974), actinolite >250°C up to ~ 450°C (Liou et al., 1974), chlorite >200°C up to 450°C, and mixed-layer clays >100°C up to 230°C (K.M Gillis, Muehlenbachs, Stewart, Gleeson, & Karson, 2001; Kathryn M Gillis, 1995; Heft, Gillis, Pollock, Karson, & Klein, 2008; Robinson, Schmidt, & Santana de Zamora, 2002). Tetrahedral Al in amphibole can be used as a proxy for temperature, as Al_2O_3 increases in concentration with increased temperature (Liou et al., 1974). Values of Al^{IV} >0.5 are indicative of temperatures from 450°C to 700°C, and Al^{IV} <0.5 suggests

temperatures down to ~250°C (Liou et al., 1974). Amphibole data from this study and Heft et al. (2008) indicate that amphibole dominated assemblages may have interacted with fluids that have reached temperatures of up to 700°C, with most around 450°C, throughout the sheeted dike complex (Figure 3.15). In chlorite-dominated samples, amphibole typically has lower Al^{IV} (temperatures close to or below 450°C). This is consistent with temperatures at which chlorite will form (~250-450°C). Variability in amphibole Al^{IV} content and the presence of multiple secondary minerals within an individual sample, indicate that these minerals may not represent equilibrium assemblages, having formed during multiple events.

Experimental studies predict that at the peak temperatures recorded in the sheeted dikes (350->450°C), base metals should have been mobilized and leached from the sheeted dike complex. Substantial depletion of the base metals (Co, Mn, Ni, and Cu) is not observed, however, with only ~25% of the samples showing base metal loss. This suggests that fluids do not remain at high-temperatures as they evolve and interact with the crust. Analyzed metal contents of secondary silicate and sulphide minerals suggest that metals liberated at high temperatures are redistributed in time and space.

Changes in fluid temperature can result from a number of processes. For example, upwelling hot fluids rising from the hydrothermal root-zone may mix with cool down-welling seawater within fault zones or at the sheeted dike-lava transition (Barker et al., 2010). Examination of the ΔM values near the lava-dike transition show that no samples show metal enrichment (Fig. 3.15). Therefore, if mixing did occur, the fluids remained >250°C due to the presence of chlorite and lack of metal enrichment. This is consistent with a study of a fault zone at the lava-dike transition at Pito Deep that shows mixing of

cool downwelling and hot up-welling fluids has occurred with no sign of metal enrichment (Barker et al., 2010). Metal enrichment has not occurred because fluid temperatures remain >300°C as mixing occurs, therefore some metals will continue to reside in the fluid and some will enter into the secondary phase, consequently having little effect on the final metal budget (Barker et al., 2010).

Mixing of hot and cool fluids at the lava-dike is not the only process that could cool hydrothermal fluids. Numerical models of hydrothermal systems suggest that mixing may also occur within the sheeted dike complex in regions immediately adjacent to the high-temperature up-flow zones (D Coumou, Driesner, & Heinrich, 2008). Along the edges of the upwelling zones, warm down-welling fluids (<300°C) conductively cool the edge of the high-temperature up-flow zone causing the incorporation of base metals into secondary phases. If cooling does occur then the metals originally leached from the primary phases in the rock will partition back out of the fluid and enter into secondary phases in the altered rock. This will consequently have little effect on the bulk rock base metal content, as the metals will no longer be depleted in the rock and enrichment may not occur.

4.2.2 Fluid Chemistry

The chemistry of the fluid will affect the mobility of base metals in the rock with which the fluid is interacting. The chemistry of crustal fluids is difficult to constrain, therefore different aspects of fluid chemistry must be investigated to determine the overall effect of the fluid. This section will discuss the redox state of the hydrothermal system, the pH, the salinity, and the saturation of Fe-Cu sulphides in crustal fluids at Pito Deep.

4.2.2.1 Redox State

The redox state in extinct subseafloor hydrothermal systems is hard to define. Active mid-ocean ridge systems have been modelled to be moderately reducing to oxidative, with fluid-rock reactions buffered by pyrite-pyrrhotite-magnetite (PPM) or hematite-magnetite-pyrite (HMP), respectively (e.g., Seyfried and Ding, 1993).

The presence of pyrite and only trace pyrrhotite in the sheeted dikes provides insight into the redox state in the sheeted dikes at Pito Deep. Pyrrhotite is the stable igneous Fe-sulphide and is more stable in reducing environments (high S content and buffered by PPM) (W.E. Seyfried & Ding, 1993). Pyrrhotite is observed to break down into pyrite at hydrothermal conditions, which is stable at higher oxygen fugacity (Hall, 1986; W.E. Seyfried & Ding, 1993). Therefore, the lack of pyrrhotite, abundance of pyrite, and low S content in the Pito Deep dikes indicate a possible transition from a reducing environment buffered by PPM to a more oxidative environment buffered by HMP. The transition from a reducing to a more oxidative environment as newly formed igneous rock interacts with hydrothermal fluids would increase the partitioning of all metals into the fluid.

Redox buffered experiments of mineral solubility, at conditions representative of subseafloor hydrothermal systems, demonstrate the sensitivity of Cu and Fe mobility to the intensity of redox (Foustoukos & Seyfried, 2005; Seyfried & Ding, 1993). When increases in f_{O2} occur (more oxidative environment), dissolved Cu in the fluid is observed to increase and Fe decreases (Seyfried & Ding, 1993). The effect of redox on the mobility of Ni, Mn, Zn, Co, and Pb has not been studied. Nonetheless, due to the chemical similarity between these base metals it would be predicted that the redox state

will have similar effects on all of the base metals studied here. Therefore, as the redox state of the system shifts to be more oxidative, the loss of metals from the sheeted dikes should increase (Seyfried and Ding, 1993, 1995). However that is not what is observed, subsequently some other parameter controls the mobility of each individual base metal.

4.2.2.2 pH

Vent studies have shown that the exiting hydrothermal fluids have lower pH values than seawater (approximately 3-5; Von Damm et al., 1985; Seewald and Seyfried, 1990; Beaulieu, 2010). Experimental studies have shown that as pH decreases, Mn, Ni, Zn, Cu, Co, and Pb will partition into the fluid more readily (Bowers et al., 1988; Foustoukos & Seyfried, 2005; Seewald & Seyfried, 1990; Tivey, Humphris, Hannington, & Rona, 1995). Decrease in the pH value of the hydrothermal fluid is dominantly caused by the formation of hydrous secondary phases (e.g. amphibole and chlorite). In addition, the precipitation of metal sulphides can also act to lower pH; an example reaction of sulphide formation is (Seewald & Seyfried, 1990):

$$Me^{2+} + H_2S = MeS + 2H^+$$

Where Me^{2+} is a metal cation, such as Cu or Zn, and hydrogen ion concentrations increase causing a decrease in the pH value. A reaction such as this is observed to occur in the sheeted dikes by the precipitation of secondary chalcopyrite and possibly sphalerite. Since the pH of hydrothermal fluids has been observed to differ from that of seawater, it can effect how metals will partition, and with a decrease in pH metals will increase mobility.

4.2.2.3 Salinity

The salinity of exiting vent fluids has been studied to determine its effect on metal mobility (Metz & Trefry, 2000; Michael J Mottl & Holland, 1978; Micuel J Mottl et al., 1979). Chloride is an important ligand in fluid-metal interactions, because base metals will easily complex with Cl^- (Seyfried et al., 1986) and Cl^- is the dominant anion present in hydrothermal fluids (Von Damm et al., 1985; Pester et al., 2011). As a result, the concentration of Cl^- in a hydrothermal fluid will increase the affinity of metals to partition into the fluid (Seyfried et al., 1986; Von Damm et al., 1985).

Hydrothermal fluids venting at the seafloor have a wide range in salinity (0.1-8wt% NaCl) (seawater is ~3.2wt% NaCl; see summary in Cathles, 2010). This range is thought to be primarily due to the phase separation of seawater-derived fluids at depth within the crust (Von Damm, 1990). Fluid inclusion data collected for breccias and quartz veins at Pito Deep record high-temperatures (homogenization temperature 154-315°C) and a range in salinity (2.6-5.9wt% NaCl), with most samples showing higher than seawater salinity (Heft et al., 2008). The presence of fluids with higher salinity than seawater would have enhanced metal partitioning into the fluid and transportation to the seafloor.

Zinc is observed in high concentrations (with respect to seawater) in exiting vent fluids regardless of fluid temperature. The sheeted dikes at Pito Deep are largely depleted in Zn (94% of samples show depletion). Metz and Trefry (2000) examined the relationship between Zn and Cl^- and observed a positive correlation between the two elements. Therefore in the case of Zn, the inferred higher than seawater salinity of fluids interacting with the Pito Deep sheeted dikes suggest fluid salinity may play a greater role

in Zn transport in comparison to temperature. However, leaching of Pb is also observed from the sheeted dikes, therefore an additional parameter must aid in metal uptake into the fluid.

4.2.3 Mineral Stability and Fluid Saturation

The base metals Cu, Mn, and Co have shown that they become mobilized by the breakdown of primary clinopyroxene, pyrite, and chalcopyrite, then become redistributed back into secondary phases of Fe-Ti oxides, silicates, or chalcopyrite or leave the system and exit onto the seafloor in hydrothermal fluids. The mobility of these base metals is controlled by the fluid temperature, redox state, and primary mineral breakdown. Unlike Cu, Mn, and Co, Ni, Zn, and Pb show different trends of mobility. Bulk rock Ni shows no variation from the protolith concentration, therefore Ni has either not been mobilized in the first place or has been distributed back into secondary phases. Bulk rock Zn and Pb show the opposite of Ni, in which they have been significantly depleted from the sheeted dikes. Therefore it is important to understand how and why these base metals show a difference.

Changes in S values in the sheeted dike complex provide insight into the availability of S in the hydrothermal system. Vent fluid data show that with increased temperature there is increased H_2S concentration in the exiting fluid (Metz & Trefry, 2000; Von Damm et al., 1985). This is achieved by the breakdown of pyrite and pyrhottite in the sheeted dikes, for example (Seyfried and Ding, 1993; Barker, et al., 2010):

$$2FeS+FeS_2+4H_2O=4H_2S+ Fe_3O_4$$

Seawater SO_4 is also present in hydrothermal fluids, however previous work has found that most of the SO_4 precipitates as anhydrite in the upper sheeted dikes and lavas, and is not associated with high-temperature reactions (Barker, et al., 2010).

Although the presence of H_2S in hydrothermal fluids does not directly control the mobility of metals, the breakdown of sulphides releases metals into the fluid. Bulk rock ΔS and Δ metal values at Pito Deep (Chapter 2) show that there is no direct correlation between the amount of S available in the hydrothermal system (e.g. how much S has been leached from the sheeted dikes) and the mobility of the metals. In other words, most samples show S-depletion but not metal depletion. Eight samples, however, show depletion in all metals (including Cu) with respect to S (Fig. 2.3g). The 8 samples have remained fresh (<10% alteration), suggesting they interacted with a high temperature fluid for a brief amount of time, and consequently metals were not able to precipitate into a secondary phase. This will be discussed further in the following section.

The simple breakdown of the primary sulphide phases will release metals into the hydrothermal fluid, and therefore is an important process for the mobility of certain base metals. Chalcopyrite, sphalerite, and galena, are all important and significant sources of Cu, Zn, and Pb in the rock, respectively. Previous work on fresh samples have observed sphalerite in the sheeted dike and gabbros, although galena has not been observed it could be present as micro-inclusions in clinopyroxene or other primary sulphides (Puchelt et al., 1996). Due to trace amount of base metals found in the bulk rock, if these primary phases are present in the protolith and subsequently breakdown, it will appear as though significant leaching of the metals has occurred. The systematic breakdown of these minerals is temperature dependent where galena will dissolve first, then sphalerite, and

finally chalcopyrite. Therefore, Zn and Pb will leave the system first as their host minerals of sphalerite and galena break down at lower temperatures (<300°C; Craig and Scott, 1974; Fleet, 2006), and then finally Cu will enter the hydrothermal system as temperatures become sufficient enough to breakdown chalcopyrite.

Chalcopyrite is observed to have dissolved in the sheeted dikes (lack of primary chalcopyrite in the rocks) subsequently introducing Cu into the hydrothermal fluid, however only 25% of the rocks show Cu depletion. A possible explanation as to why Cu has not simply left the system is that the chalcopyrite has become oversaturated in the hydrothermal fluid. Vent fluid studies have shown that exiting hydrothermal fluids are almost completely saturated in chalcopyrite (Butterfield et al., 1994; Metz and Trefry, 2000). Therefore even though Cu has been introduced into the hydrothermal system, it will preferentially go back into a secondary phase because the fluid has become oversaturated and will not transport Cu to the seafloor.

Secondary sulphides are present in the sheeted dikes, however they are generally not the dominant sinks of the base metals. This may be caused by the chemistry of the fluid at the time of alteration prohibiting sulphide formation. Analysis of vent fluids from the EPR and other mid-ocean ridge systems, as well as fluid inclusions from Hess Deep show an affect of the salinity of the hydrothermal fluid on H_2S and Fe concentrations. As Cl^- concentrations increase H_2S decreases and Fe increases, which can inhibit sulphide formation and promote chlorite or amphibole formation (Saccocia and Gillis, 1995; Von Damm et al., 1995). The significant depletion in bulk rock Zn and the analysis of fluid inclusions form Pito Deep (Heft et al., 2008) show that salinity in hydrothermal fluids is higher than that of seawater and could potentially inhibit sulphide precipitation.

The chemistry of the fluid does affect the ability for metals to partition in and out of the hydrothermal system. A decrease in pH, an increase in salinity and redox state, and an increase in sulphide breakdown and available sulfur species should all promote metal uptake into the fluid and subsequently leach the majority of metals from the ocean crust. Since simple leaching is not observed the following section will discuss how the timing of metal mobilization will effect how metals are distributed.

4.3 Timing of metal mobilization

In a hydrothermal cell, when and where (e.g. at depth or at the lava-dike boundary) fluids interact with rock will vary and subsequently effect how base metals are partitioned and potentially redistributed. A section of ocean crust may pass through several different hydrothermal cells, various parts of one or more cells, or may interact with a single part of one cell as it moves away from the axial region. Due to this variability, secondary mineral assemblages may form in equilibrium at one time or be sequentially deposited during successive stages; the metal content of these minerals may fluctuate because of these different possibilities. To assess how the structure of the hydrothermal cell impacts metal mobility in the sheeted dike complex, two models were considered: 1) metals were mobilized during one hydrothermal event and 2) metals were mobilized during multiple hydrothermal events.

The first model assumes a section of ocean crust experiences a single hydrothermal event at the mid-ocean ridge. A section of crust passes into a high-temperature discharge zone, interacts with the hydrothermal fluids, leading to the alteration of the crust, and then exits the cell with little to no additional alteration

occurring (Figure 4.1). Thus it is assumed that any high-temperature alteration recorded in the secondary mineral assemblages is coeval. In this case, differences in the metal content of actinolite and chlorite in 2 samples with <15% alteration demonstrates a preference for metals to partition into one mineral over another. Specifically, the generally higher concentrations of Cu, Ni, and Co in chlorite (2-3 times higher than amphibole) suggest that these elements preferentially partition into chlorite over actinolite. This is not the case for Mn as there are consistently higher concentrations in amphibole over chlorite (1.5-2 times higher) showing that Mn preferentially enters actinolite. Zinc shows no preference of one mineral over another. Due to poor quality of Pb data it cannot be determined where Pb preferentially partitions. This model of a single hydrothermal event can apply to samples that show bulk rock depletion of all of the metals, as well as S-depletion, but have remained relatively fresh (<15% alteration). A single hydrothermal event, however, will not apply to all samples that are highly altered and yet show no change in bulk rock metal. If this were the case, it would be expected that the metal content of a single secondary phase would be consistent from grain to grain (not mineral to mineral), which is not observed. In this situation, metals will have been removed from the rock first and then redistributed back in during multiple events.

The second model is based on the prediction that hydrothermal cells are evolving systems that start/stop and change locations along a mid-ocean ridge segment (e.g. Coumou et al., 2006, 2008). This means that a section of ocean crust may interact with more than one hydrothermal cell and may pass through different positions (recharge versus discharge) within each cell (Figure 4.1). The simplest scenario is that a section of ocean crust travels through a recharge zone of one cell and then the discharge zone of

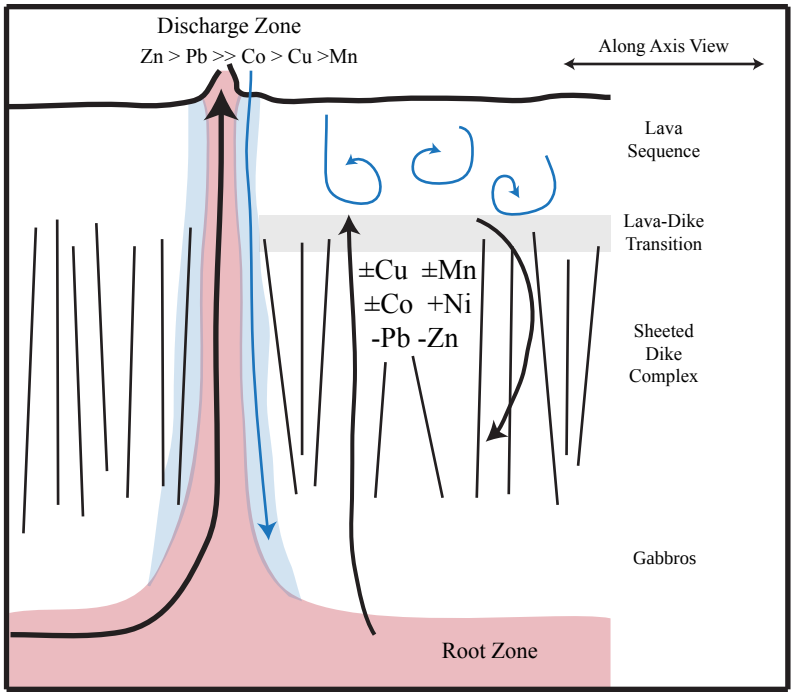

Figure 4.1: Schematic illustration summarizing the mobilization and redistribution of metals in the sheeted dike complex. Metals are leached when high temprature fluids interact with the rock and are transported to the surface in the discharge zone (red zone), or are redistributed back into the sheeted dikes. Discharging fluids can cool when recharging fluid conductively removes heat (blue zone), or when mixing of recharging seawater occurs at the lava-dike boundary (grey zone).

another as it moves off-axis. A more probable scenario is that as a section of crust moves off-axis it interacts with multiple discharge and recharge zones. The secondary mineral assemblage and bulk composition of the altered dikes thus reflects the cumulative metal content of numerous hydrothermal events (e.g. Coogan, 2008; Heft et al., 2008). Due to the large range in metal concentrations of secondary minerals observed within a single sample, it is likely that an initial hydrothermal event leaches the metals from the primary sulphides, Fe-Ti oxides, and clinopyroxene, and then during multiple later events (with fluids that have traveled from elsewhere) the metals are precipitated back into secondary phases. The variability of metal concentrations within the secondary minerals, in a single sample, provides evidence for fluctuations in hydrothermal fluid chemistry and temperature on a local scale. For example, in the same sample one grain of chlorite can be more Cu-enriched than another chlorite grain. This could be caused by a later, cooler fluid (<350°C) interacting with the rocks and partitioning Cu into the secondary phase. This cooler fluid may be an evolved fluid that has already interacted with the rocks and circulates back into the sheeted dikes instead of exiting the seafloor, or high-temperature up-welling fluids mixing with recharging seawater. Another possibility is that the Cu-enriched chlorite formed from a fluid that had higher Cu concentrations than the previous hydrothermal events, and therefore more Cu was readily available to precipitate into the chlorite. Additionally, the variability of metal content between samples suggests that the fluid chemistry and temperature also fluctuates on a regional scale. For example, some samples show consistently higher Ni, and Co concentrations (Figure 3.9), which are related to increased mixed-layer clays content and subsequently lower temperature fluids. This overprinting effect and the redistribution of metals will cause the bulk rock metal

budget to appear relatively unchanged. Unlike the previous model of a single event, the presence of actinolite and chlorite cannot be assumed to be coeval. Therefore the observed difference in metal content could be caused by the variation of the fluid chemistry and temperature at the time of alteration. That being said, it is possible that some of the chlorite and amphibole in a sample are coeval and therefore preference for some metals to enter a specific mineral will still apply. This second model, suggesting more than one event has occurred, is a more realistic model for the geologic setting at Pito Deep. Since cells can be unpredictable and evolve through time, multiple events are more likely to occur.

The previous two models of hydrothermal circulation and base metal redistribution describe the evolution of Mn, Co, and Cu in the geologic record of Pito Deep, however Ni, Zn and Pb have a more simple history. Bulk rock Ni concentrations have not changed during alteration; therefore Ni precipitates out of the fluid and into a secondary silicate (often chlorite and mixed-layer clays as previously mentioned). Therefore, independent of temperature, salinity, and redox, Ni will preferentially enter into the secondary phase rather than be transported to the surface. Zinc and Pb are the opposite and are observed to be significantly depleted in the sheeted dikes at all depths, and therefore cooling of multiple hydrothermal events have not affected bulk rock Zn and Pb concentrations. This study has hypothesized that the salinity of the fluid and mineral stabilities are two possible controlling parameters of Zn and Pb depletion. Consequently once the Zn and Pb have been removed from the system there will no longer be any available to precipitate into secondary phases. Therefore Zn and Pb cannot be used to interpret where in the cell alteration has occurred, but does suggest that an initial removal

of metals from the sheeted dikes can occur which is followed by later events that reintroduce metals into secondary phases.

As a section of crust travels off-axis, the high-temperature root zone dissipates, as there is limited heat available from the axial magma chamber (AMC) to drive convection. Lower temperature fluids can continue to recirculate off-axis and new low-temperature fluids can enter the crust off-axis, resulting in later overprinting. If the fluids contain any metals they will be precipitated in the overprinting phase(s) (such as mixed-layer clay and potentially sulphides) and the metals originally leached from the sheeted dikes will be redistributed back into the rock. The fluids that are recirculating may have already precipitated a large amount of their metal content, and therefore the low-temperature mixed-layer clays will appear to have low metal concentrations because the fluids no longer contain any. Additionally, fluids entering off-axis may have little to no metals present and will also precipitate secondary phases with low metal content. At Pito Deep, the mixed-layer clays have higher concentrations of Ni and Pb relative to chlorite and have higher Ni, Co, Pb, and to a lesser extent Cu and Zn concentrations with respect to amphibole (refer to Figure 3.10 and 3.14). In samples where mixed-layer clays are dominant, Ni, Co, and Pb are observed to be enriched in the bulk rock content, with respect to chlorite-rich samples (Figure 3.9), however it cannot be confirmed if this overprinting occurred on or off-axis. Therefore, it can be said that if metals are still present in the off-axis fluids (new or recirculating), overprinting by secondary phases enriched in metals leads to the total metal budget of the sheeted dike complex being largely unchanged with respect to the fresh rock values (except for Zn).

4.4 Summary

Although the exact conditions under which alteration occurred within the sheeted dike complex cannot be ascertained, this study has documented how base metals are mobilized and redistributed in hydrothermal systems. Base metals become mobilized due to the breakdown of primary sulphides, clinopyroxene, and Fe-Ti oxides, and partition into the hydrothermal fluid. As the fluids evolve through time and space Ni, Mn, Co, and Cu are redistributed back into secondary phases, and Zn and Pb are transported to the seafloor.

Temperature and mineral stability are the dominant parameters controlling the mobility of Cu, Ni, Mn, Co, Zn, and Pb. With increasing temperature, primary minerals breakdown and base metals partition into the hydrothermal fluid. Fe-Cu sulphides and clinopyroxene are the dominant source of base metals in the sheeted dikes. Mass balance calculations show that the cumulative effect of the breakdown of clinopyroxene is more important for Mn, Co, Ni, and Zn than the breakdown of Fe-Cu sulphides, due its higher modal abundance (Chapter 3). Fe-Cu sulphides are still the dominant source of Cu in the sheeted dikes. Once metals are partitioned into hydrothermal fluids, they are either transported to the surface in a discharge zone or are precipitated into a secondary mineral phase, leading to local redistribution.

Cooling of hydrothermal fluids is necessary to explain the observed redistribution of Mn, Co, and Cu in the sheeted dikes at Pito Deep because decreases in temperature promote the precipitation of metal-bearing phases (secondary silicates and sulphides, Chapter 3). Fluids may cool by mixing hot discharging fluids with cool recharging

seawater near the lava-dike boundary, or by the interaction of fluids adjacent to the pipe-like discharge zone (Figure 1.2).

In most cases, the chemistry of the hydrothermal fluids will only negligibly affect metal mobility, except for Zn and Pb. In the sheeted dikes, Zn and Pb are the only base metals that are significantly depleted regionally. If temperature were the controlling parameter, then it would be expected that Zn would have similar depletion patterns to the other metals. It is proposed that Zn and Pb mobility are dominantly influenced by fluid salinity and the solubility of sphalerite and galena. Once Zn and Pb partition into the fluid they remain complexed with Cl^- instead of precipitating in a secondary mineral when fluid temperatures cool.

In addition to temperature and fluid chemistry, it is important to also understand when and where the crust interacts with hydrothermal fluids, as this will provide further insight into the mobility and redistribution of metals. Evidence presented in this thesis suggests that the sheeted dikes have seen multiple hydrothermal events. Due to the difficulty of constraining exact parameters at the time of alteration the exact locations of the multiple events cannot be hypothesized, however the new mineral data and analysis of the bulk rock data show metals are not simply leached from the crust and deposited on the seafloor.

The similarity of the Δ metal content in the sheeted dike complex at Pito Deep, Hess Deep, and IODP 1256D discussed in Chapter 2, along with observed alteration patterns, Sr-isotope data, and the lack of systematic trends with temperature in the sheeted dike complex (Heft et al., 2008; Alt et al., 2010) suggests that the model of an

evolving hydrothermal system is appropriate for fast-spreading ridges in general. Figure 4.1 summarizes the mobility, distribution, and transport path of the metals in the sheeted dikes along a fast-spreading ridge.

Chapter 5

Conclusions and Future Work

5.1 Conclusions

Studies conducted at Pito Deep have provided detailed insight into the evolution of hydrothermal alteration in the sheeted dike complex of fast-spreading ocean crust. Bulk rock data and geochemical analyses of primary and secondary silicates, Fe-Ti oxides, and Fe-Cu sulphides were used to interpret the controls on metal mobility in the sheeted dike complex. The primary conclusions of this study are as follows:

1. Base metals are not homogenously depleted in the sheeted dike complex with respect to sample location, depth, or degree of alteration. The average metal depletion is: Mn is less than 16% depletion; Cu is less than 50% depletion, Co show less than 22% depletion; and Zn shows an average of 36% depletion, and Pb and S are almost completely leached showing over 50%% depletion, and Ni shows no depletion or enrichment in the sheeted dikes. Of all the samples studied, only 25% show Cu depletion, 16% show Mn depletion, 21% show Co depletion, 0% show Ni depletion, 75% show Zn depletion, 97% show S depletion, and 71% show Pb depletion. Of the remaining samples 3%, 2%, 10%, and 29% show enrichment of Co, Cu, Pb and Mn, respectively. The relative depletion of the bulk rock base metals in the sheeted dikes is Pb > Zn >> Co > Cu > Mn; Ni shows no change.

2. The extent of metal enrichment and depletion in the sheeted dikes is equivalent to those observed at Hess Deep and Hole 1256D. Therefore Pito Deep is analogous to other sections of fast-spreading ridges.
3. The source of base metals in the sheeted dike complex varies from sample to sample, however general trends have emerged from this study. The primary source of Cu is primary chalcopyrite (if present) or clinopyroxene. Cobalt, Ni, Pb, and Zn are hosted in clinopyroxene, and Mn resides in either titanomagnetite or clinopyroxene. Pyrite, chalcopyrite and pyrrhotite are the only sources of S. Plagioclase is not a dominant source of any metal. Sulphides of sphalerite and galena are most likely the dominant source of Zn and Pb, respectively, however they have broken down during alteration and are no longer observed, therefore this is speculative.
4. Base metal concentrations of Mn, Co, and Ni in amphibole and and to a lesser extent chlorite are predominantly influenced by the primary phase it replaces (clinopyroxene).
5. Metals are observed to enter into the secondary phases present in the rocks. When only one secondary silicate phase is present (either phyllosilicates or amphibole), all base metals enter into that phase. One exception is if secondary chalcopyrite is present, then Cu will preferentially enter into that crystal structure over the silicates. If both chlorite and amphibole are present within the same sample, then Co and Ni preferentially enter chlorite, Mn will enter amphibole, Zn will leave the system, and Pb has no preference for one over the other (due to poor data quality interpretation of Pb was difficult)

6. This thesis proposes that metals are not simply leached from the sheeted dike complex, but rather are precipitated back into secondary phases. The lack of any patterns with temperature, region, depth, or dominant alteration phase suggests that the sheeted dikes interact with multiple hydrothermal events and that the history of the sheeted dike complex is not the same for all geographic locations Each sample has a evolution unique to that sample, making a general interpretation difficult.
7. The source region needed to form a large (3000 tonnes) EPR VMS deposit, assuming the metals are leached from the sheeted dike complex, is sufficiently small (0.002-0.004 km^3) to accommodate deposit spacing of 25-50km along fast-spreading ridges. This suggests that no external introduction of metals, such as magmatic fluids, is needed to form a deposit.
8. No one parameter controls the mobility of metals in the sheeted dikes. Salinity, mineral stability, fluid saturation, and temperature can all affect the base metal content within the sheeted dikes.

5.2 Future Work

To further constrain the controls of the distribution and mobility of metals in the ocean crust, additional analyses of coexisting amphibole and chlorite in the sheeted dike groundmass, along with direct precipitate silicate minerals in hydrothermal breccias, may provide more insight into the preferential partitioning of metals within the sheeted dikes.

Additional studies of base metal concentrations in silicate minerals, Fe-Ti oxides, and Fe-Cu sulphides in more samples from Pito Deep, Hess Deep, and Hole 1256D will contribute to the understanding of the variability of base metal concentrations within the

sheeted dikes at fast-spreading ridges. Core-rim analyses and scanning electron microprobe data may help to identify the distribution and location of metals within a single grain, and subsequently indicate if metals build up on the surface of a grain or are evenly distributed within it.

Finally, experimental studies should be conducted on the partitioning of base metals between the phases observed, in the altered rocks and hydrothermal fluids, at conditions representative of the hydrothermal fluid and sheeted dike complex. Experimental data would contribute the most to understanding how and why metals have partitioned (as has been observed in these rocks) and how the fluid has evolved through time and space.

References

Adam, J., and Green, T., 2006, Trace element partitioning between mica- and amphibole-bearing garnet lherzolite and hydrous basanitic melt: 1. Experimental results and the investigation of controls on partitioning behaviour.: Contributions to Mineralogy and Petrology, v. 152, p. 1–17, doi: 10.1007/s00410-006-0085-4.

Alt, J.C., 1995, Subseafloor processes in mid-ocean ridge hydrothermal systems, *in* Humphris, S., J. Lupton, L. Mullineaux, and R. Zierenberg, (eds.) Seafloor hydrothermal systems: physical, chemical, and biological interactions,: Geophysical Monograph Series, American Geophysical Union, Washington, D.C., p. 85–114.

Alt, J.C., and Bach, W., 2003, Alteration of ocean crust: Subsurface water-rock interactions *in* Halbach, V. Tunnicliffe, and J.R. Hein, (eds.) Energy and mass transfer in marine hydrothermal systems, P.E., Dahlem University Press, p. 7–28.

Alt, J.C., Laverne, C., Coggon, R.M., Teagle, D. a. H., Banerjee, N.R., Morgan, S., Smith-Duque, C.E., Harris, M., and Galli, L., 2010, Subsurface structure of a submarine hydrothermal system in ocean crust formed at the East Pacific Rise, ODP/IODP Site 1256.: Geochemistry Geophysics Geosystems, v. 11, p. Q10010, doi: 10.1029/2010GC003144.

Alt, J.C., Lonsdale, P., Haymon, R., and Muehlenbachs, K., 1987, Hydrothermal sulfide and oxide deposits on seamounts near 21 ° N , East Pacific Rise.: Geological Society of Amerca Bulletin, v. 2, p. 157–168, doi: 10.1130/0016-7606(1987)98<157.

Backer, H., Lange, J., and March, 1985, Hydrothermal activity and sulphide formation in axial valleys of the East Pacific Rise crest between 18 and 22 degrees S: Earth and Planetary Science Letters, v. 72, p. 9–22.

Bailey, S.W., 1988, Hydrous Phyllosilicates: Reviews in Mineralogy, Ribbe, P.H., (ed.) Virginia, USA., v. 19, pp. 725.

Baker, T., Achterberg, E. V, Ryan, C.G., and Lang, J.R., 2004, Composition and evolution of ore fluids in a magmatic-hydrothermal skarn deposit: Geology, v. 32, p. 117, doi: 10.1130/G19950.1.

Baker, E.T., and Urabe, T., 1996, Extensive distribution of hydrothermal plumes along the superfast spreading East Pacific Rise.,: v. 101, p. 8685–8695.

Barker, A. K., Coogan, L. A., and Gillis, K.M., 2010, Insights into the behaviour of sulphur in mid-ocean ridge axial hydrothermal systems from the composition of the sheeted dyke complex at Pito Deep: Chemical Geology, v. 275, p. 105–115, doi: 10.1016/j.chemgeo.2010.05.003.

Barker, A.K., Coogan, L. A., Gillis, K.M., Hayman, N.W., and Weis, D., 2010, Direct observation of a fossil high-temperature, fault-hosted, hydrothermal upflow zone in crust formed at the East Pacific Rise: Geology, v. 38, p. 379–382, doi: 10.1130/G30542.1.

Barker, A. K., Coogan, L. A., Gillis, K.M., and Weis, D., 2008, Strontium isotope constraints on fluid flow in the sheeted dike complex of fast spreading crust: pervasive fluid flow at Pito Deep: Geochemistry Geophysics Geosystems, v. 9, doi: 10.1029/2007GC001901.

Beaulieu, S.E., 2010, InterRidge Global Database of Active Submarine Hydrothermal Vent Fields, Version 2.0, http://www.interridge.org/irvents/.

Bettison, L.A., and Schiffman, P., 1988, Compositional and structural variations of phyllosilicates from the Point Sal ophiolite: American Mineralogist: v. 73, p. 62–76.

Bischoff, J.L., and Seyfried, W.E.J., 1979, Hydrothermal chemistry of seawater from 25-350 degrees C: American Journal of Science, v. 278, p. 838–860.

Blundy, J., and Wood, B., 1994, Predictions of crystal-melt partition coefficients from elastic moduli: Nature, v. 372, p. 452–454.

Bowers, T.S., Campbell, A.C., Measures, C.I., Spivack, J., Khadem, M., and Edmond, J.M., 1988, Chemical controls on the composition of vent fluids at 13-11N and 21N , East Pacific Rise: Journal of Geophysical Research, v. 93, p. 4522–4536.

Butterfield, D.A., McDuff, R.E., Franklin, J., and Wheat, C.G., 1994, Chapter 20. Geochemistry of hydrothermal vent fluids from Middle Valley, Juan de Fuca Ridge *in* Mottl, M.J., Davis, E.E., Fisher, A.T., and Slack, J.F. (eds.) Proceedings of the Ocean Drilling Program, Scientific Results, v. 139, p. 395-410.

Cann, J., and Gillis, K., 2004, Hydrothermal insights from the Troodos ophiolite, Cyprus, *in* Elderfield, H. and Davis, E. (eds.), The Hydrology of the Oceanic Lithosphere, Cambridge University Press, p. 274–310.

Cann, J.R., and Strens, M.R., 1989, Modeling periodic megaplume emission by black smoker systems: Journal of Geophysical Research, v. 94, p. 12227–12237.

Cathles, L.M., 2010, What processes at mid-ocean ridges tell us about volcanogenic massive sulfide deposits: Mineralium Deposita, v. 46, p. 639–657, doi: 10.1007/s00126-010-0292-9.

Coogan, L. A., 2008, Reconciling temperatures of metamorphism, fluid fluxes, and heat transport in the upper crust at intermediate to fast spreading mid-ocean ridges: Geochemistry Geophysics Geosystems, v. 9, p. Q02013, doi: 10.1029/2007GC001787.

Coogan, L. A., and Dosso, S., 2012, An internally consistent, probabilistic, determination of ridge-axis hydrothermal fluxes from basalt-hosted systems: Earth and Planetary Science Letters, v. 323-324, p. 92–101, doi: 10.1016/j.epsl.2012.01.017.

Coumou, D., Driesner, T., Geiger, S., Heinrich, C.A., and Matthäi, S., 2006, The dynamics of mid-ocean ridge hydrothermal systems : Splitting plumes and fluctuating vent temperatures: v. 245, p. 218–231, doi: 10.1016/j.epsl.2006.02.044.

Coumou, D., Driesner, T., and Heinrich, C. A, 2008, The structure and dynamics of mid-ocean ridge hydrothermal systems.: Science (New York, N.Y.), v. 321, p. 1825–1828, doi: 10.1126/science.1159582.

Craig, J.R., and Scott, S.D., 1974, Sulfide Phase Equilibria, *in* Ribbe, P.H. (ed.) Sulfide Mineralogy, Mineral Society of America, Short Course Notes, Virginia, USA., pp. 350.

Curewitz, D., and Karson, J.A., 1998, Geological consequences of dike intrusion at mid-ocean ridge spreading centers, *in* Faulting and Magmatism at Mid-Ocean Ridges. Geophysical Monograph 106., American Geophysical Union, p. 117–136.

Deer, W., Howie, R., and Zussman, J., 1992, An Introduction to the Rock-Forming Minerals: Pearson.

Delaney, J.R., Kelley, D.S., Lilley, M.D., Butterfield, D. A., Baross, J.A., Wilcock, W.S.D., Embley, R.W., and Summit, M., 1998, The quantum of oceanic crustal accretion : impacts of diking at mid-ocean ridges: Science, v. 281, p. 222–230.

Detrick, R.S., 1991, Ridge crest magma chambers: a review of results from recent marine seismic experiments, *in* Tj. Peters, A. Nicolas, R. G. Coleman (eds.) Ophiolites: genesis and evolution of oceanic lithosphere, Bouder, CO, p. 7–20.

Detrick, R.S., Buhl, O., Vera, E., Mutter, J., Orcutt, J., Madsen, J., and Brocher, T., 1987, Multi-channel seismic imaging of a crustal magma chamber along the East Pacific Rise: Nature, v. 326, p. 35–41.

Draper, D.S., and Green, T.H., 1997, P – T phase relations of silicic, alkaline, aluminous mantle-xenolith glasses under anhydrous and C– O–H fluid-saturated conditions: Journal of Petrology, v. 38, p. 1187–1224.

Edmond, J., 2011, Ocenic Vents: Science, v. 271, p. 1508.

Elsdon, R., 1972, Iron-titanium oxide minerals in the Upper Layered Series , Kap Edvard Holm , East Greenland: Mineralogical Magazine, v. 38, p. 946–956.

Fellows, S. A., and Canil, D., 2012, Experimental study of the partitioning of Cu during partial melting of Earth's mantle: Earth and Planetary Science Letters, v. 337-338, p. 133–143, doi: 10.1016/j.epsl.2012.05.039.

Fisher, A.T., 1998, Permeability within basaltic oceanic crust: Reviews of Geophysics, v. 36, p. 143–182.

Fisher, A.T., and Wheat, C.G., 2007, Seamounts as Conduits for Massive Fluid, Heat, and Solute Fluxes on Ridge Flanks: Oceanography, v. 23, p. 74–87.

Fleet, M.E., 2006, Phase equilibria at high temperatures, Reviews in mineralogy and geochemistry,Mineralogical Society of America, v. 61, p. 365–419.

Fontaine, F.J., and Wilcock, W.S.D., 2007, Two-dimensional numerical models of open-top hydrothermal convection at high Rayleigh and Nusselt numbers: Implications for mid-ocean ridge hydrothermal circulation: Geochemistry, Geophysics, Geosystems, v. 8, doi: 10.1029/2007GC001601.

Foustoukos, D.I., and Seyfried, W.E., 2005, Redox and pH constraints in the subseafloor root zone of the TAG hydrothermal system, 26° N Mid-Atlantic Ridge: Earth and Planetary Science Letters, v. 235, p. 497–510, doi: 10.1016/j.epsl.2005.04.042.

Galley, A.G., Hannington, M.D., and Jonasson, I.R., 2007, Volcanogenic massive sulphide deposits, *in* Goodfellow, W.D. (ed.), Mineral Deposits of Canada: A Synthesis of Major Deposit-Types, District Metallogeny, the Evolution of Geological Provinces, and Exploration Methods: Geological Association of Canada, Mineral Deposits Division, Special Publication No. 5, p. 141-161.

Gillis, K.M., 1995, Controls on hydrothermal alteration in a section of fast-spreading oceanic crust: Earth and Planetary Science Letters, v. 134, p. 473–489.

Gillis, K.M., 2002, The Rootzone of an Ancient Hydrothermal System Exposed in the Troodos Ophiolite, Cyprus: The Journal of Geology, v. 110, p. 57–74.

Gillis, K.M., Coogan, L. A., and Pedersen, R., 2005, Strontium isotope constraints on fluid flow in the upper oceanic crust at the East Pacific Rise: Earth and Planetary Science Letters, v. 232, p. 83–94, doi: 10.1016/j.epsl.2005.01.008.

Gillis, K.., Muehlenbachs, K., Stewart, M., Gleeson, T., and Karson, J.A., 2001, Fluid flow patterns in fast spreading East Pacific Rise crust exposed at Hess Deep: Journal of Geophysical Research, v. 106, p. 26311–26329.

Hall, A.J., 1986, Pyrite-Pyrrhotite redox reactions in nature: Mineralogical Magazine, v. 50, p. 223–229, doi: 10.1180/minmag.1986.050.356.05.

Hannington, M.D., 2013, The role of black smokers in the Cu mass balance of the oceanic crust: Earth and Planetary Science Letters, v. 374, p. 215–226, doi: 10.1016/j.epsl.2013.06.004.

Hannington, M.D., Jamieson, J., Monecke, T., and Petersen, S., 2010, Modern sea-floor massive sulfides and base metal resources: toward an estimate of global sea-floor massive sulfide potential: Society of Economic Geology Special Publication, v. 15. p. 317-338

Hannington, M., Jamieson, J., Monecke, T., Petersen, S., and Beaulieu, S., 2011a, The abundance of seafloor massive sulfide deposits: Geology, v. 39, p. 1155–1158, doi: 10.1130/G32468.1.

Hannington, M.D., Jamieson, J., Monecke, T., Petersen, S., and Beaulieu, S., 2011b, The Abundance of Seafloor Massive Sulfide Deposits- Supplemental Material: GSA Data Repository, www.geosociety .org/pubs/ft2011.htm.

Hart, S.R., and Dnnn, T., 1993, Experimental cpx / melt partitioning of 24 trace elements: Contributions to Mineralogy and Petrology, v. 113, p. 1–8.

Heft, K.L., Gillis, K.M., Pollock, M. A., Karson, J. A., and Klein, E.M., 2008, Role of upwelling hydrothermal fluids in the development of alteration patterns at fast spreading ridges: Evidence from the sheeted dike complex at Pito Deep: Geochemistry Geophysics Geosystems, v. 9, p. Q05O07, doi: 10.1029/2007GC001926.

Hekinian, R., Fevrier, M., Bischoff, J.L., Picot, P., and Shanks, W.C., 1980, Sulfide deposits from the East Pacific Rise near 21 ° N: Science, v. 207, p. 1433–1444.

Hekinian, R., Francheteau, J., Armijo, R., Cogne, J.P., Constantin, M., Girardeau, J., Hey, R., Naar, D.F., and Searle, R., 1996, Petrology of the Easter microplate region in the South Pacific: Journal of Volcanology and Geothermal Research, v. 72, p. 259–289.

Herzig, P.M., and Hannington, M.D., 1995, Polymetallic massive sulfides at the modem seafloor: A review: Ore Geology Reviews, v. 10, p. 95–115.

Hey, R., Baker, E., Bohnenstiehl, D., Massoth, G., Kleinrock, M., Martinez, F., Naar, D., Pardee, D., Lupton, J., Feely, R., Gharib, J., Resing, J., Rodrigo, C., Sansone, F., Walker, S., 2004, Tectonic/volcanic segmentation and controls on hydrothermal venting along Earth's fastest seafloor spreading system, EPR 27°-32°S: Geochemistry, Geophysics, Geosystems, v. 5, doi: 10.1029/2004GC000764.

Hooft, E.E.E., Detrick, R.S., and Kent, G.M., 1997, Seismic structure and indicators of magma budget along the Southern EPR: Journal of Geophysical Research, v. 102, p. 27319–27340.

Humphris, S.E., Alt, J.C., Teagle, D.A.H., and Honnorez, J.J., 1998, Chapter 19. Geochemical changes during hydrothermal alteration of basement in the stockwork beneath the active TAG hydrothermal mound *in* Herzig, P.M., Humphris, S.E., Miller, D.J., and Zierenberg, R.A. (eds.), Proceedings of the Ocan Drilling Program, Scientific Results., v. 158.

Humphris, E., and Cann, J.R., 2000, Constraints on the energy and chemical balances of the modern TAG and ancient Cyprus seafloor sulfide deposits: Journal of Geophysical Research, v. 105, p. 28,477–28,488.

Hutnak, M., and Fisher, A. T., 2007, Influence of sedimentation, local and regional hydrothermal circulation, and thermal rebound on measurements of seafloor heat flux: Journal of Geophysical Research, v. 112, p. B12101, doi: 10.1029/2007JB005022.

Jenner, F.E., and O'Neill, H.S.C., 2012, Analysis of 60 elements in 616 ocean floor basaltic glasses: Geochemistry Geophysics Geosystems, v. 13, p. Q02005, doi: 10.1029/2011GC004009.

Jowitt, S.M., Jenkin, G.R.T., Coogan, L. A., and Naden, J., 2012, Quantifying the release of base metals from source rocks for volcanogenic massive sulfide deposits: Effects of protolith composition and alteration mineralogy: Journal of Geochemical Exploration, v. 118, p. 47–59, doi: 10.1016/j.gexplo.2012.04.005.

Karson, J. A., 2002, Geologic Structure of the Uppermost Oceanic Crust Created At Fast- to Intermediate- Rate Spreading Centers: Annual Review of Earth and Planetary Sciences, v. 30, p. 347–384, doi: 10.1146/annurev.earth.30.091201.141132.

Karson, J.A., 2005, unpublished Pito Deep Cruise Report: Structure & Composition of Super-Fast Spread Crust at Pito Deep : AT11-23 Alvin, Jason II, DSL-120.

Karson, J. A., Francheteau, J., Gee, J.S., Gillis, K.M., Hayman, N.W., Hekinian, R., Hey, R.N., Hurst, S.D., Klein, E.M., Naar, D.F., and Varga, R.J., 2005, Nested-Scale Investigation of Tectonic Windows into Super-Fast Spread Crust Exposed at Pito Deep Rift, Easter Microplate, SE Pacific: InterRidge News, v. 14, p. 5–8.

Kirchner, T.M., and Gillis, K.M., 2012, Mineralogical and strontium isotopic record of hydrothermal processes in the lower ocean crust at and near the East Pacific Rise: Contributions to Mineralogy and Petrology, v. 164, p. 123–141, doi: 10.1007/s00410-012-0729-5.

Leake, Bernard, E., 1997, Nomenclature of Amphiboles : Report of the Subcommittee on Amphiboles of the International Mineralogical Association Commission on New Minerals and Mineral Names: Mineralogical Magazine, v. 61, p. 295–321.

Lee, C.A., 2013, Copper Systematics in Arc Magmas: Science, v. 64, doi: 10.1126/science.1217313.

Lee, C. A, Luffi, P., Chin, E.J., Bouchet, R., Dasgupta, R., Morton, D.M., Le Roux, V., Yin, Q., and Jin, D., 2012, Copper systematics in arc magmas and implications for crust-mantle differentiation.: Science, v. 336, p. 64–8, doi: 10.1126/science.1217313.

Liou, J.G., Kuniyoshi, S., and Ito, K., 1974, Experimental studies of the phase relations between greenschist and amphibolite in a basaltic system: American Journal of Science, v. 274, p. 613–632.

Lowell, R.P., Cappellen, P. V., and Germanovich, L.N., 1993, Silica precipitation in fractures and the evolution of permeability hydrothermal upflow zones: Science, v. 260, p. 192–194.

Lowell, R.P., and Germanovich, L.N., 1995, Dike injection and the formation of megaplumes at ocean ridges.: Science, v. 267, p. 1804–1807, doi: 10.1126/science.267.5205.1804.

Manceau, A., Calas, G., and Decarreau, A., 1985, Nickel-bearing clay minerals: I. Optical spectroscopic study of Nickel crystal chemistry: Clay Minerals, v. 20, p. 367-387.

Manning, C.E., and Bird, D.K., 1986, Hydrothermal clinopyroxenes of the Skaergaard intrusion: Contributions to Mineralogy and Petrology, v. 92, p. 437–447, doi: 10.1007/BF00374426.

Marchig, V., Blum, N., and Roonwal, G., 1997, Massive sulfide chimneys from the East Pacific Rise at 7°24 S and 16°43 S: Marine Georesources & Geotechnology, v. 15, p. 49–66, doi: 10.1080/10641199709379934.

Metz, S., and Trefry, J.H., 2000, Chemical and mineralogical influences on concentrations of trace metals in hydrothermal fluids: Geochimica et Cosmochimica Acta, v. 64, p. 2267–2279.

Morimoto, N., 1989, Nomenclature of pyroxenes: Canadian Mineralogist, v. 27, p. 143–156.

Morton, J.L., and Sleep, N.H., 1985, A mid-ocean ridge thermal model: constraints on the volume of axial hydrothermal heat flux: Journal of Geophysical Research, v. 90, p. 11345–11353, doi: 10.1029/JB090iB13p11345.

Mottl, M.J., 1983, Hydrothermal processes at seafloor spreading centers: Applications of basalt-seawater experimental results., *in* Rona, P.A., Bostrom, K., Laubier, L., Smith, K.L. Jr., (eds.), Hydrothermal Processes at Seafloor Spreading Centers, Plenum, New York, p. 199–224.

Mottl, M.J., and Holland, H.D., 1978, Chemical exchange during hydrothermal alteration of basalt by seawater-I . Experimental results for major and minor components of seawater: Geochimica et Cosmochimica Acta, v. 42., p. 1103-1115

Mottl, M.J., Holland, D., and Corr, F., 1979, Chemical exchange during hydrothermal alteration of basalt by seawater-II. Experimental results for Fe, Mn, and sulfer species: Geochimica et Cosmochimica Acta, v. 43, p. 869-884.

Mottl, M.J., Seewald, J.S., Wheat, C.G., Tivey, M.K., Michael, P.J., Proskurowski, G., McCollom, T.M., Reeves, E., Sharkey, J., You, C.-F., Chan, L. -H., Pichler, T., 2011, Chemistry of hot springs along the Eastern Lau Spreading Center: Geochimica et Cosmochimica Acta, v. 75, p. 1013-1038.

Naar, D.F., and Hey, R.N., 1991, Tectonic evolution of the Easter Microplate: Journal of Geophysical Research, v. 96, p. 7961–7993.

Neo, N., Yamazaki, S., and Miyashita, S., 2009, Data report: bulk rock compositions of samples from the IODP Expedition 309/312 sample pool: ODP Hole 1256D: IODP Proceedings 309/312, doi: 10.2204/iodp.proc.309312.204.2009.

Nielsen, S.G., Rehkämper, M., Teagle, D. A. H., Butterfield, D. A., Alt, J.C., and Halliday, A.N., 2006, Hydrothermal fluid fluxes calculated from the isotopic mass balance of thallium in the ocean crust: Earth and Planetary Science Letters, v. 251, p. 120–133, doi: 10.1016/j.epsl.2006.09.002.

Perk, N.W., Coogan, L. A., Karson, J. A., Klein, E.M., and Hanna, H.D., 2007, Petrology and geochemistry of primitive lower oceanic crust from Pito Deep: implications for the accretion of the lower crust at the Southern East Pacific Rise: Contributions to Mineralogy and Petrology, v. 154, p. 575–590, doi: 10.1007/s00410-007-0210-z.

Pester, N.J., Rough, M., Ding, K., and Seyfried, W.E., 2011, A new Fe/Mn geothermometer for hydrothermal systems: Implications for high-salinity fluids at 13°N on the East Pacific Rise: Geochimica et Cosmochimica Acta, v. 75, p. 7881–7892, doi: 10.1016/j.gca.2011.08.043.

Pollock, M. A., Klein, E.M., Karson, J. A., and Coleman, D.S., 2009, Compositions of dikes and lavas from the Pito Deep Rift: Implications for crustal accretion at superfast spreading centers: Journal of Geophysical Research, v. 114, p. B03207, doi: 10.1029/2007JB005436.

Proenza, J.A., Lewis, J.F., Gali, S., Tauler, E., Labrador, M., Melgarejo, J.C., Longo, F., Bloise, G., 2008, Garnierite Mineralization from Falcondo Ni-Laterite Deposit (Dominican Republic): La Sociedad Espanola de Mineralogia,v. 9, p 197-198.

Puchelt, H., Prichard, H.M., Berner, Z., Maynard, J., 1996, Chapter 5. Sulfide mineralogy sulfur content, and sulfur isotope composition of mafic and ultramafic rocks from Leg 147 *in* Mével, C, Gillis, K.M., Allan, J.F., and Meyer, P.S. (eds.), Proceedings of the Ocean Drilling Program, Scientific Results, v. 147, p. 91-101

Rajamani, V., and Naldrett, A. J., 1978, Partitioning of Fe, Co, Ni, and Cu between sulfide liquid and basaltic melts and the composition of Ni-Cu sulfide deposits: Economic Geology, v. 73, p. 82–93, doi: 10.2113/gsecongeo.73.1.82.

Richardson, C.J., Cann, J.R., Richards, H.G., and Cowan, J.G., 1987, Metal-depleted root zones of the Troodos ore-forming hydrothermal systems, Cyprus: Earth and Planetary Science Letters, v. 84, p. 243–253, doi: 10.1016/0012-821X(87)90089-6.

Robinson, D., Schmidt, S.T., and Santana de Zamora, A., 2002, Reaction pathways and reaction progress for the smectite-to-chlorite transformation: evidence from hydrothermally altered metabasites: Journal of Metamorphic Geology, v. 20, p. 167–175.

Le Roux, V., Dasgupta, R., and Lee, C. A., 2011, Mineralogical heterogeneities in the Earth's mantle: constraints from Mn, Co, Ni and Zn partitioning during partial melting: Earth and Planetary Science Letters, v. 307, p. 395–408, doi: 10.1016/j.epsl.2011.05.014.

Rumble, D., 1976, Oxide Minerals *in* Ribbe P.H., (ed.), Mineral Society of America, Reviews in Mineralogy,Washington, DC., v. 3. pp. 703.

Saccocia, P.J., and Gillis, K.M., 1995, Hydrothermal upflow zones in the oceanic crust: Earth and Planetary Science Letters, v. 136, p. 1–16, doi: 10.1016/0012-821X(95)00155-5.

Schiffman, P., and Fridleifsson, G.O., 1991, The smectite-chlorite transition in drillhole NJ-15, Nesjavellir geothermal field, Iceland: XRD, BSE and electron microprobe investigations: Journal of Metamorphic Geology, v. 9, p. 679–696, doi: 10.1111/j.1525-1314.1991.tb00558.x.

Seewald, J.S., and Seyfried, W.E.J., 1990, The effect of temperature on metal mobility in subseafloor hydrothermal systems constraints from basalt alteration experiments: Earth and Planetary Science Letters, v. 101, p. 388–403.

Seward, T.M., 1981, Metal complex formation in aqueous solutions at elevated temperatures and pressures: Physics and Chemistry of the Earth, v. 13, p. 113–132.

Seyfried, W.E., 1982, Hydrothermal alteration of basalt by seawater under seawater-dominated conditions: Geochimica et Cosmochimica Acta, v. 46, p. 985–1002.

Seyfried, W.E., and Ding, K., 1993, The effect of redox on the relative solubilities of copper and iron in Cl-bearing aqueous fluids at elevated temperatures and pressures: An experimental study with application to subseafloor hydrothermal systems: Geochimica et Cosmochimica Acta, v. 57, p. 1905–1917, doi: 10.1016/0016-7037(93)90083-9.

Sidhu, P.S., 1988, Transformation of trace element-substituted meghemite to hematite: Clays and Clay Minerals, v. 36, p. 31–38.

Sidhu, P.S., Gilkes, R.J., and Posner, A.M., 1980, The Behavior of Co, Ni, Zn, Cu, Mn, and Cr in Magnetite during Alteration to Maghemite and Hematite: Soil Science Society of America Journal, v. 44, p. 135–138.

Sidhu, P.S., Gilkes, R.J., Posner, A.M., and Nutrition, P., 1978, The synthesis and some properties of Co, Ni, Cu, Mn, and Cd substituted magnetites: v. 40, p. 429–435.

Sinton, J.M., and Detrick, R.S., 1992, Mid-ocean ridge magma chambers: Journal of Geophysical Research, v. 97, p. 197, doi: 10.1029/91JB02508.

Stein, C.A., and Stein, S., 1994, Constraints on hydrothermal heat flux through the oceanic lithosphere from global heat flux: Journal of Geophysical Research, v. 99, p. 3081.

Stewart, M. A., Klein, E.M., and Karson, J.A., 2002, Geochemistry of dikes and lavas from the north wall of the Hess Deep Rift: Insights into the four-dimensional character of crustal construction at fast spreading mid-ocean ridges: Journal of Geophysical Research, v. 107, p. 2238, doi: 10.1029/2001JB000545.

Teagle, Damon, A., and Alt, J.C., 2004, Hydrothermal Alteration of Basalts beneath the Bent Hill Massive Sulfide Deposit, Middle Valley, Juan de Fuca Ridge: Economic Geology, v. 99, p. 561–584.

Tivey, M.K., Humphris, E., Hannington, M.D., and Rona, P.A., 1995, Deducing patterns of fluid flow and mixing within the TAG active hydrothermal mound using mineralogical and geochemical data: Journal of Geophysical Research, v. 100.

Tolstoy, M., Waldhauser, F., Bohnenstiehl, D.R., Weekly, R.T., and Kim, W.-Y., 2008, Seismic identification of along-axis hydrothermal flow on the East Pacific Rise.: Nature, v. 451, p. 181–4, doi: 10.1038/nature06424.

Umino, S., Crispini, L., Tartarotti, P., Teagle, D. A. H., Alt, J.C., Miyashita, S., and Banerjee, N.R., 2008, Origin of the sheeted dike complex at superfast spread East Pacific Rise revealed by deep ocean crust drilling at Ocean Drilling Program Hole 1256D: Geochemistry, Geophysics, Geosystems, v. 9, doi: 10.1029/2007GC001760.

Von Damm, K.L., 1990, Seafloor Hydrothermal Activity: Black Smoker: Annual Review of Earth and Planetary Science, v. 18, p. 173–204.

Von Damm, K.L., Edmond, J.M., Grant, B., Measures, C.I., Walden, B., and Weiss, R.F., 1985, Chemistry of submarine hydrothermal solutions at 21° N , East Pacific Rise: Geochimica et Cosmochimica Acta, v. 49, p. 2197–2220.

Von Damm, K.L., Oosting, S.E., Kozlowski, R., Buttermore, L.G., Colodoner, D.C., Edmonds, L.G., Edmond, J.M., and Grebmeier, J.M., 1995, Evolution of East Pacific Rise hydrothermal vent fluids following a volcnic eruption: Nature, v. 375, p. 47–50.

Wells, J.T., and Ghiorso, M.S., 1991, Coupled fluid flow and reaction in mid-ocean ridge hydrothermal systems: The behavior of silica: Geochimica et Cosmochimica Acta, v. 55, p. 2467–2481.

Zierenberg, R.A., Iii, W.C.S., and Bischoff, J.L., 1984, Massive sulfide deposits at 21° N, East Pacific Rise: Chemical composition, stable isotopes, and phase equilibria: Geological Society of America Bulletin, v. 8, p. 922-929 doi: 10.1130/0016-7606(1984)95<922.

Appendix A: Analytical Parameters, Precision and Accuracy of Mineral Analyses

A.1: Electron Microprobe Analyses (EMP)

The parameters used for analyses collected using the University of British Columbia's fully automated CAMECA SX-50 electron microprobe are listed in table A.1. Data reduction was done using the 'PAP' $\phi(\rho Z)$ method (Pouchou & Pichoir, 1985).

For duplication purposes, table A.2 contains the standards, X-Rays lines, and crystals used for the elements considered. All EMP work was completed at the University of British Columbia using the same conditions for each session. All EMP standard information can be found in electronic Appendix A.1.

Table A.1: EMP Mineral Analysis Parameters

Mineral	Excitation Voltage (kV)	Beam Current (nA)	Peak Count Time (s)	Background Count Time (s)	Spot Diameter (μm)	Elements
Clinopyroxene	15	20	20	10	5	SiO_2, TiO_2, Al_2O_3, FeO, MnO, MgO, CaO, K_2O, Na_2O, NiO, Cr_2O_3
Plagioclase	15	20	20	10	5	SiO_2, TiO_2, Al_2O_3, FeO, MnO, MgO, CaO, K_2O, Na_2O
Fe-Ti Oxides	15	20	20	10	5	SiO_2, TiO_2, Al_2O_3, FeO, MnO, MgO, CaO, Cr_2O_3, Nb_2O_5
Chlorite	15	10	20	10	10	SiO_2, TiO_2, Al_2O_3, FeO, MnO, MgO, CaO, K_2O, Na_2O, Cr_2O_3
Amphibole	15	20	20	10	5	SiO_2, TiO_2, Al_2O_3, FeO, MnO, MgO, CaO, K_2O, Na_2O, Cl_2O, F_2O, Cr_2O_3,
Epidote	15	20	20	10	5	SiO_2, TiO_2, Al_2O_3, FeO, MnO, MgO, CaO, K_2O, Na_2O, Cr_2O_3
Sulphides	20	20	20	10	5	S, Mn, Fe, Co, Ni, Cu, Zn, As, Cd, Pb

A.2: Laser Ablation Inductively Coupled Plasma Mass Spectrometry (LA-ICP-MS) Analyses

Due to the variability in quality, thickness, size, and type of mineral analyzed using LA-ICP-MS the parameters differed from point to point. Each laser point, the parameters used, and any additional information can be found in the electronic appendix A.2: Laser Points.

A.2.1: Accuracy and Precision of LA-ICP-MS Data

Accuracy of LA-ICP-MS data was based on the standard deviation of the NIST glass standards (Table A.3). Any reported error was dependent upon the NIST concentration value that was closest to the concentration within the mineral. The % error is shown as error bars on base metal plots throughout this thesis. Electronic Appendix A.2 contains the NIST values and LA-ICP-MS accuracy.

In analytical sessions after February 14, 2013 isotopes of Zn and Cu were analyzed and used to monitor the precision of LA-ICP-MS analyses (figure A.1 and A.2). Over 90% of the analyses lie within 20% deviation from the best-fit line (a 1:1 ratio).

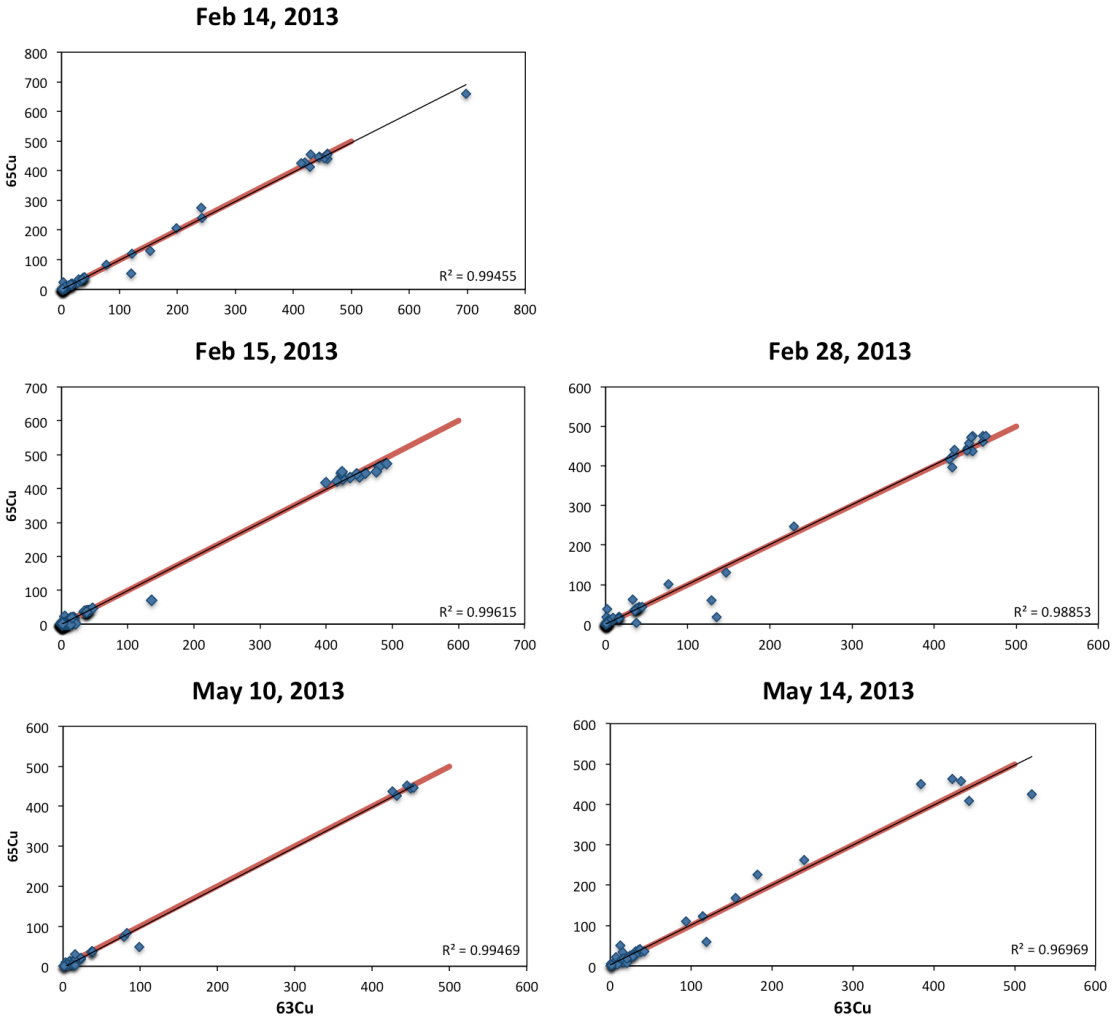
Feb 14, 2013
65Cu
R² = 0.99455
Feb 15, 2013
65Cu
R² = 0.99615
Feb 28, 2013
R² = 0.98853
May 10, 2013
65Cu
R² = 0.99469
63Cu
May 14, 2013
R² = 0.96969
63Cu

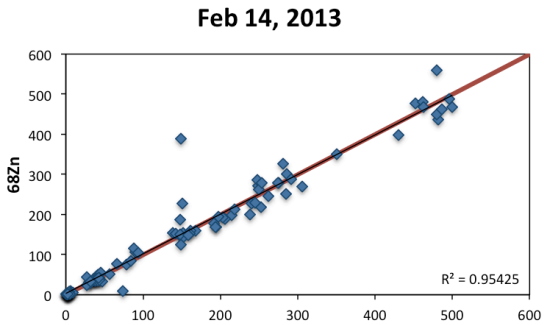
Feb 14, 2013
68Zn
R² = 0.95425

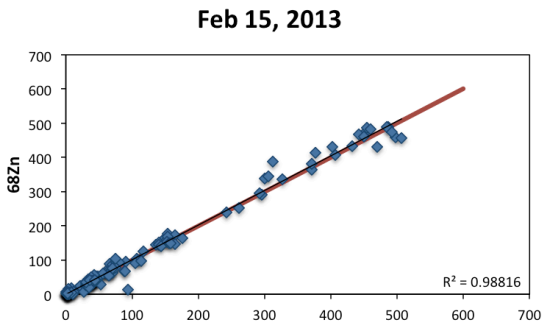
Feb 15, 2013
68Zn
R² = 0.98816

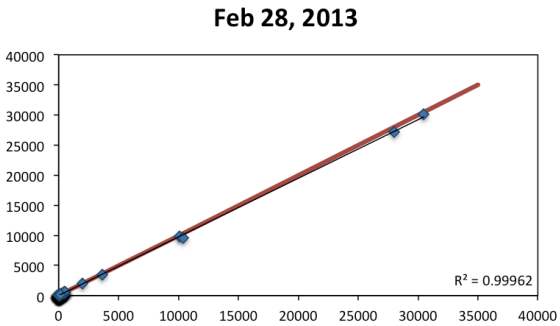
Feb 28, 2013
R² = 0.99962

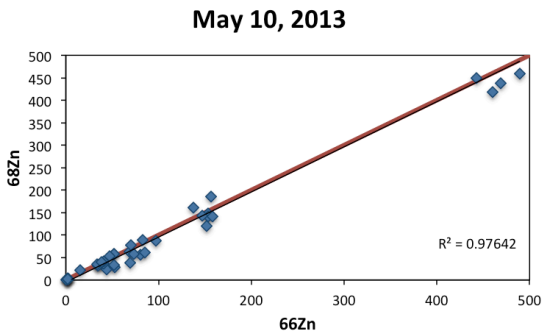
May 10, 2013
68Zn
R² = 0.97642
66Zn

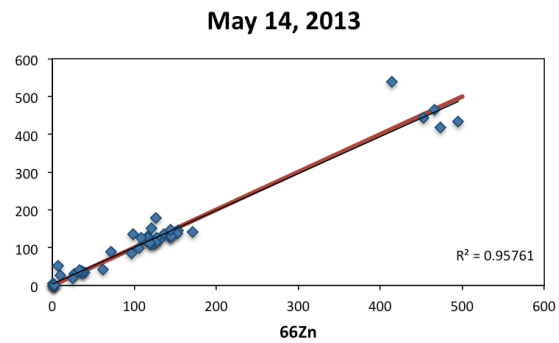
May 14, 2013
R² = 0.95761
66Zn

A.2.2 Comparison of Data from EMP and LA-ICP-MS

Concentrations of Fe, Mn, and Ti were analyzed in clinopyroxene using both EMP and LA-ICP-MS. The results for each technique were plotted against each other to check for data quality (Figure A.3). The maximum discrepancy between the line of best fit and the 1:1 ratio for Mn is ±27%, Fe ±42%, and Ti ±40%. The maximum difference between the regression line and EMP analyses is ±12wt% for Fe, ±0.5wt% for Ti, and ±0.3wt%. The maximum difference between the regression line and LA-ICP-MS analyses is ±60000ppm (6wt%) for Fe, ±1500ppm (0.15wt%) for Ti, and ±1000ppm (0.1wt%) for Mn. Therefore due to the better precision of the LA-ICP-MS data, these were the values used in the results section.

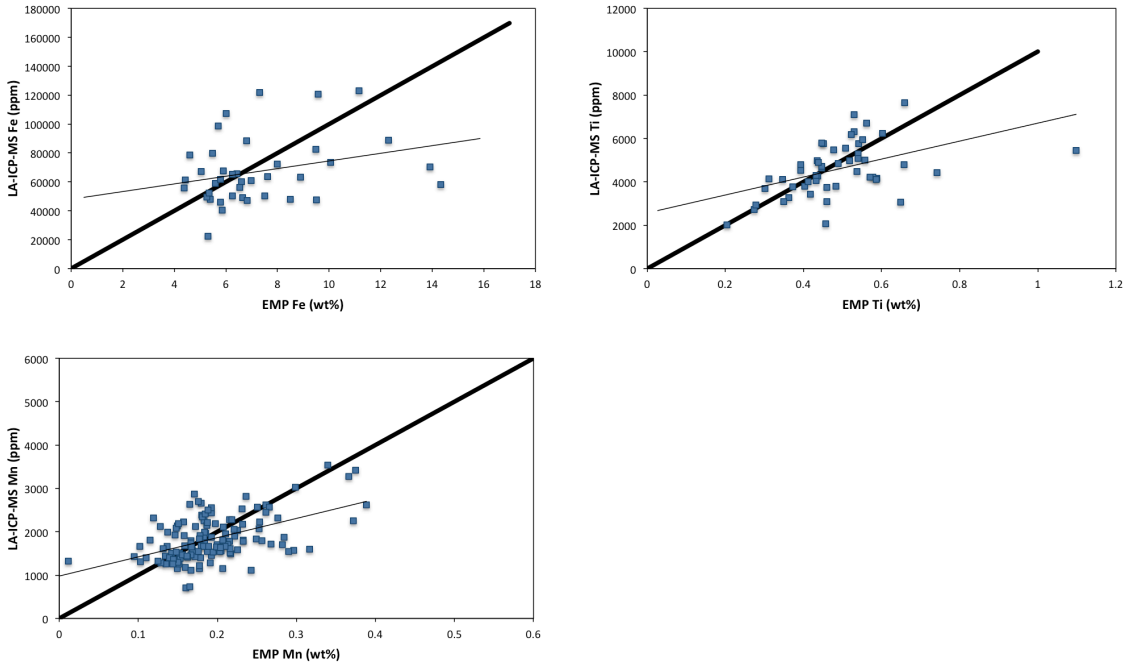

Appendix B.1: Thin Section Descriptions

Submersibles Alvin and Jason II accomplished several dives, with a total of 20 successful dive tracts (table B.1). 20 representative thin sections from the Pito Deep sheeted dike complex were used for detailed analysis of base metal concentrations in the dominant primary and secondary minerals. Description includes thin section number, depth (meters below sea level), dive, lithology, primary and secondary mineral descriptions and any additional notes. Included with descriptions are photomicrographs of each slide, plus any additional images of unique features. Descriptions are ordered in increasing degree of alteration. An additional 3 thin sections of Pito Deep breccias have been analyzed and are included in the following appendix. The same format applies.

An electronic spreadsheet (Appendix B.2) contains a summarized version of the detail found below.

Area	Vehicle	Lowering	Transect/ Dive	Start Date/Time	End Date/Time	Depth Range	# of Samples
A	Jason II	J2-119	1	7Feb05/0954	8Feb05/0146	4021-2958	30
A	Jason II	J2-119	2	8Feb05/0845	8Feb05/2302	4156-2998	28
A	Jason II	J2-119	3a	9Feb05/0632	9Feb05/1650	4163-3319	12
A	Jason II	J2-120	4	10Feb05/0404	10Feb05/1836	3602-3013	29
A	Jason II	J2-120	3b	11Feb05/0240	11Feb05/0938	3353-2871	24
A	Alvin		4075	11Feb05	11Feb05	4116-3558	11
A	Alvin		4076	12Feb05	12Feb05	3633-3056	12
A	Alvin		4077	13Feb05	13Feb05	3590-2894	17
A	Alvin		4078	14Feb05	14Feb05	3560-3207	17
A	Alvin		4079	15Feb05	15Feb05	3442-2944	25
A	Alvin		4080	16Feb05	16Feb05	3610-2850	7
B	Jason II	J2-121	1	17Feb05/1706	18Feb05/1059	4333-2860	24
B	Jason II	J2-121	2	18Feb05/2201	19Feb05/0958	4280-3203	13
B	Jason II	J2-122	3	19Feb05/2206	21Feb05/1110	4074-2616	47
B	Jason II	J2-123	4	22Feb05/0111	22Feb05/1421	4076-2553	18
B	Jason II	J2-123	5	22Feb05/1956	23Feb05/0917	3489-2627	29
B	Alvin		4081	23Feb05	23Feb05	3378-2969	14
B	Alvin		4082	24Feb05	24Feb05	3232-2647	17
B	Alvin		4083	25Feb05	25Feb05	3209-2618	18
B	Alvin		4084	26Feb05	26Feb05	3191-2693	11
B	Alvin		4085	27Feb05	27Feb05	3196-2567	17
B	Alvin		4086	28Feb05	28Feb05	3252-2630	12

Sample Number: 4081-2234
Depth: 2985 mbsl
Dive: 4081, Alvin
Study Area: B
Lithology: dike

Description: Fine grain (<0.4mm), aphyric, (rare plagioclase and clinopyroxene phenocrysts (~1mm)). Interstitial groundmass is heterogeneously dispersed throughout sample, and makes up less than 5% of the sample (based on optical observations). The interstitial groundmass is radiating intergrowths of plagioclase and clinopyroxene.

Degree of alteration: Fresh, 2%

Primary Minerals: Clinopyroxene, plagioclase, and titanomagnetite are the dominant primary minerals. Clinopyroxene is <0.2mm, anhedral, and has a thin film on surface making it appear "dirty". Pyrite is dominant sulphide present as small globulars (<0.04mm) evenly dispersed throughout sample.

Secondary minerals: Chlorite is the dominant secondary mineral replacing groundmass, clinopyroxene, and plagioclase. The chlorite is best observed replacing phenocrysts of plagioclase. Chlorite is heterogeneously dispersed throughout sample, and is <0.2-0.5mm.

Photomicrograph:

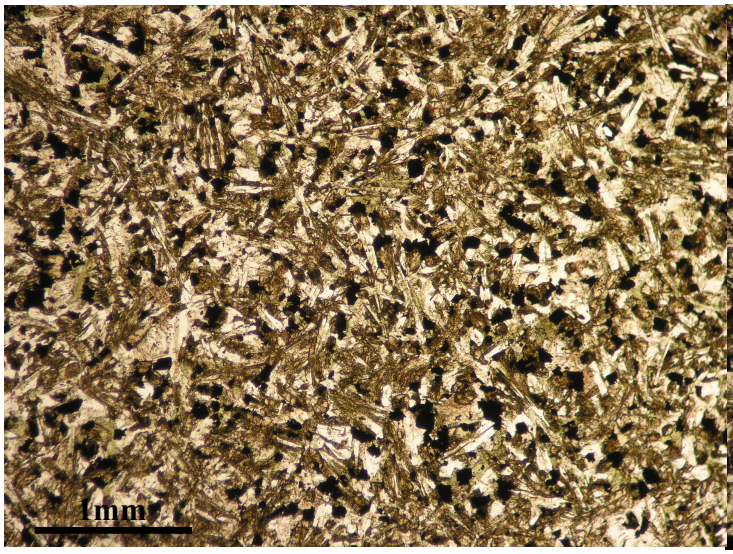

4081-2234 Overall texture

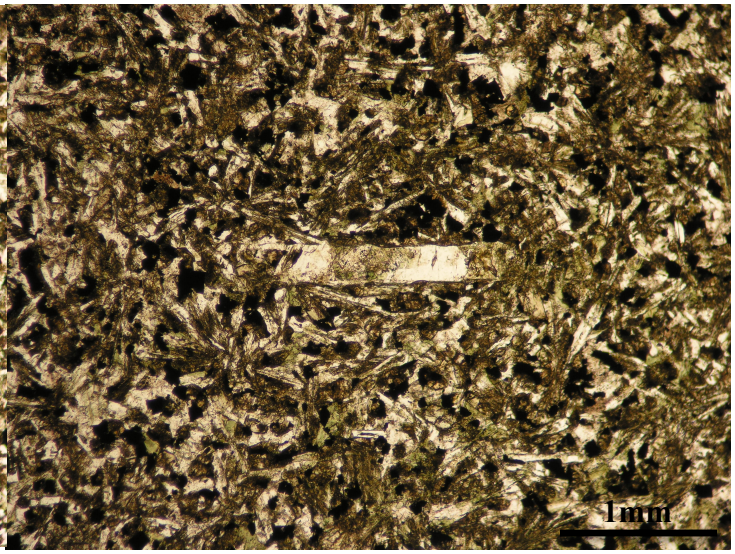

4081-2234: Plagioclase phenocryst with partial replacement by chlorite

Sample Number:4082-1620
Depth: 3121 mbsl
Dive: 4082, Alvin
Study Area: B
Lithology: dike

Description: Generally aphyric (0.25-0.75mm), with 3 large phenocrysts (~2.5mm; 2 fresh plagioclase, one altered plagioclase to chlorite). Alteration occurs in patches and is not evenly distributed in sample. No veins or large voids.

Degree of alteration: 4%

Primary Minerals: Plagioclase, clinopyroxene, and titanomagnetite are primary minerals. All primary minerals are fresh, euhedral, and evenly distributed. Dominant sulphide is pyrite that occurs as interstitial patches heterogeneously distributed.

Secondary minerals: Chlorite and mixed-layer clays are the secondary mineral phase replacing groundmass. It is not evenly distributed and occurs as patches in the sample.

Photomicrograph:

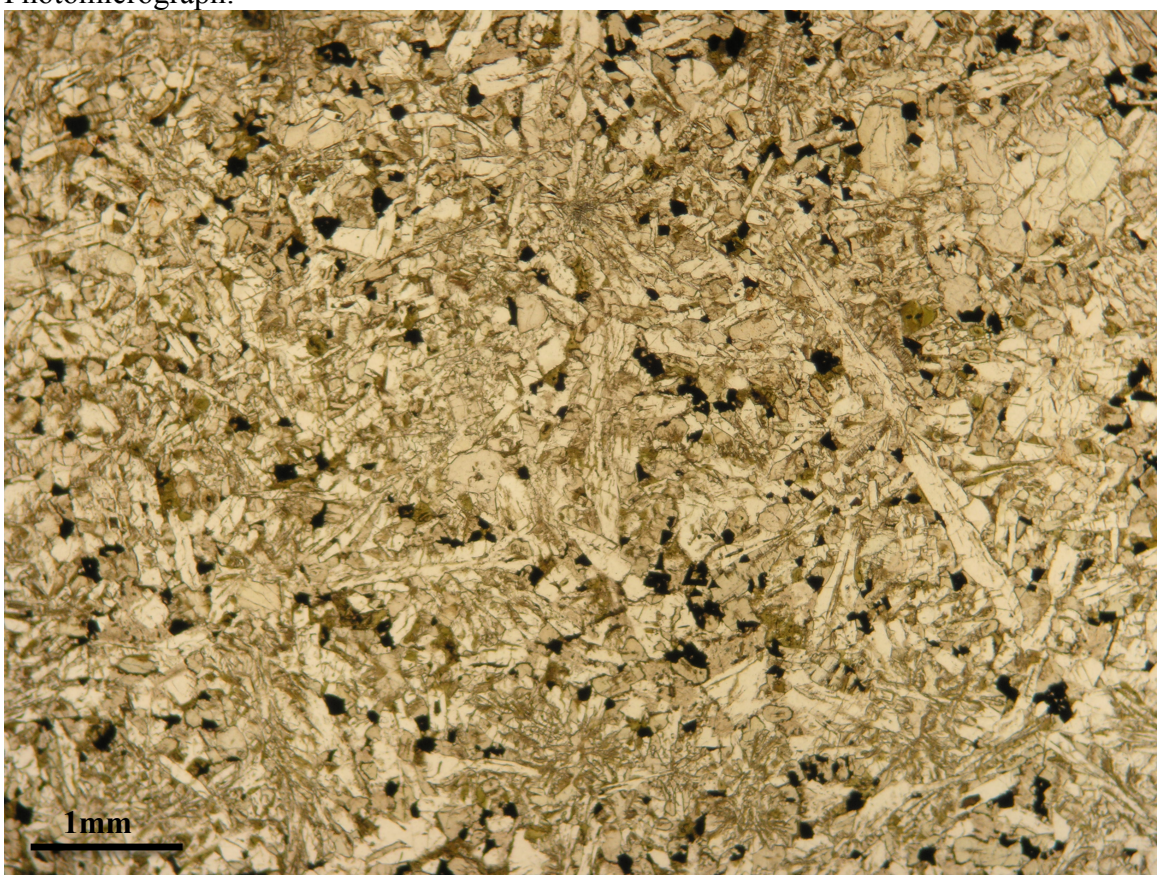

Sample Number:4078-1709
Depth: 3561 mbsl
Dive: 4078, Alvin
Study Area: A
Lithology: dike

Description: Aphyric (0.05-0.1mm) with 3 phenocrysts of plagioclase, and interstitial groundmass throughout sample. Ne veins or voids present.

Degree of alteration: 4%

Primary Minerals: Plagioclase, clinopyroxene, and titianomagnetite are fresh, euhedral, and evenly distributed throughout sample. Pyrite and chalcopyrite are found as interstitial patches within groundmass, pyrite is dominant

Secondary minerals: Minor mixed-layer clays and chlorite replace groundmass, however these are very small areas that have been detected by EMP..

Photomicrograph:

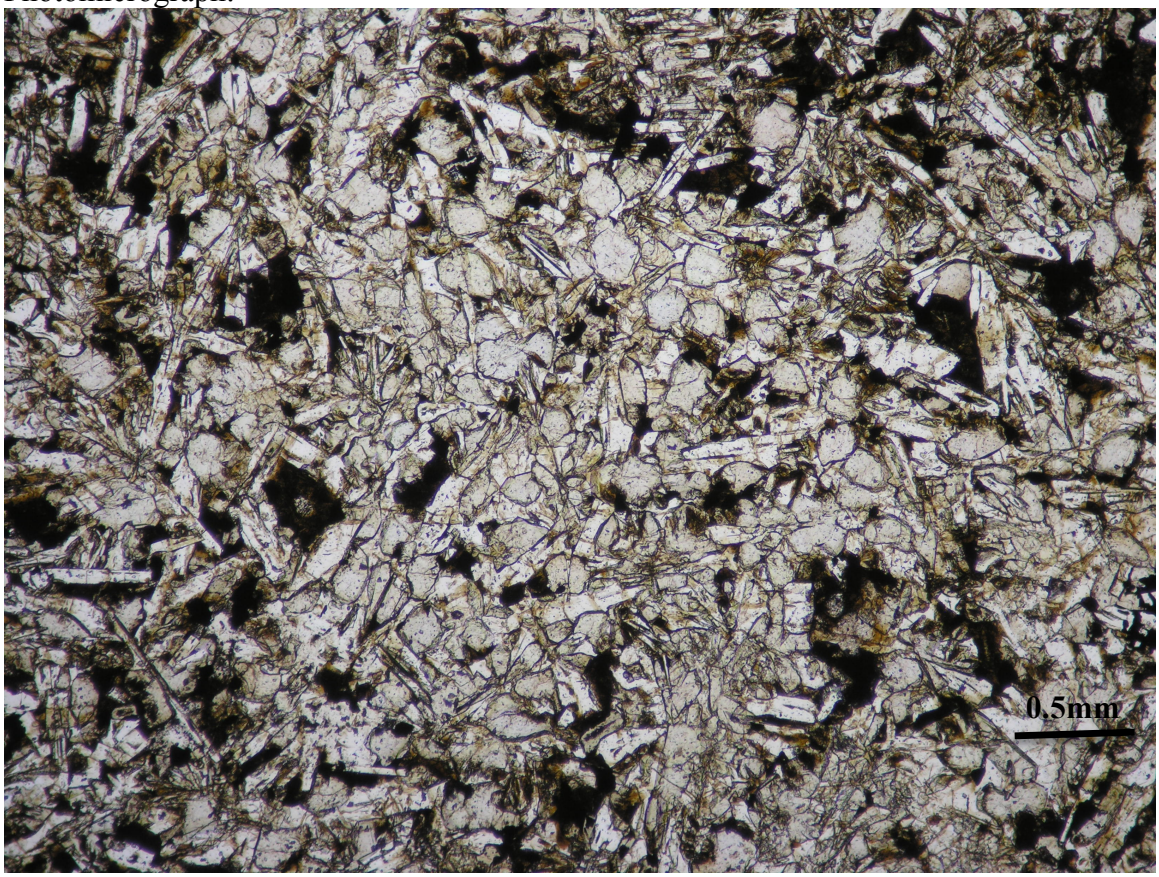

Sample Number:022205-0320
Depth: 3897 mbsl
Dive: J2-134-4, Jason
Study Area: B
Lithology: dike

Description: Plagioclase-phyric (phenocrysts: 1-1.5mm, background 0.25-0.75mm), patches (~05mm) of radiating lathes of plagioclase and groundmass are rare but distributed throughout sample. In-filled vesicles (2-3mm) contain quartz and chlorite. No veins present.

Degree of alteration: 5%

Primary Minerals: Plagioclase, clinopyroxene, and titanomagnetite are essentially unaltered, only a few clinopyroxene grains have been altered. Dominant sulphide is pyrite that has blocky habit and a rim of oxidization.

Secondary minerals: Chlorite is the secondary mineral phase. The majority of chlorite however is found as void-filling and has not replaced a primary phase.

Photomicrograph:

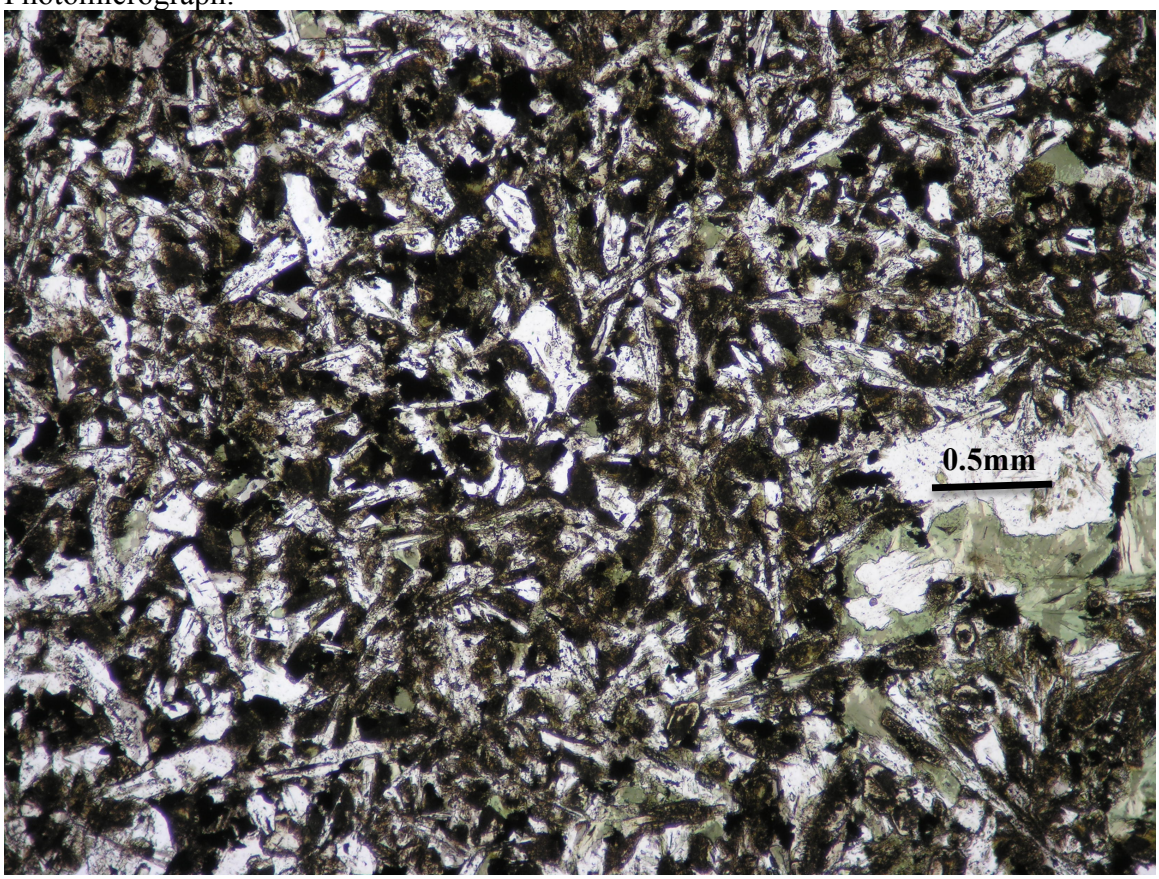

Sample Number: 4083-1829
Depth: 2937 mbsl
Dive: 4083, Alvin
Study Area: B
Lithology: dike

Description: Medium grain (0.5-1mm), equigranular, one vesicle present and is in-filled with quartz and minor chlorite. No veins are present.

Degree of alteration: 6%

Primary Minerals: Plagioclase, clinopyroxene, and titanomagnetite are the primary mineral phases. Titanomagnetite is fresh and has a skeletal habit. Very fine grain pyrite (<0/01mm, no chalcopyrite optically observed).

Secondary minerals: Chlorite and mixed layer clays replace clinopyroxene, plagioclase, and groundmass. It does not always replace these minerals completely but appears as partial alteration, especially in plagioclase.

Photomicrograph:

Sample Number: 020905-1404
Depth: 3676 mbsl
Dive: J2-119-3, Jason
Study Area: A
Lithology: dike

Description: Aphyric (<0.1mm), equigranular, no veins or voids present.

Degree of alteration: 5%

Primary Minerals: Plagioclase, clinopyroxene, and titanomagnetite are dominant primary minerals. Plagioclase and titanomagnetite are euhderal and have a blocky habit. Clinopyroxene has been partially altered and is subhedral to anhedral. Dominant sulphide is pyrite, with minor chalcopyrite, and is present in globulars evenly distribute throughout sample.

Secondary minerals: Chlorite and mixed-layer clays have partially replaced a lot of the clinopyroxene (~50% of the clinopyroxene).

Photomicrograph:

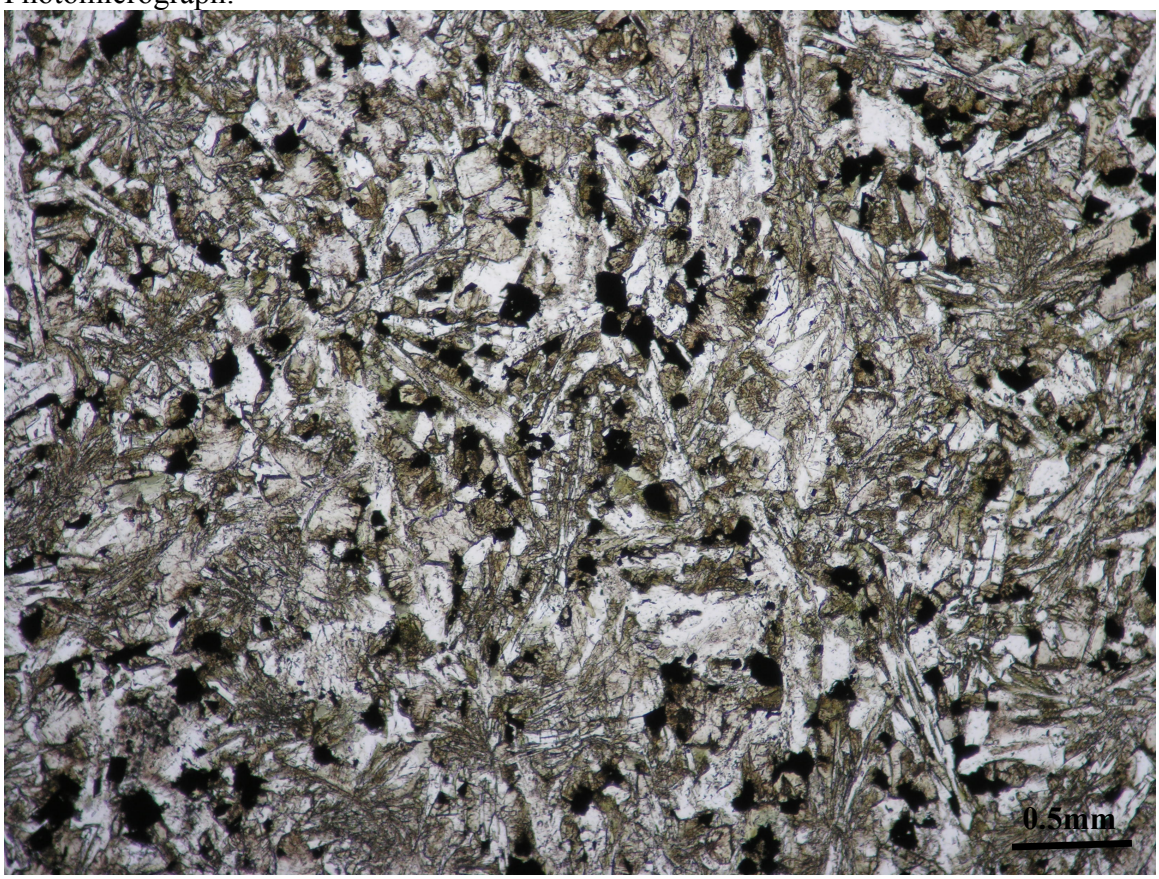

Sample Number: 020705-2131
Depth: 3523 mbsl
Dive: J2-119-1, Jason
Study Area: A
Lithology: dike

Description: Minor alteration, aphryic (~0.5mm). One small vein present (0.05mm in diameter) containing mostly quartz and a few Fe-Ti oxides. An unknown residue is present on the minerals adjacent to the vein, but the modal abundance of secondary phases does not increase close to the vein.

Degree of alteration: 6%

Primary Minerals: Plagioclase, clinopyroxene, and titanomagnetite are the dominant primary minerals. Plagioclase and titanomagnetite are fresh, euhedral and blocky in habit. Clinopyroxene has been altered (~5%) to chlorite. Little to no groundmass present.

Secondary minerals: Chlorite is the secondary mineral present in this sample, replacing clinopyroxene. Chlorite is distributed evenly throughout sample.

Photomicrograph:

Sample Number: 4081-2124
Depth: 3083 mbsl
Dive: 4081, Alvin
Study Area: B
Lithology: dike

Description: Equigranular, aphyric (~0.5mm), no veins or voids present.

Degree of alteration: 6%

Primary Minerals: Plagioclase, titanomagnetite, and clinopyroxene are the dominant primary minerals. All remain relatively fresh, while groundmass and <5% clinopyroxene have been altered to chlorite.

Secondary minerals: Chlorite is the dominant secondary mineral present replacing groundmass and to a lesser extent clinopyroxene. Plagioclase has minor alteration, however only partial replacement has occurred.

Photomicrograph:

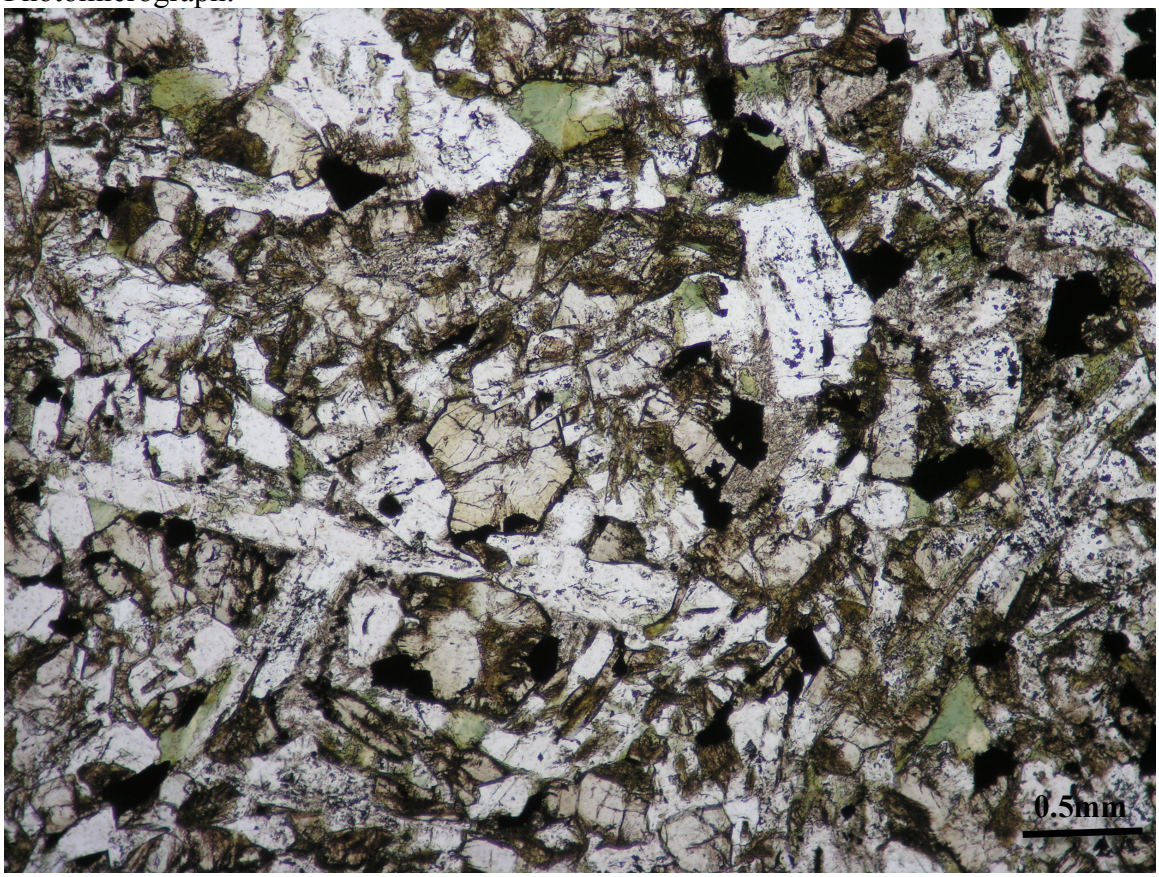

Sample Number: 4076-1725
Depth: 3580 mbsl
Dive: 4076, Alvin
Study Area: A
Lithology: dike

Description: Plagioclase ranges from 0.2-0.8mm in size, and remains euhedral. Clinopyroxene and titanomagnetite are <0.5mm and are euhdral-subhedral.

Degree of alteration: 8%

Primary Minerals: Plagioclase, clinopyroxene, and titanomagnetite are the primary phases present. Plagioclase and clinopyroxene remain fresh (however clinopyroxene appears as though it has been altered).

Secondary minerals: Mixed-layer clays are the dominant alteration phase replacing groundmass. A residue is present on the surface of the clinopyroxene, but LA-ICP-MS and EMP analyses indicate that it is not an alteration.

Photomicrograph:

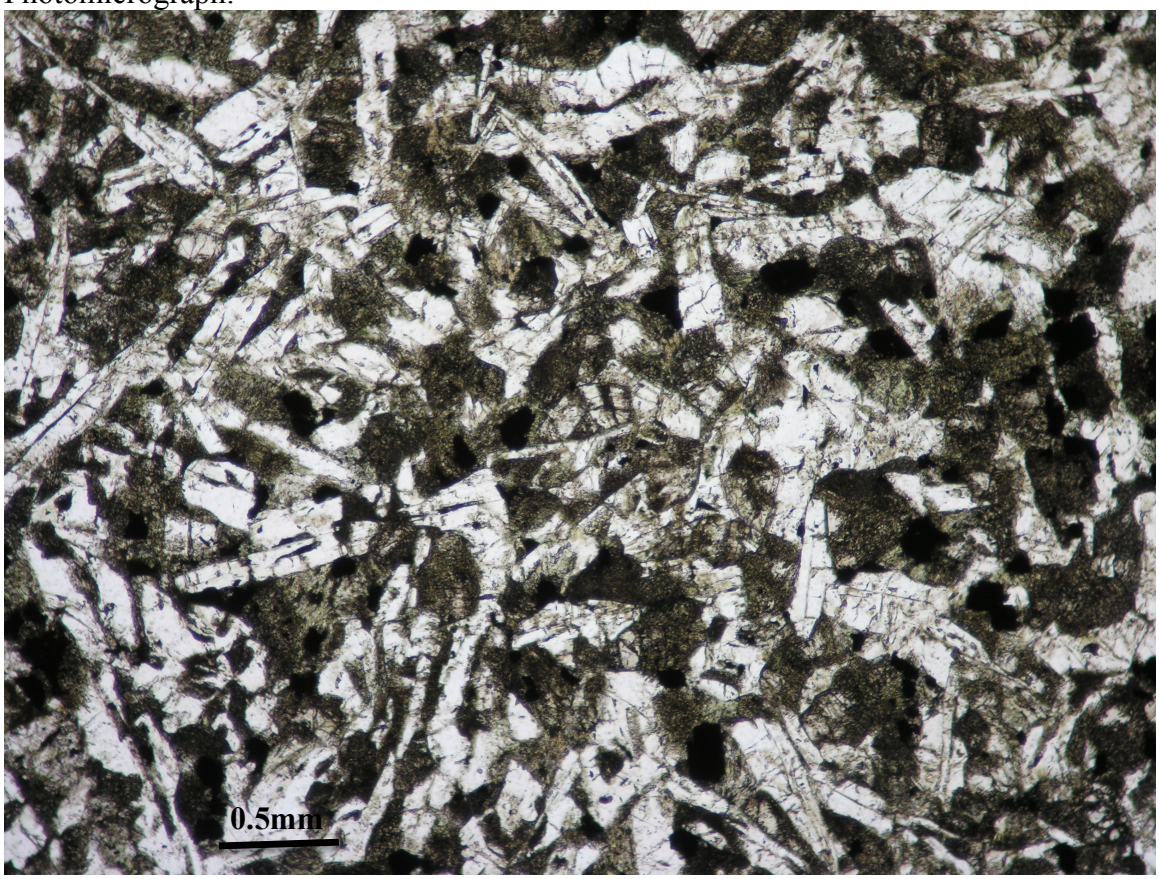

Sample Number: 4086-1711
Depth: 3095 mbsl
Dive: 4086, Alvin
Study Area: B
Lithology: dike

Description: Equigranular, 0.3-0.5mm, no veins or voids present. Little to no fresh groundmass present.

Degree of alteration: 9%

Primary Minerals: Plagioclase, clinopyroxene, and titanomagnetite are dominant primary phases. Plagioclase and titanomagnetite are fresh, will clinopyroxene has minor alteration (<7%).

Secondary minerals: Chlorite is the dominant alteration phase replacing clinopyroxene and groundmass.

Photomicrograph:

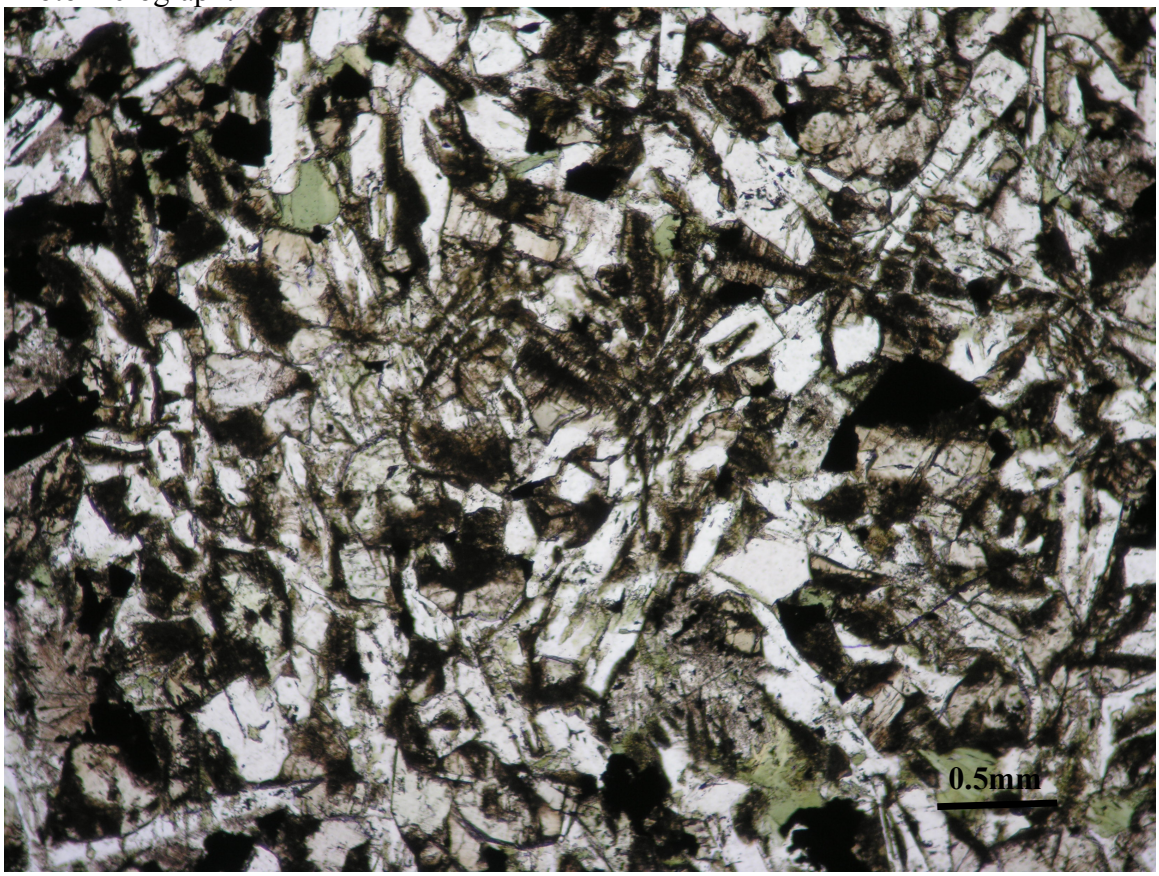

Sample Number: 022305-0509
Depth: 2979 mbsl
Dive: J2-123-5, Jason
Study Area: B
Lithology: dike
NOTE: Previous work (Heft et al., 2008) divided this sample into Area A and Area B, this study focused on an area equivalent to Area B.

Description: Fine grain (<0.1-0.5mm), inequigranular, no voids or veins present. Patches of radiating plagioclase lathes make up the majority of the groundmass present in this sample.

Degree of alteration: 10%

Primary Minerals: Plagioclase, clinopyroxene, and titanomagnetite (minor ilmenite) are present as the primary mineral phases. Plagioclase remains fresh.

Secondary minerals: Chlorite replaces clinopryoxene, and to a lesser extent groundmass.

Photomicrograph:

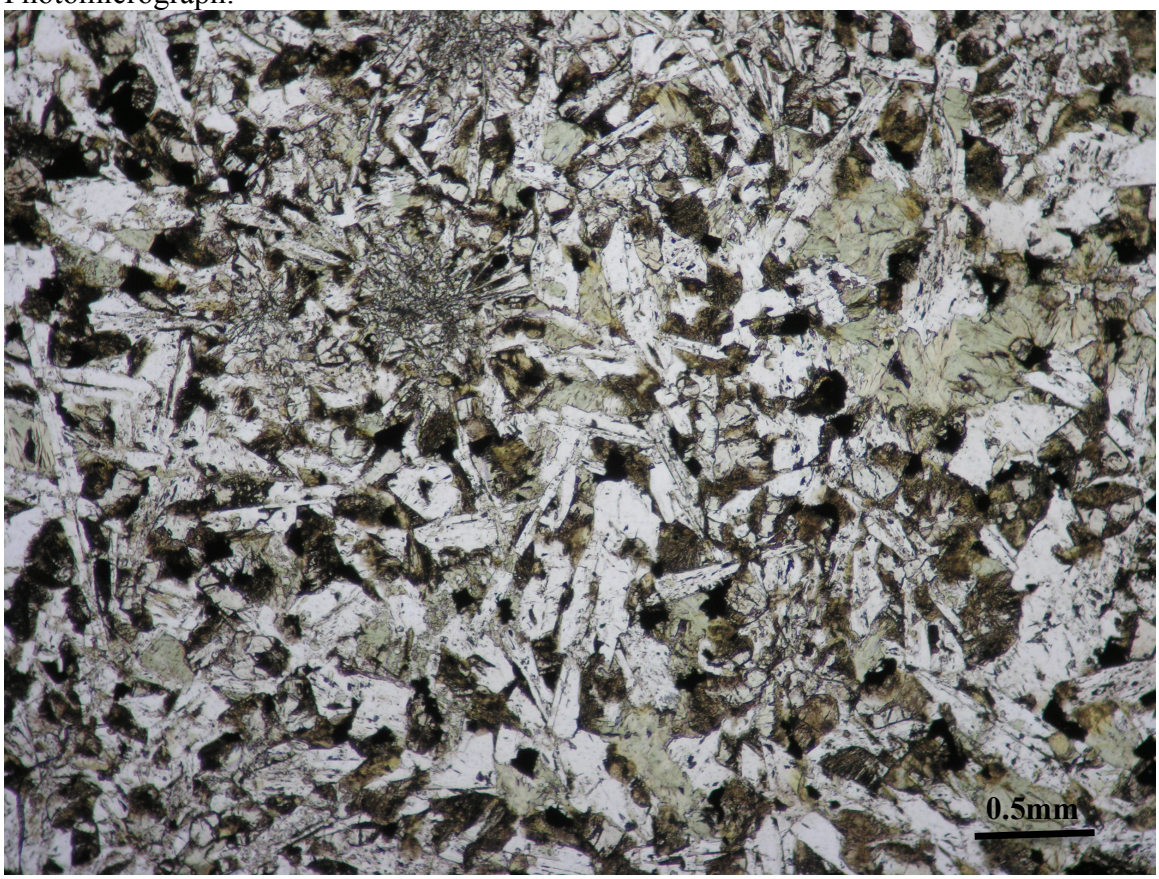

Sample Number: 4076-1629
Depth: 3625 mbsl
Dive: 4076, Alvin
Study Area: A
Lithology: dike

Description: Fine grain (0.1-05 mm), inequigranular, little to no fresh groundmass present. The thin section has a large crack down the center, but is not a vein in the sample.

Degree of alteration: 15%

Primary Minerals: Plagioclase, clinopyroxene, and titanomagnetite make up the primary phases. All have remained relatively fresh.

Secondary minerals: Chlorite makes up the secondary phase in the rock replacing groundmass, and to a lesser extent clinopyroxene.

Photomicrograph:

Sample Number: 020805-1327
Depth: 3578 mbsl
Dive: J2-119-2, Jason
Study Area: A
Lithology: dike

Description: Fine grain (<0.5mm), in equigranular. Patches of fresh plagioclase lathes in microcrystalline groundmass found in sample, however large portions of groundmass have been altered.

Degree of alteration: 17%

Primary Minerals: Plagioclase, clinopyroxene and titanomagnetite are the primary phases present. Plagioclase and clinopyroxene remain fresh (minor clinopyroxene has been altered).

Secondary minerals: Mixed-layer clays dominantly replace groundmass, with trace replacement of clinopyroxene (<1%).

Photomicrograph:

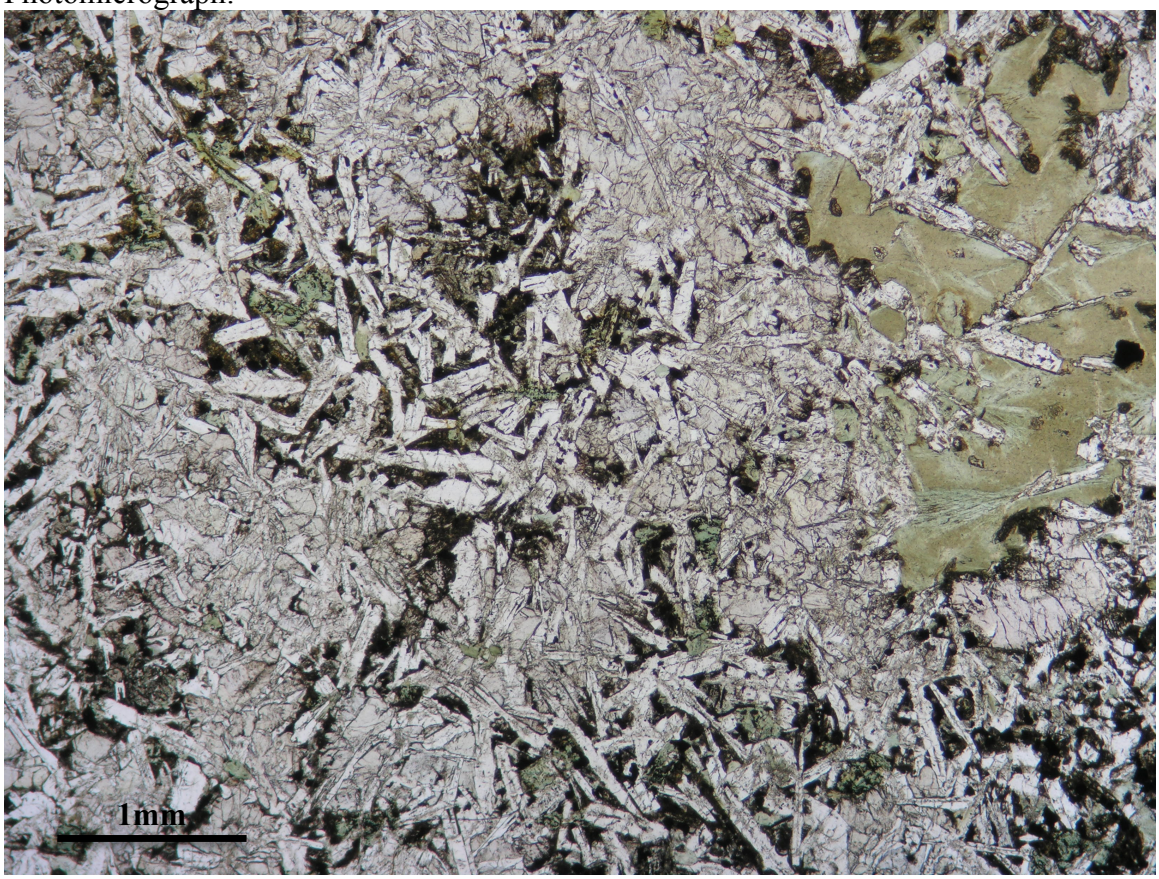

Sample Number: 4082-2008
Depth: 2942 mbsl
Dive: 4082, Alvin
Study Area: B
Lithology: dike

Description: Equigranular, grain size ranging from 0.4-0.7 mm, no voids or veins present in sample. Clinopyroxene has a dark brown residue on the surface, however this is not an alteration product.

Degree of alteration: 18%

Primary Minerals: Clinopyroxene, plagioclase, and titanomagnetite are the primary phases present. Groundmass is present in small patches.

Secondary minerals: Chlorite is the dominant alteration phase replacing clinopyroxene and groundmass. Plagioclase has remained relatively fresh (only trace alteration <1%).

Photomicrograph:

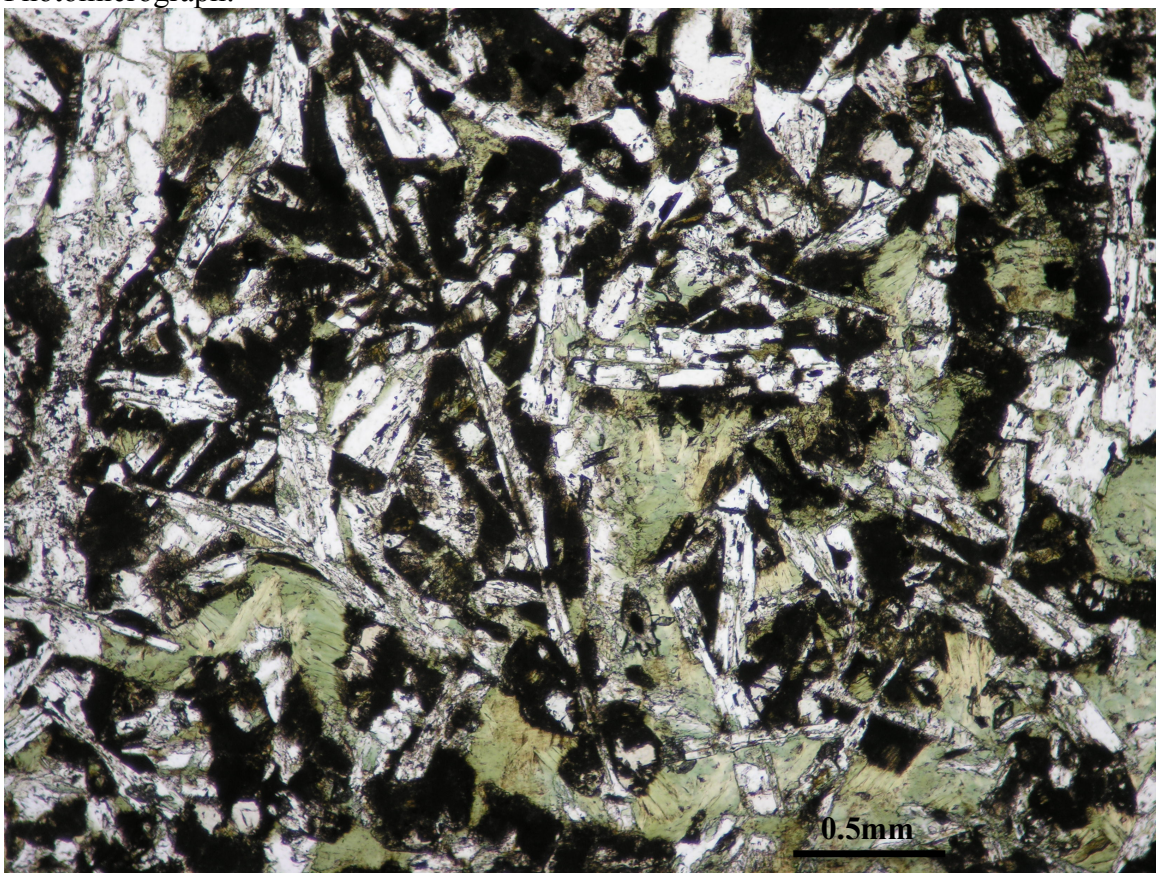

Sample Number: 4076-1654
Depth: 3622 mbsl
Dive: 4076, Alvin
Study Area: A
Lithology: dike

Description: Fine grain (<0.05-0.5 mm), inequigranular, not veins or voids present. Patches of very fine grain (<0.05 mm) if plagioclase laths found in groundmass are common.

Degree of alteration: 20%

Primary Minerals: Plagioclase, clinopyroxene, and titanomagnetite are the primary phases present.

Secondary minerals: Mixed-layer clays are dominant, only minor chlorite present. Mixed-layer clays have replaced groundmass and clinopyroxene to an equal extent, and only trace plagioclase has been altered. Chlorite only appears to replace clinopyroxene. Fe-Ti oxides appear fresh.

Photomicrograph:

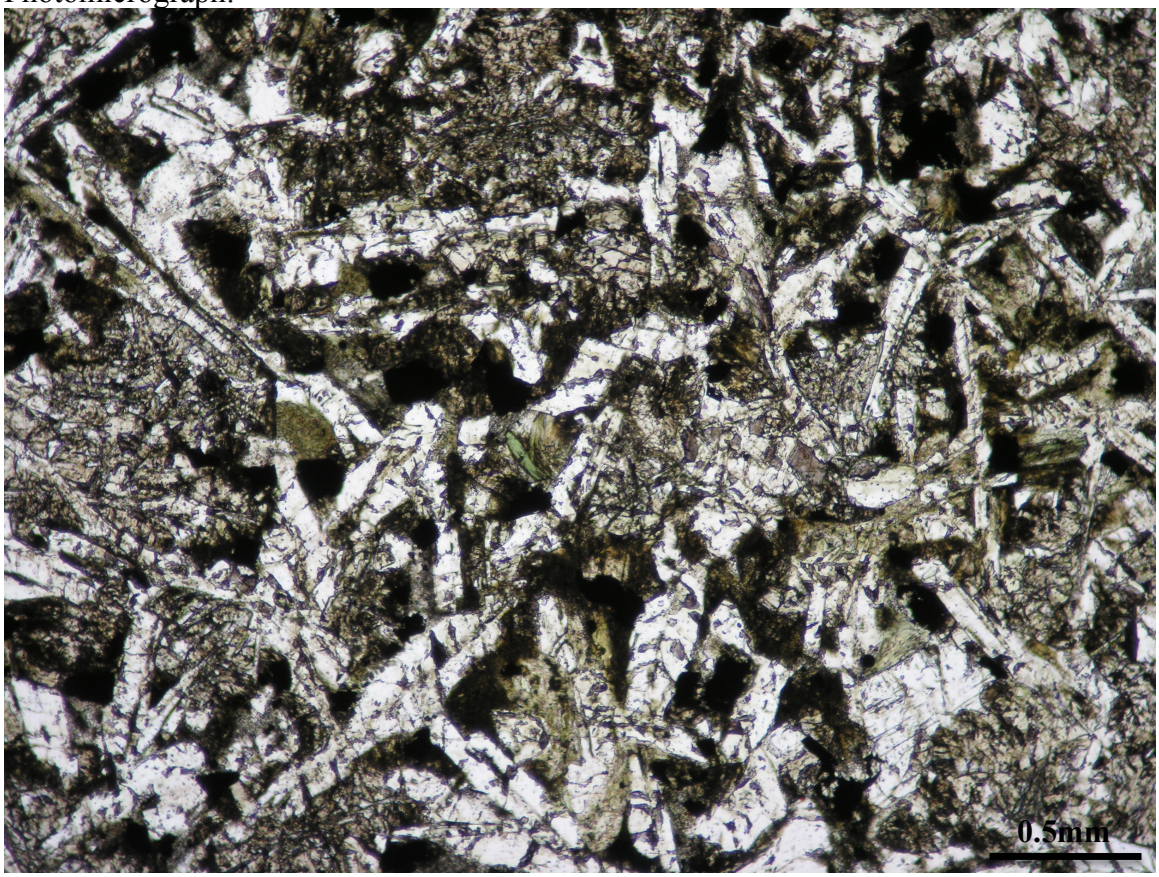

Sample Number: 020705-2225
Depth: 3425 mbsl
Dive: J2-119-1, Jason
Study Area: A
Lithology: dike

Description: Moderately and variably altered with areas of the sample more altered than others. Sample is inequigranular with patches of altered groundmass. No veins or voids are present.

Degree of alteration: 21%

Primary Minerals: Plagioclase, clinopyroxene, and Fe-Ti oxides make up the dominant mineral phases. Plagioclase is euhedral, ranging in length from 0.5 mm almost up to 1 mm. Clinopyroxene is anhedral and fine grain (0.1-0.3 mm). Fe-Ti oxides are blocky and fine grain (<0.2 mm).

Secondary minerals: Mixed-layer clay and chlorite dominantly replace groundmass and to a lesser extent clinopyroxene. Rims of oxidation are observed around some of the Fe-Ti oxides.

Photomicrograph:

Sample Number: 020705-1423
Depth: 3614 mbsl
Dive: J2-119-1, Jason
Study Area: A
Lithology: dike

Description: Aphyric, 0.1-0.5mm grain size, masses of secondary minerals (including titanomagnetite) are unevenly dispersed throughout sample. No veins or voids present.

Degree of alteration: 21%

Primary Minerals: Plagioclase, clinopyroxene, and titanomagnetite are the dominant primary minerals. Plagioclase and clinopyroxene remain relatively fresh in the sample, however clinopyroxene has a oxidation residue making it appear somewhat altered. Titanomagnetite forms as blocky and skeletal habit, primary oxides are 0.2mm, secondary oxides found in masses of secondary alteration are <0.05mm. Sulphides are unevenly distributed, and range from <0.05mm up to 0.1mm.

Secondary minerals: Chlorite and minor mixed-layer clays are the secondary phases present, dominantly replacing groundmass.

Photomicrograph:

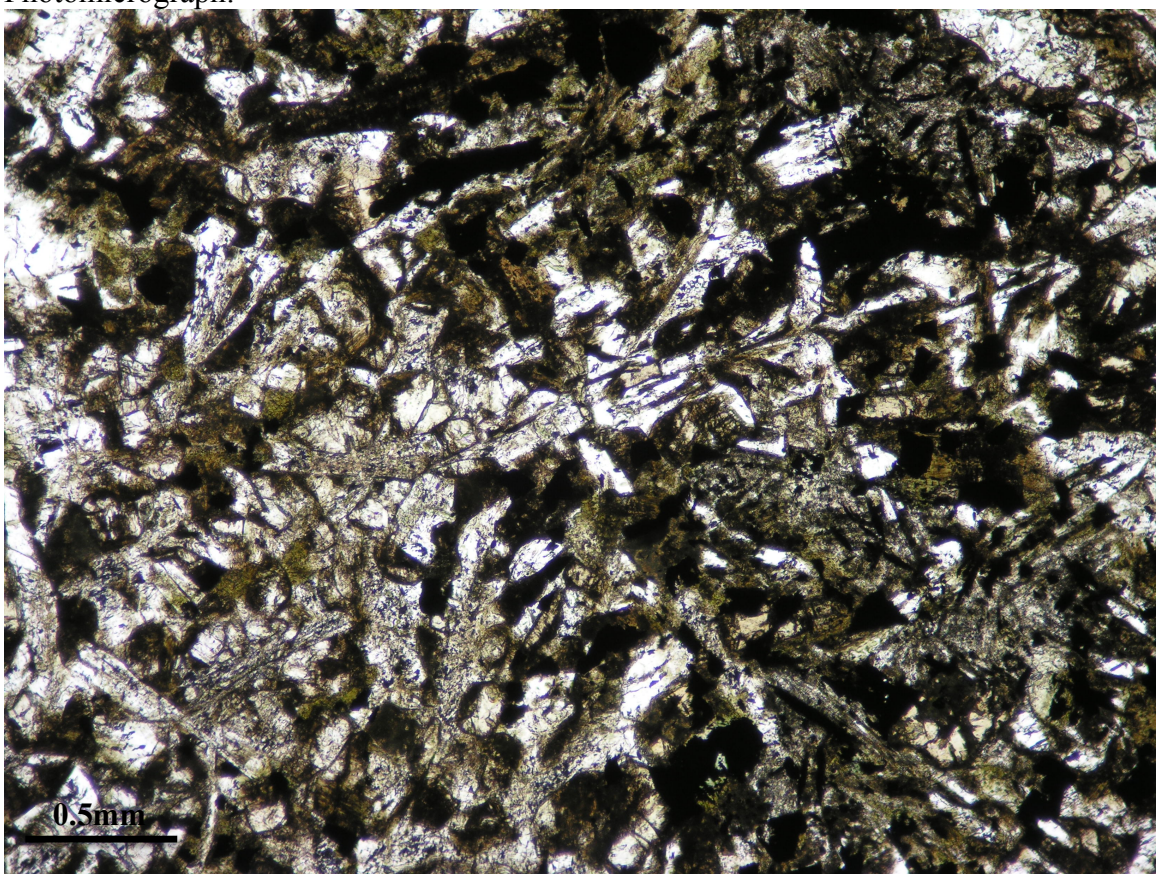

Sample Number: 4075-1832
Depth: 3899 mbsl
Dive: 4075, Alvin
Study Area: A
Lithology: dike

Description: Inequigranular, fine grain (0.2-0.5mm), heavily altered, with veins of amphibole present. Veins range from 0.1-0.4mm in width.

Degree of alteration: 40%

Primary Minerals: Plagioclase has remained relatively fresh in this sample, with only minor partial alteration. Primary clinopyroxene is almost completely replaced. Fe-Ti oxides and sulphides are cubic in habit and range from <0.1-0.3mm in size.

Secondary minerals: Amphibole is the dominant secondary phase replacing clinopyroxene. Very minor chlorite is present which is observed to be partially replacing plagioclase. Secondary chalcopyrite is present. Alteration is evenly distributed throughout sample, with almost completely replacement of clinopyroxene.

Photomicrograph:

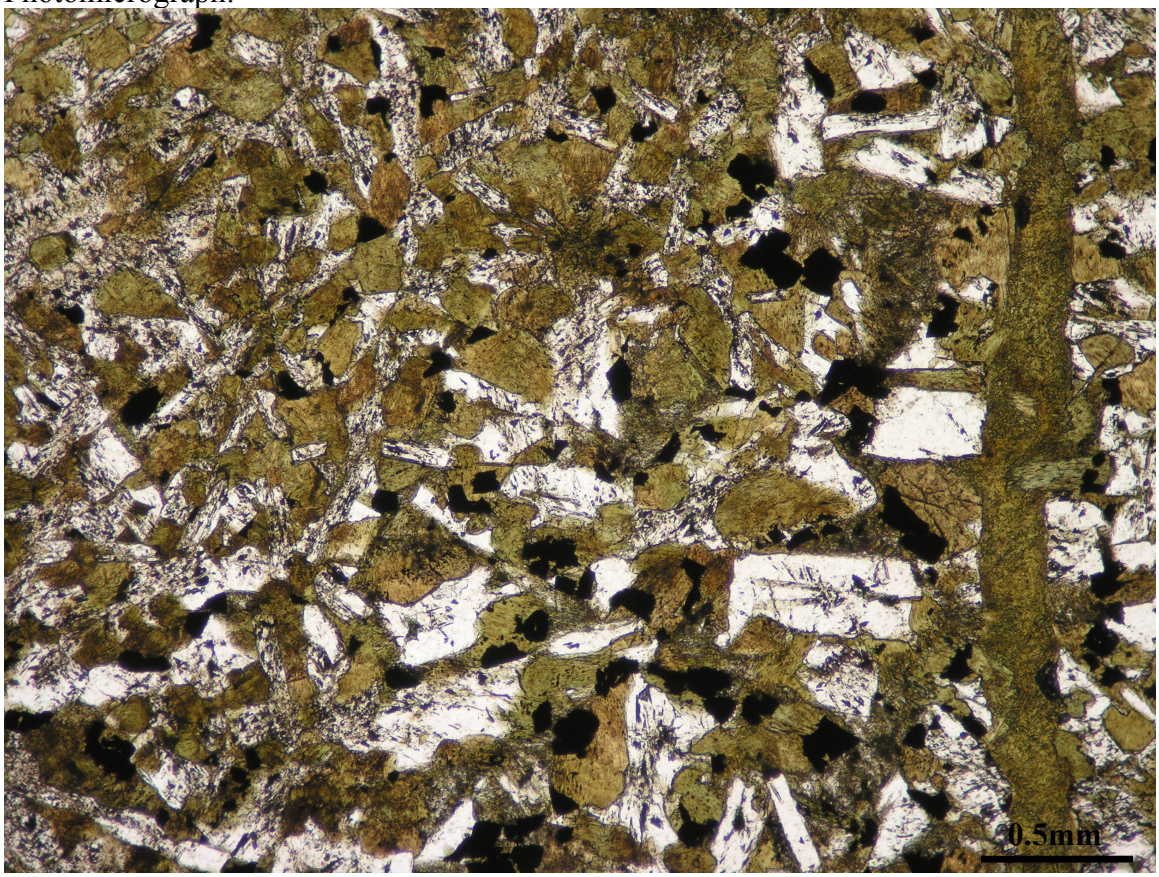

Sample Number: 021905-0409
Depth: 3518 mbsl
Dive: J2-121-2, Jason
Study Area: B
Lithology: dike

Description: Inequigranular, fine grain (<0.1-0.7mm), and heterogeneous sample. Some areas are heavily to completely altered and other areas are only partially altered. No voids or veins present in sample

Degree of alteration: 53%

Primary Minerals: Plagioclase has remained relatively fresh and euhedral-subhedral, compared to clinopyroxene which has been almost completely alteres (>95% of clinopyroxene has been replaced). Fe-Ti oxides and pyrite are both present throughout sample, ranging from 0.05-0.3mm.

Secondary minerals: Amphibole is the dominant secondary mineral phase present, completely replacing clinopyroxene. Some chlorite is present only partially replacing plagioclase (<5% of plagioclase have been partially altered).

Photomicrograph:

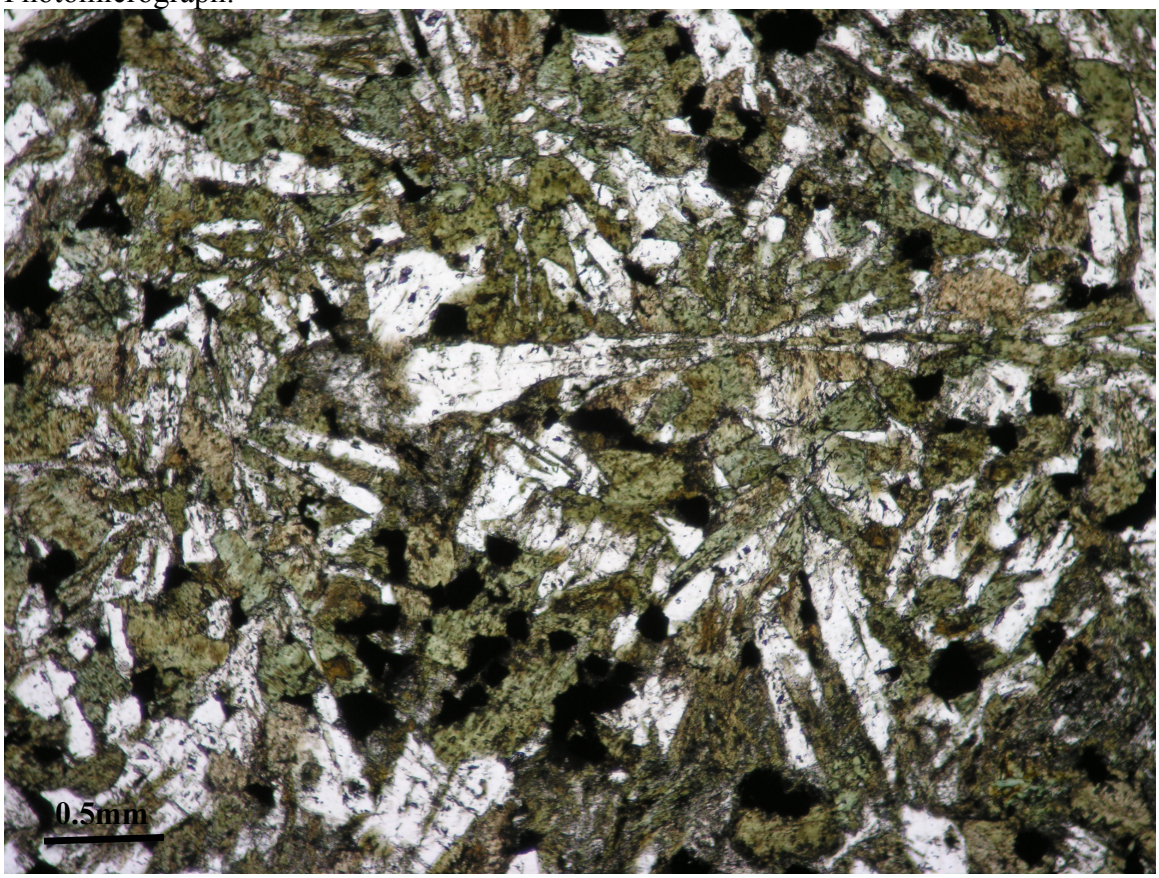

Sample Number: 020705-1106
Depth: 3976 mbsl
Dive: J2-119-1, Jason
Study Area: A
Lithology: dike

Description: Highly altered. Generally aphyric, however some areas contain coarse grain plagioclase phenocrysts (up to 2mm). No veins are present.

Degree of alteration: 62%

Primary Minerals: Plagioclase is dominant primary mineral. It is unaltered, subhedral-euhedral, patches of radiating lathes of plagioclase are present. All clinopyroxene has been altered to a certain extent; most of it (>90%) has been completely replaced. Sulphides are small grains (<0.05mm), dominantly pyrite.

Secondary minerals: Amphibole and chlorite are both present in this sample, amphibole being more dominant. Amphibole replaces clinopyroxene and groundmass. Alteration is unevenly dispersed throughout sample, appearing as blotches of alteration.

Photomicrograph: General textures in 020705-1106, 2x optical zoom.

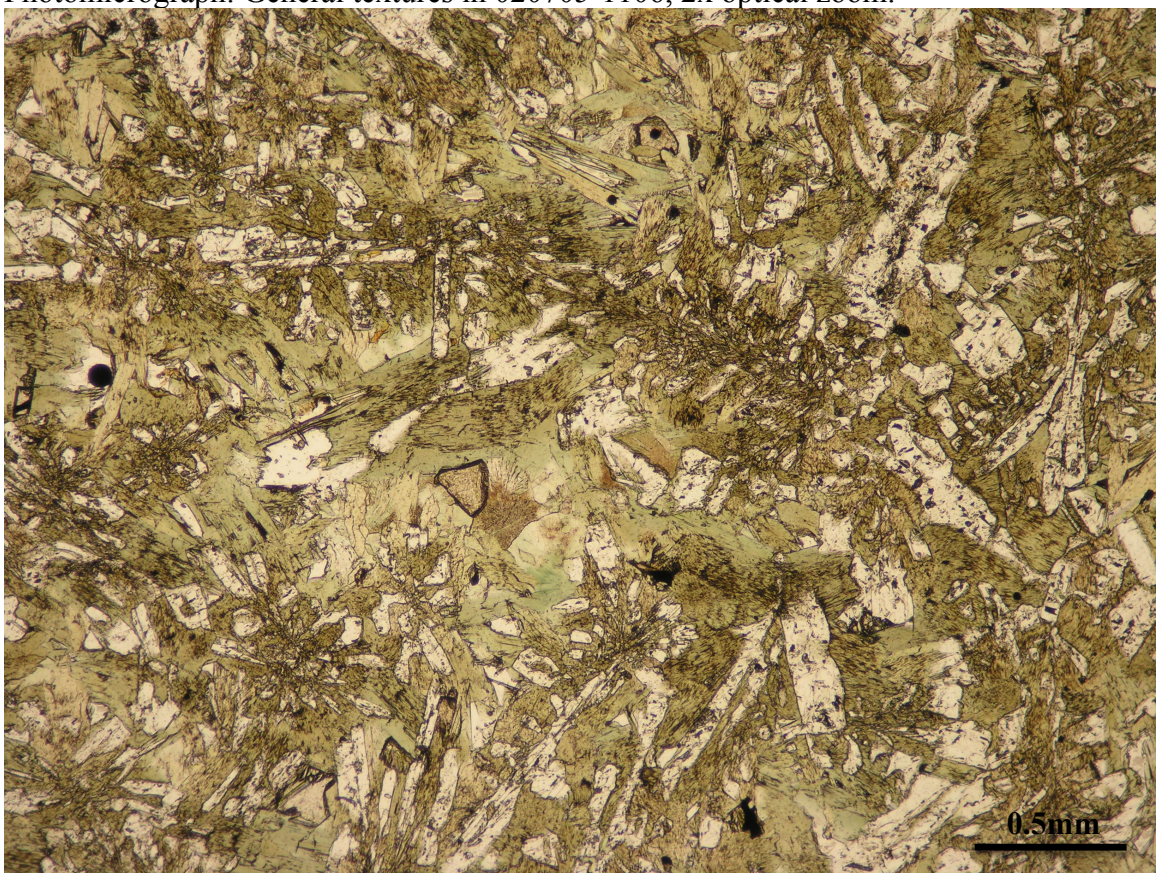

Appendix B.2: Glossary of Textures (Pictures)

1- Wormy Chlorite: fine grain, wormy texture chlorite is a hydrothermal precipitate found in hydrothermal fault breccias.

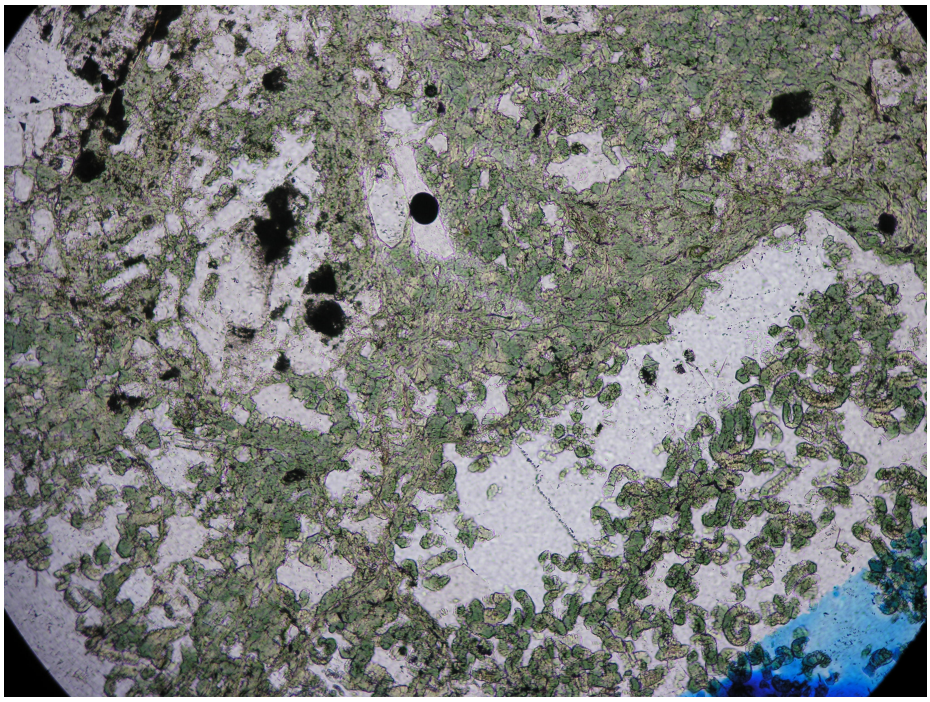

2- Interstitial Sulphide: a sulphide that is dominantly surrounded by primary phases (plagioclase and clinopyroxene), and formed along grain boundaries.

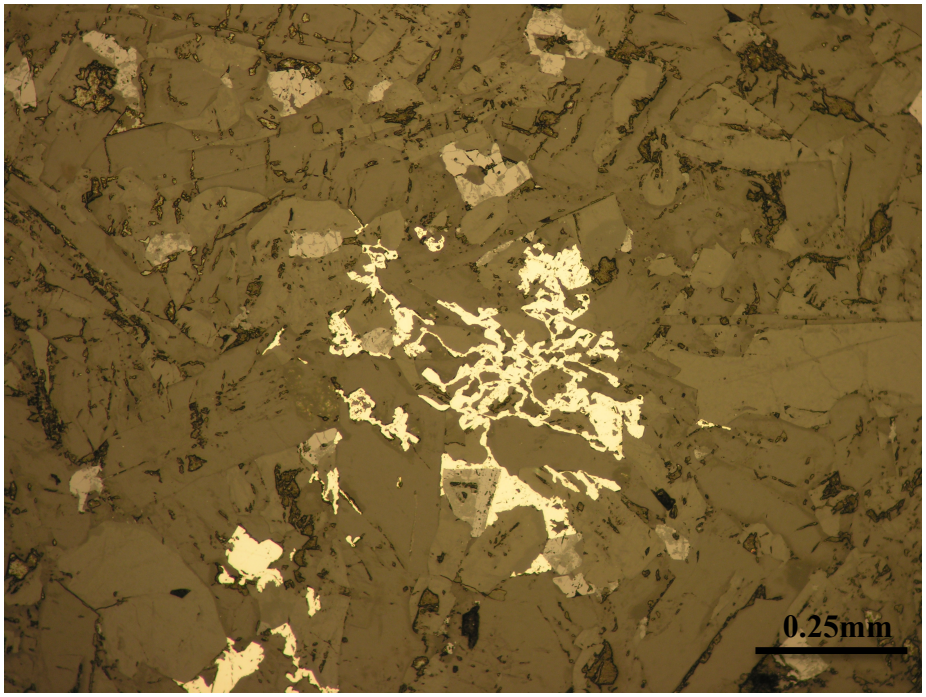

3- Void-filling Sulphide: Fe-Cu sulphide that has filled in a vein or void.

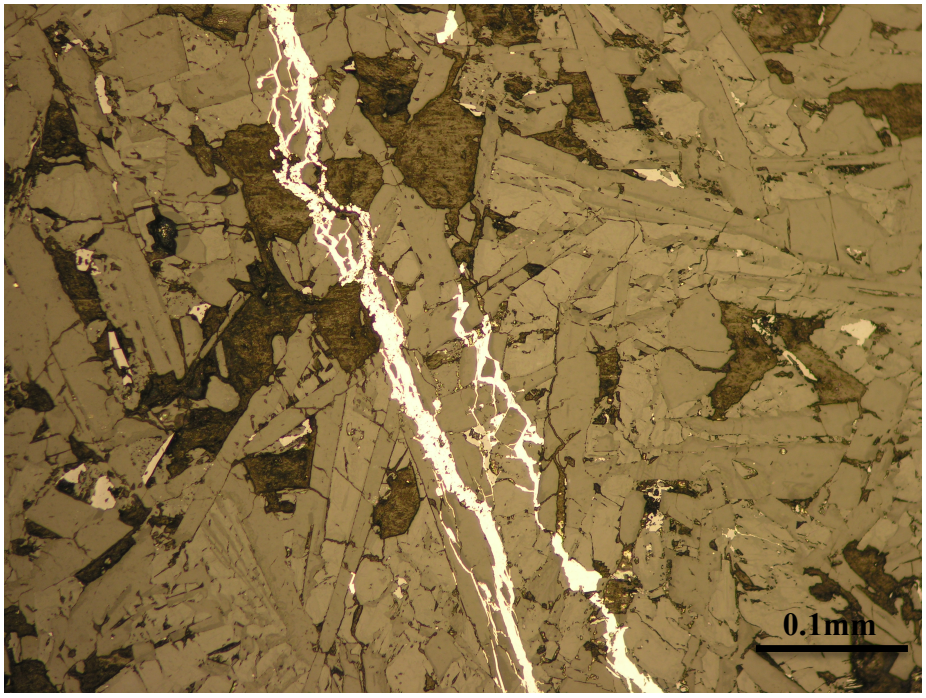

4- Skeletal Oxide: in plane-polarized light these Fe-Ti oxides appear as though they have a blocky habit, however in polarized light that form a skeletal texture.

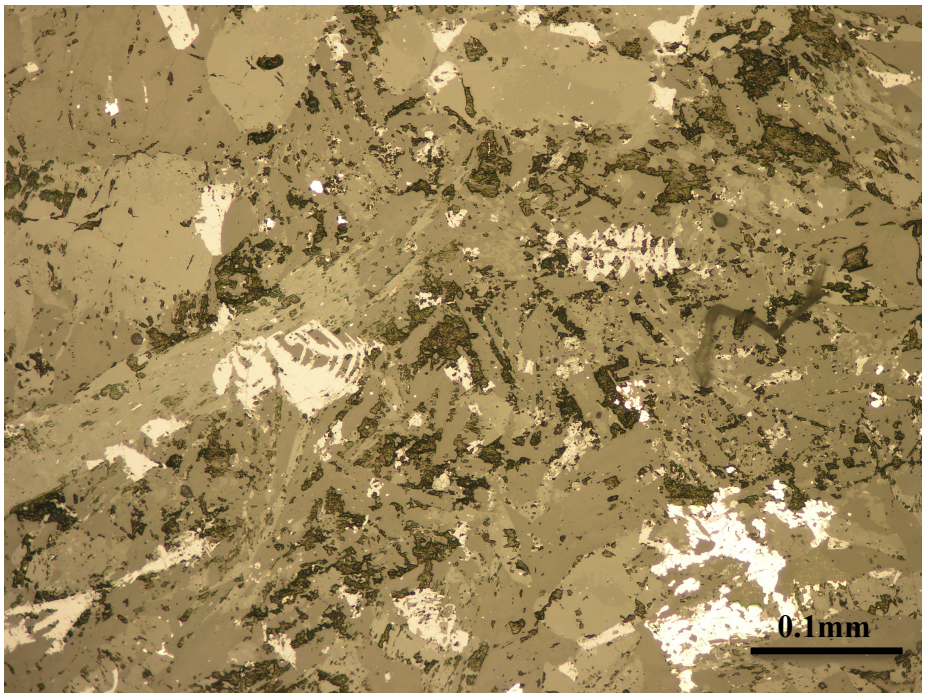

5- Mass of secondary minerals: a mass of secondary minerals is when very fine aggregates form often of mixtures of chlorite and mixed-layer clays replacing groundmass.

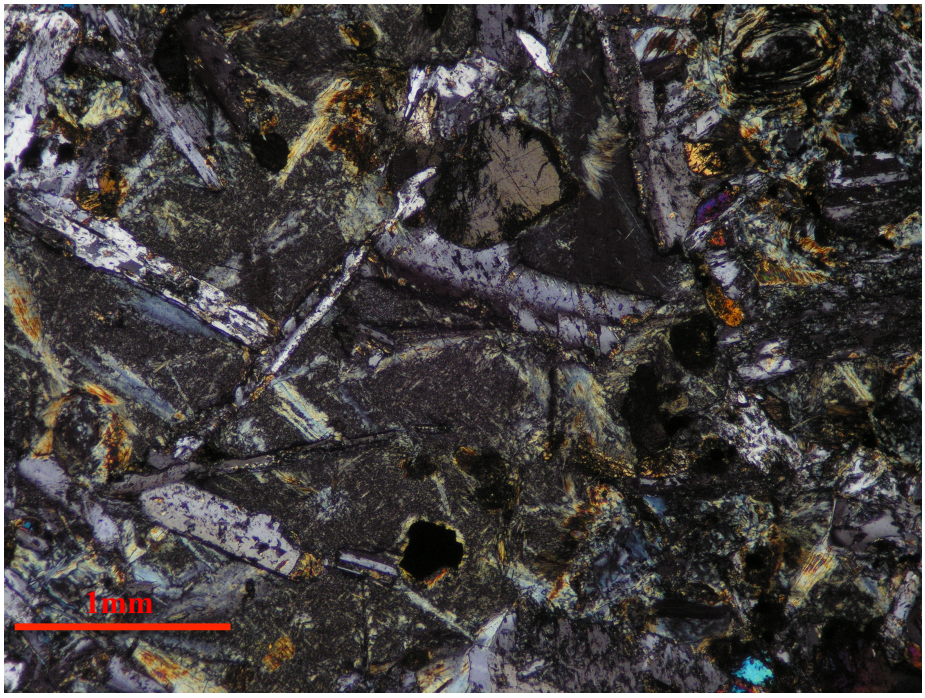

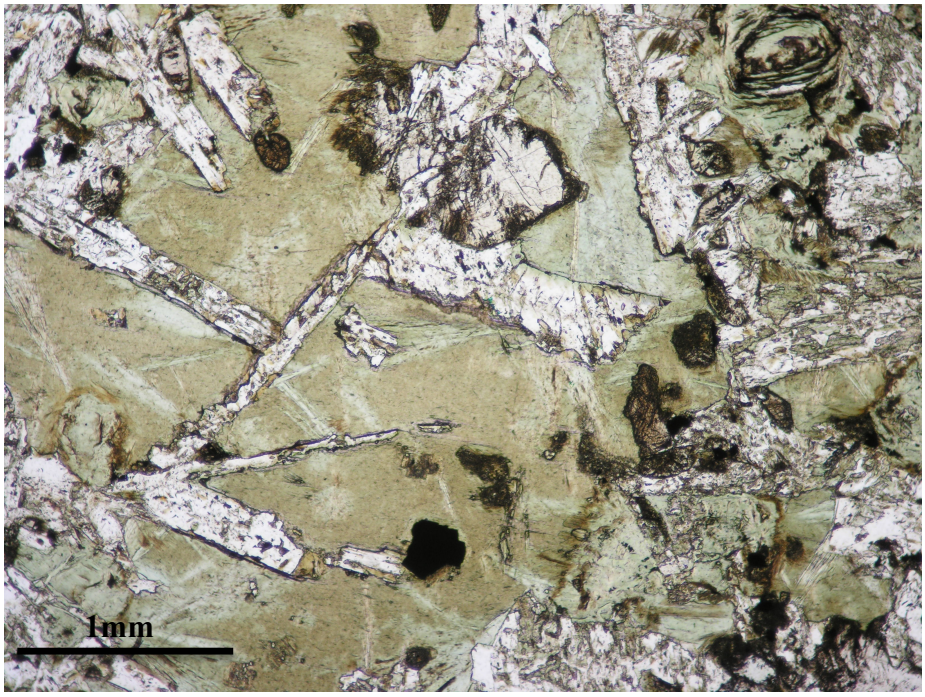

5- Well-formed chlorite: a well-formed chlorite is one that has nicely defined boundaries, is a single grain of chlorite, and has often replaced clinopyroxene.

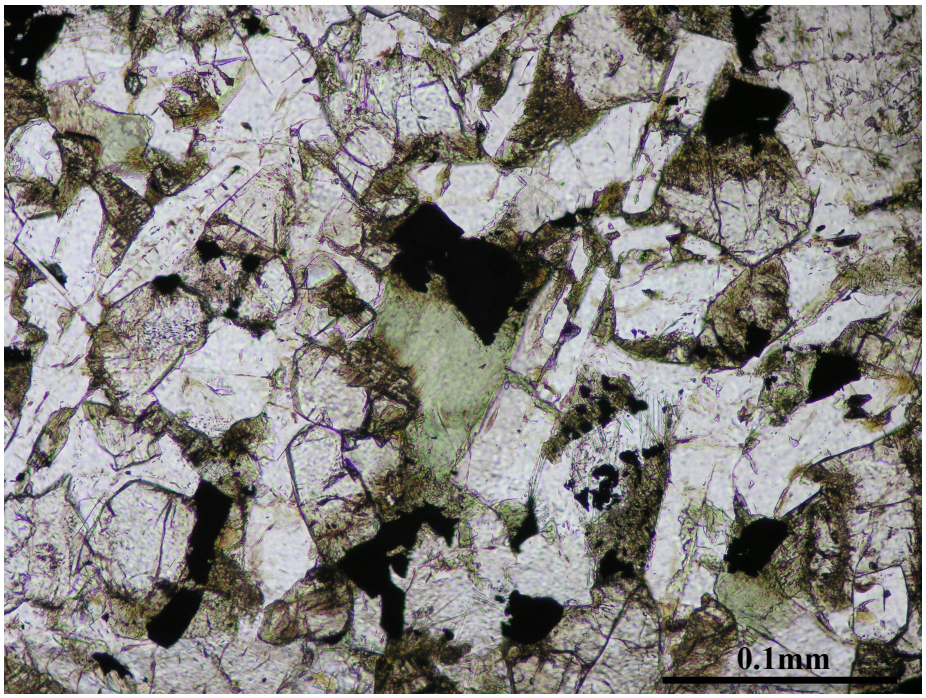

Appendix C: Maps of the Base Metal Regional Distribution

Base metal distribution maps of Area A and Area B at Pito Deep, EPR. The corresponding colour is provided in the legend and represents a range of Δmetal values for Co, Cu, Mn, Ni, Zn, and Pb (**all values are given in ppm**). Transect information can be found in Chapter 1, Appendix B.1, and Figure 1.6.

Cobalt:

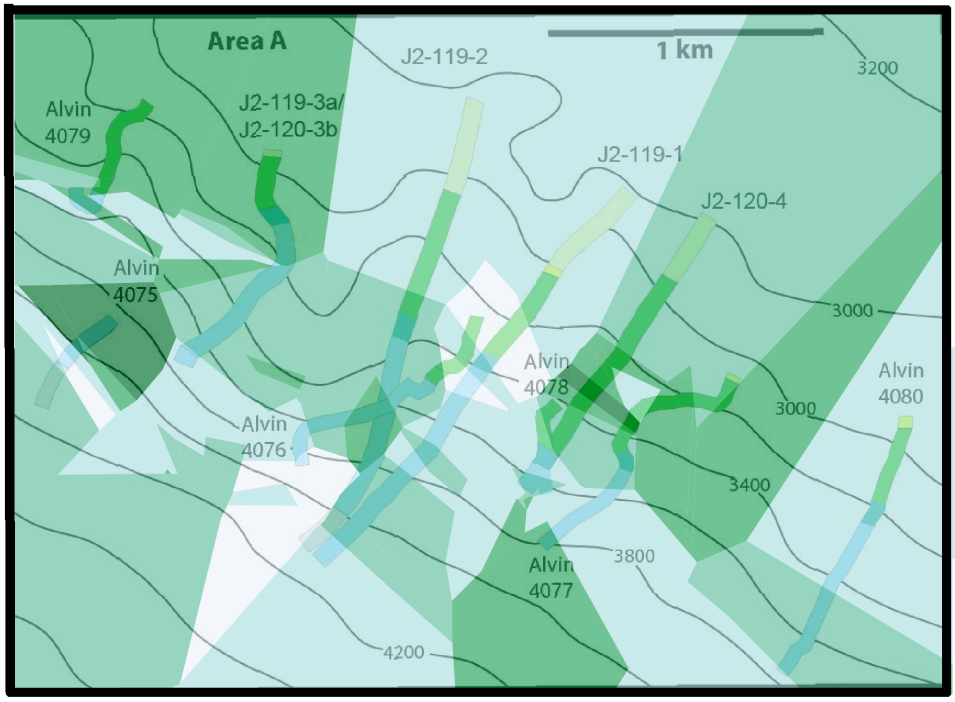
Area A
1 km
J2-119-2
3200
Alvin
4079
J2-119-3a/
J2-120-3b
J2-119-1
J2-120-4
Alvin
4075
3000
Alvin
4078
Alvin
4080
3000
Alvin
4076
3400
3800
Alvin
4077
4200

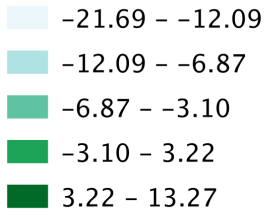
-21.69 – -12.09
-12.09 – -6.87
-6.87 – -3.10
-3.10 – 3.22
3.22 – 13.27

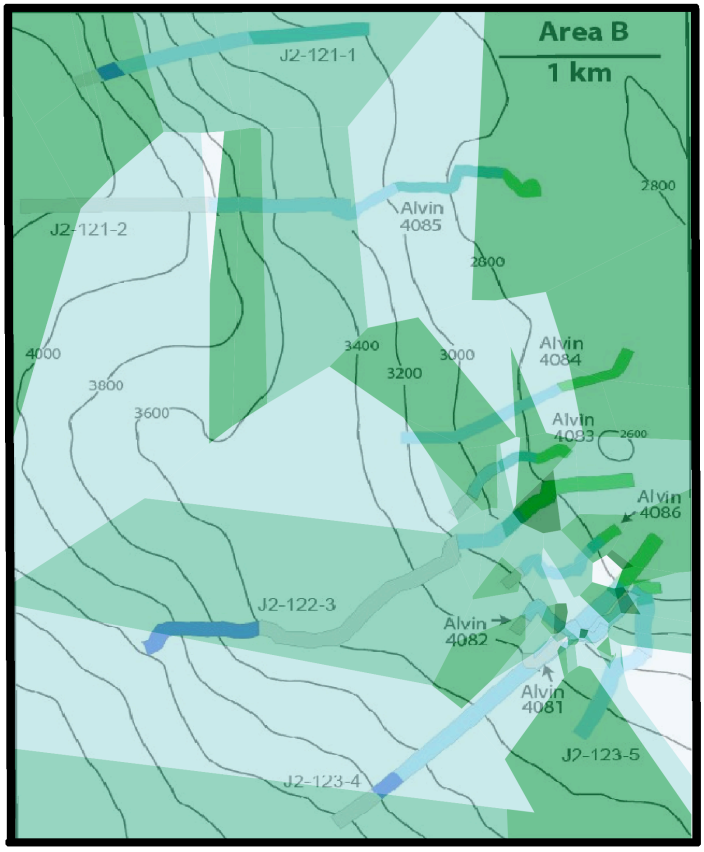
Area B
1 km
J2-121-1
2800
Alvin
4085
J2-121-2
2800
4000
3400
3000
Alvin
4084
3200
3800
3600
Alvin
4083
2600
Alvin
4086
J2-122-3
Alvin
4082
Alvin
4081
J2-123-5
J2-123-4

Copper:

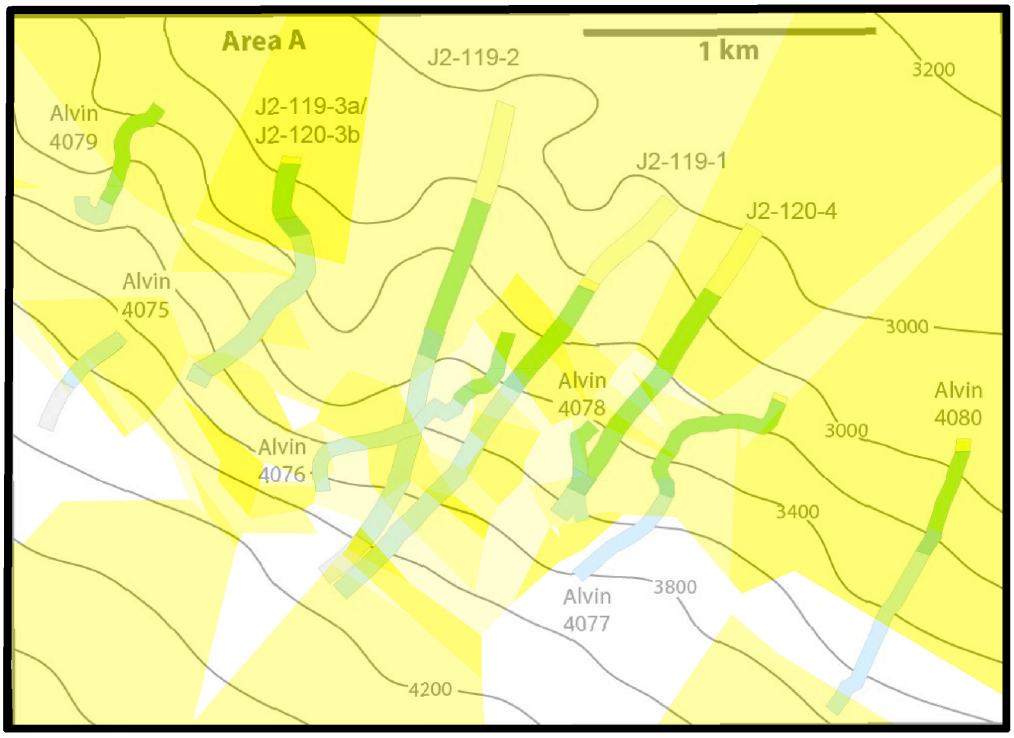

-73.30 – -45.76
-45.76 – -20.56
-20.56 – -8.06
-8.06 – 13.40
13.40 – 65.78

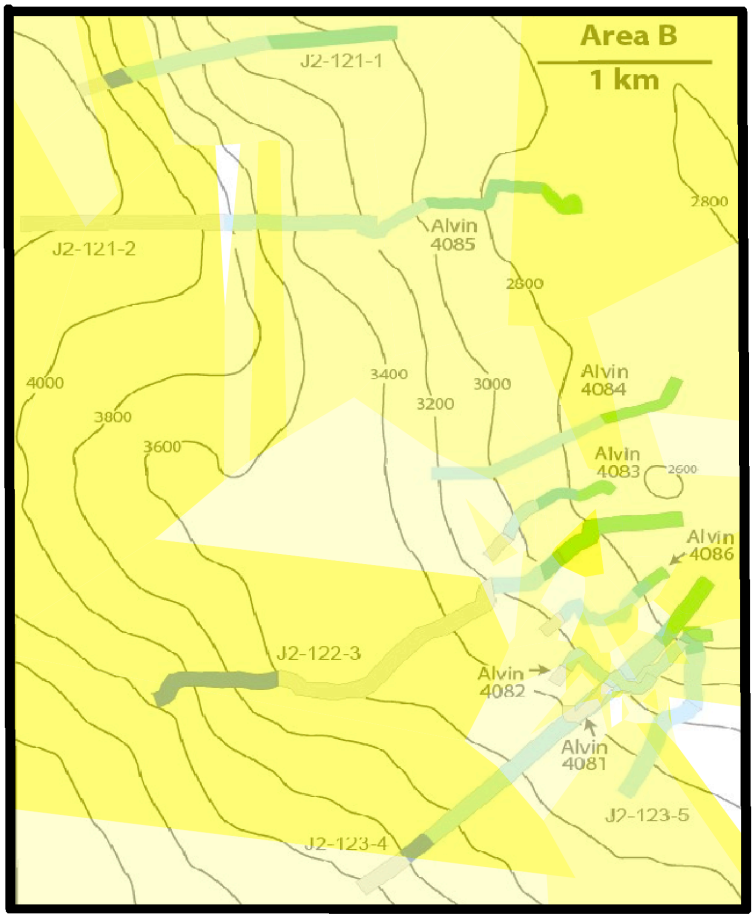

Manganese:

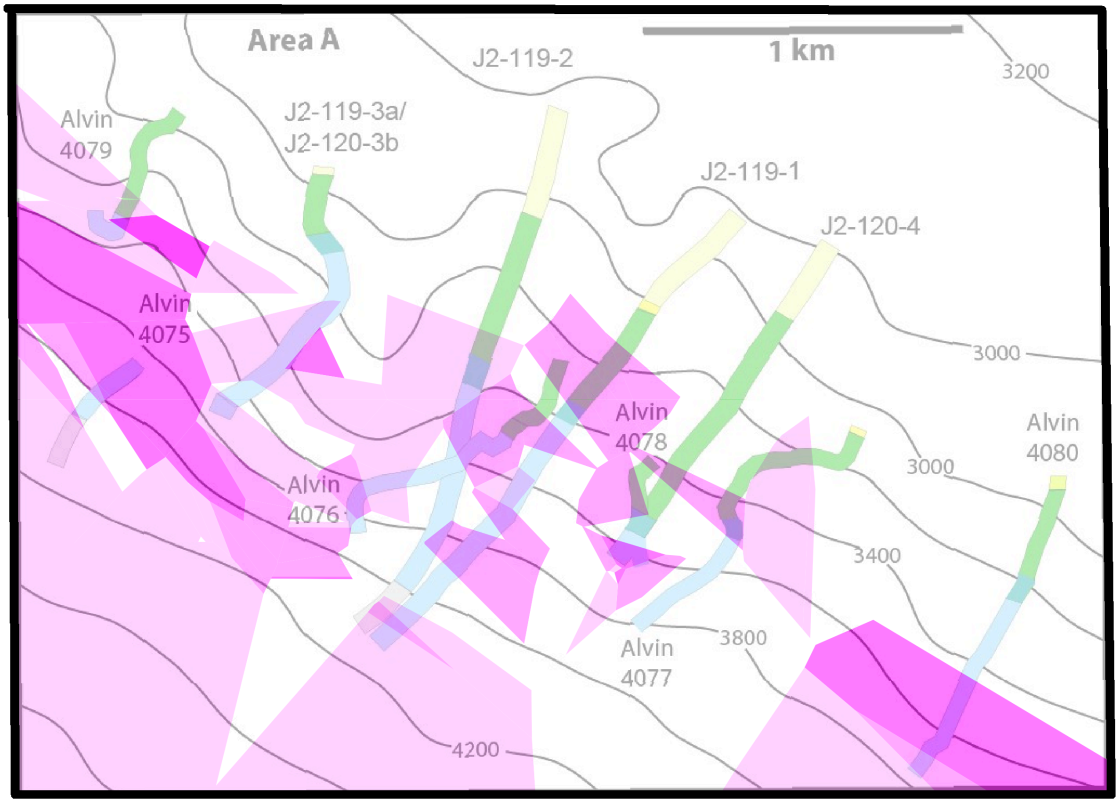

-705.18 – -321.22
-321.22 – -88.49
-88.49 – 129.97
129.97 – 479.96
479.96 – 860.13

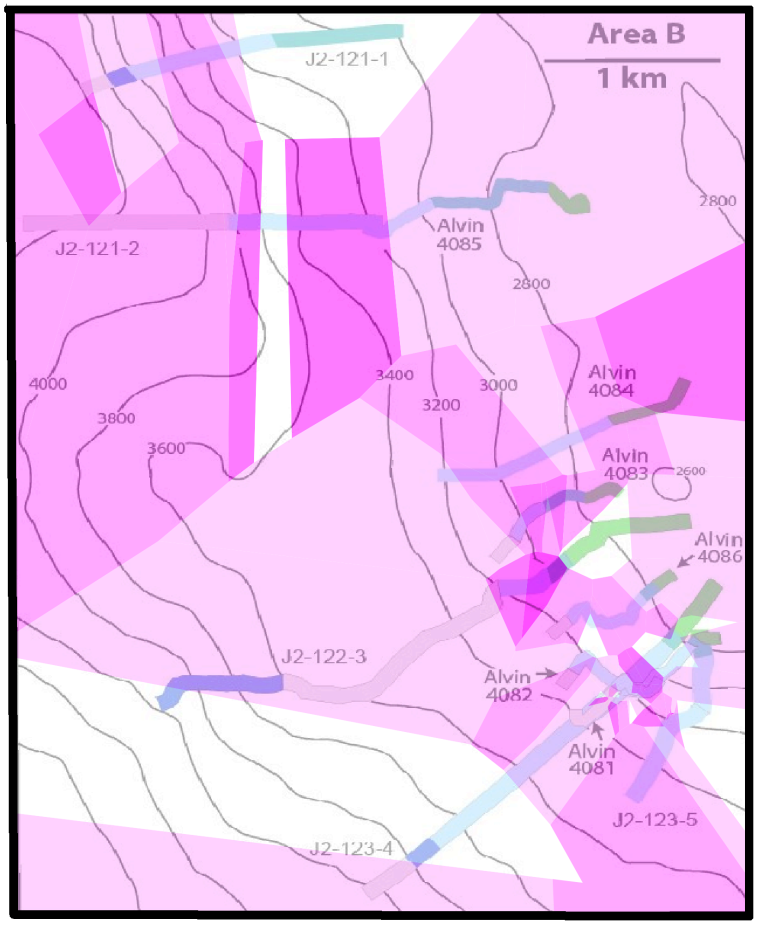

Nickel:

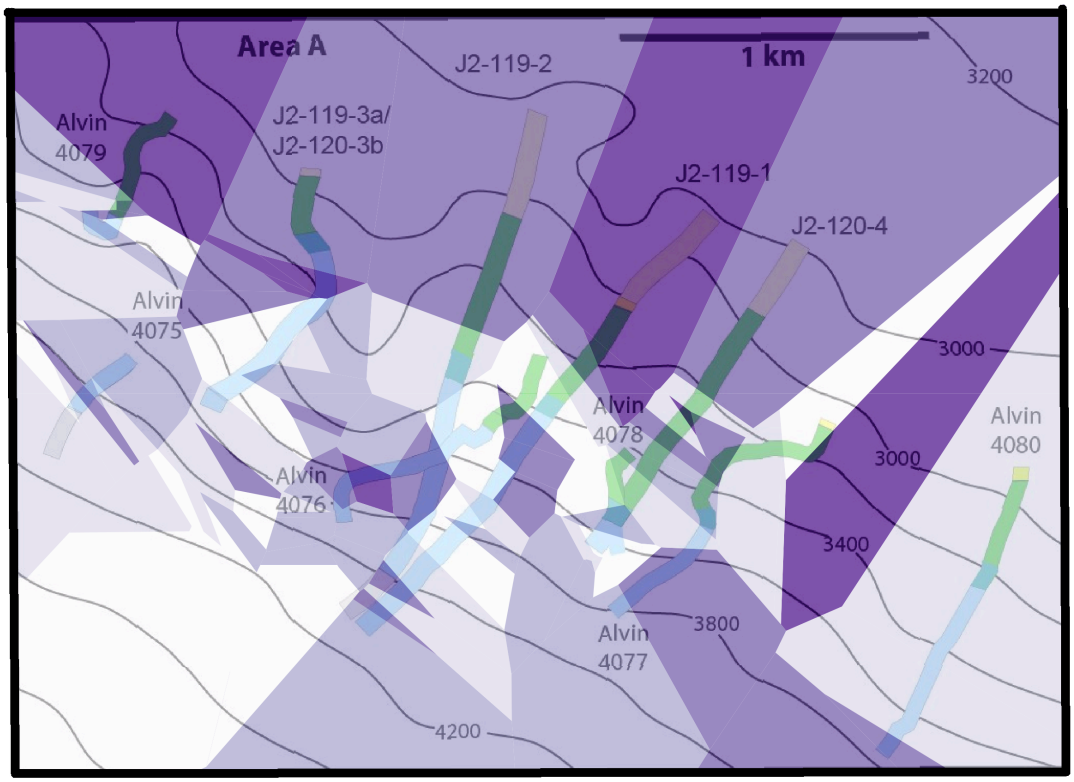

-21.95 – -5.27
-5.27 – 4.06
4.06 – 15.30
15.30 – 30.24
30.24 – 60.89

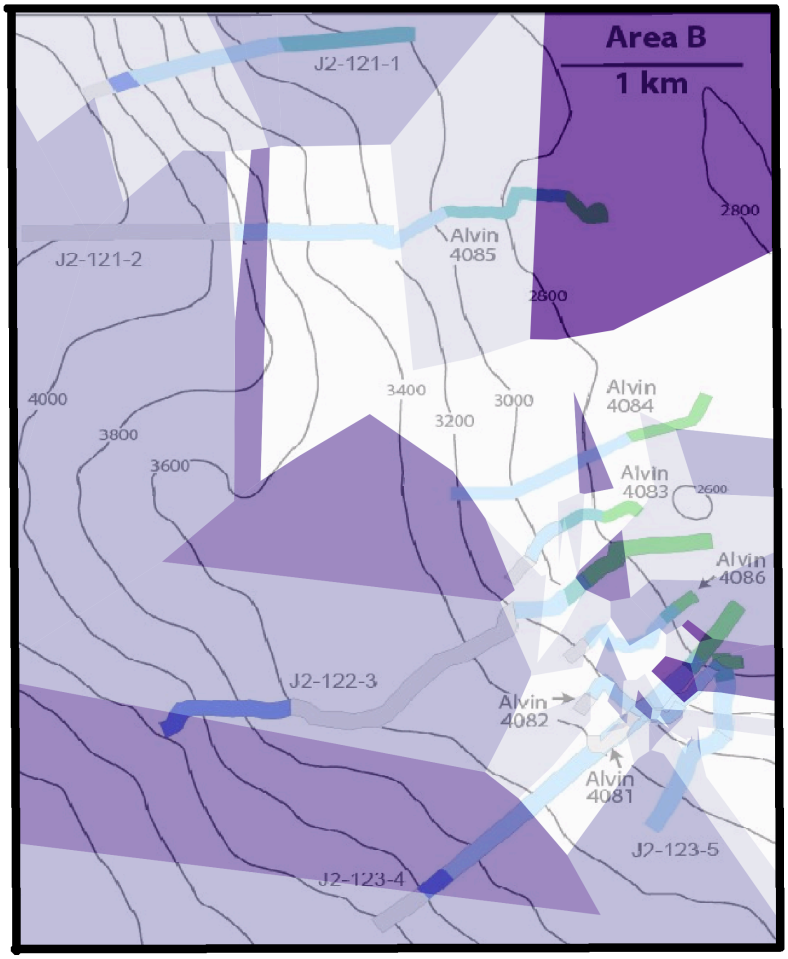

Zinc:

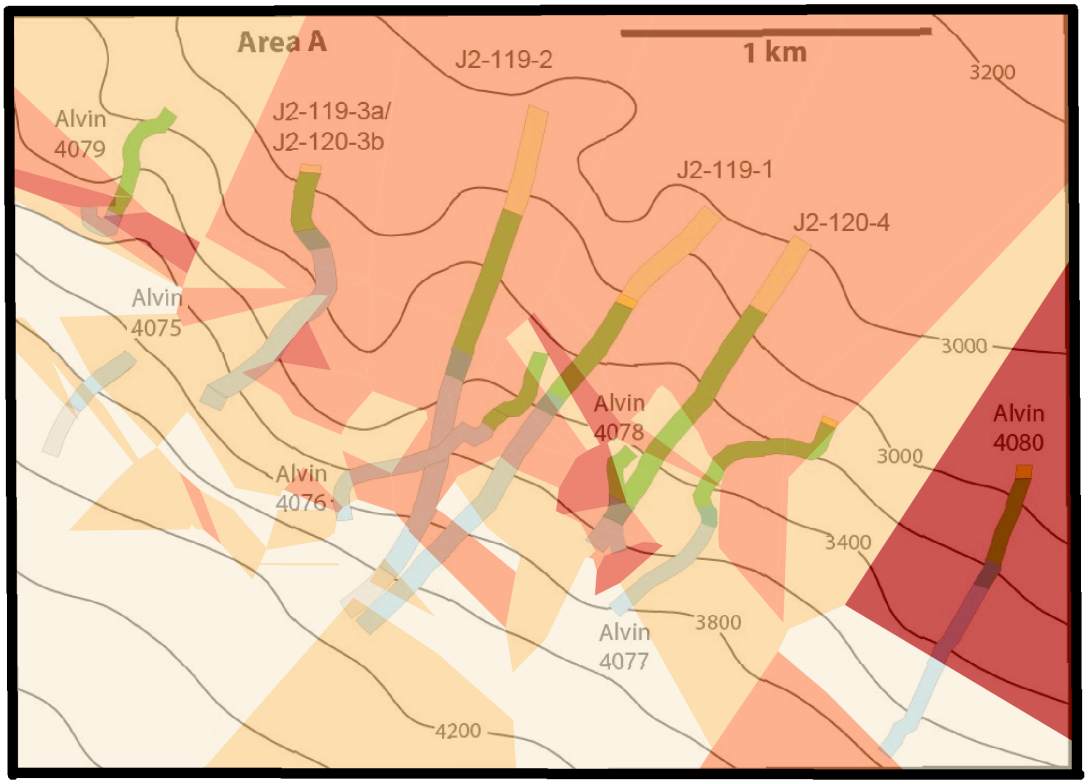

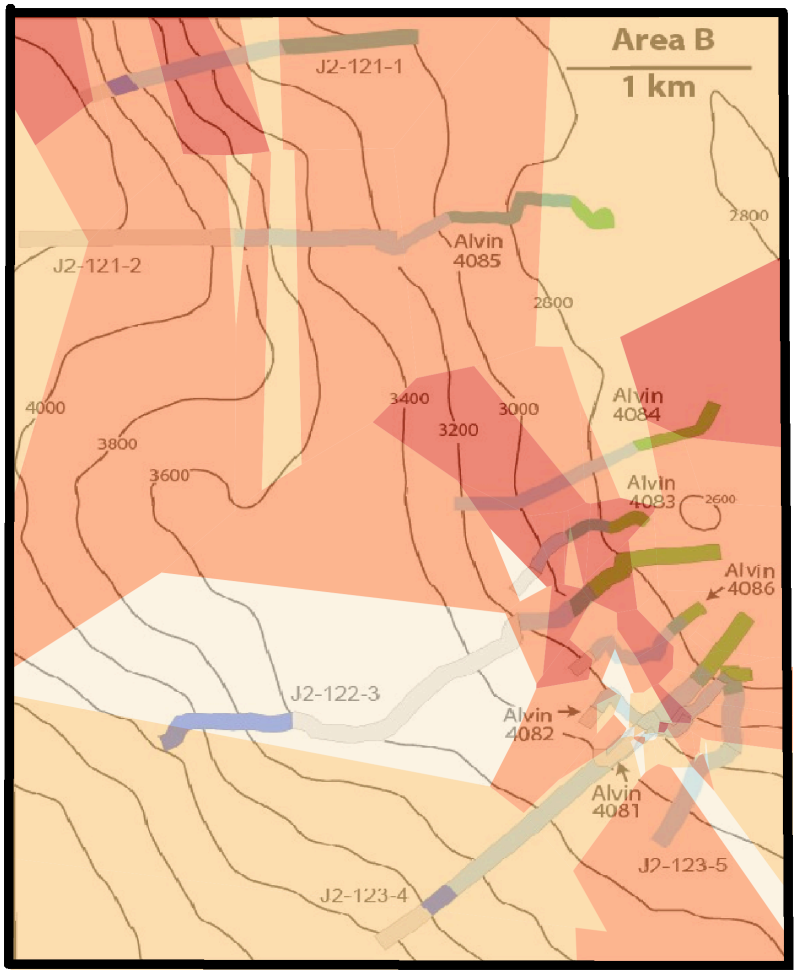

-71.55 – -43.08
-43.08 – -22.48
-22.48 – -4.04
-4.04 – 33.40
33.40 – 1145.36

Lead:

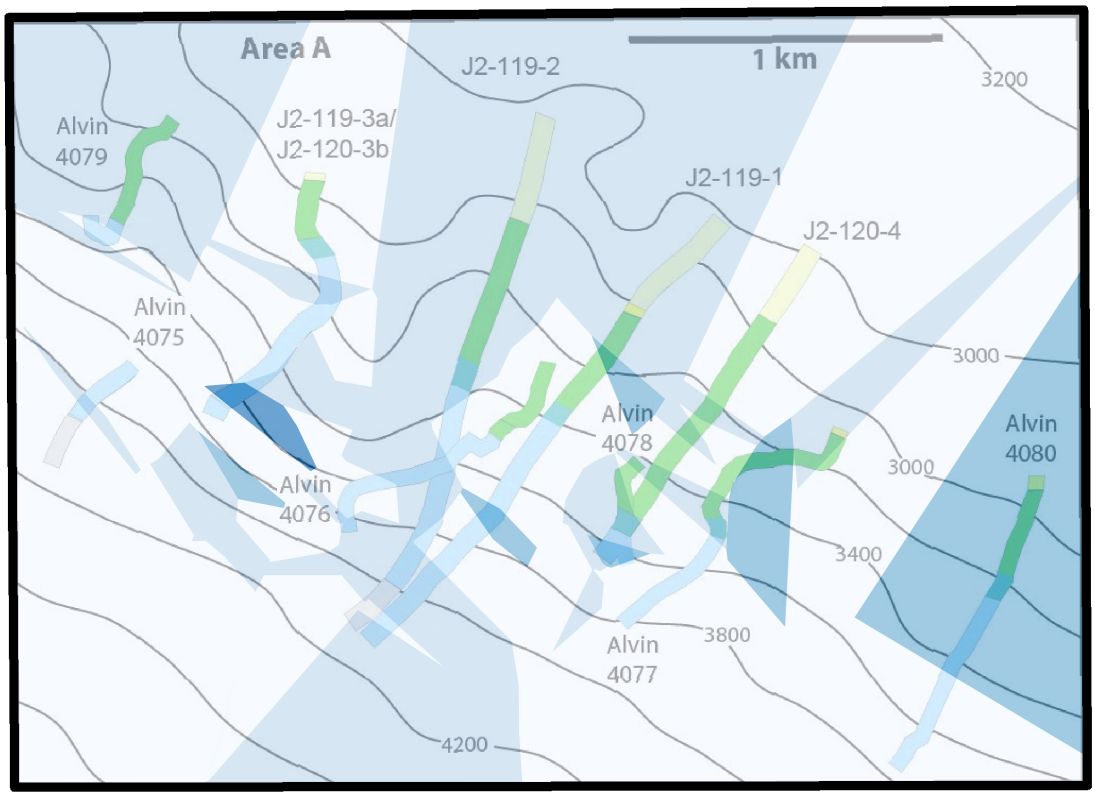
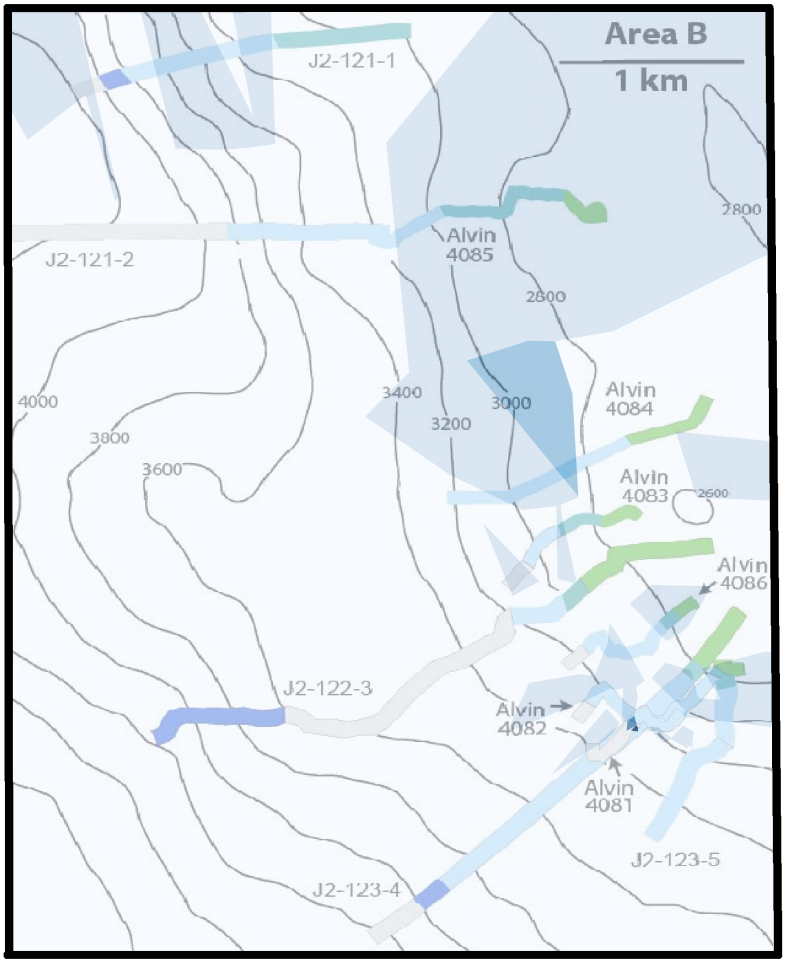
-0.53 – -0.12
-0.12 – 0.50
0.50 – 1.95
1.95 – 3.86
3.86 – 8.50